Tarduno, J.A., Duncan, R.A., Scholl, D.W., et al., 2002
Proceedings of the Ocean Drilling Program, Initial Reports Volume 197

3. Site 1203[1]

Shipboard Scientific Party[2]

BACKGROUND AND SCIENTIFIC OBJECTIVES

The main objective of Leg 197 was to test the hypothesis that the Hawaiian hotspot migrated with respect to the Earth's spin axis in Late Cretaceous to early Tertiary times. Paleomagnetic paleolatitude and radiometric age analyses of basalt recovered at sites drilled on the Emperor Seamounts were the principal analytical tools proposed to conduct the test.

The choice of the Hawaiian-Emperor chain for an investigation of hotspot motion returns us to the origins of the hotspot concept itself, which was based on the age-progressive distribution of volcanoes comprising the Hawaiian Islands (Wilson, 1963). This concept was later extended to the entire Hawaiian-Emperor chain of atolls, seamounts, and guyots (Christofferson, 1968). Many subsequent ideas about geodynamic processes were based on the proposition that hotspots like Hawaii were maintained by plumes fixed in the deep mantle that could be used as a stationary frame of reference for plate motions (Morgan, 1971). Of special importance was the bend in the chain at ~43 Ma, separating the Hawaiian and Emperor Seamounts. This bend is commonly considered to be the best example of a hotspot recording of a change in plate motion.

However, a growing body of data has suggested that hotspots may move at rates as high as several centimeters per year, driven by large-scale mantle advection of plumes (e.g., Tarduno and Gee, 1995; Steinberger and O'Connell, 1998). Therefore, hotspot tracks may record drift of the plume in the mantle as well as plate motion. Leg 197 was designed as a paleolatitude test of the hotspot drift hypothesis. If the Hawaiian hotspot has remained fixed, paleolatitudes determined from paleomagnetic analyses of drilled basalt cores from volcanoes in the chain should yield values equal to the present-day latitude of Hawaii

[1]Examples of how to reference the whole or part of this volume.
[2]Shipboard Scientific Party addresses.

Ms 197IR-103

(~19°N), allowing us to reject the hypothesis of substantial hotspot motion.

The Emperor Seamounts are especially well suited for a paleomagnetic test because of their wide latitudinal distribution and age range. A sequence of time-independent lava flows sufficient to average geomagnetic secular variation was sought at each drilling site to obtain a high-resolution paleolatitude estimate. At the same time, minimally altered volcanic material was required for radiometric analyses to constrain the crystallization age of the flows. Sites were distributed along the Emperor trend to help evaluate processes responsible for the potential hotspot motion. The basalt and volcanic glass available at these sites were also sought for geomagnetic investigations, including studies of the geometry and intensity of the Late Cretaceous to early Tertiary magnetic field. Currently, the Pacific hemisphere is underrepresented in global geomagnetic data compilations.

Sites proposed on the oldest Emperor edifice, Meiji Guyot, were unavailable for sampling during Leg 197 because clearance for drilling was denied by the Russian government (in May 2001). Detroit Seamount was chosen to sample the oldest (Late Cretaceous) part of the Emperor Seamount trend located in international waters (Fig. **F1**). Previous paleomagnetic and radiometric age data from basalt recovered at Ocean Drilling Program (ODP) Site 884 on Detroit Seamount indicate a paleolatitude of 36.2° (95% confidence limits = +6.9°/–7.2°) (Tarduno and Cottrell, 1997) at 81 Ma (Keller et al., 1995), suggesting considerable motion of the hotspot. However, the 87 m of basement penetration at the site provided a limited number of independent readings of the Late Cretaceous magnetic field. This resulted in a relatively high uncertainty in the paleolatitude estimate, limiting the use of these data for constraining a plume migration rate. Accordingly, Site 1203 on Detroit Seamount was selected to obtain a longer magnetic record with a more tightly constrained paleolatitude range.

Another important objective of Leg 197 at Site 1203 was to obtain a record useful for tracing the geochemical evolution of the Hawaiian plume through time. In particular, different models have been proposed to explain geochemical signatures derived from analyses of basalt recovered from Detroit Seamount during ODP Leg 145. These models invoke interaction of the hotspot with a spreading ridge axis (Keller et al., 2000) or temporal changes in the composition of the plume (M. Regelous et al., unpubl. data). Basalt from a longer section drilled at Detroit Seamount could help distinguish between these models as well as contribute to our understanding of the geochemical variation of hotspot magmatism on a time scale as long as 81 m.y.

Rotary coring was planned at Site 1203 with one bit change and reentry using a free-fall funnel (FFF). Cores obtained by rotary coring are azimuthally unoriented, and, hence, only paleolatitude and polarity can be determined from standard paleomagnetic analyses. The dominant north-south distribution of the Emperor Seamounts and the proposed sense of hotspot motion (Tarduno and Cottrell, 1997) make a test using only paleolatitude viable. However, a longitudinal component of hotspot drift can also be inferred from studies examining the consistency of the Hawaiian-Emperor track relative to hotspot tracks on other plates (e.g., Cande et al., 1995). Oriented basalt cores could be used to obtain paleodeclination values and paleomagnetic pole positions, which could be used to test potential longitudinal motion of the Hawaiian hotspot.

F1. Site 1203 location map, p. 51.

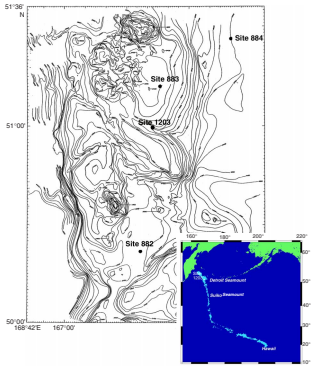

One method to reorient cores obtained by rotary coring is to use overprints from the Brunhes-age Earth's magnetic field that are sometimes preserved in the total remanent magnetization of basaltic rocks (see **"Paleomagnetism and Rock Magnetism,"** p. 23, in the "Explanatory Notes" chapter). Alternatively, logging data can be used. At Site 1203 a comprehensive logging plan was proposed to collect data needed to reorient basement cores. Specifically, we planned to use the Formation MicroScanner (FMS) to obtain an oriented image of borehole fractures. Borehole fractures imaged in this way can sometimes be matched to features identified in the recovered cores, allowing for core reorientation (see **"Physical Properties,"** p. 27, and **"Downhole Measurements,"** p. 31, both in the "Explanatory Notes" chapter). In addition, we planned to log with the three-axis fluxgate sensor Goettingen Borehole Magnetometer (GBM) and the SUSLOG 403-D magnetic susceptibility tool at Site 1203 to test how well these instruments could characterize the magnetic environment of the borehole and the magnetization of the drilled basement section. Beyond these tools, standard logging with the triple combination and natural gamma ray tools was scheduled to aid in characterizing the stratigraphy of the basement sequence drilled. We also planned to use the dipole sonic imager (DSI) to obtain compressional and shear wave velocities useful for correlation of log and seismic data.

ODP Site 1203 was chosen along a seismic profile (Lonsdale et al., 1993) revealing an area of thin (400–500 m thick) sediment cover on the summit of Detroit Seamount. To better characterize the structural and stratigraphic setting of the site, a seismic survey using the *JOIDES Resolution* was conducted immediately prior to drilling (see **"Underway Geophysics,"** p. 46). This survey confirmed the simple and seemingly flat basement structure at Site 1203. Coring was planned to commence in the sedimentary section to characterize the environment of the basement–sediment transition, determine the age of the transition using micropaleontological analysis, and potentially recover a North Pacific record of the Late Paleocene Thermal Maximum.

OPERATIONS

Transit to Site 1203 and Underway Survey

In the early afternoon of 5 July 2001, the *JOIDES Resolution* departed Yokohama, Japan, and sailed northeasterly to Detroit Seamount. This volcanic edifice, in the northwest corner of the Pacific Basin at the northern tip of the north-northwest–trending Emperor Seamount chain, was the first of four Emperor Seamounts (Detroit, Nintoku, Ojin, and Koko Seamounts) scheduled to be drilled during Leg 197.

The *JOIDES Resolution* arrived in the vicinity of Detroit Seamount in the early morning of 11 July and began a ~14-hr seismic reflection survey to record multicrossings of two proposed sites, HE-3A and HE-3B. These sites had been selected along single-channel analog records gathered in 1988 by the *Thomas Washington* (Lonsdale et al., 1993). Profiles of good quality were digitally recorded and presented at low exaggeration on EPC line-scan recorders (see **"Underway Geophysics,"** p. 46). At 1645 hr on 11 July, the survey was concluded and the seismic equipment was retrieved. The thrusters and hydrophones were extended, and the vessel was situated over the coordinates of proposed Site HE-3A

(which became Site 1203) at 1715 hr. The beacon was deployed at 1807 hr.

Hole 1203A

After the vessel settled on location, the corrected precision depth recorder (PDR) depth referenced to the dual elevator stool (DES) was obtained and indicated 2604.4 m. The bottom-hole assembly (BHA) was made up of a 9.875-in rotary core barrel (RCB) medium-hard formation C-4 bit, a mechanical bit release, a modified head sub, an outer core barrel, a modified top sub, a modified head sub, seven 8.25-in drill collars, a tapered drill collar, six 5.5-in drill pipe segments, and one crossover sub. Hole 1203A was spudded with the RCB at 0145 hr on 11 July. The drill string was drilled ahead with a wash barrel in place to a depth of 70.6 meters below seafloor (mbsf), when an electrical fault forced coring operations to be prematurely terminated.

Loss of Power

According to the engine room data management system records, at 0259 hr on 12 July a fault alarm occurred in the power control console for thruster 1. The console housing these control circuits and breaker (thyrig bay 1) is located in the forward thyrig room, just below the galley in the forward part of the vessel. The electrical fault forced one of the three main generators providing ship's power to drop off-line. As a result of the rapid drop in the supplied power, the power management system compensated by load shedding noncritical demand. The main power was stabilized when an additional generator was powered up only 4 min after the event.

At 0305 hr, smoke was detected emanating from the forward thyrig room and at the same time all thrusters were automatically dropped off-line. The vessel began to drift off location. The drill crew was instructed to immediately stop drilling and hang the drill string off at the DES with the 500-ton elevators. The vessel had drifted off location by as much as 200 m (9% of water depth) before positioning control could be restored. To ensure that no damage was inflicted on the BHA or drill string by the excursion off location, the drill string was recovered and the pin and box connections of the BHA components were subjected to a magnetic particle inspection. No cracks or bent tubulars were found.

At 1630 hr on 12 July, Hole 1203A was respudded and drilled ahead with a center bit to 300 mbsf at an average rate of penetration (ROP) of 124 m/hr. After the center bit was recovered, the core barrel was dropped and coring was initiated. Sediment coring proceeded rapidly to 462.0 mbsf, where basaltic basement was contacted. A total of 162.0 m of nannofossil calcareous ooze and chalk was cored at an average ROP of 58.9 m/hr. A total of 78 m of sediment was recovered for an average recovery of 48.2%.

Rotary coring continued 232.7 m into basement (694.7 mbsf), when operations were suspended to change the bit. The average recovery for basement was 55.8%, representing 129.7 m of basalt and volcaniclastic sediment. The average ROP in basement was 3.8 m/hr. The ROP in basement ranged from a lethargic 1.7 m/hr (Core 197-1203A-34R [608.3–612.3 mbsf]) to a frenetic 115.2 m/hr (Core 197-1203A-24R [521.5–531.1 mbsf]). No problems were encountered with hole stability or erratic torque during the first bit run. The bit accumulated 66.9 hr of rotation before being recovered.

Reentry 1

The top drive was set back, and the drill string was pulled back in the hole to 142 mbsf. A FFF was rigged up in the moonpool and was launched at 1015 hr on 17 July. The vibration-isolated subsea television camera was then deployed and positioned over the hole to observe the condition of the FFF during the extraction of the drill string. The BHA was pulled clear of the seafloor at 1205 hr. As the bit cleared the throat of the FFF, a 1- to 2-m-long squid was observed to embrace the outer core barrel.

A new C-7 hard-formation rotary bit was affixed to a fresh mechanical bit release and made up to the BHA. The FFF was reentered at 0008 hr on 18 July. The drill string was advanced to a depth of 655 mbsf. The top drive was picked up, and the drill bit was positioned at the bottom of Hole 1203A at 694.7 mbsf. Approximately 3.5 m of soft fill was found at the bottom of the hole. Rotary coring resumed in Hole 1203A at 0400 hr on 18 July and advanced through alternating layers of veined and vesicular basalt flows interbedded with volcaniclastic sediment. Coring continued until, at a total depth of 914.6 mbsf (Table T1), the time allocated for Site 1203 expired. The penetration rate while coring with the second bit varied from 1.0 m/hr (Core 197-1203A-48R [727.1–732.0 mbsf]) to 16.5 m/hr (Core 197-1203A-64R [866.6–876.2 mbsf]). Core recovery ranged from 1% to 103% (average recovery = 57.4%).

T1. Coring summary, Hole 1203A, p. 147.

A total of 219.9 m of basement was cored with the second bit at an average ROP of 2.6 m/hr. The second bit acquired 88.3 rotating hours and was still viable when released at the bottom of the hole. The thickness of basement cored was 452.6 m, with 255.87 m recovered (recovery = 56.5%) at an average ROP of 3.1 m/hr. The overall results in Hole 1203A were 300 m drilled, 614.6 m cored, and 333.91 m recovered (recovery = 54.3%). The only hole trouble experienced while drilling or coring was when the drill string stuck after picking off bottom to retrieve Core 197-1203A-49R (732.0–741.6 mbsf). After the driller worked the drill string for 30 min with applications of up to 100,000 lb of overpull, the pipe was freed.

The weather on site was, although foggy, mild and under the influence of a large Pacific high. The air temperatures ranged from 6° to 9°C. Seas and swell never exceeded 5 ft, and heave ranged from 1 to 5 ft, with 2 ft being typical. These agreeable conditions contributed to the good recovery and extended bit life.

Because of a high oil temperature problem, which was due to a misadjustment of the pump controls, the active heave compensator (AHC) was not online until 16 July. The AHC was used continuously while coring from 665.9 to 905.0 mbsf. It was intentionally turned off while cutting the final core (905.0–914.6 mbsf) to see if recovery would be affected. The recovery dropped from 47.5% to 39.5% on the last two cores. The AHC acquired 92 hr of operation on this site.

Logging

In preparation for logging, a 30-bbl sepiolite mud flush was circulated in the hole and a wiper trip was conducted between 145 and 914.6 mbsf. Following the routine displacement of the borehole with 280 bbl of sepiolite, the bit was released at the bottom of the hole. The Schlumberger equipment was assembled, and the bottom end of the BHA was placed at 202 mbsf.

During the first logging run, the triple combination (triple combo) tool string was lowered to the bottom of the hole at 915 mbsf without difficulty and logging proceeded downward (dual laterolog [DLL] and natural gamma ray). The second pass was conducted upward at 274 m/hr from 915 mbsf to the base of the pipe. Excellent data quality and repeatability were recorded along the whole section scanned during these two passes.

During the second logging run, the FMS/sonic tool string also succeeded in reaching the bottom of the hole without difficulty and logging proceeded upward at 274 m/hr. The first pass recorded FMS and sonic data only in the basement section, from 915 to 420 mbsf. The tool string was lowered to the bottom of the hole, and a second pass was conducted in the basement as well as the sedimentary section. Data quality in the basement was excellent. However, in the sedimentary section overlying basement and in some of the volcaniclastic interbeds in the basalt, the borehole was washed out, and, consequently, the FMS data are not usable.

The third logging run was made with the GBM. The first pass was interrupted by an apparent oversaturation of the x-component of the three-axis measured magnetic field. The problem was quickly corrected, and the tool was lowered; good quality data were recorded downhole and uphole. The fourth logging run was devoted to the magnetic susceptibility tool. This run was canceled when an electronic power supply fault could not be repaired in a timely fashion. The logging operations were secured at 0200 hr on 25 July.

After the logging equipment was rigged down, the drill string was recovered and the BHA was dismantled in preparation for the short trip to Site 1204. The beacon was successfully recalled and retrieved. After the drilling equipment was secured, the vessel departed at 0730 hr on 25 July to run an underway survey over a northern proposed site, HE-3, which is at ODP Site 883.

LITHOSTRATIGRAPHY

At Site 1203, the first 300 m of pelagic sediment was drilled ahead with a center bit and the lower sedimentary section was RCB cored before reaching basalt at 457 mbsf. At nearby Site 883 (15.5 nmi), drilled during Leg 145 (Rea, Basov, Janecek, Palmer-Julson, et al., 1993), the whole sedimentary section was cored by advanced piston corer/extended core barrel, to which reference is made for younger sediment not recovered at Site 1203.

The recovery in Hole 1203A was low, owing to the type of drilling used (RCB) and the possible occurrence of sandy intervals that washed out of the core barrel. Therefore, it is not possible to conduct a full-scale comparison of the sediment recovered from Site 1203 with that from Site 883. But the main features of the lithologies reported from Site 883 are recognizable at Site 1203. Three major sedimentary units, Units I, II, and III, early Eocene to late Miocene in age, have been identified at Site 1203, for a total of ~157.56 m. Units I and III have each been divided into subunits, IA and IB and IIIA and IIIB (Fig. **F2**), on the basis of downcore change in carbonate content (Table **T2**). These units overlie a fourth lithologic sequence, basaltic basement. Farther downhole, short sequences of interbedded sediment of mainly volcaniclastic origin are present; these are described in **"Physical Volcanology and Igneous Petrology,"** p. 11. The upper part of the Hole 1203A cores (Unit I) consist

F2. Lithology, units, time framework, and principal components, p. 52.

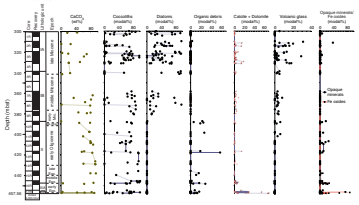

T2. Carbonate abundance, p. 149.

of pelagic sediment composed of siliceous and calcareous oozes (Cores 197-1203A-1R to 9R). In Subunit IA, alternating nannofossil and diatom ooze beds are present in varying proportions, characterized by gradational contacts. Nannofossil and diatom abundance is complementary and accounts for nearly all of the sediment. Below, in Subunit IB, diatom abundance decreases until this component virtually disappears in Unit II, which is calcareous chalk. Close to the Subunit IB/Unit II boundary (Section 197-1203A-10R-1), large sponge spicules and other siliceous microfossils (e.g., radiolarians and silicoflagellates) are abundant. Vesicular fragments of unaltered volcanic glass are present toward the top of Unit II.

The disappearance of diatom-bearing sediment marks the Subunit IB/Unit II boundary. In Unit II, nannofossil and calcareous chalk beds contain clay as a minor component. Foraminifers are also present, both as fragments and preserved silt-sized tests, thus forming nannofossil foraminifer ooze (see **"Site 1203 Smear Slides,"** p. 265). Unit III contains firm sandy silt beds directly overlying basement volcanic rock with a peak in the authigenic carbonate content (up to 60–70 modal% of calcite, dolomite, and, possibly, other carbonates) at its base (Subunit IIIB). At the topmost part of Subunit IIIB, red and brown clay deposits are present.

The calcareous taxa *Thoracosphaera* spp. and foraminifers are present throughout the units, although they are commonly more abundant (i.e., as much as 19% at 455.8 mbsf [Section 197-1203A-17R-2] and 21% at 331.4 mbsf [Section 197-1203A-4R-CC]). At some levels, authigenic rhombohedral calcite was observed where nannofossils are less abundant (i.e., Sections 197-1203A-4R-1, 70 cm [329.7 mbsf], and 197-1203A-4R-CC, 7 cm [331.5 mbsf]).

Further detailed description of cores are provided in the barrel sheets (see **"Site 1203 Core Descriptions,"** p. 1).

Description of Lithologic Units

Unit I

Interval: 197-1203A-1R-1, 0 cm, to 10R-2, 20 cm
Depth: 300.0–388.9 mbsf
Age: early Oligocene to late Miocene

Unit I (300.0–388.9 mbsf) consists of nannofossil ooze and diatom ooze beds, with diatom abundance diminishing downhole. This unit consists of core sections characterized by alternation of two end-member lithologies (i.e., nannofossil ooze and diatom ooze) along with a hybrid sediment type containing approximately equal amounts of siliceous and calcareous microfossils. We refer to the hybrid type as nannofossil-diatom mixed ooze. A drastic reduction in diatom abundance occurs in Cores 197-1203A-3R and 7R (Fig. **F2**).

Unit I has been divided into two subunits, Subunits IA and IB, based on the downhole variation in carbonate content (Table **T2**), which matches estimated nannofossil content from smear slides (Fig. **F2**) (see **"Site 1203 Smear Slides,"** p. 265) and sediment color.

Subunit IA

Interval: 197-1203A-1R-1, 0 cm, to 5R-CC, 10 cm
Depth: 300.0–341.7 mbsf
Age: middle to late Miocene

Subunit IA contains nannofossil-diatom mixed ooze, nannofossil ooze, and diatom ooze. The diatom component can vary greatly over a short core interval (10%–90%), but it is consistently at a relatively high level down to the bottom of Core 197-1203A-5R. Compositional variations within and between the different types of ooze result in distinct light green and grayish green bedding and lamination throughout Subunit IA. Large gaps in recovery are present in Cores 197-1203A-5R and 6R (which recovered only 23 cm in the core catcher), and therefore we were not able to exactly place the boundary between Subunits IA and IB. The best approximation for the Subunit IA/IB boundary is at the bottom of Core 197-1203A-5R, where there is a change in the downhole trend of carbonate abundance along with the presence of distinct alternation of diatom-rich vs. nannofossil-rich sediment. Specifically, diatom ooze containing 88%–97% diatoms is more common in Subunit IA (Fig. **F2**) than in Subunit IB, and in the latter, nannofossil ooze dominates with the exception of a middle Miocene peak in diatom abundance (i.e., 97% at 371.4 mbsf).

Subunit IB

Interval: 197-1203A-5R-CC, 10 cm, to 10R-2, 20 cm
Depth: 341.7–388.9 mbsf
Age: late Oligocene to middle Miocene

Subunit IB is characterized by alternating white nannofossil to light gray nannofossil chalk and siliceous microfossil sediment. Distinct *Zoophycos* trails are present (Fig. **F3A**). It is marked by an increase in the carbonate content and high nannofossil and variable diatom content (12%–77%). At the top of Core 197-1203A-10R, olive-colored (2.5Y 5/3) sediment indicates input of clay and organic-rich debris in a meter-thick interval.

The Subunit IB/Unit II boundary is located at Section 197-1203A-10R-2, 19 cm (388.9 mbsf), and is characterized by a gradational and bioturbated contact between white (2.5Y 8/2) siliceous nannofossil chalk and light brownish gray (2.5Y 6/2) nannofossil chalk (Fig. **F3B**). This boundary signifies the beginning of the diatom deposition at 388.9 mbsf during the late Oligocene and corresponds to the Subunit IIIB/IVA boundary at 652 mbsf established at Site 883 (Leg 145) (Rea, Basov, Janecek, Palmer-Julson, et al., 1993).

F3. Core photos of lithologies observed, p. 53.

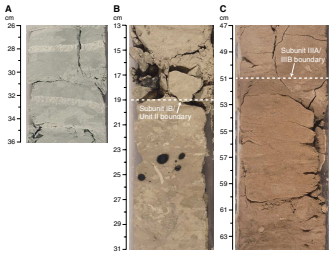

Unit II

Interval: 197-1203A-10R-2, 20 cm, to 16R-2, 66 cm
Depth: 388.9–447.3 mbsf
Age: middle Eocene to late Oligocene

Unit II consists mainly of pinkish gray to pale red nannofossil chalk and calcareous chalk (with minor clay and foraminifers) that changes to pinkish white or white nannofossil chalk downhole. Intervals of darker olive-colored sediments (e.g., interval 197-1203A-13R-1, 0–100 cm) reflect dilution by influx of opaque minerals, feldspar, and organic debris. Horizontal burrows are filled with organic-rich chalk containing pyrite (Fig. **F3A**). Carbonate abundance is consistently high throughout the unit.

The Unit II/Subunit IIIA boundary is at Section 197-1203A-16R-2, 66 cm. At this level (447.3–457.6 mbsf), we observe the termination of the

cyclic deposition of Fe-rich clay and calcareous silty clay in organic-rich(?) intervals.

Unit III

Interval: 197-1203A-16R-2, 66 cm, to 17R-3, 47 cm
Depth: 447.3–457.6 mbsf
Age: early to middle Eocene

Unit III is a sandy-silty sequence directly overlying the basement volcanic rock. Nannofossil chalk remains the dominant sediment type but is accompanied by intervals enriched in clay, Fe oxide, pyrite, and organic debris (see **"Site 1203 Smear Slides,"** p. 265). The nannofossil and calcareous chalk (generally finely laminated and bioturbated) are interbedded with authigenic 2- to 5-cm-thick beds of stiff red clayey Fe oxide bands (i.e., Section 197-1203-17R-3 [456.9–457.6 mbsf]) and silty sand (interval 197-1203A-17R-2, 49–61 cm). At the contact with basement, this unit contains a dark brown interval (7.5YR 5/3) that almost entirely consists of calcite-dolomite silty sand.

Subunit IIIA

Interval: 197-1203A-16R-2, 66 cm, to 17R-2, 53 cm
Depth: 447.3–456.3 mbsf
Age: early to middle Eocene

This subunit exhibits bioturbation, and distinct orange *Zoophycos* trace fossils are common. Several erosional contacts and reddish brown to pink silt and clay beds indicate an oxidating environment and alternation between relatively high- to low-energy depositional settings. The Subunit IIIA/IIIB boundary (at Section 197-1203A-17R-2, 51 cm [456.3 mbsf]) (Fig. **F3C**) is characterized by a gradational contact between pink (7.5YR 7/4) calcareous nannofossil chalk and reddish yellow (7.5YR 6/6) sandy silt nannofossil chalk.

Subunit IIIB

Interval: 197-1203A-17R-2, 53 cm, to 17R-3, 47 cm
Depth: 456.3–457.4 mbsf
Age: early to middle Eocene

Subunit IIIB is a sandy-silty clay nannofossil chalk with a high Fe oxide content. The subunit is thoroughly bioturbated, with distinct *Zoophycos* trails indicating oxygenated bottom conditions. Erosional contacts and sandy beds at the bottom of the sedimentary sequence and finely laminated beds and high contents of biogenic carbonate debris and dolomite formation indicate variable fluid velocities and oxygen availability at the time of deposition. Several depositional cycles are indicated by a sequence of beds with distinct colors between pink, reddish yellow (7.5YR 7/6), and light brown (10YR 6/4), which contains high concentrations of Fe oxides (30%–60%).

Discussion

Despite incomplete coring and only partial recovery of cored intervals at Site 1203, we were able to observe many similarities to the sedimentary section completely cored at nearby Site 883 (Rea, Basov, Janecek, Palmer-Julson, et al., 1993). In particular, the Site 1203 Unit I/II

boundary at 388.9 mbsf, marking the onset of diatom production in late Oligocene time, is equivalent to the Subunit IIIB/IVB boundary at 652 mbsf at Site 883. Such a drastic change in sediment type has been related to changes in deepwater circulation patterns (Woodruff and Savin, 1989) revealed in detail at Leg 145 sites (Rea, Basov, Janecek, Palmer-Julson, et al., 1993). It is also worth noting that in Hole 1203A, the beginning of silica deposition (i.e., radiolarians, well-preserved silicoflagellates, and large sponge spicules at 402.1 mbsf [Section 197-1203A-11R-4, 61 cm]) occurred earlier (early Oligocene) than the onset of diatom deposition (Section 197-1203A-10R-2, 20 cm [388.9 mbsf]; early Miocene). However, we set the Unit I/II boundary at the beginning of diatom production and deposition rather than at the first occurrence of silica deposition for purposes of comparison with previous findings at Site 883. A significant difference is the presence of vitric ash layers in the lowermost 150 m at Site 883, which are absent at Site 1203. However, a dramatic increase in opaque minerals and Fe oxyhydroxide clay in Subunit IIIB may be weathering products from these ash layers or exposed basement volcanic rock.

BIOSTRATIGRAPHY

Hole 1203A was drilled in a water depth of 2594 m. The hole was drilled ahead to 300 mbsf with the rotary core bit, where coring commenced. Seventeen sediment cores were recovered above basalt, which was encountered at 462 mbsf. We made biostratigraphic assignments to core catcher and other selected samples using calcareous nannofossils. Table **T3** and Figure **F4** show a summary of biozonal assignments.

T3. Biozonal assignment summary, p. 150.

F4. Calcareous nannofossil zones in Hole 1203A, p. 54.

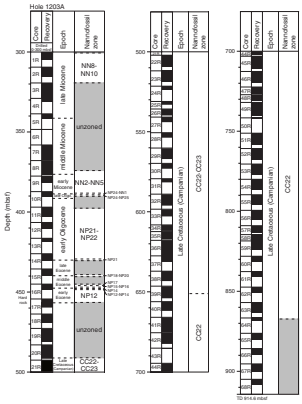

Calcareous Nannofossils

Samples from Cores 197-1203A-1R to 17R contain nannofossils ranging from few to dominant (mostly common) in abundance. Preservation is generally poor, with a few samples displaying moderate preservation. Nannofossil preservation in Cores 197-1203A-16R and 17R is generally better than in the overlying cores.

Tertiary Zonation

Samples 197-1203A-1R-1, 68–69 cm, to 3R-1, 50–51 cm, are in the NN8–NN10 zonal interval (late Miocene), based on the presence of *Discoaster bollii, Discoaster brouweri, Discoaster calcaris,* and *Discoaster* cf. *Discoaster hamatus*. We could not zone sediments between Sample 197-1203A-3R-1, 50–51 cm, and 8R-5, 50–51 cm, owing to poor preservation and lack of diagnostic marker species. Samples 197-1203A-8R-5, 50–51 cm, and 9R-CC contain *Discoaster druggii* and are within the zonal interval of that species, NN2–NN5 (early to middle Miocene). *Cyclicargolithus abisectus* is present in Sample 197-1203A-10R-2, 82–83 cm, suggesting an assignment to Zone NP24–NN1 (late Oligocene to early Miocene); *C. abisectus* together with *Reticulofenestra bisecta* in Sample 197-1203A-10R-CC indicates a zonal interval of NP24–NP25 (late Oligocene). The species normally so helpful for Oligocene nannofossil zonation (*Sphenolithus ciperoensis* and *Sphenolithus distentus*) are not present in these cores, probably owing to poor preservation.

Sample 197-1203A-11R-2, 83–84 cm, contains both *Chiasmolithus oamaruensis* and *Reticulofenestra umbilicus,* suggesting a zonal range of

NP18–NP22. However, the assignment of Zone NP21 below this level (in Sample 197-1203A-14R-CC) indicates that the interval from Sample 197-1203A-11R-2, 83–84 cm, to 13R-1, 50–51 cm, can be assigned to Zones NP21–NP22. *Isthmolithus recurvus* together with common *Ericsonia subdisticha* (i.e., the acme of *E. subdisticha*) in Sample 197-1203A-14R-CC indicates Zone NP21 (Eocene/Oligocene boundary). Sample 197-1203A-15R-CC contains *Discoaster barbadiensis* and *C. oamaruensis,* indicating a zonal interval of NP18–NP20 (late Eocene). The absence of *Chiasmolithus solitus* and *C. oamaruensis* and the presence of *Chiasmolithus grandis* in Samples 197-1203A-16R-1, 15–16 cm, and 16R-1, 29–30 cm, suggest the assignment of Zone NP17. Samples 197-1203A-16R-1, 70–71 cm, to 16R-1, 131–132 cm, are in Zones NP15–NP16 (middle Eocene), based on the co-occurrence of *R. umbilicus* and *C. solitus*. Sample 197-1203A-16R-2, 20–21 cm, is in Zone NP14 (early Eocene/middle Eocene boundary) on the basis of the co-occurrence of *Discoaster lodoensis* and *Nannotetrina* sp. Sample 197-1203A-16R-CC contains *D. lodoensis, Tribrachiatus orthostylus,* and *Coccolithus crassus,* indicating Zone NP12 (early Eocene). Overlying Samples 197-1203A-16R-2, 61–62 cm, to 16R-3, 81–82 cm, are therefore in the zonal interval NP12–NP14. Zone NP12 continues downward to the last soft sediment sample (197-1203A-17R-3, 47–48 cm) immediately overlying basalt. The lower and upper boundary ages of Zone NP12 are estimated to be 52.8 and 50.6 Ma, respectively (see **"Biostratigraphy,"** p. 9, in the "Explanatory Notes" chapter). However, *C. crassus* occurs in all the Zone NP12 samples, narrowing the age assignment to 51.5–50.6 Ma.

Cretaceous Zonation

Some volcaniclastic sediment intercalated in basalt in this hole contains a sparse but moderately to well-preserved assemblage of nannofossils. Volcaniclastic beds in Samples 197-1203A-20R-6, 36–40 cm; 29R-2, 116–117 cm; 29R-3, 19–20 cm; and 33R-CC all contain the same Campanian species: *Ceratolithoides aculeus, Quadrum gothicum, Quandrum sissinghii, Quandrum trifidum, Micula decussata,* and *Micula concava*. We assign these samples to the CC22–CC23 zonal interval. *Q. trifidum* is the zonal indicator species. It ranges from the base of Zone CC22 (76.0 Ma) to just above the middle of Zone CC23 (71.3 Ma). Samples 197-1203A-39R-3, 61–62 cm, and 39R-4, 18–19 cm, contain the same nannofossil assemblage, together with *Eiffellithus eximius* and *Aspidolithus parcus*. These samples are therefore in Zone CC22 (75.0–76.0 Ma). Zone CC22 is also assigned, based on this assemblage, to volcaniclastic Samples 197-1203A-63R-5, 55–56 cm; 63R-5, 74–75 cm; 63R-5, 118–119 cm; 63R-6, 10–11 cm; and 64R-1, 112–113 cm.

PHYSICAL VOLCANOLOGY AND IGNEOUS PETROLOGY

We encountered basement at 462 mbsf (drilling depth [457.5 mbsf curated depth]) at Site 1203 (Hole 1203A) and cored a ~457-m volcanic section, with an average recovery of 56.5% (see **"Operations,"** p. 3). The basement sequence consists of 18 basalt lava units (216 m of recovered core), 12 volcaniclastic interbeds with occasional biogenetic sediments, and 1 recrystallized silty chalk interbed that contains sand-sized vitric material (Figs. **F5, F6, F7;** Table **T4**). The general lithology of the basement units correlates well with logging and drilling rate data (Figs.

F5. Basement rocks and biostratigraphic ages, p. 55.

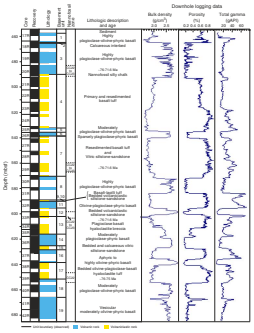

F6. Basement rock lithologic features, p. 57.

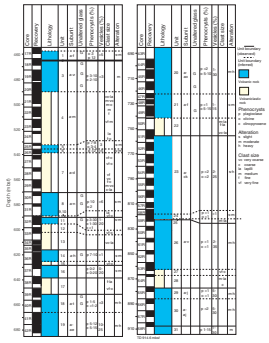

F7. Basement units, drilling rate, and recovery, p. 58.

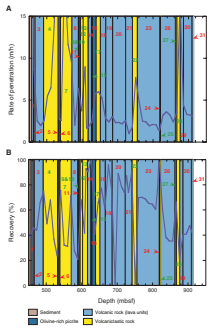

T4. Basement units/subunits, p. 154.

F5, F6), and we note that the units exhibit a range of alteration intensity between slight and complete (see "Downhole Measurements," p. 40, and "Alteration and Weathering," p. 24).

Site 1203 is ~26 nmi south of Site 883 and 36 nmi southwest of Site 884 (see "Background and Scientific Objectives," p. 1), where basement rocks were recovered from Detroit Seamount during ODP Leg 145 (Rea, Basov, Janecek, Palmer-Julson, et al., 1993). Drilling at Site 883 (Hole 883E: penetration = 37.8 m; recovery = 63% and Hole 883F: penetration = 26.7 m; recovery = 41%) indicated that the uppermost carapace of the volcanic basement consists of altered plagioclase-phyric pillow basalt and massive basalt lavas. At Site 884 basalt lava flows from Hole 884E (penetration = 87 m; recovery = 66.5%) and 40 cm of altered aphyric pillow basalt from the last core of Hole 884B were recovered. The basalt units described from Hole 884E are aphyric to plagioclase-olivine-phyric with plagioclase phenocrysts up to 2.5 cm in size (Rea, Basov, Janecek, Palmer-Julson, et al., 1993). An ^{40}Ar-^{39}Ar age of 81 Ma for Site 884 basalt has been reported by Keller et al. (1995).

At Site 1203 the lava flow units (Table T4) are composed of aphyric to plagioclase-olivine-phyric basalt. Units 14 and 31 contain large plagioclase phenocrysts, similar to the basalt lava units reported from Site 884, but the size of the plagioclase crystals is generally smaller (e.g., Fig. F8). We define unit boundaries primarily on the basis of changes from lava flow to volcaniclastic deposit (e.g., the boundary between Units 8 and 9) (Fig. F9), major changes in lithology of the lavas (e.g., between Units 10 and 11), and the presence of weathered flow tops in the core (e.g., the boundary between Units 23 and 24) (see "Physical Volcanology and Igneous Petrology," p. 10, in the "Explanatory Notes" chapter). The age of the basement and overlying sediment has been constrained by nannofossil assemblage identification (see "Biostratigraphy," p. 10). The age of the sediment immediately above basement is 50.6–51.5 Ma. The age of volcaniclastic Units 4, 7, and 12 has been determined to be 71.6–76 Ma, whereas that of Units 17 and 27 is 75–76 Ma, at least 5 m.y. younger than basement at Site 884 (Keller et al., 1995).

F8. Large plagioclase phenocrysts, p. 59.

F9. Boundary between Units 8 and 9, p. 60.

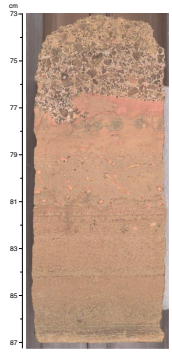

T5. Characteristics of volcaniclastic units, p. 155.

T6. Features of basement lava flow units, p. 156.

Macroscopic Description

We briefly describe the major lithologies of the basement sequence (see Table T4). More detailed descriptions can be found in the visual core descriptions (see "Site 1203 Core Descriptions," p. 1). The major lithologic features of each unit are summarized in Figures F5 and F6 and Tables T4, T5, and T6.

Volcaniclastic Units

The volcaniclastic units are composed of a range of sediment types, including primary tephra (pyroclastic and hyaloclastite) deposits and their resedimented derivatives, along with clastic and calcareous sediments. We identified the tephra deposits as basalt tuff, lapilli tuff, lapillistone, and breccia, whereas the clastic sediments are made up of vitric siltstones and sandstones that are often intercalated with nannofossil-bearing calcareous siltstones and mudstones. In total, we identified eight scoria fall and four hyaloclastite (Units 7c–7d, 17, and 25) tephra units along with six resedimented tuff and ten sediment units in the volcaniclastic sequences (Tables T4, T5). The volcaniclastic deposits and associated sediments are generally highly altered because their ma-

jor component is basalt glass that has been converted to palagonite and/or replaced by other alteration products (green clay and/or zeolite). Pore spaces are typically filled with carbonate or zeolite. Note, however, that unaltered basalt glass is present in the tuffs of Unit 4.

Basalt Tuffs (Units 4b–4i, 4k, 4m, 7c–7d, 17, 25, and 31a)

The basalt tuff units are massive and laminated or thin- to medium-bedded tuffs with occasional trains of lapilli scoria. They generally exhibit good to moderate sorting, and the composition of these deposits is dominated by vitric basaltic fragments (Table T5) and minor amounts of plagioclase crystal fragments. The tuffs occasionally exhibit cross-bedding and are cemented by carbonate and zeolites.

The basalt tuffs are divided into three groups on the basis of their clast morphology, texture, and depositional structures: ash fall (Subunits 4c and 4f–4h), resedimented (Subunits 4b, 4d, 4i, 4k, and 4m), and hyaloclastite (Subunits 7c–7d and 31a and Units 17 and 25) tuffs (Table T5). The ash fall tuffs are characterized by massive to normal graded beds consisting almost entirely of highly vesicular basalt glass fragments that often exhibit fluidal morphologies (e.g., Figs. F10, F11). The resedimented tuffs contain a clast population identical to that of the ash fall deposits but feature structures indicative of deposition by traction and origin by resedimentation of primary fall deposits. The hyaloclastite tuffs are distinguished on the basis of their nonvesicular, splinterlike clast population (Table T5).

We interpret the tuffs to be fall deposits formed by subaerial strombolian (explosive) eruptions, but deposited in water, because of the high vesicularity and fluidal shapes of the ash particles along with mature normal size grading and distinctive bedding. The resedimented tuffs represent primary tephra fall deposits that have been subjected to reworking and redeposition either during or shortly after the eruptions. The hydroclastite tuffs are typically associated with pillow lavas and are interpreted to have formed by quench fragmentation in association with subaqueous lava flow emplacement.

Basalt Lapilli Tuff and Lapillistone (Units 4l, 9, and 22b)

These deposits are brownish green to dark green, thinly to thickly bedded, clast-supported basalt lapillistones and lapilli tuffs composed of massive or normally size-graded beds. They are moderately sorted and made up of fine to medium lapilli scoria and occasionally contain clasts >25 mm in size. These deposits consist of highly vesicular (>70%) scoria (80 to >95 modal%), often featuring fluidal outlines (Figs. F12, F13). They also contain occasional cognate basalt lava lithics and blocks as well as armored lapilli, where a lava lithic is wrapped in vesicular glass (Fig. F12B). These units are cemented by zeolites (analcite and natrolite?) or carbonate. On the basis of the overall clast texture and depositional structures, along with the preponderance of delicate and highly vesicular scoria clasts, we identify these units as scoria fall deposits. The overall coarseness of the deposits suggests proximity to source because meter-thick lapilli scoria fall deposits are typically found within 5 km of their source vents (Cas and Wright, 1987; Thordarson and Self, 1993).

Volcanic Breccias (Units 13 and 28 and Part of Unit 21)

We recognize three breccias in the basement sequence. Two of these are Units 13 and 28, whereas the third forms the brecciated top of basalt Unit 21. All breccia deposits are massive, poorly sorted, and matrix supported, where the coarse fraction (20–125 mm) is composed of an-

F10. Vesicular reticulite-like basalt tephra clasts, p. 61.

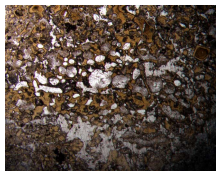

F11. Basalt tephra clasts with fluidal outlines and elongate vesicles, p. 62.

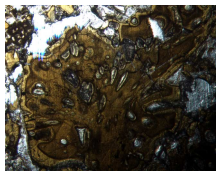

F12. Scoria fall deposit features, p. 63.

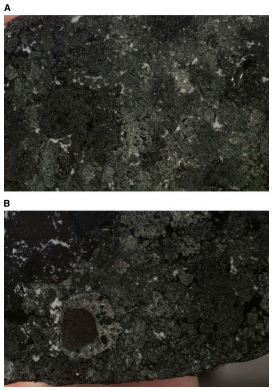

F13. Vesicular cuspate basalt tephra clasts, p. 64.

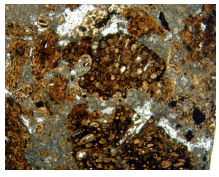

gular basalt lava lithics and blocks of basalt identical to those of the underlying lava unit (Fig. F14). In addition, a 20-cm interval at the top of Unit 28 consists of brownish white lapilli breccia, composed of 5- to 30-mm angular basalt and plagioclase-phyric dacite(?) lithic fragments that feature a felsic groundmass texture (i.e., feldspar and quartz after devitrified glass).

The matrix composition is variable. In Unit 13 and at the top of Unit 21, the matrix consists of 1- to 8-mm angular particles composed of sparsely vesicular, aphyric to highly plagioclase-phyric basalt glass and lava fragments with variolitic groundmass textures. The phenocrysts in the matrix fragments are identical to those found in the larger breccia clasts, hence indicating a monomict clast population. However, the color of the matrix fragments ranges from brownish gray to dark greenish gray to dark gray because of the differences in the degree and type of alteration that results from variations in the igneous groundmass textures of the clasts. These breccias are cemented by white carbonate (Fig. F14). In the lower part of Unit 28, the breccia contains small aphyric lava toes (4–7 cm thick) and pieces broken from larger basalt lava lobes resting in a very fine grained calcareous matrix that contains a well-preserved specimen of coralline red algae (Fig. F15). The lithology of the basalt toes and fragments is identical to that of the underlying lava. However, these lithic clasts show no indication of being produced by quenched fragmentation (i.e., jigsaw-fit texture or evidence for thermally induced disintegration of glassy lobe margins). Also, the calcareous matrix does not appear to have experienced any heating, as would be expected if it was invaded by hot lava.

We interpret Unit 13 and the brecciated interval on top of lava Unit 21 to be hyaloclastite breccia produced by quench fragmentation of the underlying pillow lavas. The presence of calcareous matrix in the basalt lithic breccia in Unit 28 indicates subaqueous deposition, although the exact mode of formation remains ambiguous. However, we regard a hyaloclastite origin for Unit 28 breccia to be unlikely because there is no direct evidence in the core for interaction between hot lava and water-logged sediment (e.g., Cas and Wright, 1987). Unlike the other breccia units, basalt + dacite(?), the origin of the dacite lithic breccia at the top of Unit 28 shows clear evidence of provenance from two lithologic sources, but its origin is unknown at this time.

Vitric and Volcaniclastic Siltstone and Sandstone (Units 4j, 7a–7b, 10, 12, 15a–15b, 22a, and 27)

These units are sequences of poorly to moderately sorted, laminated to thinly bedded vitric sediments that typically exhibit horizontal planar bedding with alternating beds of siltstone and sandstone. Most common colors are greenish and bluish grays and dark grays; coarser beds are typically lighter in color. Normally graded or cross-stratified beds and fine-scale laminations are common. Several intervals are variably disturbed by slumping and loading, as evidenced by an abundance of soft-sediment deformation structures (Table T5). These sediments are made up of variable proportions of highly to completely altered basaltic glass, siliciclastic fragments, and detrital carbonate. Clasts are subrounded to angular.

Lava Flow Units

The major lithologic features of each unit are summarized in Figures F5 and F6 and Table T4. Lavas in the upper part of the basement se-

F14. Volcanic breccia in a carbonate-rich matrix, p. 65.

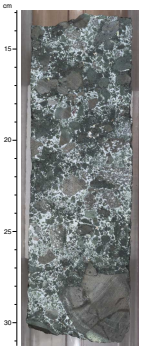

F15. Coralline algae, p. 66.

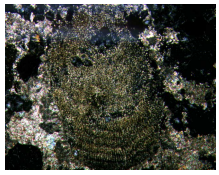

quence (i.e., Cores 197-1203A-17R to 31R) generally show well-developed pillow structures with low vesicularity (typically <5%), whereas pahoehoe lava is more common in the lower part of the sequence (i.e., Cores 197-1203A-41R to 68R) and where the lavas exhibit a marked increase in vesicularity (15%–35%). Glassy lobe margins are present in all basalt units except Units 6 and 24. Unaltered glass is present in the chilled lobe margins (0.2–1.2 cm thick) throughout the sequence (e.g., Figs. **F7, F11, F16, F17**), whereas in the lower part of the sequence glassy lobe margins are bright green and highly to completely altered (Fig. **F17B**) (see **"Alteration and Weathering,"** p. 24). They are identical to lobe margins that characterize pahoehoe and pillow lavas (Self et al., 1998).

Olivine-rich zones containing >10 modal% olivine are present in Units 11 and 16. We also note large plagioclase phenocrysts in Units 14 and 31 (Fig. **F8**). Phenocryst size is variable; plagioclase crystals and glomerocrysts in Units 14 and 31 reach 1.3 cm in length but are generally <6 mm in size elsewhere. On rare occasions the olivine phenocrysts have survived postemplacement alteration, but most commonly they are present as olivine pseudomorphs of carbonate, talc, serpentine, and/or Fe oxyhydroxide. Most plagioclase phenocrysts show evidence of incipient alteration to sericite, and interstitial groundmass glass (mesostasis) is partly to completely devitrified. Vesicles are variably filled with secondary minerals, of which calcite is the most common, but zeolite and secondary sulfide minerals are present in vesicles from the lower part of the basement section (see **"Alteration and Weathering,"** p. 24).

F16. Glassy margins and fragments in calcite matrix, p. 67.

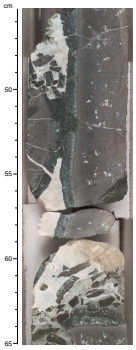

F17. Altered glassy lobe margins, p. 68.

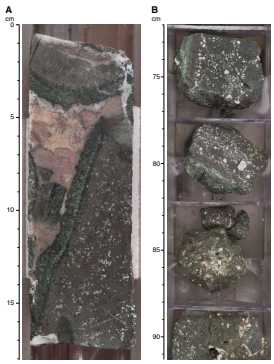

Physical Volcanology

The volcanic succession at Site 1203 is composed of 18 lava units (representing at least 14 eruption units [i.e., lava flow fields]) and 14 volcaniclastic units. As described above, the latter lithologies consist of primary and resedimented basaltic tephra deposits, as well as clastic and calcareous sediments rich in volcanic components. Here we present more detailed descriptions of the internal architecture of the lava units at Site 1203 and the observed lithofacies associations.

Lava Flows

The lava flow units at Site 1203 range from tholeiitic to alkalic basalt compositions (see **"Geochemistry,"** p. 21) and are 1.9 to ~63 m in (cored) thickness. Because of very good core recovery through the lava units (average = 69% and range = 40%–95% on the basis of curated thicknesses), we obtained comprehensive information about the internal architecture and the characteristic lobe structure of individual units. Key features of the lava units are listed in Table **T6,** and the main characteristics of each lava type are summarized below. On the basis of this information, we identified three lava flow types in the Site 1203 basement sequence. These lava flow types are pillow, compound pahoehoe, and simple pahoehoe lavas. A total of five lava units are categorized as "simple" lavas because in the core section they are typically composed of a single lobe (i.e., cooling unit). They range in thickness from ~2 to 10 m, comprise ~8% of the lava sequence, and have internal architecture and lobe margins consistent with that of inflated pahoehoe lobes in flood lava flow fields (Thordarson and Self, 1998). A total of 13 units are categorized as compound lavas (i.e., lava flow or an eruption unit consisting of multiple lobes) and are divided into pillow and pahoehoe

lavas based on the characteristic internal architecture of their lobes (Table T6). However, Units 20 and 21 appear to be hybrid pillow-pahoehoe units. Together, the compound lavas make up ~91% of the lava sequence.

Pillow Lavas (Units 1, 3, 8, 14, 18, and 31[?])

The pillow lava units are all tholeiites (see "Geochemistry," p. 21) and are more abundant in the upper half of the Site 1203 succession (Figs. F5, F6; Table T6). They range in thickness from ~8 to 25 m and comprise ~24% of the lava flow units. The pillow lava lobes are bounded by smooth glassy lobe margins and range in thickness from 8 to 164 cm (average = 55 cm) (see Fig. F18). The lobe thickness distribution is skewed toward the smaller lobe sizes (see Fig. F19).

The distinguishing features of the pillow lobes are as follows. Thin (<10 mm), sparsely to nonvesicular glassy lobe margins are now generally altered to yellow-brown palagonite (Fig. F20), with occasional domains of sideromelane glass several millimeters across. The lava closest to the lobe margins is without exception defined by a variolitic groundmass texture and features a centimeter-thick microvesicular band with small (<3 mm wide and <10 mm long) tube- or drop-shaped vesicles. The lobe interiors are typically fine grained and nonvesicular and exhibit a distinct cubelike cooling joint pattern (Fig. F18).

The presence of a variolitic texture and cubelike jointing in the pillow lavas is indicative of high cooling rates and emplacement under water. The low vesicularity of the pillow lobes can be attributed to either suppressed degassing at great water depths (≥1000 m), due to high external pressures, or to arresting of gas exsolution of partly degassed lava as it flows from land into water. We favor the latter interpretation because the lithofacies associations in the Site 1203 succession suggest a relatively shallow water depth (see below).

Compound Pahoehoe (Units 19, 23, 26, 29, and 30)

The compound pahoehoe lava flow units except for Unit 19 are all alkali basalt (see "Geochemistry," p. 21) and are confined to the lower half of the Site 1203 basement sequence (Figs. F5, F6; Table T6). They vary in thickness from ~8 to 64 m and account for 50% of the total thickness of lava in the succession. The thickness of lobes in the compound pahoehoe ranges from 9 to 252 cm (average = 56 cm), and the lobe thickness distribution is strongly skewed toward the smaller lobe sizes (Fig. F19). Individual lobes are defined by smooth glassy lobe margins (Figs. F16, F17).

The distinguishing features of the compound pahoehoe lobes are as follows. The glass at lobe margins is typically highly vesicular and completely altered to yellow to dark brown palagonite, clay, and/or zeolite minerals. The groundmass of the lava in the vicinity of the lobe margins is typically aphanitic (hypohyaline to hypocystalline) with an intersertal texture, whereas the lobe interiors are fine grained and characterized by an intergranular texture. Most commonly, the lobes have highly vesicular upper and lower crusts and sparsely to nonvesicular lobe interiors, although some of the smaller lobes are moderately to highly vesicular throughout (Fig. F21). They often feature small pipe vesicles at the lobe base and small vesicle cylinders along with horizontal vesicle sheets and irregular pockets of vesicular segregated material extending up through the massive lobe interior.

The internal architecture and vesicularity of the compound pahoehoe lavas at Site 1203 are very similar to those found in modern pahoe-

F18. Pillow lava unit graphic log and photograph, p. 69.

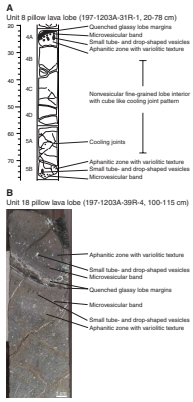

F19. Lobe thickness distribution of lavas, p. 70.

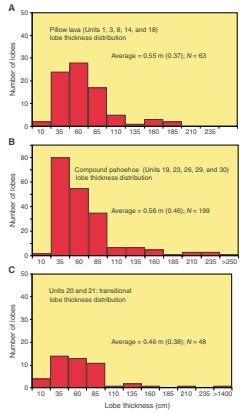

F20. Microlites in a glassy lobe margin, p. 71.

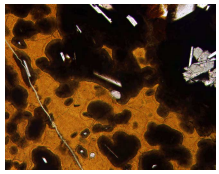

F21. Lobe structures in compound pahoehoe lava, p. 72.

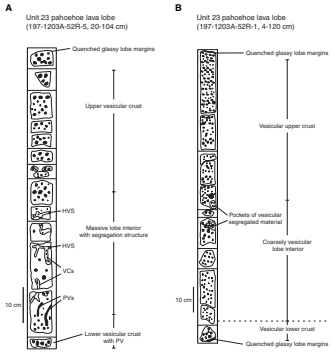

hoe flow fields in Hawaii and elsewhere (e.g., Wilmoth and Walker, 1993; Mattox et al., 1993; Hon et al., 1994), and, therefore, we interpret these to be lavas emplaced in an subaerial environment.

Hybrid Pillow-Pahoehoe Lavas (Units 20 and 21)

The hybrid pillow-pahoehoe lava units are tholeiitic in composition (see "Geochemistry," p. 21) and are present in the Hole 1203A core where the transition from subaerial pahoehoe– to subaqueous pillow lava–dominated succession occurs (Fig. F5; Table T4). The volcanic architecture of these hybrid lavas is transitional between that of the pillow and compound pahoehoe and indicates emplacement in relatively shallow water. Their characteristic features are as follows.

They consist of multiple decimeter- to meter-thick pillowlike lobes (Figs. F16, F22), with typical lobe thicknesses between 20 and 200 cm (average = 57 cm). As in other compound lavas at Site 1203, the lobe thickness distribution is skewed toward smaller lobe sizes (Fig. F19). The lobes are defined by sparsely vesicular glassy (normally altered to palagonite) lobe margins (Fig. F16). As in the pillow lobes described above, the lava closest to the lobe margins is characterized by variolitic groundmass texture, containing a centimeter-thick microvesicular band and small pipe vesicles. In the lobe interior, the lava is fine grained and often features a cubelike joint pattern indicative of water-enhanced cooling (Fig. F22). The lobes of these hybrid lavas are typically finely vesicular, and vesicle abundance is highly variable (range = <5%–30%). However, the vesiculation pattern is distinctive and different from that found in pillow and pahoehoe lavas. The lava itself is usually sparsely to nonvesicular (<5 modal%), but it contains domains (i.e., vesicle cylinders, horizontal vesicle sheets, and irregular pockets) filled with highly vesicular (up to 40 modal%) segregated material (Fig. F22). This vesiculation pattern implies that the water pressure at the site of emplacement was high enough to suppress primary (first) vesiculation during initial stages of lobe emplacement but low enough to allow secondary vesiculation (i.e., "second boiling") during melt segregation. Typically, such melt segregation in basalt lavas is driven by volatile enrichment (mainly H_2O; increase by a factor of 1.5–2) in residual melts after ~35%–45% crystallization (Goff, 1996; Self et al., 1998; Thordarson and Self, 1998). If the volatile content of the lava at the point of deposition is known, this vesiculation pattern can be used to constrain the water depth at the time of emplacement.

Simple Pahoehoe (Sheet Lobes) (Units 5, 6, 11, 16, and 24)

A total of five units are identified as simple pahoehoe lava. They are all tholeiitic basalt (see "Geochemistry," p. 21) and are more abundant in the upper half of the Site 1203 succession (Figs. F5, F6; Table T6). They range in thickness from ~2 to 10 m and account for 8% of the total thickness of lava flows in the succession.

We were able to accurately document the volcanic architecture of Units 5, 11, and 16 because of very good recovery (Table T6). The upper and lower lobe boundaries of these units were recovered and are in all cases smooth glassy pahoehoe surfaces. Units 11 (~4.6 m thick) and 16 (~10.4 m thick) feature a distinct threefold division into vesicular upper crust, massive lobe interior, and vesicular lower crust (Fig. F23), which is the diagnostic structure of inflated pahoehoe sheet lobes (e.g., Thordarson and Self, 1998). In both lobes, the upper and lower crusts are characterized by relatively high vesicularity (10–30 modal%), except for the top 50 cm of the upper crust, where the lava is finely vesicular (di-

F22. Hybrid pillow-pahoehoe lava structures, p. 73.

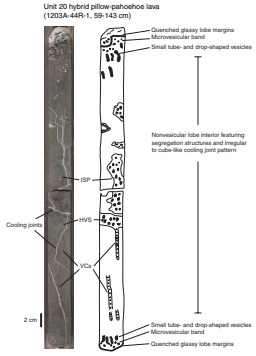

F23. Structure of pahoehoe sheet lobes, p. 74.

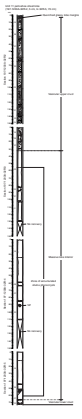

ameter < 1 mm) and characterized by unusually lower vesicularity (≤8 modal%). The pahoehoe sheet lobe of Unit 5 is ~2 m thick and sparsely vesicular (≤5 modal%) throughout.

Despite reasonable core recovery (49% and 68%) (see Table T6), only parts of the sheet lobes that make up Units 6 and 24 (i.e., vesicular basal crust, the massive lobe interior including horizontal vesicle sheets, and small portions of the vesicular upper crusts) were recovered. Partial preservation is the most likely explanation of incomplete recovery, suggesting that these lavas were subjected to significant erosion prior to burial by later formations.

The sheet lobes of Units 5, 11, and 16 all have conformable contacts with water-lain volcaniclastic sediments, which implies subaqueous flow emplacement. The unusually low vesicularity along with very small vesicle size in the Unit 5 sheet lobe as well as in the top 0.5 m of the vesicular upper crust of the lobes of Units 11 and 16 may indicate suppression of volatile exsolution resulting from water-enhanced cooling of the lava. In the case of the two latter units, vesiculation appears to have progressed in a normal fashion when the upper crust had thickened enough to seal the molten lava interior from its surroundings, whereas the Unit 5 sheet lobe never achieved such insulation because of its small thickness.

Synthesis of the Physical Volcanology

The compound pahoehoe and the pahoehoe sheet lobes at Site 1203 commonly exhibit a threefold division into vesicular upper crust, massive lobe interior, and vesicular lower crust and contain segregation structures such as pipe vesicles, vesicle cylinders, and horizontal vesicular sheets (Table T6), which are the characteristic architecture of subaerial pahoehoe flows formed by endogenous emplacement (i.e., transport of lava under an insulating stationary crust and growth by lava inflation).

The similarity between compound pahoehoe and pillow lavas in terms of lobe sizes and overall morphology, along with the presence of segregation structures in the pillowlike lobes of Units 20 and 21, is consistent with the notion that the emplacement mechanism of these two lava types is essentially the same. They differ only in the environment of emplacement and cooling rates.

The most striking lithofacies change at Site 1203 is the shift from the dominance of compound pahoehoe lava flows in the lower part of the succession to pillow lava flows in the upper part. Intuitively, this implies a change from a subaerial to a submarine setting for the Site 1203 environment, which most likely was caused by gradual subsidence on a regional scale. The presence of hybrid pillow-pahoehoe lavas along with a more frequent occurrence of hyaloclastite tuffs and breccias in the middle part of the succession as well as thicker volcaniclastic sequences in the upper part are compatible with this inference (Table T4; see also Fig. F56, p. 83, in the "Leg 197 Summary" chapter). However, the presence of calcareous interbeds in the lower part of the succession as well as the presence of thick primary tephra fall deposits in the upper part shows that land and sea were never far apart.

Petrography

Volcaniclastic Units

In thin section we characterize the volcaniclastic lithologies by the abundance of vitric particles (fresh and altered sideromelane) along with subordinate amounts of lithic fragments (both juvenile and cognate) and occasional crystal fragments. Vitric particles typically comprise up to 99% of the clast population.

In the primary basalt tephra fall deposits (e.g., Units 4f–4h, 9, and 22b), highly vesicular scoria with fluidal shapes are by far the most abundant clast type, exhibiting delicate morphologies, highly cuspate clasts, and containing occasional plagioclase laths (Fig. F13). These units contain tephra clasts (Fig. F10) that have an elongate and twisted outline and numerous elliptical vesicles. The presence of these characteristics is consistent with our interpretation that these deposits were produced by fire-fountaining or explosive activity in subaerial Hawaiian or Strombolian eruptions (Fisher and Schmincke, 1984).

The vesicles in tephra clasts are commonly filled with radiating zeolite minerals (natrolite or mesolite?) or analcite. Hairline cooling fractures often penetrate the scoria clasts and are formed during quenching of the scoria clasts during transport through the air or upon contact with water when still hot. The preservation of such delicate structures demonstrates that these deposits have not been reworked after transport and deposition and adds support to our interpretation that these deposits are primary tephra fall deposits. The lithic population is composed mainly of cognate crystalline basaltic fragments.

The hyaloclastite tuffs (Table T4) are characterized by abundant nonvesicular platy or splinterlike clasts. The lack of vesicles and the elongate shardlike morphologies are consistent with our interpretation that these tuffs were produced by nonexplosive fragmentation when the underlying lava flowed into water (Table T5).

Inspection of the fine-grained matrix in the basalt-lithic breccia that comprises the lower part of Unit 28 shows that it consists of partly recrystallized calcareous mudstone containing dispersed basalt glass and plagioclase fragments and one specimen of fossilized coralline red algae (Fig. F15). This observation is consistent with our interpretation of subaqueous deposition for this breccia unit. Furthermore, the composition of the volcaniclastic sandstone in Unit 27 and the breccia interval at the top of Unit 28 appears to differ from the other clastic sedimentary units. It contains a significant amount of dacite(?) lava lithic fragments (mixed with basalt fragments) in which feldspar phenocrysts are imbedded in felsic groundmass. The presence of dacite lithic fragments suggests influx from an external sediment source.

Basalt Units

The lava flow units are aphyric to olivine- and/or plagioclase-phyric. They consist of variable amounts of glomerocrystic plagioclase and/or olivine in a groundmass of plagioclase, clinopyroxene, titanomagnetite, with varying abundance of mesostasis consisting of glass and postemplacement alteration products. Plagioclase is the most abundant phenocryst phase, usually present as glomerocrysts forming aggregates up to 10 mm in size; individual phenocrysts reach up to 1.3 cm in size in Units 14 and 31. Individual crystals within the glomerocrysts are typically oscillatory zoned (Fig. F24), fractured, and, occasionally, glass in-

F24. Zonation in plagioclase, p. 75.

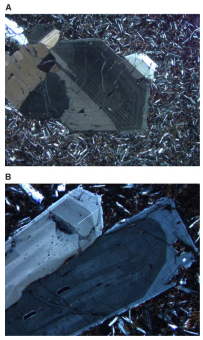

clusions are present (Fig. F25). Some phenocrysts have rounded or embayed margins (Fig. F26), indicating disequilibrium. Olivine, where present, is also often found as glomerocrysts (Fig. F27). It is typically pseudomorphed by a combination of carbonates (calcite and, rarely, magnesite and siderite), iddingsite, and green/brown clay or Fe oxyhydroxide (see "Alteration and Weathering," p. 24); it is recognized by its equant form and preservation of the characteristic fracture patterns. Occasionally, it is skeletal in form (8:1 aspect ratio) and up to 3 mm in length (Fig. F28). Unaltered olivine is present in several flows, where it comprises up to 35 modal% of the rock in certain thin sections (e.g., Fig. F29) and commonly contains rare inclusions of glass and Cr spinel (Fig. F30).

Toward lobe margins the lavas show evidence of quenching where groundmass plagioclase laths are skeletal and are surrounded by acicular parallel arrays of clinopyroxene (usually in optical continuity) in a subvariolitic texture, along with dendritic titanomagnetite (Fig. F31). Immediately adjacent to lobe margins a well-developed variolitic texture is present, with spherical structures formed from plumose clinopyroxene radiating around minute plagioclase microlites (Fig. F20). This is indicative of high cooling rates (quenching) of the lava. Unaltered glass is often present in the areas between varioles. In the larger lobe interiors and massive basalt units, intergranular to subophitic textures predominate (e.g., Fig. F32).

Vesicle-rich segregations are common in the interiors of some lava flows (e.g., Units 20, 21, 23, and 26). They consist of usually vertically oriented concentrations of pipe vesicles and vesicle cylinders partially to wholly filled with vesicular segregated material. These are generally finer grained than the surrounding groundmass and are composed of comb-textured acicular clinopyroxene and abundant acicular and dendritic titanomagnetite, along with interstitial devitrified glass (Fig. F33). Plagioclase is typically sparse in these regions. Titanomagnetite can locally comprise up to 20% of the segregated material in, for example, Units 23, 26, 29, and 30 (e.g., Figs. F33, F34).

Opaque Mineralogy of the Lava Flow Units

The opaque mineralogy of the Site 1203 basalt is dominated by oxide minerals, primarily titanomagnetite, with minor primary pentlandite. Secondary pyrite is present in some sections, but this is restricted to mesostasis, glass-rich portions of the basalt groundmass, which are most susceptible to alteration and replacement, or veins and vesicles. The sulfides are generally extremely small (<0.01 mm in size) blebs included in primary phases, except in the olivine-rich zones of Units 11 and 16, where pentlandite comprises up to 1% of the modal mineralogy. The presence of pentlandite indicates that subsolidus reequilibration has occurred (Augustithis, 1979).

The magnetic characteristics of basalt are recorded in the micron-sized oxide phases, predominantly magnetite and titanomagnetite. Titanomagnetite is a solid solution between ulvöspinel (Fe_2TiO_4) and magnetite (Fe_3O_4), and it can be oxidized by two mechanisms (Haggerty, 1991): (1) at low pressure and <600°C to produce cation-deficient titanomagnetite or metastable titanomaghemite that can, on occasion, be subsequently converted to members of the hematite-ilmenite series and (2) at low to moderate pressures and >600°C with the direct formation of minerals from the hematite-ilmenite solid-solution series. In the Site 1203 basalt units, we see trellis-type ilmenite "oxidation exsolu-

F25. Melt inclusions in plagioclase, p. 76.

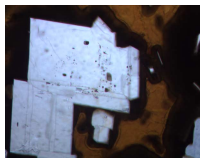

F26. Resorption of plagioclase phenocryst with melt inclusions, p. 77.

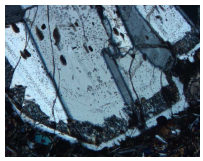

F27. Olivine glomerocryst with calcite vein at top, p. 78.

F28. Skeletal olivine pseudomorph, p. 79.

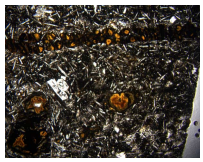

F29. Olivine-rich zone, p. 80.

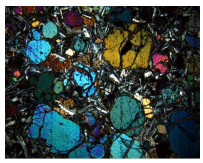

F30. Cr spinel inclusions in olivine, p. 81.

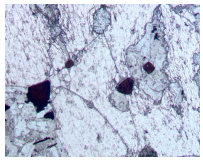

tion" (cf. Buddington and Lindsley, 1964) and maghemite/titanomaghemite lamellae in the titanomagnetites (Figs. F35, F36). Note that in this and other site chapters, we do not make the distinction between maghemite and titanomaghemite, as they are indistinguishable using reflected-light microscopy.

The secondary mineralogy demonstrates that the basement sequence at Site 1203 has experienced oxidative alteration (see "Alteration and Weathering," p. 24); the textures of the primary titanomagnetite support this and indicate that oxidation has occurred both above and below 600°C. For example, in several basalt lava units micrometer-sized and larger titanomagnetite grains visible under reflected-light microscopy have been completely replaced by maghemite (e.g., Units 1, 3, and 29) (Fig. F37), and in others, ilmenite oxidation exsolution lamellae are present (Fig. F35). We note partial alteration to maghemite in Units 29 and 30 (Fig. F38). Titanomagnetite is, for the most part, unaltered in Units 6, 11, 14, 16, 18–21, 23, and 24 (e.g., Fig. F39). The condition of titanomagnetite in the Site 1203 basalt units is summarized in Table T7.

In the olivine-rich sections of Units 11 and 16, Cr spinel is present as inclusions in olivine (Fig. F40). Where the Cr spinel has been in contact with the magma, it has either reacted completely or partially to titanomagnetite (e.g., Fig. F41) but remains unaffected where armored by olivine. The presence of Cr spinel in this basalt is significant, as the Cr content of such spinels can be used to estimate melt compositions as well as fractional crystallization processes (cf. Allan et al., 1988, 1989; Sack and Ghiorso, 1991).

Geochemistry

We conducted major and trace element analyses by inductively coupled plasma–atomic emission spectroscopy (ICP-AES) (see "Physical Volcanology and Igneous Petrology," p. 10, in the "Explanatory Notes" chapter) on 26 samples from the basalt units, 1 basaltic clast each from volcaniclastic Units 13 and 22, and 1 whole-rock volcaniclastite (Table T8). In an alkalis ($Na_2O + K_2O$) vs. SiO_2 classification plot, samples from the lava flow units range from tholeiitic to alkalic basalt (Fig. F42). The volcaniclastite sample has a very high $Na_2O + K_2O$ (6 wt%) that we interpret to be a secondary feature reflecting the altered nature of the basalt glass shards, ash, and lapilli particles. Hence, for the basalt samples we evaluate the compositional effects of postmagmatic alteration processes. First, loss on ignition (LOI) in Site 1203 basalt generally exceeds 1 wt% and ranges from 0.86 to 6.7 wt%, except for the volcaniclastite with 11.7 wt% (Table T8), whereas recent Hawaiian lavas have LOI < 1 wt% (e.g., Rhodes, 1996). All of the Site 1203 basalt samples that extend well into the alkalic field have LOI > 2 wt% (Fig. F42). Some but not all of these alkalic basalt samples have a relatively high K_2O content (Table T8); the sum of $Na_2O + K_2O$ in these basalt samples overlaps with the range in basalt from Site 883 (Fig. F42). The mobility of K_2O is clearly shown in Figure F43, where abundance of the incompatible elements Na, Ti, P, and Zr are highly correlated but K abundances are scattered, especially to high values. The Site 1203 samples with the highest K_2O contents (1.3–1.8 wt%) (Table T8) are from Unit 20, with high LOI values (5.2 wt%), and the three samples from Units 29 and 30 (LOI = 4.0–6.7 wt%) that contain a high proportion of clay-filled vesicles.

F31. Parallel acicular clinopyroxene crystals, p. 82.

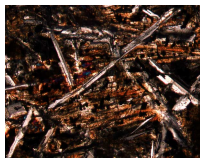

F32. Example of subophitic texture, p. 83.

F33. Segregated material in vesicle cylinder (Unit 23), p. 84.

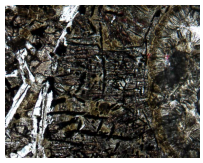

F34. Segregated material in vesicle cylinder (Unit 26), p. 85.

F35. Ilmenite exsolution in titanomagnetite, p. 86.

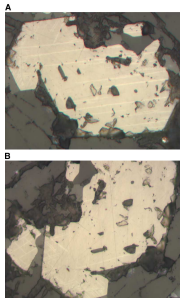

F36. Titanomagnetite with maghemite alteration, p. 87.

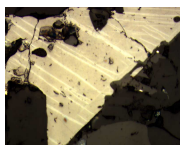

A similar result is seen for data from Site 883 Detroit Seamount basalt samples (Fig. F43). There is also evidence for CaO loss during alteration, most conspicuously in the volcaniclastite sample (≤2 wt%) (Table T8). Despite the evidence for K_2O mobility during alteration, we conclude that the Site 1203 lava compositions range from alkalic to tholeiitic. In particular, samples from flow Units 23, 26, 29, and 30, which have variable K_2O because of alteration, are all characterized by relatively high abundances of Na, Zr, Ti, and P (Fig. F43) and they are truly alkalic basalt. The alkalic basalt units range in thickness from 8 to 63 m. These units are from the lowermost 160 m of the ~450 m of basement penetration. Units 23 (63 m) and 26 (41 m) are the thickest flow units recovered (Table T4); both units are dominantly aphyric, highly vesicular basalt. In detail, the Ti vs. Zr plot shows different trends for basalt from Units 29 and 30 compared to that defined by basalt from Units 23 and 26. Note that Units 29 and 30 are similar; the boundary between them was defined by the presence of a 127-cm section of breccia in Section 197-1203-66R-1, a change from aphyric (Unit 29) to sparsely plagioclase-phyric (Unit 30) and a slight decrease in TiO_2 and Zr content.

Another important feature of basalt from Units 23, 26, 29, and 30 is that it has relatively constant Sr and Ba contents despite a Zr content that ranges from 200 to 315 ppm (Fig. F43). Unlike tholeiitic basalt samples from Detroit Seamount, Sr and Ba were not highly incompatible elements during the petrogenesis of these alkalic lavas. Four samples from Unit 23 were analyzed (Table T4). Relative to the other three samples, Sample 197-1203A-52R-6, 12–14 cm, is enriched in the incompatible elements Ti, Zr, P, Y, and Ba by ~20%, whereas Sr contents are similar. These enrichments can be explained by the abundance of highly evolved segregated melt in this sample (Fig. F44). The absence of Sr enrichment is consistent with this evolved melt being in equilibrium with plagioclase.

Two of the analyzed samples are basalt clasts in volcaniclastic Units 13 and 22. The compositions of these clasts are not identical to the underlying basalt lava units (Table T8), but they are transitional in composition like other Site 1203 basalt units with <2 wt% LOI (Fig. F42). Two other samples are from olivine-rich portions of Units 11 and 16. They are MgO rich and SiO_2 poor relative to other Detroit Seamount basalt samples (Table T8; Fig. F42A), a result of olivine addition. The olivine addition trends are especially clear in plots of Na_2O vs. Zr and MgO vs. Ni, Sc, CaO, and Sr (Figs. F43, F45).

Comparison with Other Hawaiian Island–Emperor Seamount Basalt Lavas

Although the high Ni content of the two picritic Detroit Seamount lavas is consistent with olivine accumulation, the Ni abundances of the remaining basalt (50–280 ppm) do not correlate with MgO content (Fig. F45). Except for Site 884 lavas, Sc abundance from basalt recovered from Detroit Seamount tends to increase with decreasing MgO content, thereby showing that basalt from Sites 883 and 1203 did not experience major fractionation of clinopyroxene. The CaO-MgO panel shows a distinctive field for the alkalic basalt samples at Site 1203; they have relatively low CaO and range to higher MgO contents than the transitional and tholeiitic basalt samples. The Sr-MgO plot shows that at a given MgO content, basalt from each drill site has a different range of Sr content, with the lowest abundances in the Site 884 tholeiitic basalt sam-

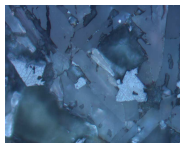

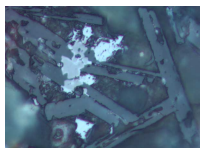

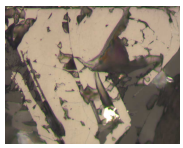

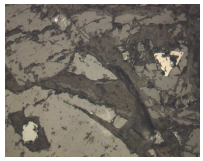

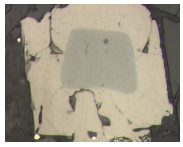

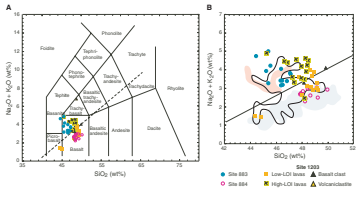

ples and the highest abundances in the Site 1203 alkalic basalt. At each drill site, Sr and MgO abundances are inversely correlated, suggesting that despite the presence of plagioclase-phyric lavas, plagioclase fractionation was not a major process controlling the lava compositions.

An objective of Leg 197 is to compare the compositions of basalt lavas from the Emperor Seamounts and the Hawaiian Islands. We use Mauna Kea Volcano, Hawaii, for this comparison because the compositions of the dominantly alkalic postshield stage and dominantly tholeiitic shield-stage lavas are well documented (Frey et al., 1990, 1991; Rhodes, 1996). In the classification plot (Fig. **F42**), Detroit Seamount lavas from Site 884 are within the tholeiitic shield field. Site 883 lavas are in the alkalic field, but Keller et al. (1995) concluded that these may be transitional lavas that plot in the alkalic field because of K_2O addition during alteration. Site 1203 lavas range from tholeiitic to alkalic basalt. Although some Detroit Seamount lavas appear similar in major element composition to Hawaiian lavas, those from Sites 883 and 884 differ significantly in abundances of incompatible elements (Keller et al., 2000; M. Regelous et al., unpubl. data). For example, in plots of MgO vs. TiO_2, P_2O_5, Zr, Ba, and Sr at a given MgO content, Detroit Seamount lavas from Site 883, and especially Site 884, are offset to lower incompatible element abundances than the Hawaiian trend defined by lavas from the Mauna Kea and Mauna Loa Volcanoes on the island of Hawaii (Fig. **F46**). In general, the Site 1203 transitional to tholeiitic lavas fill the gap between lavas from Sites 883 and 884; the Site 1203 alkalic basalt lavas (Units 23, 26, 29, and 30), however, overlap with those of the postshield stage from Mauna Kea Volcano in Ti, Zr, and P, but they have lower Sr and Ba contents (Fig. **F46**).

An important characteristic of Hawaiian volcanoes is their temporal evolution from preshield-, to shield-, to postshield-, to rejuvenated-stage lavas. Lava compositions and isotopic ratios change systematically with time (e.g., Chen and Frey, 1985; Clague and Dalrymple, 1987; West et al., 1987). Therefore, it is of interest to compare the temporal geochemical variations in extensive volcanic sections through the Emperor Seamounts with sections from Hawaiian volcanoes. Suiko Seamount, an Emperor Seamount drilled during Deep Sea Drilling Project Leg 55, shows a classic Hawaiian transition from older tholeiitic lavas to younger alkalic lavas (Jackson et al., 1980). In contrast, at Detroit Seamount the alkalic lavas, distinguished by a relatively low Ti/Zr value, occur deep in the Site 1203 section (Fig. **F47**). The Site 1203 alkalic basalt lavas that erupted as compound pahoehoe lavas in subaerial to shallow-marine environments may be analogous to the dominantly alkalic postshield-stage lavas that erupt as Hawaiian volcanoes migrate away from the hotspot. If the overlying tholeiitic to transitional pillow lavas at Site 1203 erupted from the same volcanic center as the alkalic lavas, the only analogous alkalic-to-tholeiitic transition in the Hawaiian Islands is the preshield stage represented by Loihi Seamount (e.g., Clague and Dalrymple, 1987). A scenario that could explain the alkalic-to-tholeiitic transition at Site 1203 is that the drilling penetrated lavas erupted from two distinct volcanic centers that were in different stages of growth. For example, such a lava sequence would be encountered in Hawaii where tholeiitic shield-stage lavas from Mauna Loa Volcano overlie alkalic postshield-stage lavas erupted from Hualalai Volcano. This possibility receives support from the observation that Unit 24, erupted within the alkalic sequence (Units 23, 26, 29, and 30), plots in

F43. Ti, P, Na, K, Sr, and Ba vs. Zr, p. 94.

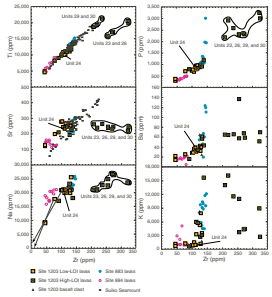

F44. Segregated material in vesicle cylinder, p. 95.

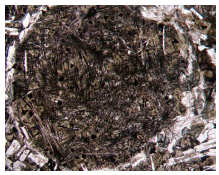

F45. Ni, Sc, Sr, and CaO vs. MgO, p. 96.

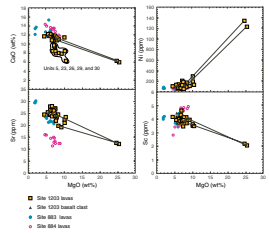

F46. TiO_2, P_2O_5, Zr, Sr, and Ba vs. MgO, p. 97.

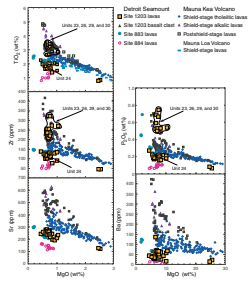

F47. Ti/Zr abundance ratio vs. depth, p. 98.

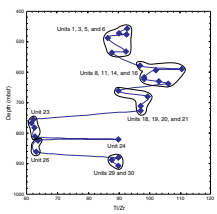

the tholeiitic field and has a Ti/Zr value similar to the younger tholeiitic lavas.

ALTERATION AND WEATHERING

Thirty-one basement units have been identified at Site 1203 (Hole 1203A). The sequence includes up to 18 basaltic units interpreted as pillow lava, compound pahoehoe, and pahoehoe sheet lobes (see "Physical Volcanology and Igneous Petrology," p. 11) and 13 units of volcaniclastic sediment or sediment interbeds consisting of tuff, lapilli tuff (lapillistone), and breccia. They represent either primary pyroclastic (tephra) and hyaloclastite deposits or resedimented tuff that are intercalated with vitric siltstone and sandstone and calcareous siltstone to mudstone (see "Physical Volcanology and Igneous Petrology," p. 11).

All basaltic rocks and volcaniclastic sediments have undergone secondary alteration and/or weathering. Alteration mineralogy was defined in rocks from Site 1203 by color, habit, and hardness in hand specimen, by optical properties in thin section, and by analogy with well-studied minerals identified during previous legs. Although X-ray diffraction measurements were conducted on samples from Site 1203, instrumental problems did not allow precise identification of the clay and zeolite minerals. The identification of secondary minerals in Hole 1203A therefore remains tentative, pending further shore-based studies.

The effects of alteration in rocks from Site 1203 are defined in the basaltic units in terms of (1) alteration assemblages and vein and vesicle filling and (2) alteration chemistry.

Basaltic Units

Alteration Assemblages

In this section, we describe the alteration paragenesis for each basaltic unit as recorded during core description and following thin section examination. For a summary of alteration assemblages downhole, see Figure F48. We also include the vein and vesicle filling as recorded during hand specimen observation (Figs. F49, F50). Additional data on vein fillings were recorded during thin section observation (Fig. F51; see also "Site 1203 Thin Sections," p. 268). All vein information was recorded in the alteration and vein logs (see "Site 1203 Alteration Logs," p. 340, and "Site 1203 Vein Logs," p. 343). Vesicle and vein fillings at Site 1203 indicate complex multistage alteration events. No preferred vein orientation was evident in the basement units. Veins mostly indicate complex patterns, occasionally reflecting ancient cooling joints.

Unit 1

Basement Unit 1 consists of lobes, interpreted as pillow lava. All the lobes are slightly to moderately altered. The extent of alteration increases toward veins, vesicles, and fine-grained lobe margins. This is mainly in the form of Fe oxyhydroxide formation as highlighted by changes in color from medium light gray–light gray (N6–N7) to light brownish gray (5YR 6/1). Olivine phenocrysts are completely replaced by white carbonate minerals (magnesite or calcite), brown amorphous clay or oxides (iddingsite), and, sometimes, green clay (likely saponite).

F48. Principal alteration minerals, p. 99.

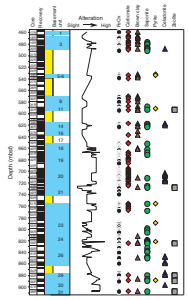

F49. Vesicle filling with depth, p. 100.

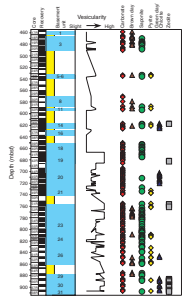

F50. Vein filling with depth, p. 101.

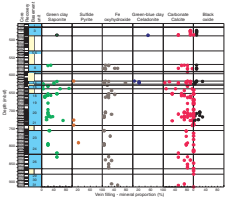

F51. Vein filling from thin sections, p. 102.

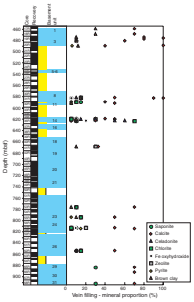

Veining is sparse throughout Unit 1. Veins and vesicles are filled with white carbonate (calcite), brown clay, and black to brown Fe oxyhydroxide.

Unit 3

As in basement Unit 1, Unit 3 is composed of slightly to highly altered lava lobes. The extent of alteration increases toward veins, vesicles, and glassy lobe margins. Alteration is usually high <2 cm from veins and vesicles and moderate >2 cm away from veins. Color throughout the unit varies from medium light gray–light gray (N6–N7) to light brownish gray (5YR 5/3 and 6/1) in the interior of lobes and dark, moderate, and pale yellowish brown (10YR 4/4, 5/4, and 6/2) at altered fine-grained lobe margins, around veins, and next to vesicles. The only exception is in interval 197-1203A-20R-3, 20–25 cm, where the color is medium gray (N5) with a light bluish green tint (5BG 6/6).

As highlighted by color, Fe oxyhydroxide formation is pervasive through the unit and is most prominent at the lobe margins. Most of the olivine phenocrysts are replaced by either white carbonate (magnesite or calcite) or reddish brown Fe oxyhydroxide (iddingsite), generally near fractures, and green clay (saponite) away from fractures. Plagioclase is moderately altered to green/white phyllosilicates (illite/sericite) near fractures and is slightly altered elsewhere. Glass is unaltered to moderately altered. Groundmass is also moderately altered near fractures, being replaced by brown clay and Fe oxyhydroxide, and is slightly altered elsewhere. In Section 197-1203A-20R-3, color reflects changes in alteration minerals and style: Fe oxyhydroxide is succeeded by dark blue-green clay (celadonite), which likely reflects a change from highly oxidizing to more reducing conditions.

Unit 3 is sparsely to highly veined. Veins are 2–4 mm wide in lobe interiors to 1–2 mm wide near lobe margins. They are filled with white carbonate (calcite), brown clay, green clay (saponite), and brown and black Fe oxyhydroxide. In Section 197-1203A-20R-3, veins are additionally filled with blue-green clay (celadonite) and sulfide (pyrite). Vesicles are filled with white carbonate (calcite), brown clay, and green clay (saponite).

Units 5 and 6

Units 5 and 6 are massive lava flows and are slightly altered. Color varies from medium dark gray (N4) to medium gray (N5) and medium light gray (N6). Olivine phenocrysts are replaced by white carbonate (magnesite or calcite) or reddish brown Fe oxyhydroxide (iddingsite). Part of the groundmass is replaced by brown clay and Fe oxyhydroxide. Small amounts of sulfide (pyrite) are present in the groundmass. These two units are sparsely veined, with veins being 0.1–3 mm wide. They are filled with white carbonate (calcite), followed by sulfide (pyrite). Vesicles are filled with white carbonate (calcite), green clay (saponite), and sulfide (pyrite).

Unit 8

Unit 8 consists of slightly altered lava lobes ≤30 cm in diameter. Color varies in the unit from medium dark gray (N7) in lobe interiors to pale yellowish brown (10YR 6/2) near glassy lobe margins and veins because of Fe oxyhydroxide formation. Olivine is replaced by reddish

brown Fe oxyhydroxide (iddingsite) and white carbonate (magnesite or calcite). Groundmass is altered to brown clay and Fe oxyhydroxide.

Unit 8 is sparsely to highly veined, mostly near glassy lobe margins. Most veins are <1–3 mm wide. They are mostly filled with white carbonate (calcite), brown and black Fe oxyhydroxide, and green clay (saponite). Additionally, celadonite and chlorite were identified in thin section. Vesicles are filled with white carbonate (calcite), brown clay, green clay (saponite), and sulfide (pyrite).

Unit 11

This massive lava flow unit is slightly altered. No variation in color was noted (gray black [N2]). In the most altered part of the unit, olivine phenocrysts are replaced by white carbonate (magnesite or calcite) and reddish brown Fe oxyhydroxide (iddingsite). The groundmass is altered to brown clay, Fe oxyhydroxide, and green clay (saponite). Zeolite and sulfide (pyrite) are present occasionally throughout the groundmass.

Unit 11 is sparsely veined, and veins are preferentially filled with white carbonate (calcite). Minor saponite, chlorite, and sulfide (pyrite) are also present. Vesicles are mainly filled with white carbonate (calcite) associated with minor amounts of green clay (saponite), brown clay, and sulfide (pyrite). One megavesicle, present at the top of Section 197-1203A-32R-1, is shown in Figure **F52.** It is round and partially filled with coarse calcite; the irregular central vug remains unfilled.

Unit 14

Unit 14 is characterized by alternating slightly altered massive basalt and moderately altered pillowed intervals. Color varies from medium gray (N5) to medium light gray (N6) and dark yellowish orange (10YR 6/6) in more altered patches. Fe oxyhydroxide has formed throughout the unit but mostly near veins and within 2 cm of the upper margin of the flow. Plagioclase phenocrysts are slightly altered to sericite and/or illite. Blue-green clay (celadonite), green clay (saponite), and brown clay replace the groundmass mostly near veins and within 2 cm of the glassy margins.

Unit 14 is sparsely to moderately veined. Veins are <0.1–5 mm wide. They show complex, sequential fillings, as shown in Figures **F53** and **F54.** White carbonate (calcite), black Fe oxyhydroxide, green clay (saponite), blue-green clay (celadonite), and sulfide (pyrite) were identified in hand specimen. Chlorite and zeolite were further identified in thin section. Vesicles also display multiple fillings composed of white carbonate (calcite), brown clay, green clay (saponite), blue-green clay (celadonite), zeolite, and sulfide (pyrite).

Unit 16

Unit 16 is massive and interpreted as a classic pahoehoe sheet lobe. Alteration is slight, and the whole unit is characterized by its gray-black color (N2). Olivine phenocrysts are partially altered to white carbonate (magnesite or calcite) or talc. Some brown clay is observed in the groundmass. Veins are sparse in Unit 16 and filled mostly with white carbonate (calcite) and green clay (saponite) with minor amounts of Fe oxyhydroxide.

F52. Megavesicle filled with calcite, p. 103.

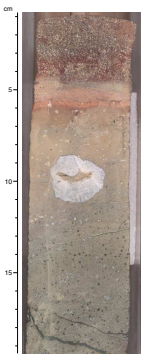

F53. Complex vein filling, p. 104.

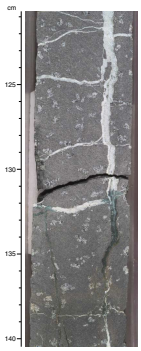

F54. Additional complex vein filling, p. 105.

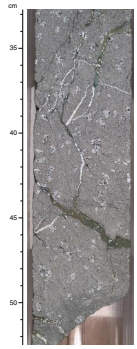

Units 18 to 21

Units 18 to 21 consist of a sequence of lava flows, each with multiple lobes that can be highly vesicular and up to 2 m thick. Depending on the position from the veins (within 1–2 cm) or in the lobes (interior or margins), basalt is, respectively, slightly to highly altered. Color reflects the degree of alteration and varies from medium-light gray (N6), medium gray (N5), medium-dark gray (N4), and dark gray (N3) to moderate brown (5YR 4/4), light brown (5YR 6/4 and 5/6), pale brown (5YR 5/2), pale yellowish brown (10YR 6/2), or dark yellowish orange (10YR 6/6) in more altered regions. Altered glass rims are dark greenish gray (5G 4/1). Fe oxyhydroxide is pervasive in alteration halos adjacent to glassy margins and around veins (up to 8 cm wide). Similar alteration halos are present around vesicle cylinders, although these are narrower. Olivine phenocrysts are replaced by white carbonate (magnesite or calcite), reddish brown Fe oxyhydroxide (iddingsite), and green clay (saponite). When present (e.g., Unit 18), plagioclase phenocrysts are sometimes slightly altered to sericite and/or replaced by illite or calcite. The groundmass is variably altered to brown clay, green clay (saponite), and Fe oxyhydroxide. Alteration to saponite is, however, minor in Unit 19. Glassy margins are usually completely devitrified and replaced by brown clay and Fe oxyhydroxide. In Unit 20, however, glass and groundmass are mainly replaced by blue-green clay (celadonite). Zeolite minerals were also identified in the Unit 21 matrix.

Units 18 to 21 are sparsely to moderately veined. Veins are most abundant near pillow margins and brecciated tops. They are <0.1–6 mm wide in the interior of lobes and larger (up to 15 mm wide) next to lobe margins. Voids are present in several of the larger veins. Veins are mostly filled with white carbonate (calcite), brown to black Fe oxyhydroxide, green clay (saponite), and sulfide (pyrite, mainly in massive sections). Zeolite minerals were identified in thin section. In brecciated areas, veins can contain angular glass fragments derived from adjacent glassy margins. Brown alteration halos (1–5 mm in size), rich in Fe oxyhydroxide, are present around veins. Vesicles are filled with mainly white carbonate (calcite), green clay (saponite), blue-green clay (celadonite) (Unit 20), and pyrite (Unit 21).

Units 23 and 24

Units 23 and 24 consist of a sequence of highly vesicular lava lobes. The degree of alteration is slight in the interior of lobes to moderate/high toward the veins and lobe margins and complete in the glassy margins. Color varies from dark gray (N3), medium-dark gray (N4), medium gray (N5), and medium-light gray (N6) to moderate reddish brown (10R 4/6) and moderate yellowish brown (10YR 5/4) around veins, in alteration halos, and toward lobe margins. Altered glass is dark greenish gray (5G 4/1). Olivine microphenocrysts are replaced by white carbonate (magnesite or calcite) and reddish brown Fe oxyhydroxide (iddingsite). Glass is completely devitrified, and the mesostasis is altered to green clay (saponite), brown clay minerals, or Fe oxyhydroxide. Sulfide (pyrite) is present in the mesostasis, mostly adjacent to veins and vesicles.

Units 23 and 24 are sparsely veined. Veins are 0.1–4 mm wide and are filled with white carbonate (calcite), Fe oxyhydroxide, green clay (saponite), and sulfide (pyrite). Zeolite and chlorite were identified in thin section. Vesicles are partially to totally filled with white carbonate (cal-

cite), green clay (saponite), brown clay, zeolite, and pyrite, but are also unfilled and lined with green clay (saponite).

Unit 26

Unit 26 is a succession of slightly (interiors) to moderately (next to margins) altered lobes. Color varies from dark gray (N3), medium-dark gray (N4), medium gray (N5), and medium-light gray (N6) to moderate yellowish brown (10YR 5/4) and grayish orange (10R 7/4) adjacent to veins and in alteration halos. Medium bluish gray (5B 5/1) colors are present at the base of the unit. Sparse olivines are altered to reddish brown Fe oxyhydroxide (iddingsite). The mesostasis is altered to brown clay, green clay (saponite), and Fe oxyhydroxide (goethite). Glass is completely altered to green clay (saponite). Minor sulfide (pyrite) and zeolite were identified in the upper part of the unit. Blue-green clay (celadonite) is present at the base of the unit.

Sparse veins, 0.1–3 mm wide, are present in Unit 26. They are filled with white carbonate (calcite), Fe oxyhydroxide (goethite), and minor amounts of green clay (saponite). Minor chlorite is also present and was identified in thin section. Most vesicles are filled with white carbonate (calcite), green clay (saponite), brown clay, and, rarely, sulfide (pyrite) and blue-green clay (celadonite).

Units 29 to 31

Units 29 to 31 are composed of lobes with brecciated tops and massive interiors. They are slightly altered (interiors) to moderately or highly altered (brecciated tops or glassy margins). Color varies from medium-dark gray (N4) and medium gray (N5) to moderate brown (5YR 3/4) and light brown (5YR 6/4) in highly altered areas, grayish orange (10R 7/4) to pale reddish brown (10R 5/4) adjacent to veins, and dark greenish gray (5G 4/1), grayish green (10GY 5/2), or grayish blue green (5GB 5/2) at altered glassy lobe margins. When present (e.g., Units 30 and 31), plagioclase phenocrysts are slightly altered to sericite and/or illite. The mesostasis is altered to green clay (saponite), brown clay, white carbonate (calcite), blue-green clay (celadonite), or zeolite. Fe oxyhydroxide (goethite) alteration is pervasive throughout these units. Occasional sulfide (pyrite) was identified in the groudmass and adjacent to veins. Glassy clasts in the brecciated flow top and in lobe margins are completely altered to green clay (saponite) and brown clay.

Units 29 to 31 are sparsely to moderately veined. Veins are 0.1–5 mm wide and are principally filled with white carbonate (calcite) and subordinate amounts of green clay (saponite) and Fe oxyhydroxide (goethite). Vesicles are filled with minor amounts of white carbonate (calcite) and brown clay. The main filling minerals are green clay (saponite), blue-green clay (celadonite), zeolite, and sulfide (pyrite).

Alteration Chemistry

Chemical analyses were performed on board by ICP-AES (see **"Physical Volcanology and Igneous Petrology,"** p. 10, in the "Explanatory Notes" chapter). These data were used to estimate the effects of alteration throughout the basement section. However, only the freshest pieces were sampled. The chemical variations reported here could therefore underrepresent the overall alteration-related chemical effects

downhole. Further shore-based studies will be undertaken to address this issue.

Variations in the abundances of some chemical elements and LOI vs. depth are reported in Figures **F55** and **F56.** LOI is a proxy for the degree of alteration. LOI values vary downhole from ~1 to ~7 wt%, with a significant increase in Unit 19 downward (the sample with 11.73 wt% LOI was taken from volcaniclastic Unit 4). This trend confirms macroscopic and petrographic observation of the samples. Igneous rocks from the lower units of Hole 1203A show higher degrees of groundmass alteration compared to upper units. Zeolite abundances increase, whereas carbonate replacement decreases downhole. As shown in Figure **F55,** CaO decreases downhole, with a significant decrease from the top of Unit 23. In the same interval, K_2O increases, although K_2O abundances are more scattered overall. Na_2O, Ba, and Sr are approximately constant with depth.

Figure **F56** illustrates the variability of Zn/Zr, Co/Zr, and Cu/Zr ratios with depth. The normalization to the incompatible and immobile element Zr is used here to minimize the effects of magma evolution and to reveal the effects of low-temperature alteration. The Zn/Zr ratio is fairly constant in the upper units of Site 1203 and decreases slightly from Unit 19 downward. The highest Zn/Zr ratios are reported for the two olivine-rich samples (e.g., Sample 197-1203A-32R-3, 85–87 cm, and 37R-3, 10–13 cm) and are more likely a primary feature than an alteration effect, given the observation of primary sulfide inclusions in olivine (see **"Physical Volcanology and Igneous Petrology,"** p. 11). Likewise, the Co/Zr ratio remains constant in the upper part of Hole 1203A and decreases slightly from Unit 20 downward. High Co/Zr ratios are also displayed by the same olivine-rich samples. Although Cu/Zr ratios are more scattered, the same overall trend is seen in Hole 1203A, with higher ratios within the upper units compared with Unit 20 downward. Some samples from Units 11, 14, 16, and 24 show higher Cu/Zr ratios.

In Figure **F57,** K_2O, Co, Cu, and Zn are reported against Zr, together with data from Hawaiian volcanoes Mauna Kea and Loihi and results from ODP Leg 145, Sites 883 and 884. Two groups are easily distinguished at Site 1203, based on Zr abundances. As previously noted, K_2O data are quite scattered and trend away from the highly correlated data from unaltered Hawaiian lavas. The increase in K_2O abundances is likely an effect of low-temperature alteration, K being fixed in celadonite and smectites. Zn abundances of samples from Site 1203 plot within the field reported for Hawaiian lavas, and ODP Leg 145 Sites 883 and 884 and are consistent with magmatic evolution and minimal secondary mobilization. Co, which behaves as a compatible element, exhibits distinctly higher abundances in the lower units at Site 1203 (Units 23, 26, 29, and 30) at a given Zr than Hawaiian lavas and may reflect enrichment by alteration processes. Most samples from Site 1203 have lower Cu abundances than reported for the unaltered Hawaiian lavas. The lower abundances in Cu could reflect loss during hydrothermal alteration. Cu and Co abundances in samples from Site 1203 are difficult to interpret at this stage and will require further shore-based analyses. Mobilization of these two elements would suggest circulation of high-temperature hydrothermal fluids (T = >350°C). However, no high-temperature minerals or assemblages were observed in samples from Site 1203 (e.g., quartz or amphibole).

F55. LOI, CaO, K_2O, Na_2O, Ba, and Sr, p. 106.

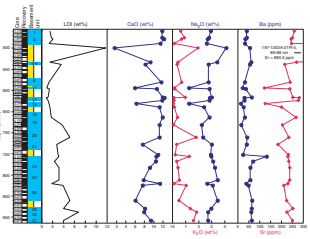

F56. Zn/Zr, Co/Zr, and Cu/Zr, p. 107.

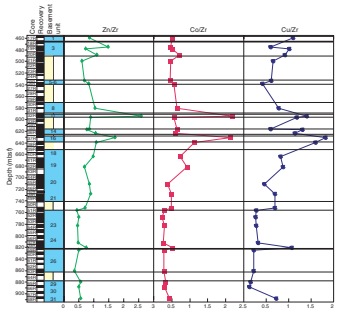

F57. Zr vs. K_2O, Cu, Co, and Zn, p. 108.

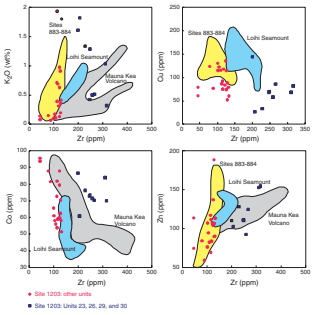

Volcaniclastic Units

The volcaniclastic succession is dominantly basaltic in composition but consists of a range of sediment types comprising tuff, lapilli tuff (lapillistone), and breccia, representing primary pyroclastic (tephra) and hyaloclastite deposits as well as resedimented tuff intercalated with vitric siltstone and sandstone and calcareous siltstone to mudstone. Alteration features associated with these deposits are described in **"Physical Volcanology and Igneous Petrology,"** p. 11.

Summary

Igneous rocks recovered at Site 1203 (Hole 1203A) have undergone low-temperature alteration and/or weathering to varying extents. Alteration features are defined in the basaltic units in terms of secondary mineral paragenesis, apparent as vesicle filling, vein filling, and replacement of groundmass and primary minerals. Overall, the basalt flows are slightly to moderately altered (Cores 197-1203A-17R to 41R) with an increase downhole (from Core 197-1203A-42R to 68R) to moderately to highly altered. In the upper sequence, the alteration paragenesis is clearly dominated by carbonate, Fe oxyhydroxide, and brown and green clay (saponite) formation. The minor associated minerals are sulfide (pyrite), blue-green clay (celadonite), and zeolite. A change in the alteration conditions is seen in the lower sequence, where zeolite minerals increase and carbonates decrease. The same change is seen downhole in the vesicle-filling parageneses. Most vesicles are filled with calcite and/or saponite. Near the bottom of the hole (from Unit 29), they are mostly filled with zeolite and Fe oxyhydroxide (sometimes crystallized as goethite). The recovered basalt is sparsely to highly veined. The major constituent of veins is calcite, which is frequently associated with saponite, brown clay, and Fe oxyhydroxide. Less frequently, chlorite, celadonite, zeolite minerals, and pyrite were identified.

Igneous rocks from Site 1203 show complex multistage alteration features. Mineral associations indicative of low-temperature interactions between rocks and fluids dominate throughout the sequence. The abundant occurrence of Fe oxyhydroxide, smectites (saponite and brown clay), and associated celadonite suggests that most of the sequence was altered at low temperature. This paragenesis is typical of the two lowest temperature stages of oceanic crust alteration (also known as "seafloor weathering" and "alkali fixation" zone) (Alt, 1995). Temperature estimates for smectite and celadonite formation are in the range 30° to 150°C. Fe oxyhydroxide, smectite (nontronite? and saponite), and celadonite suggest circulation of large volumes of oxidizing fluids in the lava pile. As the fluid penetrated deeper in the sequence, more reducing conditions developed and secondary sulfides were formed (pyrite in Hole 1203A). Carbonate and zeolite are formed in both environments. Despite the clear dominance of low-temperature fluid circulation, minerals such as chlorite indicate that at least part of the volcanic pile has reacted with higher-temperature fluids (T = 250°–300°C). Although it is difficult to extract the succession of these different events, some sulfides are likely coeval with minerals such as chlorite, suggesting a reducing environment during at least some of these higher-temperature fluid circulations.

PALEOMAGNETISM AND ROCK MAGNETISM

Paleomagnetic and rock magnetic measurements at Site 1203, which is located in the summit region of Detroit Seamount, were aimed at assessing the nature of the natural remanent magnetization (NRM) of basement rock and obtaining a preliminary estimate of the paleolatitude of the site during basement formation (~75–76 Ma, as estimated by nannofossil biostratigraphy) (see "Biostratigraphy," p. 10). Basalt and sediment discrete samples (minicores) were used for measurements. In addition, the magnetization of sediment recovered above basement was measured to define geomagnetic polarity. For magnetostratigraphic analysis, half-round core sections were analyzed. We start by describing these magnetostratigraphic measurements, analyses, and results. We follow this with a presentation of rock magnetic and paleomagnetic analyses of basalt and sediment comprising the Site 1203 basement sequence.

Paleomagnetism of Sedimentary Rocks Recovered above Basement

Natural remanent magnetizations from archive half-round core sections from sedimentary units recovered above basement in Hole 1203A (Cores 197-1203A-1R to 17R) were measured using the shipboard 2-G Enterprises superconducting quantum interference device (SQUID) magnetometer. The sediments are mostly poorly consolidated oozes and chalks (see "Lithostratigraphy," p. 6). The measurement interval was 5 cm. Progressive alternating-field (AF) demagnetizations were applied to peak fields ranging from 20 to 40 mT. The effectiveness of this demagnetization varied throughout the core, as seen in orthogonal vector plots of the decay of NRM with applied field for select measurement intervals (Fig. F58). From some intervals, the NRM was found to be composed of an apparent Brunhes-age component overprinting a reversed characteristic remanent magnetization (e.g., Fig. F58).

Inclinations derived from vector end points after AF demagnetization were used to assign geomagnetic polarity (Fig. F59). Because the core sections analyzed were derived from rotary drilling, a few caveats are needed before further considering even this preliminary polarity interpretation. Rotary drilling of sediments can result in the recovery of long core sections with only minor disturbance. However, sometimes the disturbance is severe. If the sediment is not well lithified, zones (commonly called "biscuits") can rotate within the core liner. Unconsolidated sediment recovered by rotary drilling can also have a pervasive internal disruption. In general, a polarity was assigned only if several consecutive measurement intervals demonstrated a consistent polarity; single-point estimates suggesting a polarity opposite to that of adjacent intervals were ignored and assumed to reflect core disturbance (or insufficient demagnetization) in this preliminary analysis.

Correlations with the Geomagnetic Polarity Timescale

Correlation of the observed polarity intervals in the upper part of the sedimentary sequence (Cores 197-1203A-1R to 10R) to the geomagnetic timescale is hindered by limited recovery, core disturbance, and poor preservation of nannofossils (see "Biostratigraphy," p. 10). Using the available nannofossil data, a few preliminary correlations can be dis-

F58. Orthogonal vector plots for sediments, p. 109.

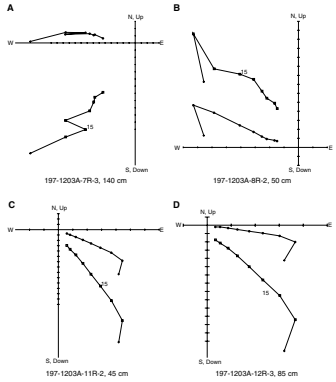

F59. Paleomagnetic inclinations vs. depth, p. 111.

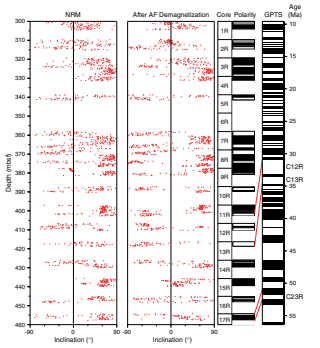

cussed for cores recovered from deeper in the section. Cores 197-1203A-11R to 13R have been assigned to the early Oligocene NP21 to NP22 nannofossil zone (see "Biostratigraphy," p. 10). These assignments suggest that the reversed polarity intervals identified in the same cores probably correspond to the polarity chron sequence between reversed polarity Chrons 12r and 13r (~32–34 Ma) (Berggren et al., 1995). Core 197-1203A-17R is assigned to the early Eocene NP12 nannofossil zone. This assignment suggests the polarity intervals identified in this core may correspond to Chron C23 (~52 Ma).

Overall, the relatively frequent magnetic reversals observed in the sedimentary cores recovered above basement are more consistent with an early Tertiary rather than a Late Cretaceous age. The latter time interval is characterized by a lower reversal frequency (and a correspondingly greater duration of individual polarity chrons) than that apparently recorded by the sediment cored in Hole 1203A above basement. This relative age assignment is consistent with biostratigraphic data indicating a significant hiatus between igneous basement and the overlying sediment at Site 1203.

Rock Magnetism of Basalt and Sediment Comprising Basement

The basement section at Site 1203 is composed of basalt flows and volcaniclastic sediments (see "Physical Volcanology and Igneous Petrology," p. 11). The sediments were well indurated, so samples for paleomagnetic and rock magnetic analyses were collected as drilled minicores or sawed cubes.

Magnetic Susceptibility and Koenigsberger Ratio

Low-field volume-normalized (bulk) magnetic susceptibility was measured on every sample collected from basement (after AF demagnetization) with a Kappabridge KLY-2 magnetic susceptibility meter. For each sample, measurements were taken three times and then averaged. In general, measurements on a single sample agreed to within 1%. Magnetic susceptibility values range from 0.2×10^{-3} to 66×10^{-3} SI (mean = 9.8×10^{-3} SI). The Koenigsberger ratio (Q) was calculated for each sample according to the following formula:

$$Q = \mathrm{NRM}/(K \times \mathrm{H}),$$

where,

NRM = natural remanent magnetization intensity,
K = bulk volume susceptibility, and
H = present geomagnetic field intensity at Site 1203, which is estimated to be 38.8 A/m using the International Geomagnetic Reference Field (Barton et al., 1995).

Koenigsberger ratios range from 0.02 to 176 (mean = 15.4). Median destructive field (MDF) was calculated based on detailed stepwise AF demagnetization data used for constraining characteristic remanent directions (see below).

Figure F60 shows a plot of (bulk) volume magnetic susceptibility (K), the Q-ratio, and MDF vs. depth. The basalt samples measured generally

F60. Magnetic susceptibility, Koenigsberger ratio, and MDF, p. 112.

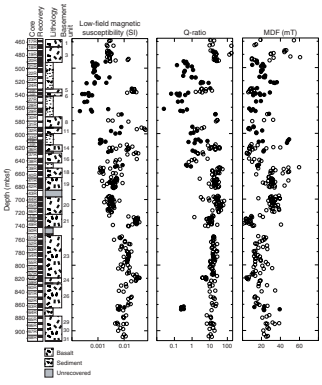

have *Q*-ratios > 1.0. Basalt recovered between 650 and 720 mbsf is characterized by much higher *Q*-ratios and higher MDF values relative to other parts of the basement sequence drilled. These basalt samples correspond to basement Units 18–20 (see "Physical Volcanology and Igneous Petrology," p. 11).

Basement Units 1 and 3 (~460–490 mbsf) also show high *Q*-ratios and high MDF values. Analyses of polished thin sections of these rocks using reflected-light microscopy reveal the presence of maghemite (see "Physical Volcanology and Igneous Petrology," p. 11). Whereas the grain size of the maghemite observed is far greater than the grains that are likely responsible for carrying a remanent magnetization, its presence indicates that caution is needed in interpreting the preliminary paleomagnetic results from these basement units.

A plot of magnetic susceptibility vs. NRM intensity is shown in Figure F61. Compared to the wide range in NRM intensities displayed by the sediment samples, the basalt samples show a rather narrow variation. Two sediments samples with high intensity are from volcanic breccia and hyaloclastite tuff. A plot of the log of bulk volume magnetic susceptibility vs. MDF is shown in Figure F62. Magnetic susceptibility data from basalt samples are clearly negatively correlated with MDF values, whereas the data from sediment samples are scattered. Basalt samples with lower MDF values (<10 mT) are from the visually fine-grained and fresh parts of the recovered core material, typified by Section 197-1203A-48R-1 to Core 197-1203A-49R (basement Unit 21). The low MDF values may reflect unoxidized titanomagnetite with a relatively large grain size. All the sediment samples with relatively high MDFs (>40 mT) are from intervals of volcanic breccia.

F61. Magnetic susceptibility vs. NRM, p. 113.

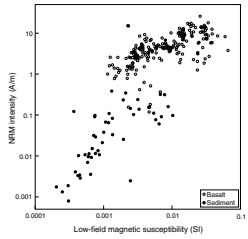

F62. Magnetic susceptibility vs. MDF, p. 114.

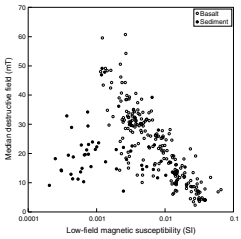

Lowrie-Fuller Tests

The Lowrie-Fuller test (Lowrie and Fuller, 1971) is based on AF demagnetization of strong-field and weak-field thermoremanent magnetization (TRM) and permits a rapid estimate of magnetic domain state in igneous rocks. Magnetic domain state can be used further to help constrain magnetic grain size. The Lowrie-Fuller test is based on the experimental observation that in large multidomain (MD) grains, strong-field TRM requires larger destructive fields than weak-field TRM to reach the same normalized remanence level. In practice, the strong-field TRM is usually represented by a laboratory-induced saturation isothermal remanent magnetization (SIRM) and the weak-field TRM is represented by an anhysteretic remanent magnetization (ARM). Given an unknown magnetic mineralogy, the test can be considered only as qualitative because changes in magnetic coercivity related to different magnetic minerals can mimic changes in magnetic grain size.

The Lowrie-Fuller test was performed on one or two samples from each basaltic flow unit. First, an ARM was produced by demagnetizing the sample in a 140-mT alternating field in the presence of a 30-µT direct-current field using the D-2000 AF demagnetizer. The ARM was then progressively AF demagnetized. An SIRM was then acquired in a 0.8-T field using an IM-10 impulse magnetizer then was subsequently AF demagnetized. All AF demagnetizations were conducted using the D-2000 AF demagnetizer, and all remanences were measured with the shipboard Molspin Minispin magnetometer.

In interpreting these data in terms of magnetic domain state, we rely on the relative shapes of the ARM and SIRM demagnetization curves. For some samples (e.g., Sample 197-1203A-26R-2, 29–31 cm [basement

Unit 6]) (Fig. F63), the two demagnetization curves are similar and clear constraints on magnetic domain state are not possible. In other samples, the rapid decay of ARM relative to SIRM suggests the presence of MD grains (e.g., Sample 197-1203A-37R-2, 76–78 cm [basement Unit 16]) (Fig. F64). In still other samples, the resistance of ARM to demagnetization relative to SIRM suggests the presence of single- to pseudo-single-domain grains (e.g., Samples 197-1203A-42R-5, 65–67 cm [basement Unit 19]; 52R-2, 101–103 cm [basement Unit 23]; 61R-1, 131–133 cm [basement Unit 26]; and 67R-1, 18–20 cm [basement Unit 30]) (Fig. F63).

In general, the *Q*-ratios, median destructive field values, and results of the Lowrie-Fuller tests indicate that most of the recovered basalt and volcaniclastic sediments are capable of preserving primary magnetizations suitable for paleolatitude analyses. The only potential exception is represented by basalt from basement Units 1 and 3. The potential maghemitization of remanence carriers suggested by reflected-light observations and its potential effect on the remanence record should be addressed in shore-based studies (see "Discussion," p. 36).

Paleomagnetism of Basalt and Sediments Comprising Basement

Minicore samples of basalt and minicore or cube samples of the volcaniclastic sediments were measured with the 2-G Enterprises SQUID magnetometer and the Molspin Minispin magnetometer. After the measurement of the untreated NRM, samples were progressively demagnetized by AF demagnetization. In general, a 5-mT field increment was used and the peak field applied was 80 mT. Paleomagnetic measurements collected after each step form the basis of the data set described below.

Demagnetization Behavior

Most basalt samples show an extremely well-defined, simple demagnetization pattern when viewed on orthogonal vector plots (Fig. F64). After the removal of a low-coercivity (<10 mT) viscous component of magnetization, a stable single component of magnetization, identified as the characteristic remanent magnetization (ChRM), was defined. A steep overprint component, similar to that reported in some paleomagnetic studies of ODP cores and thought to be imparted by the drill string, was not observed. Volcaniclastic sediment samples showed a similar behavior (Fig. F65), although sometimes with less apparent magnetic stability.

A few samples displayed a more complex behavior, signaling potential inadequacies of AF demagnetization in isolating the characteristic remanent magnetization. In a few basalt samples, the demagnetization data defined a linear trend that bypassed the origin of an orthogonal vector plot, indicating the presence of high-coercivity magnetic minerals (Fig. F66). In a few other cases the AF treatment failed to reduce the magnetization to <10% of the untreated NRM. Sediment samples sometimes exhibited more complex behavior as well. This included the failure of the demagnetization to isolate a stable component with a trend to the origin. Whereas high-coercivity phases may be partly responsible for this behavior, resolution limits of the shipboard magnetometer may have contributed to the observed scatter.

F63. Lowrie-Fuller tests on basalt, p. 115.

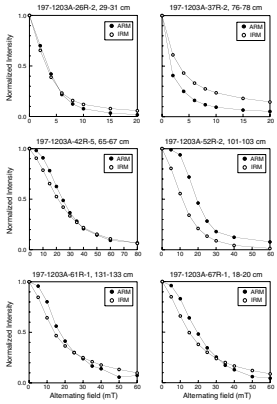

F64. Orthogonal vector plots for basalt samples, p. 116.

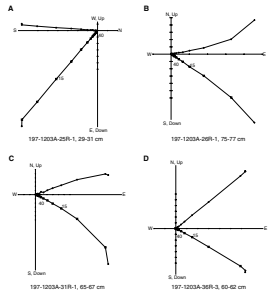

F65. Orthogonal vector plots for volcaniclastic sediment, p. 118.

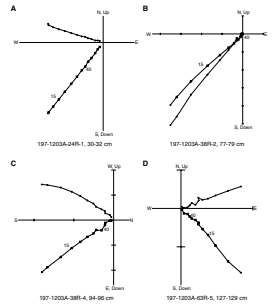

F66. Orthogonal vector plots for basalt and volcaniclastics, p. 119.

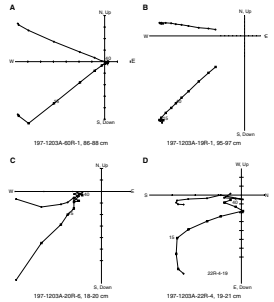

Modified Conglomerate Test

Samples were collected from the coarse volcaniclastic sediment/breccia of basement Unit 13 to further assess the nature of the NRM. These samples can be used to conduct a variant of the conglomerate test (Graham, 1949). In the classical test, the NRM of individual clasts composing a conglomerate is measured. Magnetization directions from these clasts are expected to be random if the conglomerate and adjacent rocks have not experienced a thermal or chemical event (or both) after formation sufficient to cause remagnetization.

In our case, individual clasts were not sampled but each minicore was composed of numerous relatively large (~0.1–0.25 cm) basaltic clasts separated by a calcite matrix. Because the drilled cores are azimuthally unoriented, we must rely on an analysis of the components seen in the orthogonal vector plots. These plots show that in each sample the magnetization is stable during AF demagnetization but that several magnetic components are often recorded (Fig. F67). In general, the samples show a relatively high coercivity, and it is possible that a mineral such as hematite carrying a chemical remanent magnetization contributes to the total NRM. However, the magnetic components that can be isolated by AF demagnetization are not consistent between minicores, indicating that the breccia and other basement section rocks likely did not experience a remagnetization event.

F67. Orthogonal vector plots of volcaniclastic sediment, p. 120.

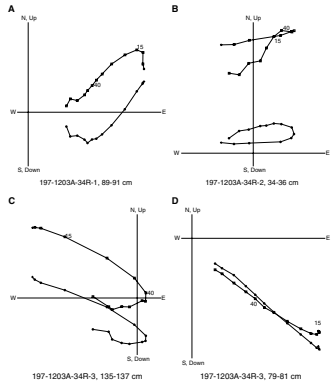

Characteristic Remanent Magnetization Directions

ChRM directions for basalt and sediment were fit using principal component analysis (Kirschvink, 1980). In general, the ChRM directions were defined between 15 and 70 mT for basalt samples and maximum angular deviations of the line fits were <3°. For the volcaniclastic sediment samples, the ChRM directions were generally isolated between 15 and 50 mT and the maximum angular deviations of the fits were generally <5°. Of 202 basalt samples demagnetized and measured, 199 yielded ChRM directions. The three rejected basalt samples had demagnetization data that did not trend to the origin of orthogonal vector plots. Of the 56 sediment samples measured, 34 yielded ChRM directions useful for constraining paleolatitude. Seven sediment samples from volcanic breccia used for the modified conglomerate test were not considered. Data from 15 samples failed to show stable magnetization during AF demagnetization and were also not considered.

Paleomagnetic Inclinations and Paleolatitudes from Volcaniclastic Sediment

Because the magnetization of a standard paleomagnetic sediment sample is thought to have been locked in over a time interval much greater than that of a single lava flow, we give equal weight to each sample in the following analysis. Applying the inclination-only averaging procedure outlined by McFadden and Reid (1982), the 34 paleomagnetic inclinations from the characteristic remanent magnetizations derived from the volcaniclastic sediments have a mean value of 54.7°, an estimated precision parameter (k) = 24.8, and a 95% confidence region = +3.1°/–6.4°. If these data are accurate recorders of the time-averaged geomagnetic field, the results suggest a paleolatitude of 35.2° (95% confidence region = +3.2°/–5.9°). These data form a distribution that is off-

set by ~16°N from the latitude expected if the Hawaiian hotspot had remained stationary in the mantle over the last 75–76 m.y. (Fig. F68).

Paleomagnetic Inclinations and Paleolatitudes from Basalt

ChRM inclinations derived from basalt samples were averaged using inclination-only statistics (McFadden and Reid, 1982) to obtain lava flow means. Sixteen of the eighteen lava flows recovered from Site 1203 were sampled and yielded flow mean inclinations (Table T9). Assigning equal weight to each flow, these data yield a mean inclination of 48.0° (95% confidence interval = ±8.4°), which suggests a mean paleolatitude of 29° (95% confidence interval = +6.3°/–7.8°). The latter value assumes the directions are adequately represented by AF demagnetization, secular variation is averaged by the section, and extremely short intervals between some lava flows do not cause a bias in the mean (see "Discussion," p. 36). The paleolatitude average is 10° farther north than that predicted by a fixed hotspot reference frame (Fig. F69). Statistics of inclination averages from basalt are summarized in Table T9.

Discussion

We compare the distribution of inclinations derived from the volcaniclastic sediments with a synthetic Fisher distribution (Fisher, 1953) having the same mean inclination and precision parameter (*k*) as displayed by the experimental data in Figure F70. A similar comparison between the flow-mean basalt inclinations and a synthetic Fisher distribution is seen in Figure F71. Inclination values from the volcaniclastic sediments appear to have a distribution that suggests the mean represents an adequate sampling of a hypothetical parent distribution. However, the magnetization of coarse sedimentary rocks such as some of the volcaniclastic rocks can be affected by detrital inclination error (King, 1955). Furthermore, compaction can induce inclination shallowing in finer-grained marine sediments (e.g., Arason and Levi, 1990; Tarduno, 1990). Paleolatitudes determined from paleomagnetic analyses of the volcaniclastic sediments should therefore be considered to be minimum values. An effect of inclination shallowing may be present in the group of inclinations with values <45°.

The distribution of paleomagnetic inclinations derived from Hole 1203A basalt seems to represent the range of values typical of a model Fisher distribution. Values near the mean, however, appear to have been undersampled. There is also a hint of potential serial correlation in the data with inclinations <45°. The overall estimated dispersion of the data (S = 17.7°) (Table T9) is slightly higher than that expected from global lava flow data spanning the 45- to 80-Ma interval (McFadden et al., 1991).

Another consideration is the possibility that the characteristic remanent magnetizations isolated by AF demagnetization in basement Units 1 and 3 do not accurately represent the field direction during basalt cooling because of later alteration (signaled by the occurrence of maghemite identified by reflected-light optical microscopy). To investigate the potential effect that inaccurate field values from these units might have, we calculated a new mean, excluding basement Units 1 and 3 (Table T10). The average inclination of 50.0° (95% confidence interval = ±9.0°) is slightly steeper than that calculated with Units 1 and 3 included and may be a more conservative estimate, given the rock magnetic uncertainties.

F68. Inclination from volcaniclastic sediment, p. 121.

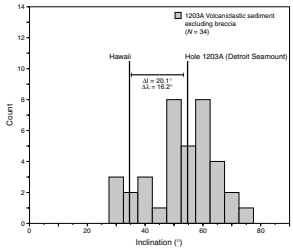

T9. ChRM inclination averages, p. 161.

F69. Inclination from basement basalt, p. 122.

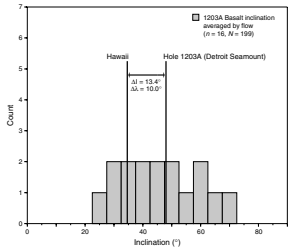

F70. PCA vs. synthetic Fisher distribution of volcaniclastic sediment, p. 123.

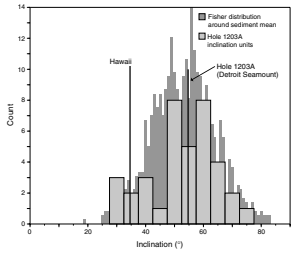

F71. PCA vs. synthetic Fisher distribution for basalt, p. 124.

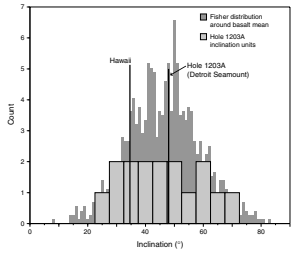

T10. ChRM inclination averages excluding Units 1 and 3, p. 162.

Overall, the sediment and basalt inclination means discussed above represent a paleolatitude range between 29° and 35°N. These values are within the uncertainty region of the paleolatitude of 36°N (95% confidence interval = ±7°) derived from analyses of older basalt (81 Ma) recovered at ODP Site 884 on the eastern flank of Detroit Seamount (Tarduno and Cottrell, 1997). The Hole 1203A data, however, are preliminary and must be confirmed with detailed shore-based rock magnetic characterizations and thermal demagnetizations to isolate remanence components.

PHYSICAL PROPERTIES

The objective of the physical properties program at Site 1203 was to assist in interpretation of lithologic variations and correlation with downhole geophysical logs. All cores were run through the multisensor track (MST), which included magnetic susceptibility and gamma ray attenuation (GRA) bulk density measurements for sediment Cores 197-1203A-1R to 17R and natural gamma radiation (NGR) measurements for all cores. Compressional wave velocities were determined from the split cores in the transverse (x-direction) for the soft sediment cores (Cores 197-1203A-1R to Section 17R-3) and for discrete samples of basalt and volcaniclastic sediment without the core liner. Index properties determinations for both sediment and discrete basalt samples included bulk density, moisture content, porosity, and grain density. These were calculated from wet and dry sample masses and dry volumes. Thermal conductivity was also determined for both sediment and basalt samples at a frequency of one per core.

MST Measurements

Magnetic Susceptibility

Magnetic susceptibility was determined on Cores 197-1203A-1R through Section 17R-3 at 5-cm intervals (see **"Physical Properties,"** p. 27, in the "Explanatory Notes" chapter). Values typically ranged between -1×10^{-6} and 100×10^{-6} SI through most of the sedimentary column (300–440 mbsf), but higher values (between ~20×10^{-6} and 1800×10^{-6} SI) were observed in Unit III in the bottom ~15 m (Table **T11;** Fig. **F72A**).

GRA Density

Bulk density was measured by the GRA densitometer every 5 cm on whole sections of Cores 197-1203A-1R through Section 17R-3 (see **"Physical Properties,"** p. 27, in the "Explanatory Notes" chapter), providing a semicontinuous record; discontinuities in the data correspond to regions of reduced core recovery (Table **T12;** Fig. **F72B**). The GRA density data offer the potential for direct correlation with downhole bulk density of discrete samples (Fig. **F73**) and can also be compared with the downhole logging data. Overall, GRA bulk densities show a slight increase downhole through the sediment, from ~1.5 g/cm³ at 300 mbsf to ~ 1.7 g/cm³ at 400 mbsf and ~ 2.3 g/cm³ at the base of the sediment at ~458 mbsf. There appear to be small-scale variations of density with depth (e.g., a peak of ~1.8 g/cm³ at ~324 mbsf followed by a trough of ~1.5 g/cm³ at ~330 mbsf), which are especially pronounced in

T11. Magnetic susceptibility, p. 163.

F72. GRA density, magnetic susceptibility, and NGR, p. 125.

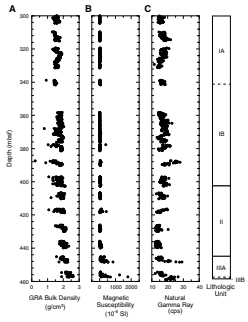

T12. GRA bulk density, p. 164.

F73. Sedimentary unit index properties, p. 126.

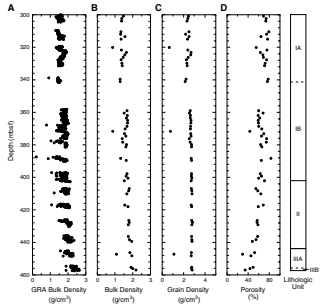

the upper part of the sediment column. However, there are also considerable nonsystematic variations of ~0.5 g/cm³ between the highest and lowest values at any given depth, making it difficult to draw conclusions about density variations on short spatial scales. A number of sample points show very low GRA bulk densities (<1 g/cm³); these probably represent void spaces or drilling disturbed areas of the core.

Natural Gamma Radiation

NGR was measured every 10 cm on both sediment and basalt cores in Hole 1203A. Total counts are reported here because the corrected counts (which are less by ~16 counts per second [cps]) include negative values, which are physically unreasonable. Data were generally acquired on unsplit sections; however, Cores 197-1203A-24R, 28R, and 33R were split before NGR data were measured, so measurements were taken on the split-half sections.

Gamma ray values are fairly constant in the upper 450 m of the core (Table T13; Fig. F72C), with most values between ~14 and 21 cps; an exception is a positive peak of 28 cps at ~388 mbsf in Subunit IA. The NGR count increases slightly at ~448 mbsf in sedimentary Unit III; this may be due to greater amounts of iron-rich clays in this unit (see "Lithostratigraphy" p. 6).

For basement rocks (below ~458 mbsf), somewhat higher gamma ray values were measured (Table T13; Fig. F74A). For basalt, measurements generally ranged between ~15 and 25 cps in the depth range 457–690 mbsf and between ~20 and 30 cps in the depth range 690–910 mbsf. Particularly high NGR counts were measured for some of the volcaniclastic units (e.g., ~25–50 cps for basement Units 7, 10, 17, and 28 at ~550, 590, 645, and 867 mbsf, respectively) (see "Physical Volcanology and Igneous Petrology" p. 11). A particularly large peak of ~65 cps is seen at ~640–652 mbsf in basement Unit 27, a volcaniclastic sandstone.

Core Imaging

All whole-core pieces that could be successfully rotated through 360° were imaged on the Deutsche Montan Technologie (DMT) digital color CoreScan system. Contiguous pieces were imaged together where possible. Pieces too small or uneven to be scanned effectively were also measured, to allow for them in the total core barrel lengths.

In total, >200 m of whole core was scanned using this method. This accounts for ~60% of the material recovered from Hole 1203A. The size and quality of the images varies greatly throughout the core, corresponding closely to core recovery. An example of the core images acquired is shown in Figure F75.

Thermal Conductivity

Thermal conductivity was determined at a frequency of one per core for both sediment and basalt from Hole 1203A (Fig. F76; Table T14). In the sedimentary section (Cores 197-1203A-1R through Section 17R-3), thermal conductivity values average ~0.9 W/(m·K), with most values between 0.7 and 1.1 W/(m·K) (Fig. F76A). Values tend to increase with depth; a smooth curve drawn through the data points suggests an increase from ~ 0.7 W/(m·K) at 300 mbsf to 1.1 W/(m·K) at 450 mbsf.

T13. Gamma ray measurements, p. 165.

F74. Physical properties in basement units, p. 127.

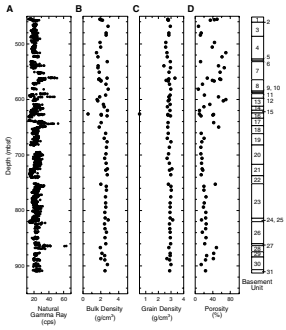

F75. DMT image of basalt with glassy margin, p. 128.

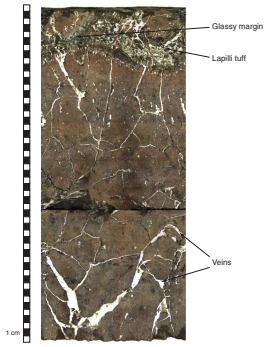

F76. Thermal conductivity measurements, p. 129.

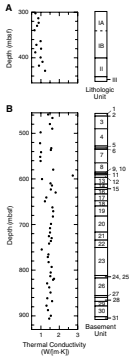

T14. Thermal conductivity, p. 166.

The volcanic basement units generally exhibit higher thermal conductivity values (Fig. F76B). Values for basalt and volcanic breccia generally range between 1.3 and 1.7 W/(m·K) (mean = ~1.5 W/[m·K]). A large positive peak of 2.7 W/(m·K) occurs in basement Unit 11 (see "Physical Volcanology and Igneous Petrology," p. 11), which is an olivine-plagioclase-phyric basalt. Values for other basement units range between 0.9 and 1.3 W/(m·K) (mean = ~1.0 W/[m·K]).

Index Properties

The index properties of Hole 1203A were determined with a pycnometer and a Scientech balance. Values of wet mass, dry mass, and dry volume of discrete samples were measured and used to calculate moisture content, bulk density, grain density, and porosity (Table T15; Figs. F73, F74).

In the sedimentary units of Hole 1203A, bulk density shows an overall slight increase with depth, from 1.47 g/cm³ at 300 mbsf to 2.18 g/cm³ at 457 mbsf. At most depths bulk density corresponds well to the GRA density measured on the MST (Fig. F73A, F73B) but tends to be slightly lower (on the order of 10%). Grain density varies very little downhole in the sediment and has a mean value of 2.51 g/cm³. Three samples, at ~320, 372, and 447 mbsf, show considerably lower grain density (<1.00 g/cm³), which does not appear to correlate to any particular lithologic changes. At ~323 mbsf a small positive peak occurs in all three density measurements; this probably represents sampling of a small pyrite nodule located in the sediment at this depth.

In the basement (Fig. F74), the basaltic units correspond to higher bulk density and lower porosity than volcaniclastic sediment. For the basaltic units, bulk density ranges from 2.37 to 2.83 g/cm³ (mean = ~2.6 g/cm³) and porosity ranges from 7% to 26%. Porosity of basalt tends to be higher at greater depth. For the volcaniclastic sediment, bulk density ranges from 1.52 to 2.38 g/cm³ (with the exception of one outlier discussed below) (mean = ~1.9 g/cm³) and tends to slightly increase with depth. Porosity ranges from 19% to 70%, but porosities of >54% only occur in the volcaniclastic siltstone and sandstone units.

Downhole grain density values for the basement units vary little, with a mean of ~ 2.9 g/cm³ (Fig. F74C). At a depth of 626.08 mbsf (basement Unit 15), one sample yields a grain density of 0.51 g/cm³; this unit comprises resedimented and laminated volcanic claystones and sandstones. However, this grain density value is questionable because it is considerably lower than the density values recorded in the overlying soft sediment.

Compressional Wave Velocity

At Site 1203, compressional wave velocity was determined from both split-core sections (Cores 197-1203A-1R through Section 17R-3) and discrete sample measurements. *P*-wave velocity was measured in the x-, y-, and z-directions using the PWS3 tool (see "Physical Properties," p. 27, in the "Explanatory Notes" chapter). *P*-wave velocity was measured only in the x-direction in sediment cores and ranged from 1515 to nearly 1800 m/s (Fig. F77; Table T16).

Paleomagnetic minicore samples of lava and consolidated sediment enabled velocity measurements in the z- and y-, as well as x-directions in hard rock cores. Because of time constraints, y-direction velocity was

T15. Index properties, p. 167.

F77. PWS3 velocity, p. 130.

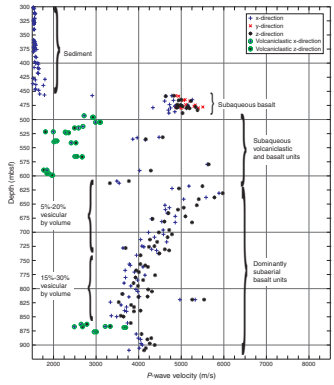

T16. *P*-wave velocity, p. 169.

measured only on Cores 197-1203A-17R through 19R. When possible, hard rock velocity was measured twice per core in the x- and z-directions. The increase in velocity to ~5000 m/s at 462 mbsf coincides with the penetration of submarine basalt flows. Between 489 and 613 mbsf, velocity varies widely from 1770 to nearly 5700 m/s, due to a marine sequence of alternating basalt and volcaniclastic sediment. Subaerially erupted basalt, with velocities >5000 m/s, begin at ~615 mbsf and are interbedded with shallow-marine volcaniclastic rocks. Velocity steadily decreases with depth (<4000 m/s) until ~880 mbsf, where velocity becomes >4000 m/s.

Figure F77 shows that z-direction velocities average ~191 m/s more than x-direction velocities. This apparent anisotropy probably arises from the relatively large amount of water needed to couple the PWS3 transducers with unevenly cut minicores in the x-direction (along the axis of the minicores) to obtain a good signal. Minicore cuts in the z-direction are curved; hence, much less water was needed for z-direction measurements. Consequently, x-direction velocities should be regarded as minimum estimates compared to the more accurate z-direction velocities.

DOWNHOLE MEASUREMENTS

Logging Operations

Downhole logging was performed in Hole 1203A after it had been drilled to a total depth of 914.6 mbsf. The upper 300 m of the hole had been drilled ahead, and coring started at this depth. After drilling and coring operations were completed in Hole 1203A, the borehole was conditioned with a mixture of sepiolite drilling mud and seawater and a wiper trip was conducted. A wiper trip involves pushing the pipe all the way back to the base of the hole and then pulling the bit back to the required depth. The base of the BHA was set at 206 mbsf.

Four tool string configurations were planned to be deployed in the 1203A borehole (see "Downhole Measurements," p. 31, in the "Explanatory Notes" chapter), including the triple combo tool string, the FMS/sonic tool string, the GBM, and the susceptibility tool. The borehole proved to be in very good shape and gave no problems from start to finish. The wireline heave compensator was used during the runs to counter ship heave resulting from the mild sea conditions.

Logging operations began at 0830 hr on 23 July with the deployment of the triple combo tool string. It included the accelerator porosity sonde, the DLL, the hostile-environment natural gamma sonde, the high-temperature lithodensity tool, and the Lamont-Doherty Earth Observatory temperature/acceleration/pressure tool. The tool string was lowered from the bottom of the pipe to the bottom of the hole, coming out of the pipe without any difficulties. While going downhole, DLL and gamma ray counts were measured. The first triple combo pass was done from the bottom of the hole to the bottom of the drill pipe. During this first run, an interval from 396 to 321 mbsf was traversed where the density sensor voltage became unstable and provided unreliable density data. A repeat section was made in this interval to replace the density data on the main pass and to check the repeatability of the measurements.

For the second logging run, the FMS/sonic tool string including the FMS, the general purpose inclinometer tool (GPIT), the DSI, and the

natural gamma ray tool was deployed. The tool string was lowered down to the bottom of the hole without difficulty and logging proceeded. The first pass recorded FMS and sonic data only in the basement section, from 914.6 to 420 mbsf. The second pass was done in the basement and in the sedimentary section. During the second logging run, the FMS/sonic tool string was lowered down to the bottom of the hole without difficulty and logging proceeded upward.

The third logging run consisted of the GBM tool. The tool required an additional weight (a standard Schlumberger weight) for safe deployment. The potential magnetic influence of this weight on the tool was tested on board and found to be minimal. The first pass was interrupted because the x- and z-components measured by the magnetometer were outside the sensing range (±50,000 nT). After adapting the tool to sense fields in the range of ±100,000 nT (an additional resistor was employed and an electronic circuit that automatically increased the sensitivity of the x-component was removed), the tool was rigged and lowered back to the bottom of the hole. During the second attempt, data were recorded while going down and up without further difficulty. The fourth logging run was devoted to the magnetic susceptibility tool. Just before the deployment the tool failed, and deployment was canceled. Logging operations ended at 0230 hr on 25 July.

Data Quality

Logging data recorded in Hole 1203A range in quality from poor to high. In the upper 450 mbsf, the calipers of the hostile environment lithodensity sonde (HLDS) and FMS reached their maximum aperture (18 in). Degraded borehole width affects measurements that require eccentralization and good contact between the tool and the borehole wall. Despite the large borehole size, most of the recorded parameters provide reliable results except for the DSI and the FMS data. In the sediment section shallower than 352 mbsf, the wide hole caused problems and the DSI data are unreliable. FMS data in the sedimentary section are of low quality because the FMS pads did not contact the wall of the enlarged borehole. Most of the time, only one or two pads recorded reliable data.

In the basement section, where the major objectives of Leg 197 were addressed, logging data are of good to excellent quality for most of the measured parameters. The HLDS and FMS calipers show that the borehole is enlarged in a few intervals that correspond to sedimentary or volcaniclastic interbeds (see **"Results from Standard Downhole Measurements and FMS Images,"** p. 42) (Fig. **F78**). In these intervals, FMS data quality is highly variable, ranging from poor to good. The DSI results in the basement are generally good with only a handful of anomalous spikes, which have been deleted from the plots (Fig. **F78**). For the basaltic basement, the HLDS and FMS calipers recorded a borehole diameter ranging from 10.5 to 14 in. The interlayered basalt-volcaniclastic succession is well recorded from most of the geophysical parameters (electrical resistivity, density, porosity, and seismic velocities [V_P and V_S]). Shipboard processing provides preliminary FMS images; these images captured most of the important features of the cores.

All the logging data have been depth shifted. Usually, the mudline is located with the gamma ray data to obtain the depth of the seafloor. In Hole 1203A, the seafloor could not be detected by the natural gamma ray gradient because of the extremely low natural radioactivity of the nannofossil ooze. However, both the base of pipe and the basement

F78. Logging data summary, p. 131.

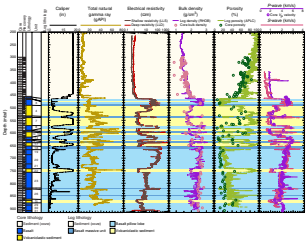

contact can clearly be identified, and both were ~4 m deeper than the equivalent driller's/core depths. Logs have been shifted to bring them in line with the sediment/basement interface in the core and base of pipe.

Results from Standard Downhole Measurements and FMS Images

High recovery and good downhole measurement quality allow correlation between the logging results and the core observations. In sections with low recovery, the combination of standard downhole measurements and FMS images allows us to calculate true bed and flow thicknesses. Because of the good correlation observed between the core lithology and the logging data (Fig. F78) and to make comparison easier between the cores and the logging data, we will adopt the core lithology nomenclature (see "Physical Volcanology and Igneous Petrology," p. 11). From standard logging data and FMS images, we identified most of the 31 lithologic units of the basement section, which are based on recovered core. Furthermore, the recovered cores have undergone physical properties measurements, including density, porosity, and seismic velocity (V_P). Plotting log data next to core data shows good correlation between these measurements (Fig. F78).

High contrast in petrophysical properties between basalt and sediment/volcaniclastic units allows a fairly good identification of these different lithologies. From FMS images as well as from the logging data, at least five main lithologies can be distinguished: (1) nonvolcanic sediment (from the base of the pipe to 467 mbsf), (2) volcaniclastic sediment (interbedded in basement), (3) pillow basalt, (4) massive basalt, and (5) basaltic breccia.

Sedimentary Unit: Base of the Pipe to 467 mbsf

This sedimentary section presents fairly constant and low gamma ray values (<15 gAPI). In the upper 450 m of the section, these low values are linked to the low abundance of clay minerals in the nannofossil ooze. An exception is the interval between 388 and 400 mbsf, where total natural gamma ray counts reach 27 gAPI, mainly associated with a significant increase in Th (up to 3 ppm). At the same depth, a strong increase in both *P*- and *S*-wave velocities is recorded. These results are correlated with a so-called "388-mbsf reflector" in seismic profiles and can also be seen in the core, corresponding to high $CaCO_3$ content (see "Lithostratigraphy," p. 6), which is related to high abundance of authigenic carbonate minerals. The high Th content measured in this zone is probably linked to the occurrence of volcanic ash (see "Lithostratigraphy," p. 6).

The gradual increase in density and decrease in porosity recorded in the sedimentary section (Fig. F78) is linked to expected consolidation and compaction effects. Because the borehole diameter exceeds the maximum extent of the tool pads in these units, information can only rarely be extracted from FMS images. From standard downhole measurements and FMS images, we can easily distinguish the boundary between sediment and basement at 467 mbsf. This boundary is marked by a strong increase in resistivity, density, and natural gamma ray and a decrease in porosity (Figs. F78, F79).

F79. Gamma ray logging data, p. 132.

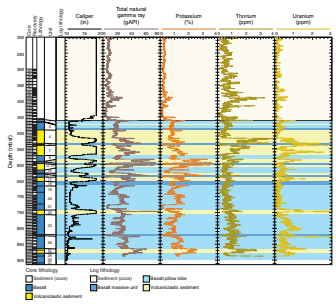

Basement Units: 457 to 915 mbsf

Strong changes or shifts in the log data are observed for all measured geophysical parameters (Figs. F78, F79) from 457 to 915 mbsf. These variations in the downhole measurements nicely reflect the complex lithology encountered in Hole 1203A where volcaniclastic sediment is interlayered with basalt. In general, the basaltic rocks are characterized by high electrical resistivity (up to 10 Ωm), low porosity (<0.5%), high density (up to 2.5 g/cm³), low natural gamma ray (<20 gAPI), and high *P*- and *S*-wave velocities (up to 4 and 2 km/s, respectively). In contrast, sediment and volcaniclastic interbeds are characterized by low resistivity (~1 Ωm), low density (<2 g/cm³), high porosity (up to 40%), and low *P*- and *S*-wave velocities (~2 and 1 km/s, respectively).

The strong differences in petrophysical properties between these lithologies allow us to distinguish the 31 basement units based on descriptions of the recovered cores (see "Physical Volcanology and Igneous Petrology," p. 11). In particular, the electrical microresistivity data record high-resolution images of the internal structure of the volcaniclastic sediments, pillow basalt, and more massive breccia units. In sections with low recovery, the combination of standard downhole measurements and FMS images allows us to estimate true bed and flow thicknesses (Fig. F80; Table T17). Basement unit numbers used in the next paragraphs are those assigned from visual core descriptions (see "Physical Volcanology and Igneous Petrology," p. 11).

Volcaniclastic Sediment in the Basement Section

Nine intervals are identified as volcaniclastic sediment units from the downhole measurements (Fig. F78). Volcaniclastic sediment interbedded with basaltic units show intermediate physical properties (except for the natural radioactivity) between basalt and sediment from the uppermost part of the borehole. This results from greater consolidation and differences in lithology compared with sediment overlying basement. High gamma ray values are recorded in these volcaniclastic sediment intervals and can be attributed to alteration and/or clay-rich layers (Fig. F79). Volcaniclastic sediment units are homogeneous with respect to physical properties but cause large differences in the FMS images. Usually, pad contact is better than in the upper sediment section, and, consequently, data quality is higher, which allows us to identify the internal organization of the volcaniclastic sediment layers. Layered bedding is evident in some intervals (Fig. F81). In other intervals a patchy texture is observed. These heterogeneities are clearly related to the wide range of particle size and sorting (lapilli tuff, lapillistone, basaltic tuff, volcaniclastic siltstones, and sandstones) (see "Physical Volcanology and Igneous Petrology," p. 11). Generally, high gamma ray values are recorded in these intervals and can be attributed to alteration and/or clay-rich layers (Fig. F79).

Pillow Basalt Lobes

Pillow lobes are easily recognized on the FMS images. Pillow basalt appears as circular to elliptical images of varying sizes (10–150 cm diameter). The rims are regions of enhanced conductivity compared with those of the central part of the pillows. One contrasting example is recorded between 667 and 701 mbsf (Unit 19), where interpillow material appears to be highly resistive compared to the rims and may correspond

F80. FMS and wireline vs. core-derived lithology, p. 133.

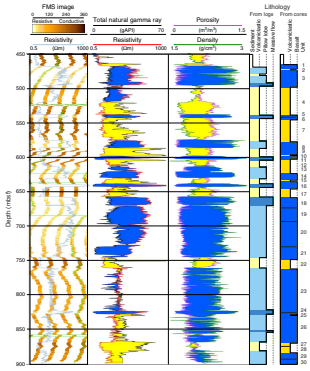

T17. Log responses vs. core lithology, p. 170.

F81. FMS image of basement Unit 7–8 transition, p. 134.

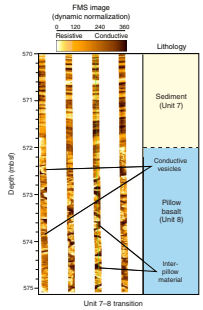

to calcite. Fractures and vesicles occur mainly as conductive features. Pillows often exhibit fractures and vesicle concentration along cooling rims as well as in the center part of the pillows (Fig. F82). Variable vesicle contents are observed along the whole section, from absent (or too small to be recorded) to high, particularly between 758 and 819 mbsf (in Unit 23, a thick pahoehoe lava flow with many cooling lobes).

A small proportion of pillow basalt appears to be highly fractured or even brecciated, showing up with angular pillow rims and with more conductive colors. So far, the occurrence of such highly fractured rocks is related only to few parts of the pillow basalt (e.g., 572–583 mbsf [part of Unit 8], 617–626 mbsf [Unit 14], or 654–666 mbsf [Unit 18]).

From 658 mbsf to the bottom of the hole, there is a clear decrease in porosity, density, resistivity, and V_P (Figs. F78, F80) (from Units 19 to 31), which can be related to a higher degree of alteration.

Massive Basalt

Massive basalt mainly occurs as single lava flows in the borehole or as massive parts of pahoehoe flows, usually occurring near the base (e.g., Units 11 and 16). Flow thicknesses can range between 4 and 12 m. A typical internal structure of a massive flow, as can be inferred from the FMS images, is as follows (Fig. F83): a highly porous zone at the top of the flow caused by horizontal fracturing as well as vesicle layers followed by a massive part in the flow center. This massive part is accompanied by large vertical fractures several centimeters in width and up to 1.5 m in length. The flow bottom appears as a thin layer with a similar appearance to the top. From the standard downhole measurements, these massive units are characterized by a sharp transition in physical properties relative to the surrounding formations. Furthermore, most of the measured geophysical parameters appear to be fairly constant. Compared to pillowed units, these massive units exhibit higher electrical resistivity (reaching 1000 Ωm) and lower natural gamma ray counts.

Breccia

The interval from 610 to 616 mbsf (part of Unit 13) has been identified as a volcanic breccia (Fig. F84). This interval consists of highly heterogeneous material, with resistive material (basaltic glassy clasts) cemented in a conductive matrix (altered glass). This unit does not exhibit any fractures but shows a random distribution of variable resistivity material. From visual core descriptions, other intervals have been described as volcanic breccia (Units 17 and 28), but, unfortunately, image quality in these intervals appears to be poor.

Magnetic Logging Results

Two tools were used to log magnetic data in Hole 1203A. The first one is the standard log in combination with the FMS/sonic tool string (GPIT), and the second one is the GBM. From the GPIT measurements (three-axis fluxgate magnetometer and three-axis accelerometer), the borehole deviation and the magnetic field are determined. These measurements are summarized in Figure F85. In Hole 1203A, the borehole deviation appears to be <1.5°.

In the upper sedimentary section (200–460 mbsf), the magnetic inclination derived from magnetic logging is ~63° (angle measured below the horizontal), which differs from the 67.9° expected from the Interna-

F82. FMS of pillow lobes in basement, p. 135.

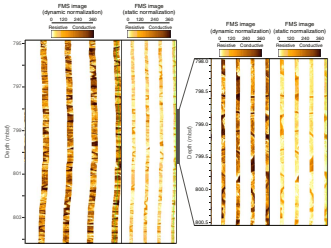

F83. FMS of thick pahoehoe flows, p. 136.

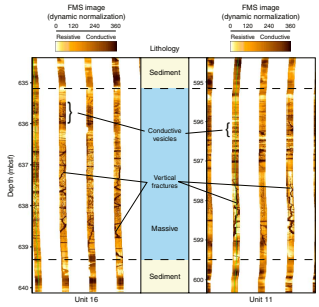

F84. FMS of breccia, p. 137.

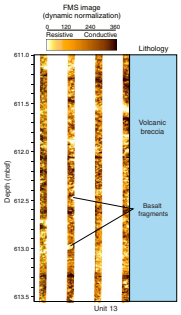

F85. Summarized GPIT data, p. 138.

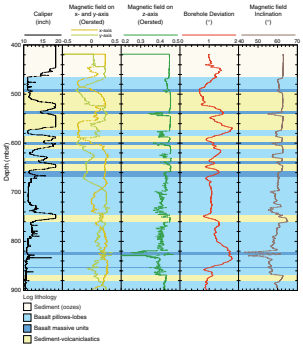

tional Geomagnetic Reference Field at this latitude. In the underlying basement, strong variations of the magnetic field were detected that correlate well with lithology. Both magnetic logs of the GPIT and GBM agree well with respect to the sequence of magnetic variations (Fig. F86). Only in a few depth intervals do both logs reveal a different shape (e.g., 580 mbsf) or show a distinct difference in magnitudes (e.g., 830 mbsf). Both logs were heave compensated, but differences of up to 2 m are occasionally seen. The z-components have a small offset from each other, which might be due to the magnetized housing and caliper arms of the tool string of the GPIT above the magnetic sensors. The logging speed of the GPIT was ~275 m/hr, and the GBM logging speed was ~300 m/hr.

The GBM tool collected data during the downhole and uphole run. This tool does not allow direct measurement of depth but records the magnetic field vs. time. The depth was obtained by comparison with the Schlumberger depth measurement. The magnetic raw data are shown in Figure F87. All data from this run are of good quality. Because of the strong magnetization of the pipe, the magnitude of the z-component of the magnetometer became saturated. Therefore, only the log data from the open hole are presented. The GPIT did not collect magnetic data in the pipe. Because of tool rotation in the borehole during lowering and raising, the horizontal components oscillate about the zero line. The anomalous magnetic field variations are obtained by subtracting the ambient geomagnetic main field (23,000 nT for the horizontal and 44,000 nT for the vertical component). The intensity of the horizontal field is derived from both horizontal components and plotted against depth (Fig. F88). The logs of the downhole and uphole run almost overlap, as can be seen by comparison of each horizontal and vertical component.

Determination of Rotation History: Fiber-Optic Gyro

In addition to the fluxgate sensors, the angular rate around the vertical spin axis was measured using a fiber-optic gyro. The rotation history of the tool is determined by the accumulation of the angular rate during a log run. This is the first time such a sensor has been used to monitor instrument rotation in a borehole. Between the rig floor and hole bottom, the tool rotated almost 60 times around its vertical body axis (Fig. F89). On its run back to the rig floor the tool followed nearly the same rotation history as on the downhole run. A check of the direction indicated by the fiber-optic gyro after the run revealed only minor deviations from the initial orientation.

Results

Magnetic Logging

At 200 mbsf the tool emerged from the drill pipe into the open hole. Between the end of the pipe and 460 mbsf, only minor variations of the magnetic field with depth were recorded. These variations can be attributed to weakly magnetized sediments (Fig. F88). In the basement below, strongly magnetized layers were detected, which correlate well with sequences of massive basalt and pillows. These stronger magnetizations are interrupted by intervals of volcaniclastic sediment. The anomalous field variations of the vertical component always point toward negative values, which indicate a general normal magnetic polarity as repre-

F86. GBM vs. GPIT magnetic field, p. 139.

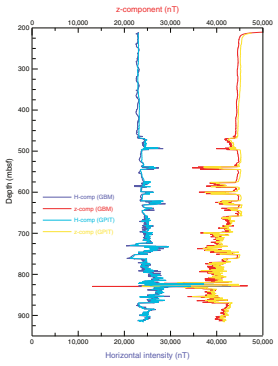

F87. GBM runs in open hole section, p. 140.

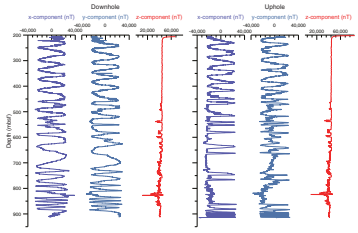

F88. Downhole and uphole run of GBM, p. 141.

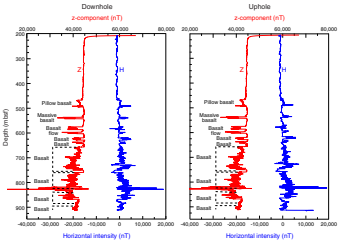

F89. Magnetometer rotation, p. 142.

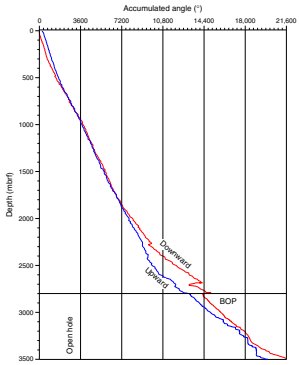

sented by the present geomagnetic field. The strength of the recorded vertical or z-component of the anomalous field (relative to the horizontal anomalous field) suggests that in the basalt section the combined remanent and induced magnetic field has an inclination >45°.

Fiber-Optic Gyro

In general, the magnetometer tool rotated uniformly during the run but increased its rotation rate with increasing cable length. Because of the friction on the borehole wall, this long-wave rotation is modified by short-wave variations. Strong deviations from the uniform spinning occurred in the pipe at 2300 and 2700 meters below rig floor. Before starting the log run, the magnetic components of the tool were aligned with the ship axis on the rig floor. After the tool returned to the rig floor, it was aligned again to double check the orientation with the initial orientation. This check is required to take into account changes of the heading of the ship and the Earth's rotation, which also adds to the angular rate (see **"Downhole Measurements,"** p. 31, in the "Explanatory Notes" chapter). The difference between the initial and final orientation value is <5°.

UNDERWAY GEOPHYSICS

Seismic Reflection Profiling

Site survey data (single-channel analog records only) from a regional marine geological study (Lonsdale et al., 1993) guided the initial selection of proposed Sites HE-3B and HE-3A, which became Site 1203. A single-channel seismic survey, 3.5-kHz PDR, and magnetometer survey were conducted in the vicinity of these proposed sites to ensure proper hole location and suitability for basement drilling. Figure **F90** shows the track line of Leg 197, Survey 1, superimposed on ETOPO5 seafloor bathymetry with a contour interval of 100 m. Tick marks along Survey 1 mark half-hour intervals. Analog lines from Lonsdale et al. (1993) are labeled *Thomas Washington, 88,* and are annotated with corresponding Julian day and Universal Time Coordinated time markers.

Survey Lines 1, 3, and 6 pass within 130 m of Hole 1203A. Approximately 5-km-long sections from Lines 1, 3, and 6 that cross the site position are shown in Figures **F91, F92,** and **F93,** respectively. The midpoint of the streamer was ~450 m astern of the water gun source, which was ~4.5–6 m deep. The water gun was fired every 6 s. Each shot record is 5 s in length, beginning 100 ms before the water gun was triggered. This 100-ms delay, created by the trigger control panel, was removed in SIOSEIS record processing. Ship speed averaged 6.36 kt (3.27 m/s) during Line 1, 5.64 kt (2.90 m/s) during Line 3, and 6.10 kt (3.14 m/s) during Line 6.

All three lines were processed with SIOSEIS seismic processing software (version 2001.3; **http://sioseis.ucsd.edu**), using multiwindow predictive deconvolution, bandpass filtering from 40 to 100 Hz, and finite-difference migration applying a simple velocity model. Table **T18** shows the SIOSEIS script processing parameters for each line. The top of basement volcanic units is imaged at 4.0 s in two-way traveltime (TWT) on the southwestern ends of the lines and gradually deepens to the northeast to ~4.06 s TWT at Hole 1203A. Drilling documents that the overlying sedimentary section is ~462 m thick. The depth to the seafloor is

F90. Ship track for Survey 1, p. 143.

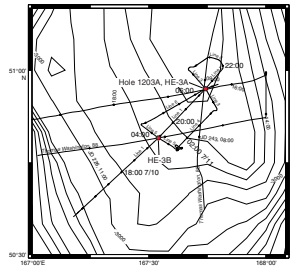

F91. Time section of Survey 1, Line 1, p. 144.

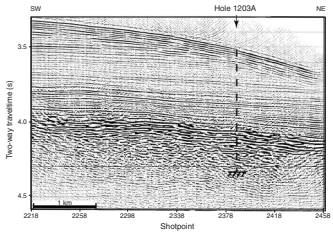

F92. Time section of Survey 1, Line 3, p. 145.

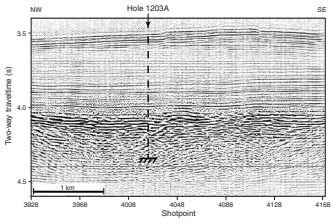

F93. Time section of Survey 1, Line 6, p. 146.

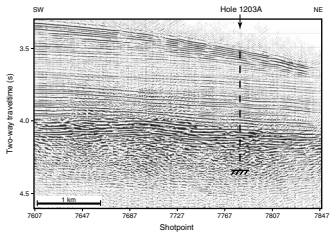

T18. SIOSEIS process parameters, p. 171.

3.52 s TWT. Thus, the corresponding average sediment velocity is 1711 m/s (462 m/0.54 s TWT/2). The volcanic basement is essentially flat-lying and unfaulted near Hole 1203A, but seismic data document structure elsewhere (e.g., faulted basement north of proposed Site HE-3B [Line 1] and basement exhibiting a dipping internal acoustic fabric [Line 4]). Lines 1 and 6 document that a slope-mantling drape of sediment ~0.1 s TWT thick unconformably lies over more flat-lying beds. This angular unconformity likely records a pattern of erosion and deposition affected by a strong bottom current, presumably that which shaped the Meiji sediment drift that thickly blankets the summit and flanks of Detroit Seamount.

REFERENCES

Allan, J.F., Batiza, R., Perfit, M.R., Fornari, D.J., and Sack, R.O., 1989. Petrology of lavas from the Lamont seamount chain and adjacent East Pacific Rise, 10°N. *J. Petrol.,* 30:1245–1298.

Allan, J.F., Sack, R.O., and Batiza, R., 1988. Cr-rich spinels as petrogenetic indicators: MORB-type lavas from the Lamont seamount chain, eastern Pacific. *Am. Mineral.,* 73:741–753.

Alt, J.C., 1995. Subseafloor processes in mid-ocean ridge hydrothermal systems. *In* Humphris, S.E., Zierenberg, R., Mullineaux, L., and Thomson, R. (Eds.), *Seafloor Hydrothermal Systems: Physical, Chemical, Biological and Geological Interactions within Hydrothermal Systems*. Geophys. Monogr., Am. Geophys. Union, 91:85–114.

Arason, P., and Levi, S., 1990. Compaction and inclination shallowing in deep-sea sediments from the Pacific Ocean. *J. Geophys. Res.,* 95:4501–4510.

Augustithis, S.S., 1979. The mineralogical and geochemical distribution of sulphides in basic and ultrabasic rocks. *In Atlas of the Textural Patterns of Basic and Ultrabasic Rocks and their Genetic Significance:* Berlin (Walter de Gruyter), 83–85.

Barton, C.E., Baldwin, R.T., Barraclough, D.R., et al., 1995. International Geomagnetic Reference Field, 1995 revision presented by IAGA Division V, Working Group 8. *Phys. Earth Planet. Int.,* 97:23–26.

Berggren, W.A., Kent, D.V., Swisher, C.C., III, and Aubry, M.-P., 1995. A revised Cenozoic geochronology and chronostratigraphy. *In* Berggren, W.A., Kent, D.V., Aubry, M.-P., and Hardenbol, J. (Eds.), *Geochronology, Time Scales and Global Stratigraphic Correlation*. Spec. Publ.—Soc. Econ. Paleontol. Mineral., 54:129–212.

Buddington, A.F., and Lindsley, D.H., 1964. Iron-titanium oxides minerals and synthetic equivalents. *J. Petrol.,* 5:310–357.

Cande, S.C., and Kent, D.V., 1995. Revised calibration of the geomagnetic polarity timescale for the Late Cretaceous and Cenozoic. *J. Geophys. Res.,* 100:6093–6095.

Cande, S.C., Raymond, C.A., Stock, J., and Haxby, W.F., 1995. Geophysics of the Pitman Fracture Zone and Pacific-Antarctic plate motions during the Cenozoic. *Science,* 270:947–953.

Cas, R.A.F., and Wright, J.V., 1987. *Volcanic Successions: Modern and Ancient:* London (Allen and Unwin).

Chen, C.-Y., and Frey, F.A., 1985. Trace element and isotopic geochemistry of lavas from Haleakala Volcano, East Maui, Hawaii: implications for the origin of Hawaiian basalts. *J. Geophys. Res.,* 90:8743–8768.

Christofferson, E., 1968. The relationship of sea-floor spreading in the Pacific to the origin of the Emperor Seamounts and the Hawaiian Island chain. *Eos,* Am. Geophys. Union, 49:214.

Clague, D.A., and Dalrymple, G.B., 1987. The Hawaiian-Emperor volcanic chain, Part I. Geologic evolution. *In* Decker, R.W., Wright, T.L., and Stauffer, P.H. (Eds.), *Volcanism in Hawaii*. Geol. Surv. Prof. Pap. U.S., 1350:5–54.

Cox, A.V., 1970. Latitude dependence of the angular dispersion of the geomagnetic field. *Geophys. J. R. Astron. Soc.,* 20:253–269.

Fisher, R.A., 1953. Dispersion on a sphere. *Proc. R. Soc. London A,* 217:295–305.

Fisher, R.V., and Schmincke, H.-U., 1984. *Pyroclastic Rocks:* New York (Springer-Verlag).

Frey, F.A., Garcia, M.O., Wise, W.S., Kennedy, A., Gurriet, P., and Albarede, F., 1991. The evolution of Mauna Kea Volcano, Hawaii: petrogenesis of tholeiitic and alkalic basalts. *J. Geophys. Res.,* 96:14347–14375.

Frey, F.A., Wise, W.S., Garcia, M.O., West, H., Kwon, S.-T., and Kennedy, A., 1990. Evolution of Mauna Kea Volcano, Hawaii: petrologic and geochemical constraints on postshield volcanism. *J. Geophys. Res.,* 95:1271–1300.

Goff, F., 1996. Vesicle cylinders in vapor-differentiated basalt flows. *J. Volcanol. Geotherm. Res.,* 97:167–185.

Graham, J.W., 1949. The stability and significance of magnetism in sedimentary rock. *J. Geophys. Res.,* 54:131–167.

Haggerty, S.E., 1991. Oxide textures: a mini-atlas. *In* Lindsley, D.H. (Ed.), *Oxide Minerals: Petrologic and Magnetic Significance.* Rev. Mineral., 25:129–219.

Hon, K., Kauahikaua, J.P., Denlinger, R., and MacKay, K., 1994. Emplacement and inflation of pahoehoe sheet flows: observations and measurements of active lava flows on Kilauea, Hawaii. *Geol. Soc. Am. Bull.,* 106:351–370.

Jackson, E.D., Koizumi, I., Dalrymple, G.D., Clague, D.A., Kirkpatrick, J., and Green, H.G., 1980. Introduction and summary of results from DSDP Leg 55, the Hawaiian-Emperor hotspot experiment. *In* Jackson, E.D., Koizumi, I., et al., *Init. Repts. DSDP,* 55: Washington (U.S. Govt. Printing Office), 5–31.

Keller, R.A., Duncan, R.A., and Fisk, M.R., 1995. Geochemistry and $^{40}Ar/^{39}Ar$ geochronology of basalts from ODP Leg 145 (North Pacific Transect). *In* Rea, D.K., Basov, I.A., Scholl, D.W., and Allan, J.F. (Eds.), *Proc. ODP, Sci. Results,* 145: College Station, TX (Ocean Drilling Program), 333–344.

Keller, R.A., Fisk, M.R., and White, W.M., 2000. Isotopic evidence for Late Cretaceous plume-ridge interaction at the Hawaiian hotspot. *Nature,* 405:673–676.

King, R.F., 1955. The remanent magnetism of artificially deposited sediments. *Mon. Not. R. Astron. Soc., Geophys. Suppl.,* 7:115–134.

Kirschvink, J.L., 1980. The least-squares line and plane and the analysis of palaeomagnetic data. *Geophys. J. R. Astron. Soc.,* 62:699–718.

Le Bas, M.J., Le Maitre, R.W., Streckeisen, A., and Zanettin, B., 1986. A chemical classification of volcanic rocks based on the total alkali-silica diagram. *J. Petrol.,* 27:745–750.

Lonsdale, P., Dieu, J., and Natland, J., 1993. Posterosional volcanism in the Cretaceous part of the Hawaiian hotspot trail. *J. Geophys. Res.,* 98:4081–4098.

Lowrie, W., and Fuller, M., 1971. On the alternating field demagnetization characteristics of multidomain thermoremanent magnetization in magnetite. *J. Geophys. Res.,* 76:6339–6349.

Macdonald, G.A., and Katsura, T., 1964. Chemical composition of Hawaiian lavas. *J. Petrol.,* 5:82–133.

Mattox, T.N., Heliker, C., Kauahikaua, J., and Hon, K., 1993. Development of the 1990 Kalapana flow field, Kilauea Volcano, Hawaii. *Bull. Volcanol.,* 55:407–413.

McFadden, P.L., Merrill, R.T., McElhinny, M.W., and Lee, S., 1991. Reversals of the Earth's magnetic field and temporal variations of the dynamo families. *J. Geophys. Res.,* 96:3923–3933.

McFadden, P.L., and Reid, A.B., 1982. Analysis of paleomagnetic inclination data. *Geophys. J. R. Astron. Soc.,* 69:307–319.

Morgan, W.J., 1971. Convection plumes in the lower mantle. *Nature,* 230:42–43.

Rea, D.K., Basov, I.A., Janecek, T.R., Palmer-Julson, A., et al., 1993. *Proc. ODP, Init. Repts.,* 145: College Station, TX (Ocean Drilling Program).

Rhodes, J.M., 1996. Geochemical stratigraphy of lava flows sampled by the Hawaii Scientific Drilling Project. *J. Geophys. Res.,* 101:11769–11780.

Sack, R.O., and Ghiorso, M.S., 1991. Chromite as a petrogenetic indicator. *In* Lindsley, D.H. (Ed.), *Oxide Minerals: Petrologic and Magnetic Significance.* Mineral. Soc. Am. Rev. Mineral., 25:323–353.

Self, S., Keszthelyi, L., and Thordarson, T., 1998. The importance of pahoehoe. *Annu. Rev. Earth Planet. Sci.,* 26:81–110.

Steinberger, B., and O'Connell, R.J., 1998. Advection of plumes in mantle flow: implications for hotspot motion, mantle viscosity and plume distribution. *Geophys. J. Int.,* 132:412–434.

Tarduno, J.A., 1990. Absolute inclination values from deep sea sediments: a reexamination of the Cretaceous Pacific record. *Geophys. Res. Lett.,* 17:101–104.

Tarduno, J.A., and Cottrell, R.D., 1997. Paleomagnetic evidence for motion of the Hawaiian hotspot during formation of the Emperor Seamounts. *Earth Planet. Sci. Lett.,* 153:171–180.

Tarduno, J.A., and Gee, J., 1995. Large scale motion between Pacific and Atlantic hotspots. *Nature,* 378:477–480.

Thordarson, T., and Self, S., 1993. The Laki (Skaftár Fires) and Grímsvötn eruptions in 1783–85. *Bull. Volcanol.,* 55:233–263.

Thordarson, T., and Self, S., 1998. The Roza Member, Columbia River Basalt Group—a gigantic pahoehoe lava flow field formed by endogenous processes. *J. Geophys. Res.,* 103:27411–27445.

West, H.B., Gerlach, D.C., Leeman, W.P., and Garcia, M.O., 1987. Isotopic constraints on the origin of Hawaiian lavas from the Maui Volcanic Complex, Hawaii. *Nature,* 330:216–220.

Wilmoth, R.A., and Walker, G.P.L., 1993. P-type and S-type pahoehoe: a study of vesicle distribution in Hawaiian lava flows. *J. Volc. Geotherm. Res.,* 55:129–142.

Wilson, J.T., 1963. A possible origin of the Hawaiian Islands. *Can. J. Phys.,* 41:863–870.

Woodruff, F., and Savin, S.M., 1989. Miocene deepwater oceanography. *Paleoceanography,* 4:87–140.

Figure F1. Location map of Site 1203.

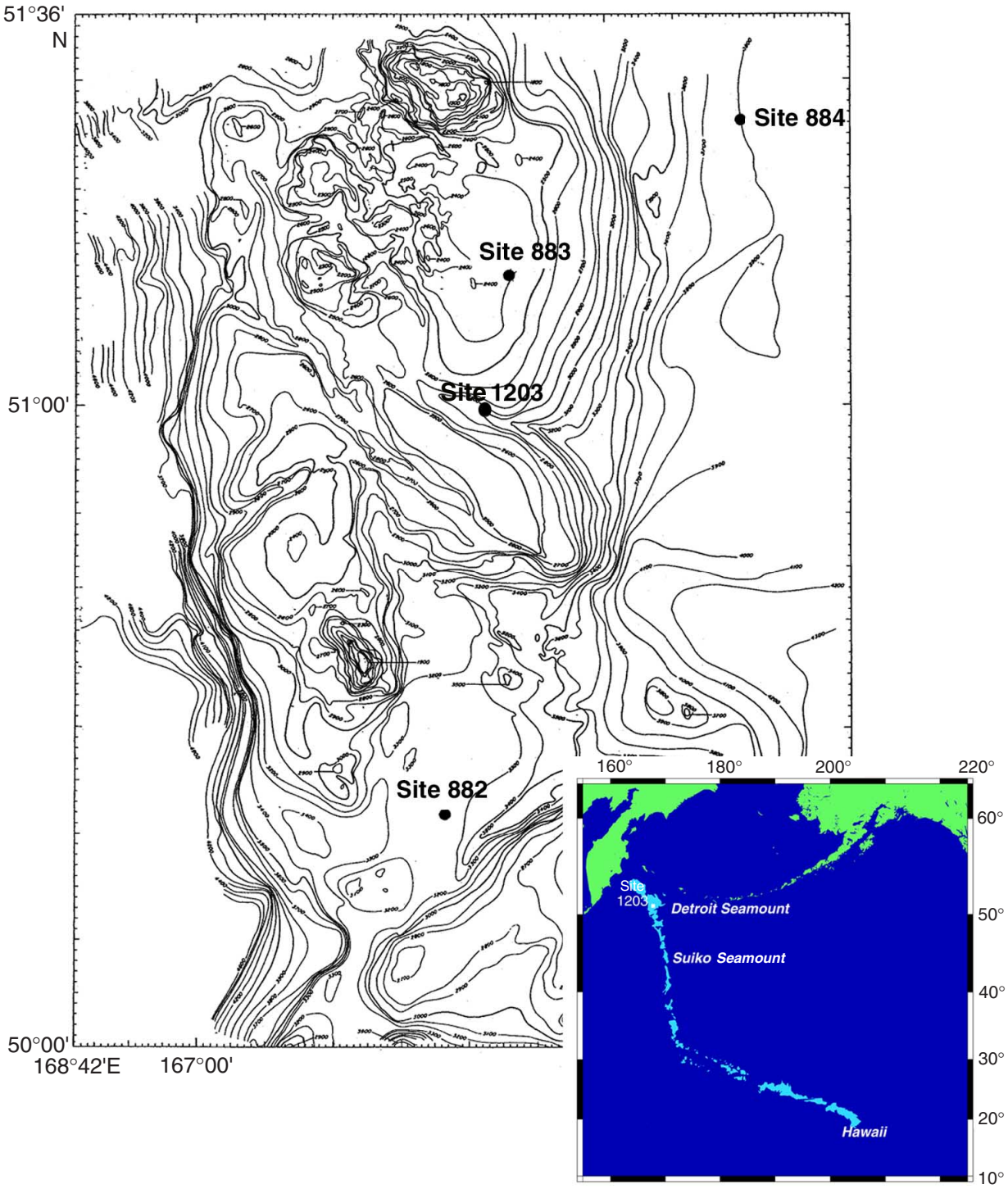

Figure F2. Lithology, units, time framework, and downhole variability of carbonate and other principal components of Hole 1203A sediment from smear slide observations.

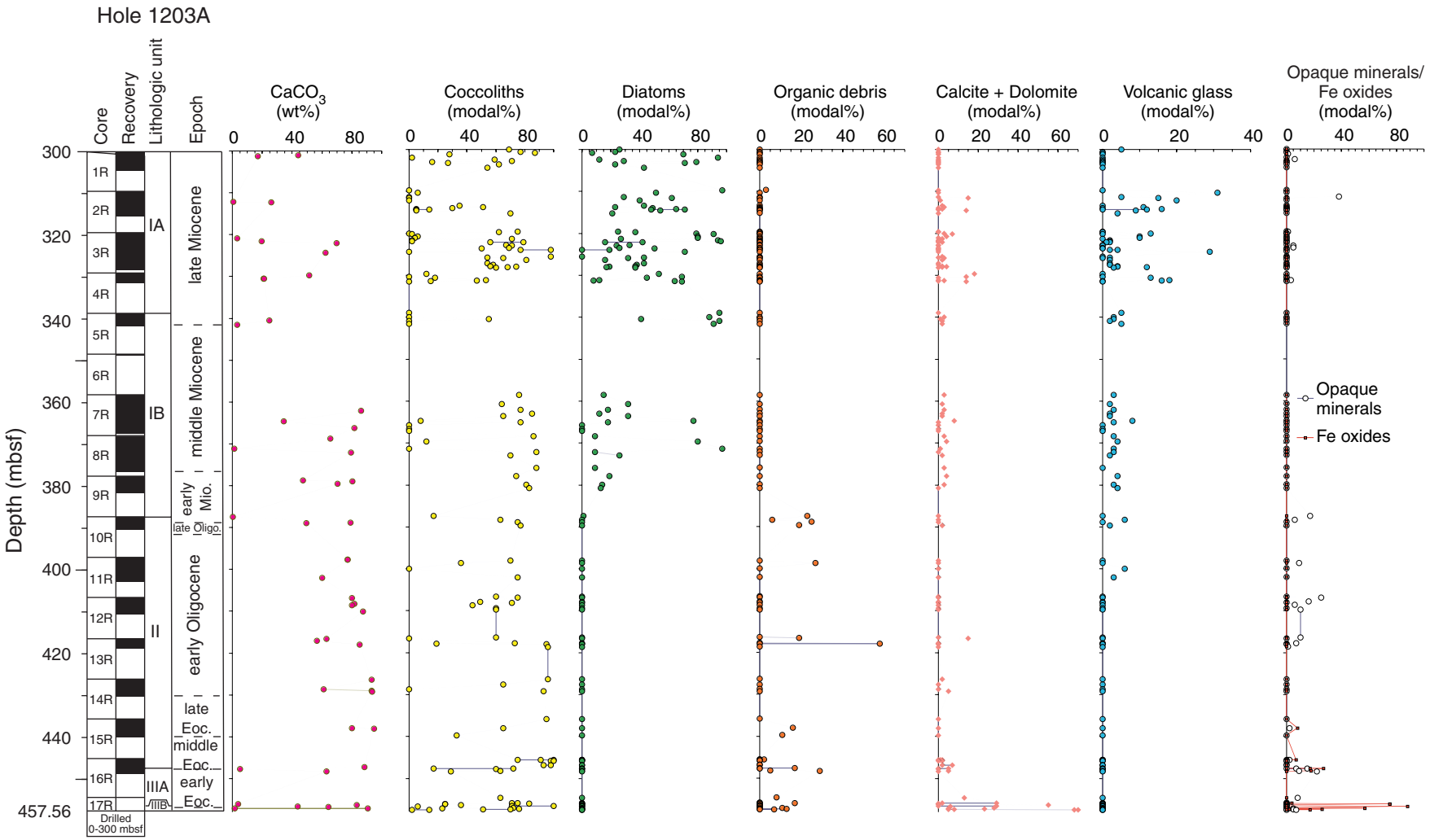

Figure F3. Close-up core photos of different lithologies observed. **A.** Burrowing *Zoophycos* (interval 197-1203A-8R-2, 26–36 cm). **B.** The boundary between Units I and II (interval 197-1203A-10R-2, 13–31 cm). **C.** The boundary between Subunits IIIA and IIIB (interval 197-1203A-17R-2, 47–64 cm).

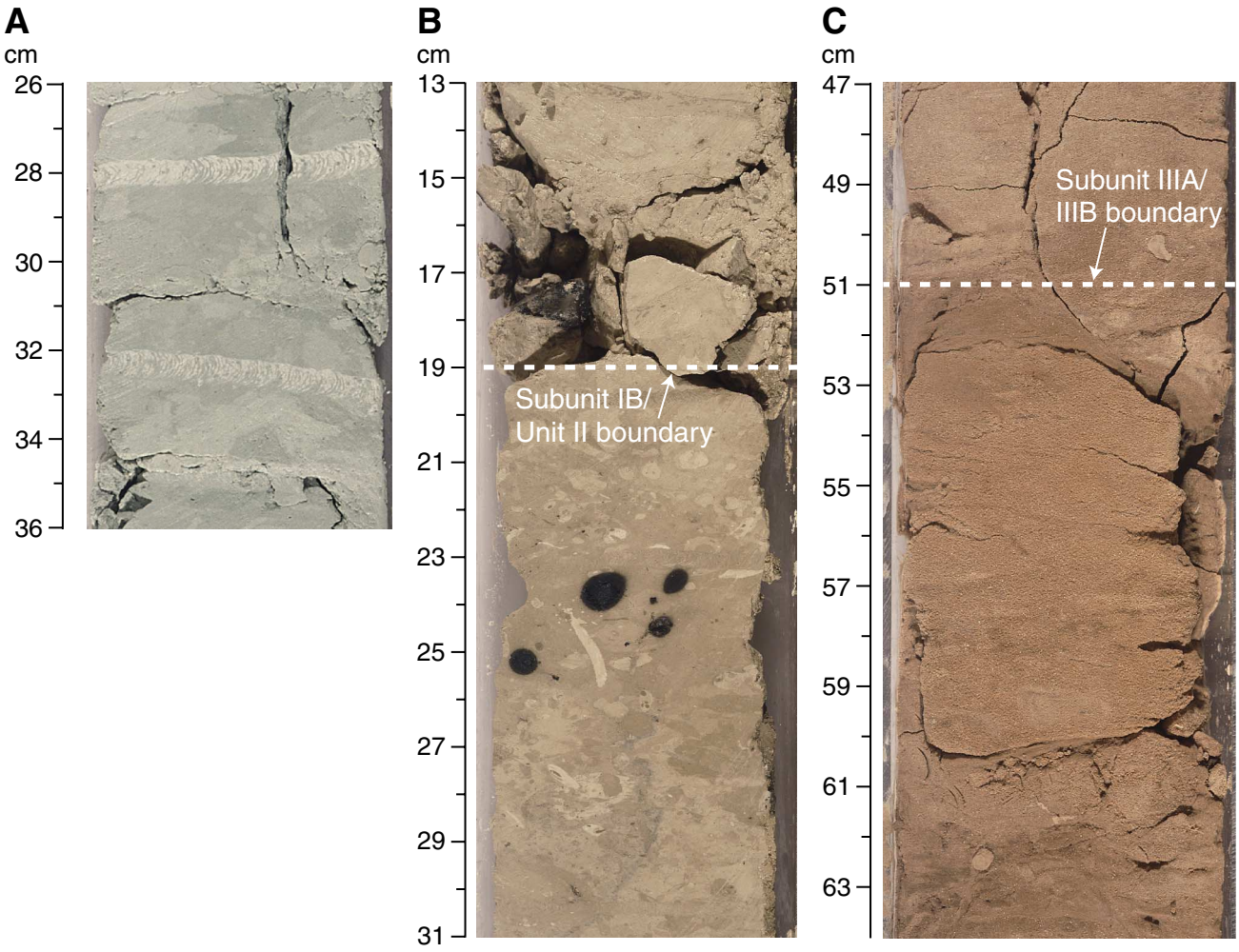

Figure F4. Calcareous nannofossil zones in Hole 1203A plotted against core recovery and epochs. Positions of zonal boundaries are only approximate, owing to the scale of the diagram. See **"Tertiary Zonation,"** p. 10, in "Calcareous Nannofossils" in "Biostratigraphy" for accurate positions of boundaries.

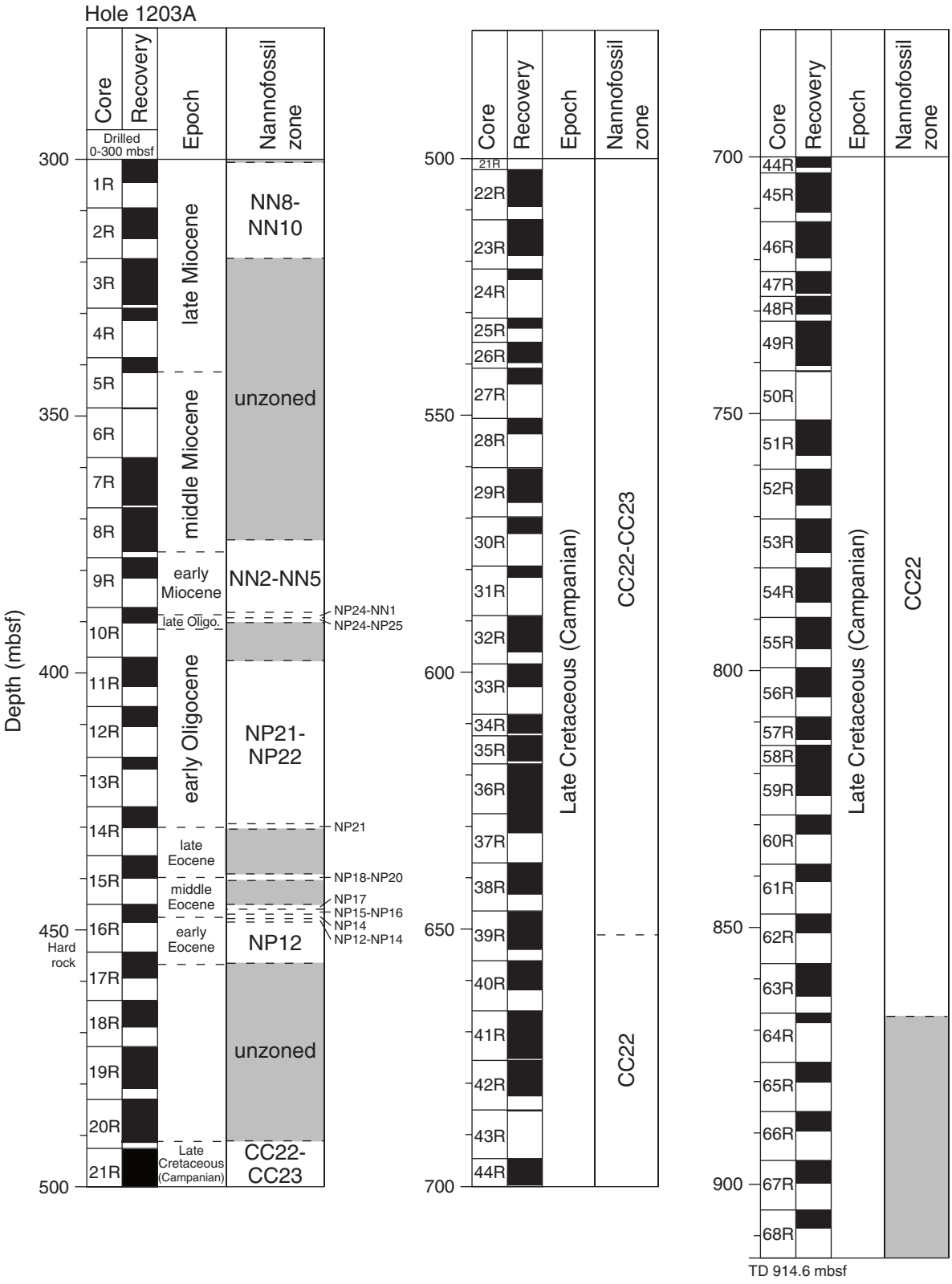

Figure F5. Summary of the Site 1203 basement rocks and biostratigraphic ages with provisional downhole logging data for comparison. TD = total depth. (Continued on next page.)

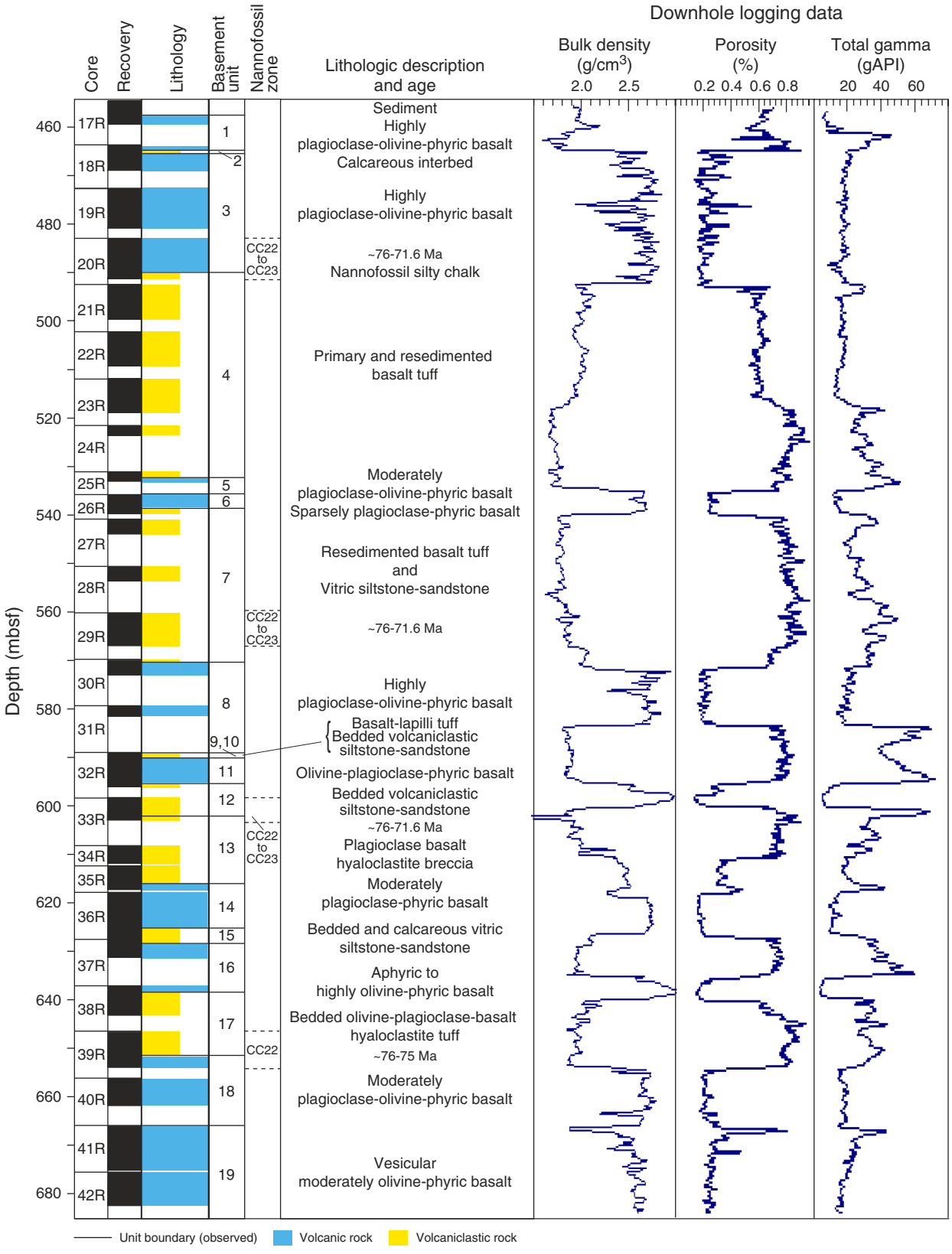

Figure F5 (continued).

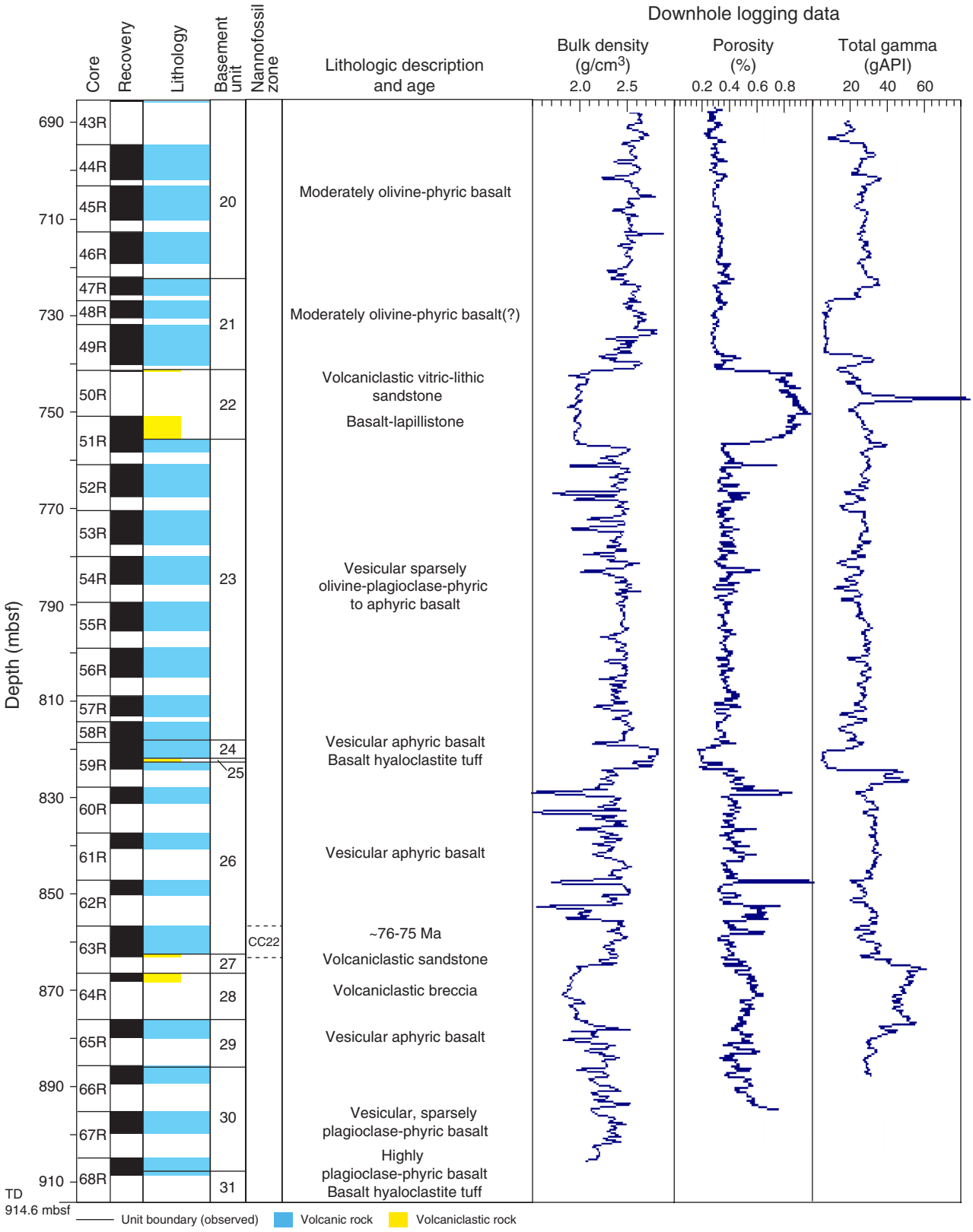

Figure F6. Downhole log showing the major lithologic features of the Site 1203 basement rocks. TD = total depth.

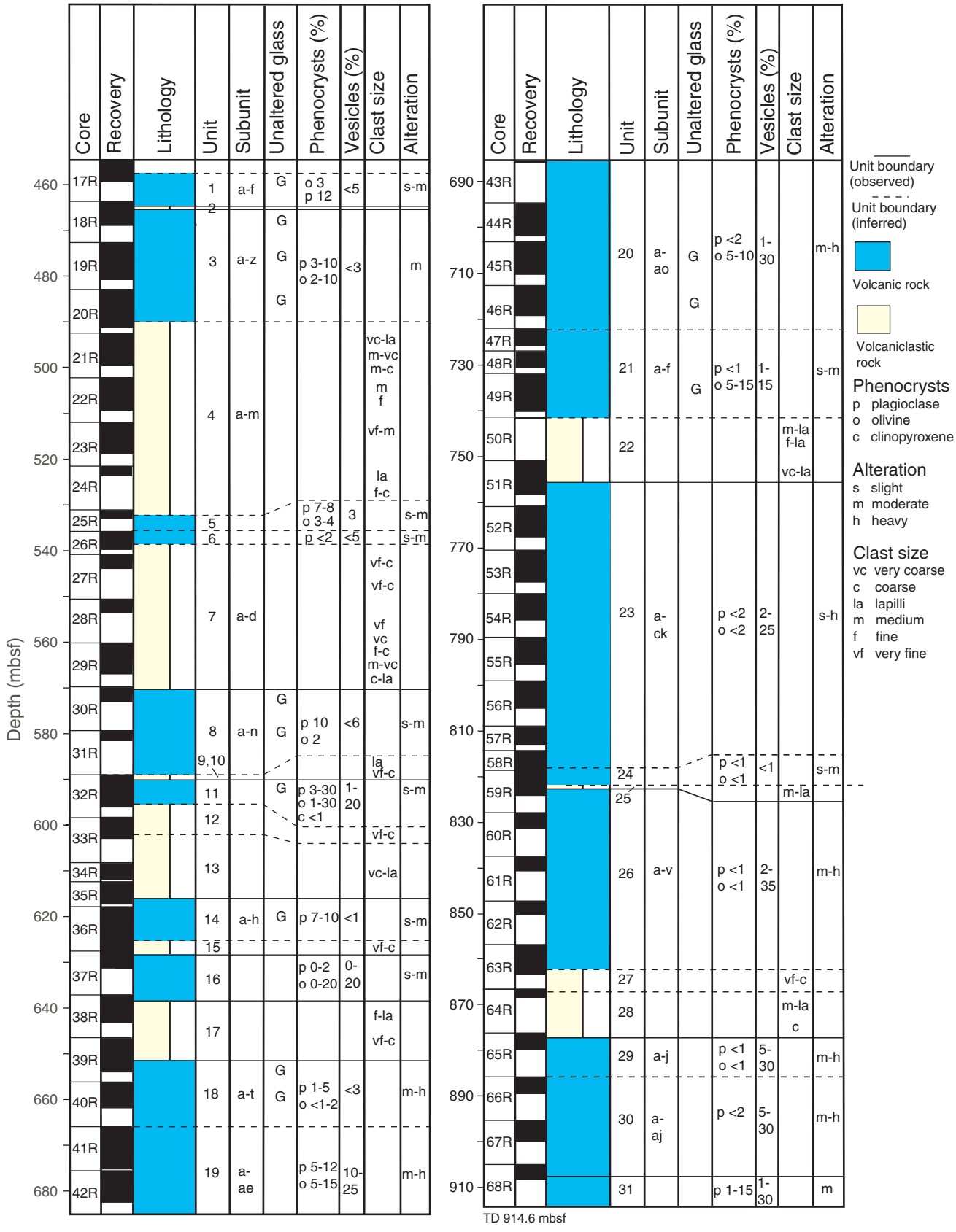

Figure F7. Integration of basement unit boundaries with (**A**) drilling rate per core and (**B**) recovery per core.

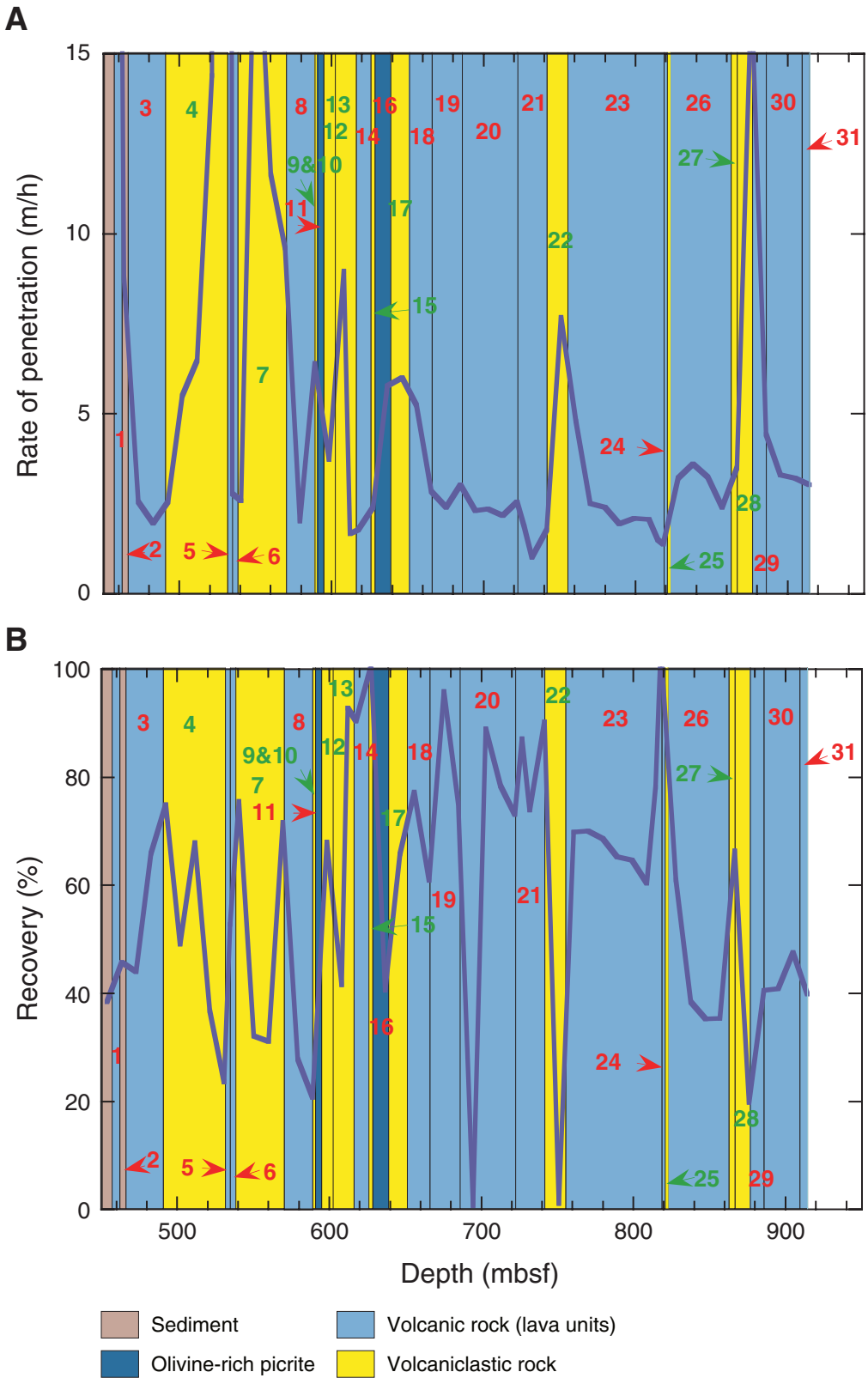

Figure F8. Close-up photograph showing the large plagioclase phenocrysts of Unit 14 (interval 197-1203A-35R-4, 131–149 cm).

Figure F9. Close-up photograph showing the boundary between Units 8 and 9 (interval 197-1203A-32R-1, 73–87 cm).

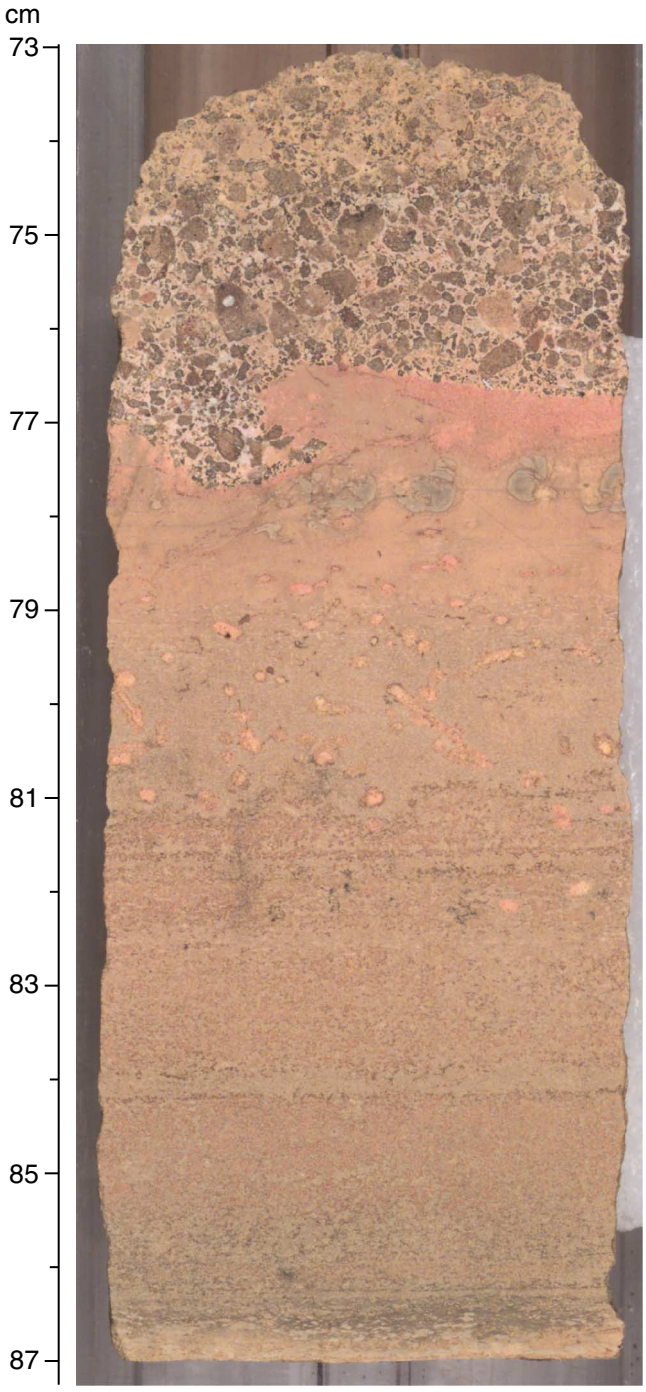

Figure F10. Photomicrograph of highly vesicular reticulite-like basalt tephra clasts in Unit 4f (Sample 197-1203A-21R-2 [Piece 12B, 141–143 cm]) (plane-polarized light; field of view = 5.5 mm; photomicrograph 1203A-73).

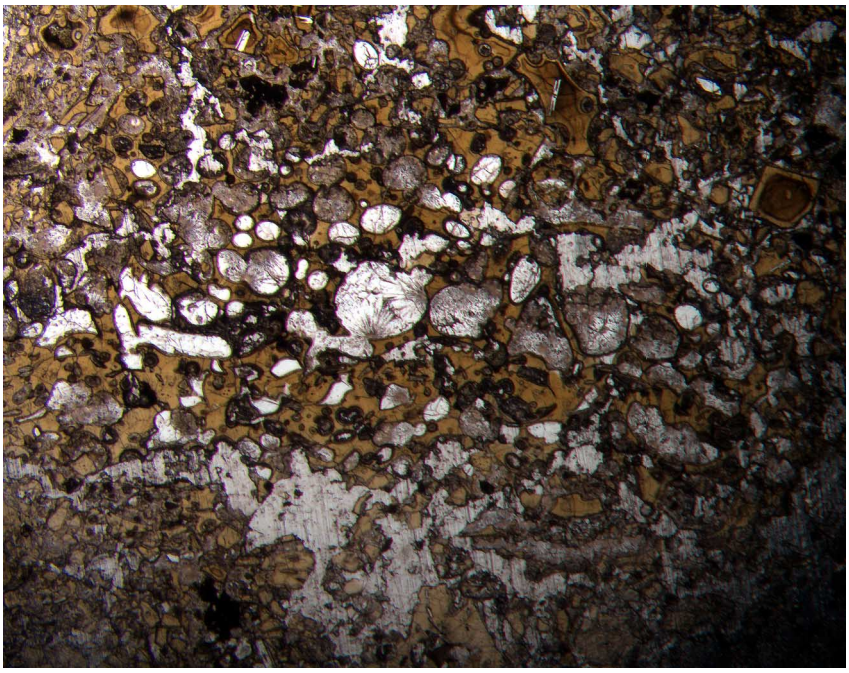

Figure F11. Photomicrograph of basalt tephra clasts in Unit 4f with fluidal outlines and elongate (stretched) vesicles (Sample **197-1203A-21R-2 [Piece 12B, 141–143 cm]**) (plane-polarized light; field of view = 1.4 mm; photomicrograph 1203A-71).

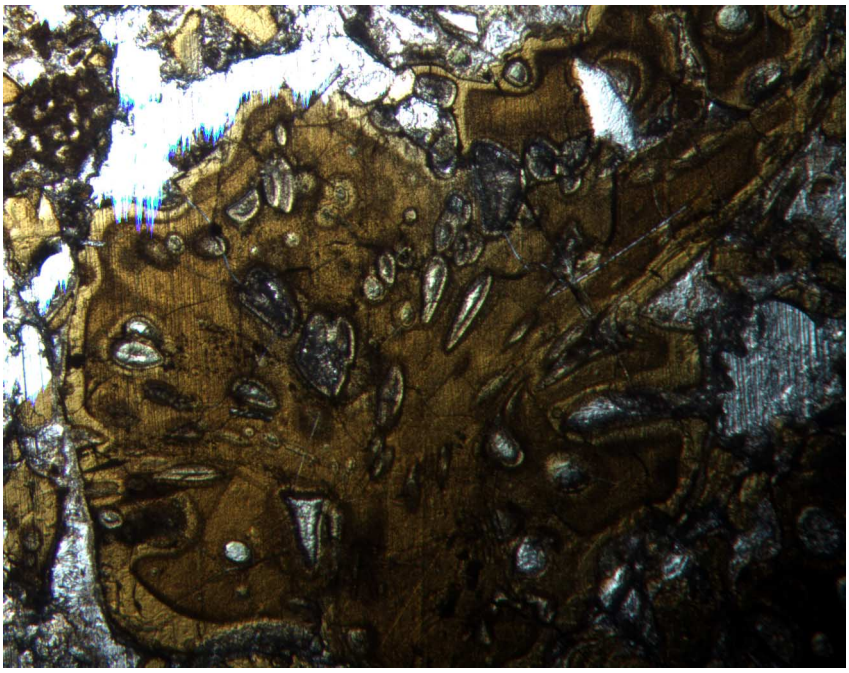

Figure F12. Close-up photographs of interval 197-1203A-51R-1, 39–46 cm, in Unit 22b, showing (**A**) highly vesicular lapilli scoria clasts that comprise the scoria fall deposit and (**B**) an armored lapillus in the scoria fall deposit, with an aphanitic lava fragment wrapped by vesicular basalt glass.

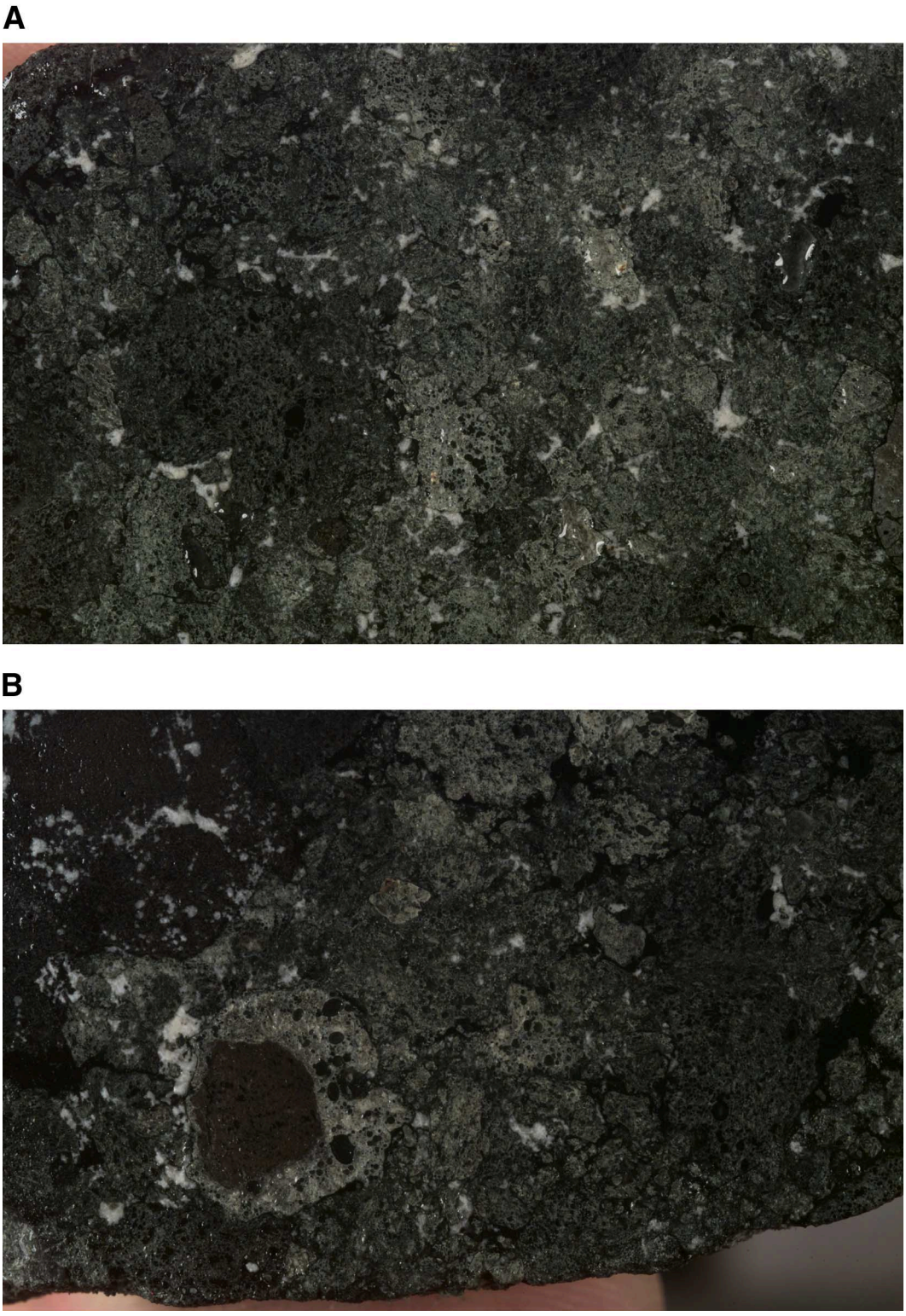

Figure F13. Photomicrograph showing highly vesicular cuspate basalt tephra clasts in Unit 9 (Sample **197-1203A-32R-1 [Piece 15, 74–77 cm]**) (plane-polarized light; field of view = 5.5 mm; photomicrograph 1203A-128).

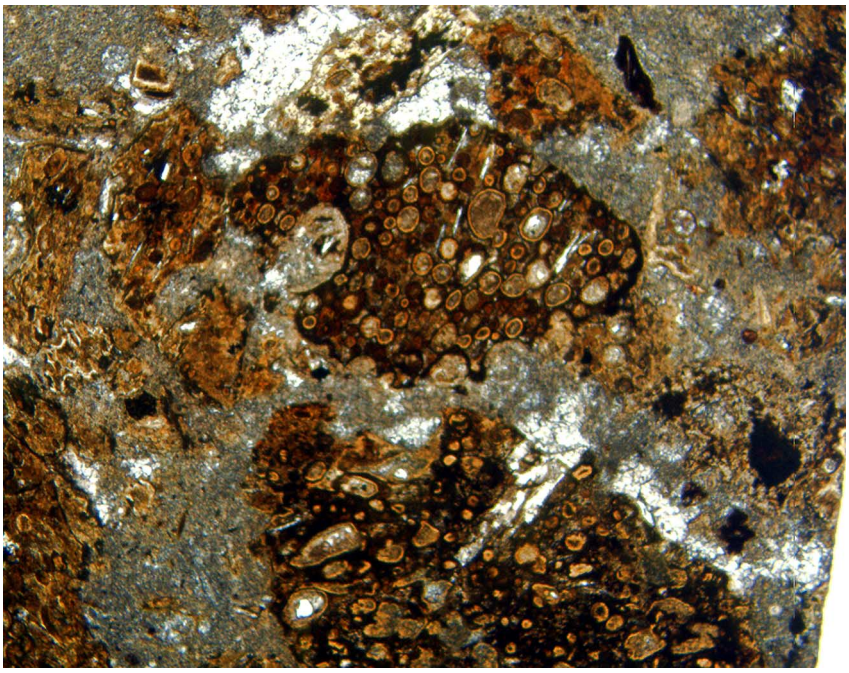

Figure F14. Close-up photograph showing volcanic breccia of Unit 13, consisting of angular clasts of basalt from the underlying lava unit and tephra in a white, carbonate-rich matrix (interval 197-1203A-34R-3, 13–31 cm).

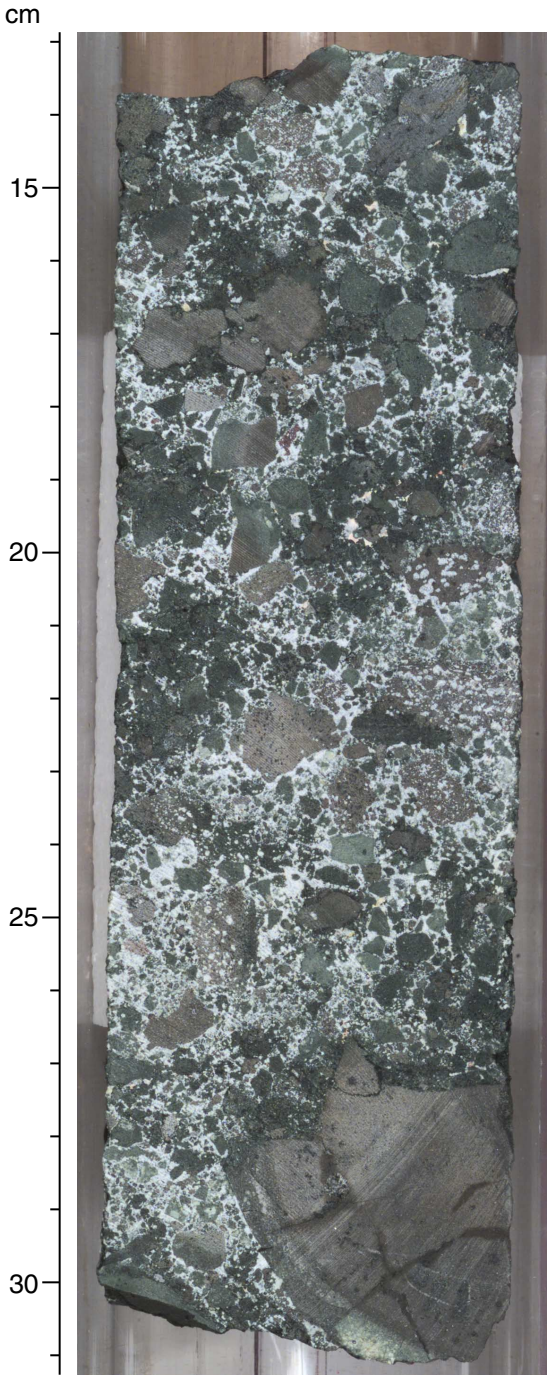

Figure F15. Photomicrograph of coralline algae in Unit 28 (Sample **197-1203A-64R-1, 45–47 cm**) (cross-polarized light; field of view = 1.4 mm; photomicrograph 1203A-170).

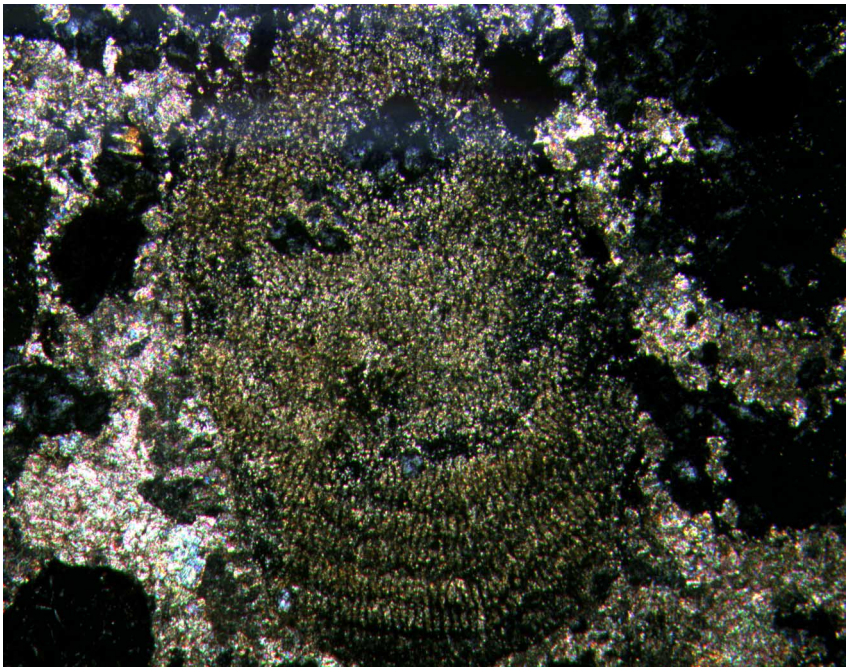

Figure F16. Close-up photograph showing unaltered glassy margins of three adjoining lobes and glass fragments between lobes, which are enclosed in a calcite matrix (Unit 20; interval 197-1203A-44R-1, 46–65 cm).

Figure F17. Close-up photographs. **A.** Partially altered glassy lobe margins with calcareous interlobe sediment (interval 197-1203A-41R-2, 0–17 cm). **B.** Completely altered (green) glassy lobe margins (interval 197-1203A-66R-2, 72–91 cm).

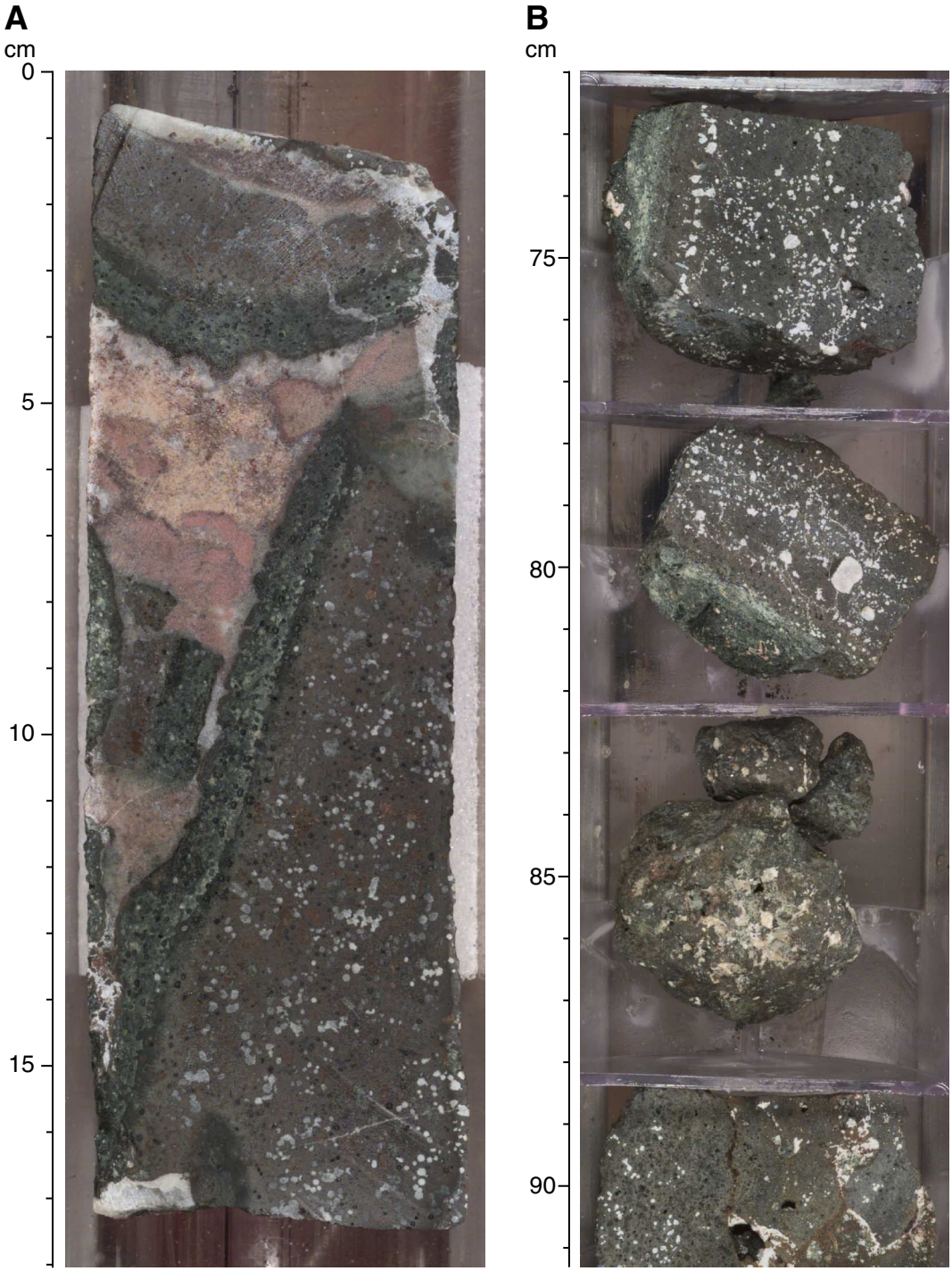

Figure F18. Pillow lava units. **A.** Graphic log showing the characteristic structures of pillowed lobes at Site 1203 using an example from Unit 8 (interval 197-1203A-31R-1, 20–78 cm). **B.** Photograph showing an example of the glassy pillow lobe margins in Unit 18 (interval 197-1203A-39R-4, 100–115 cm). Note the thin vesicle band just inside the glassy selvage and the characteristic cube-jointed pattern.

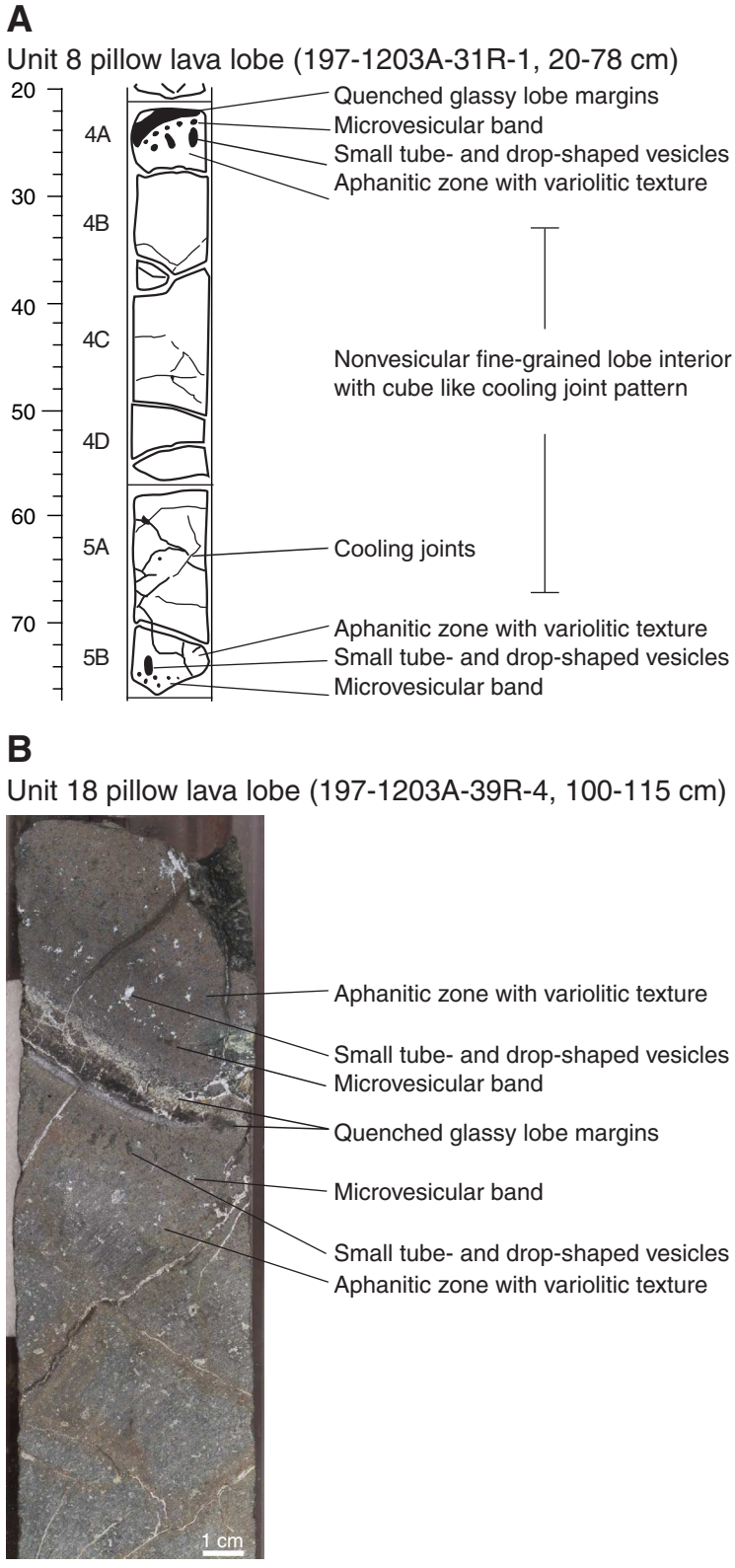

Figure F19. Lobe thickness distribution of (**A**) pillow lavas, (**B**) compound pahoehoe lavas, and (**C**) hybrid pillow-pahoehoe lavas. *N* = number of lobes.

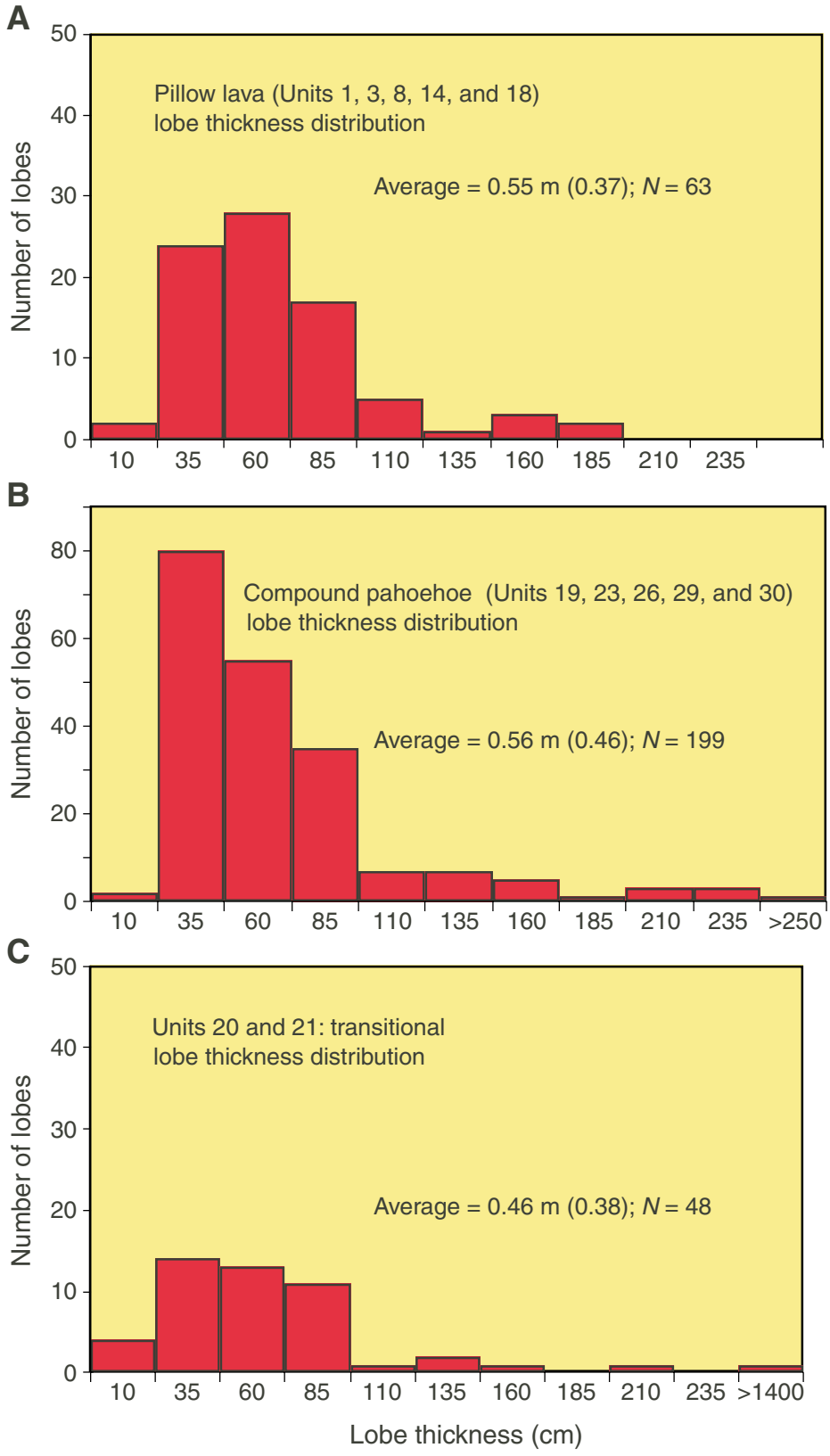

Figure F20. Photomicrograph of microlites in a glassy lobe margin of Unit 3 (Sample **197-1203A-19R-2 [Piece 3, 24–26 cm]**) (plane-polarized light; field of view = 1.4 mm; photomicrograph 1203A-1).

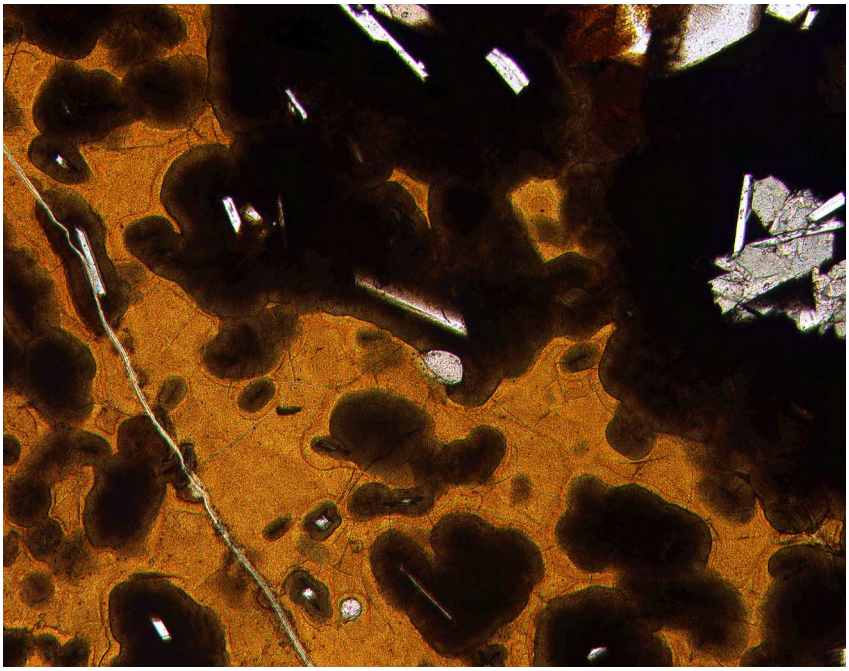

Figure F21. Graphic logs illustrating the characteristic structures of pahoehoe lobes in the Unit 23 compound pahoehoe lava at Site 1203. **A.** Lobe showing the threefold subdivision into vesicular upper crust, massive lobe interior, and vesicular lower crust. **B.** Lobe that is vesicular throughout, but coarsely vesicular in the center and finely vesicular near the margins. HVS = horizontal vesicle sheet, VC = vesicle cylinders, PV = pipe vesicles.

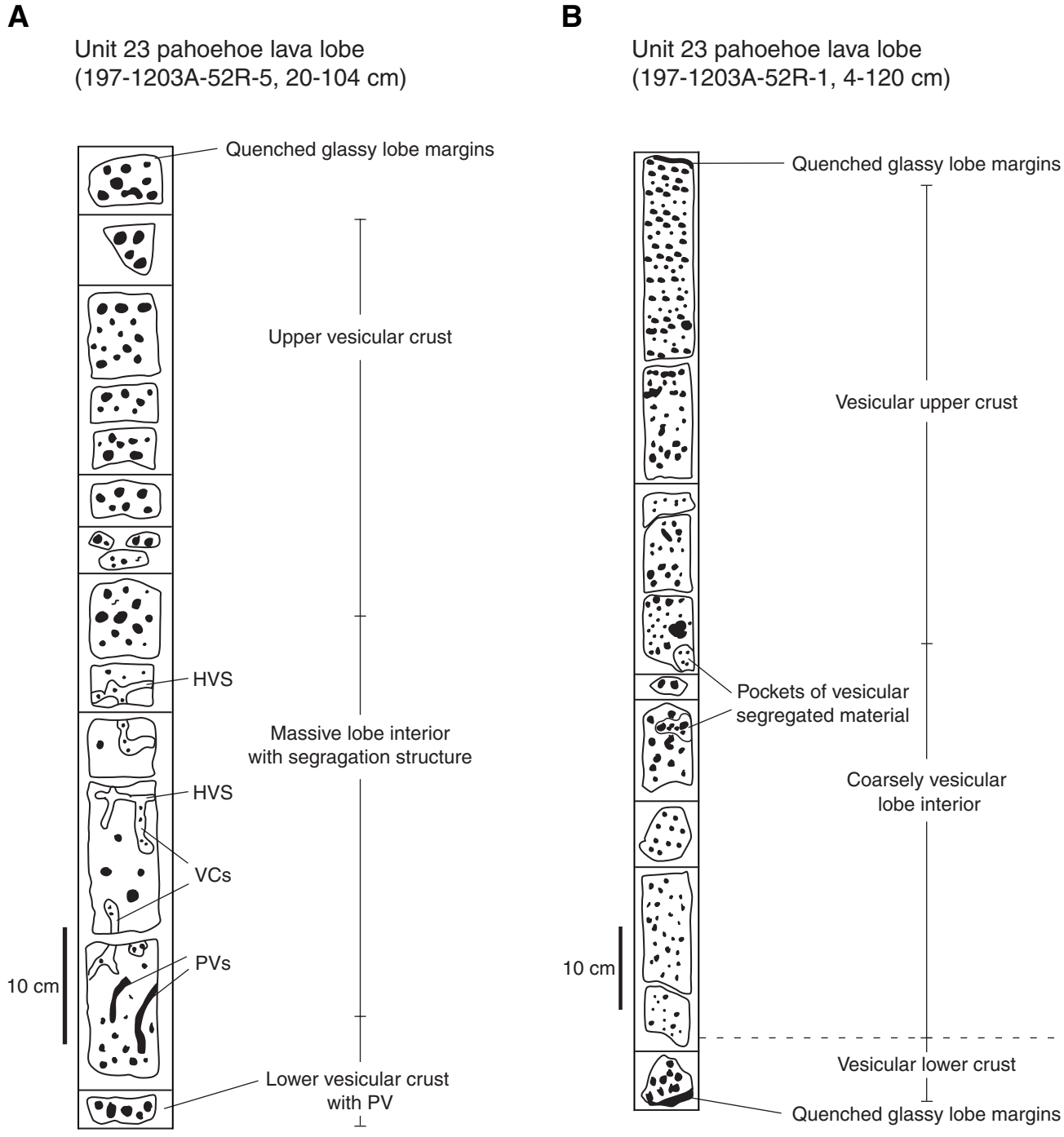

Figure F22. Graphic log and photograph illustrating the characteristic structures of the Unit 20 hybrid pillow-pahoehoe lava. ISP = irregular segregation pocket, HVS = horizontal vesicle sheet, VC = vesicle cylinder.

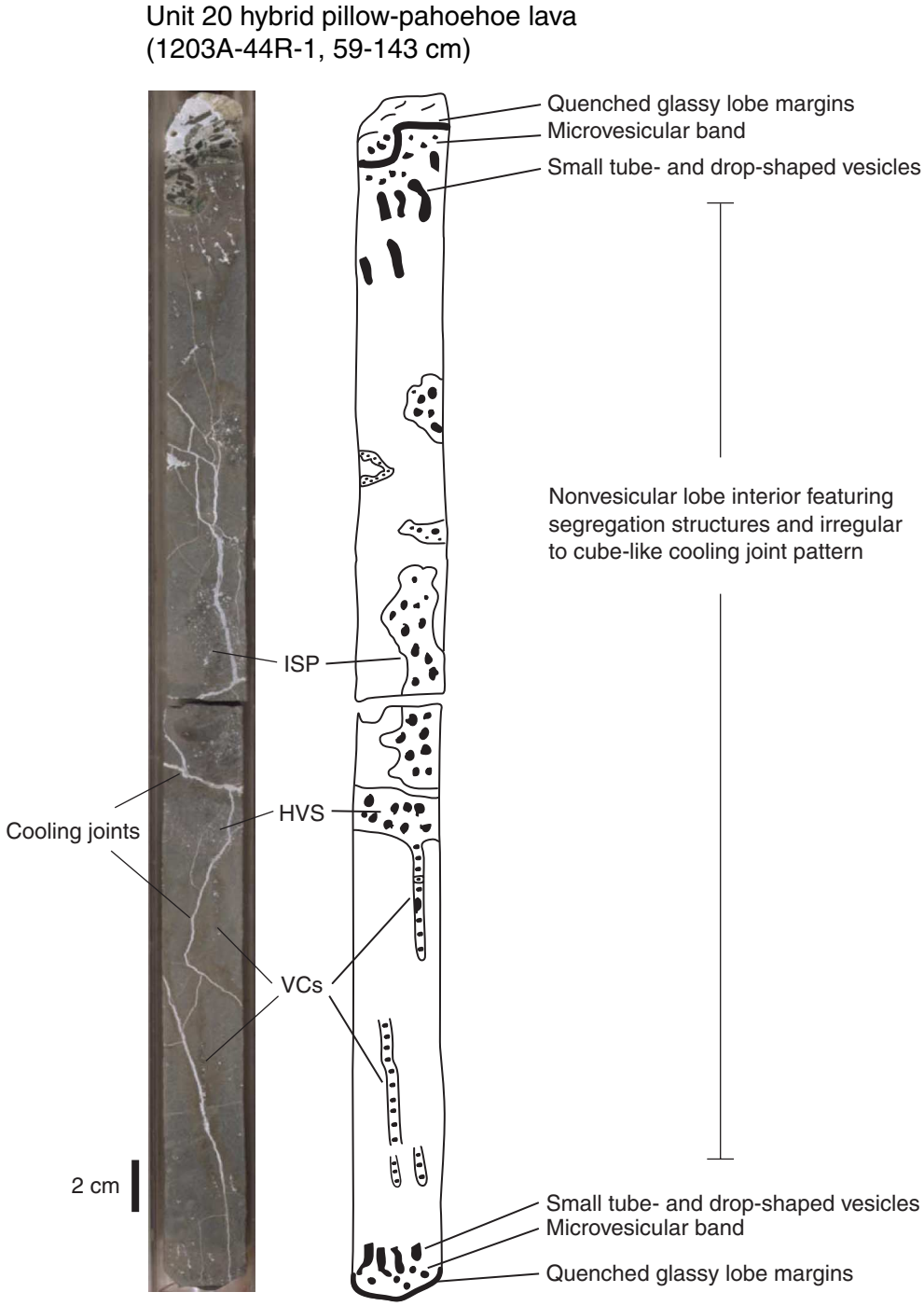

Figure F23. A graphic log illustrating the characteristic structures of pahoehoe sheet lobes at Site 1203 (Unit 11; Sections 197-1203-32R-2, 5 cm, to 32R-5, 73 cm). VZ = vesicular zone. (This figure is also available in an **oversized format.**)

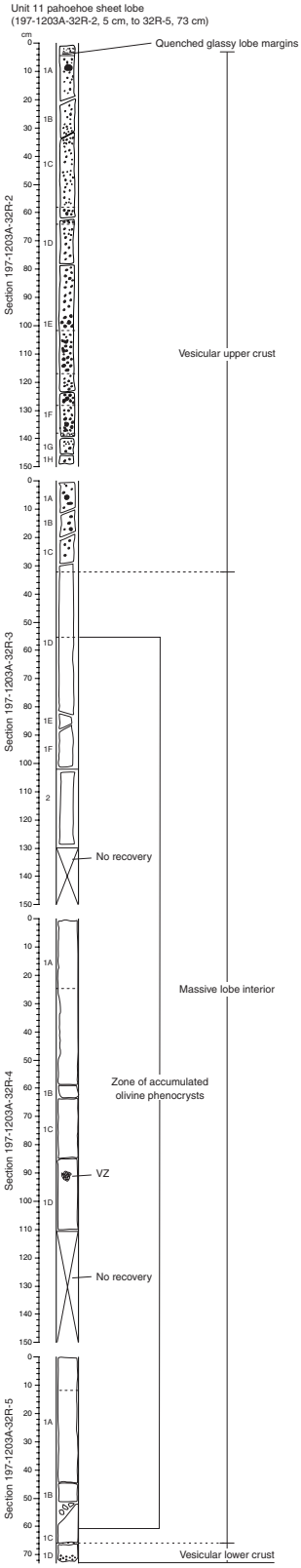

Figure F24. Photomicrographs of zonation in plagioclase (Sample 197-1203A-35R-4 [Piece 1F, 47–49 cm]) (cross-polarized light). **A.** Field of view = 10 mm; photomicrograph 1203A-59. **B.** Field of view = 2.5 mm; photomicrograph 1203A-60.

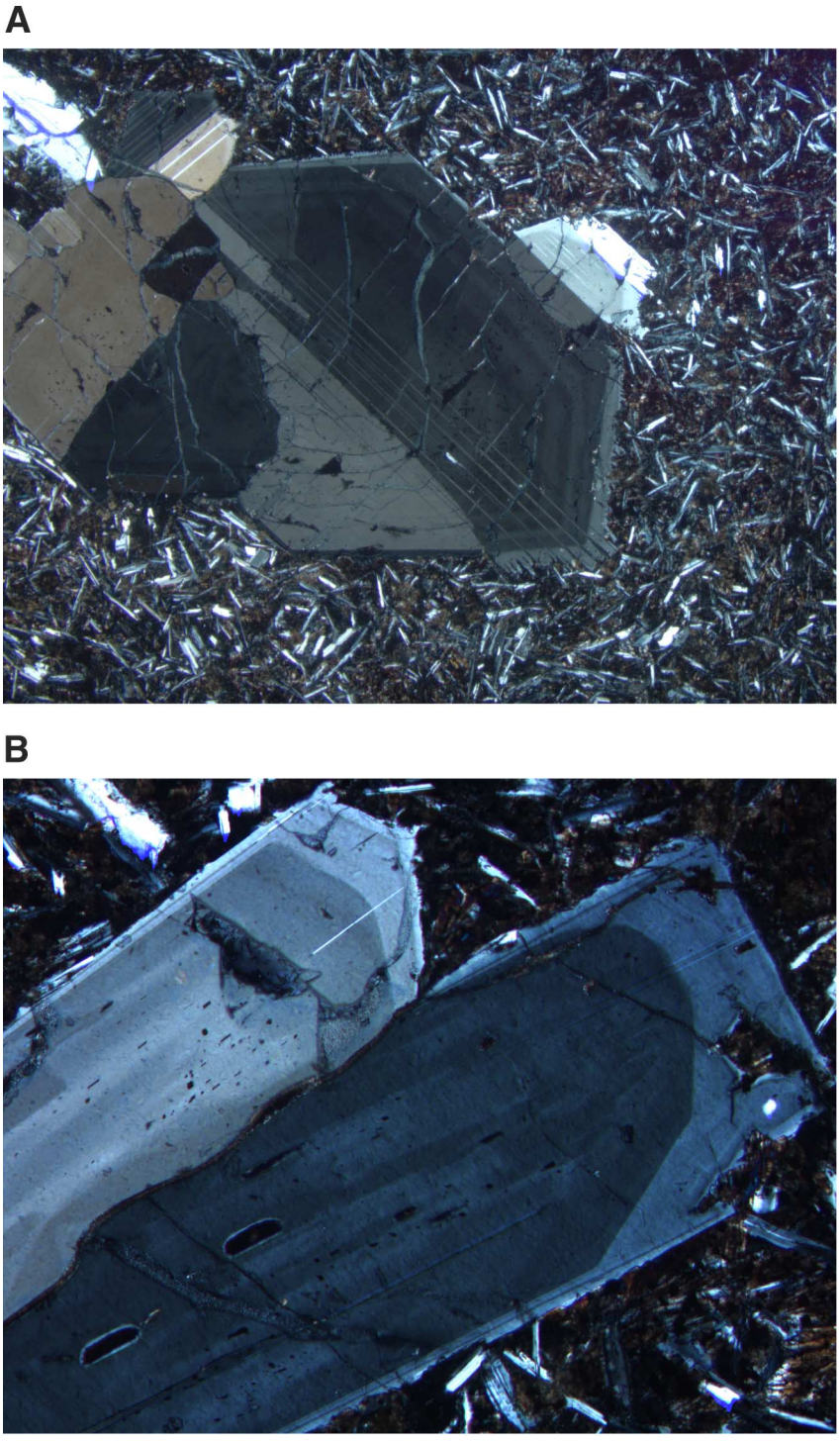

Figure F25. Photomicrograph of melt inclusions (small equant dark regions within larger crystal) in plagioclase phenocrysts from a glassy lobe margin in Unit 3 (Sample **197-1203A-19R-2 [Piece 3, 24–26 cm]**) (plane-polarized light; field of view = 1.25 mm; photomicrograph 1203A-55).

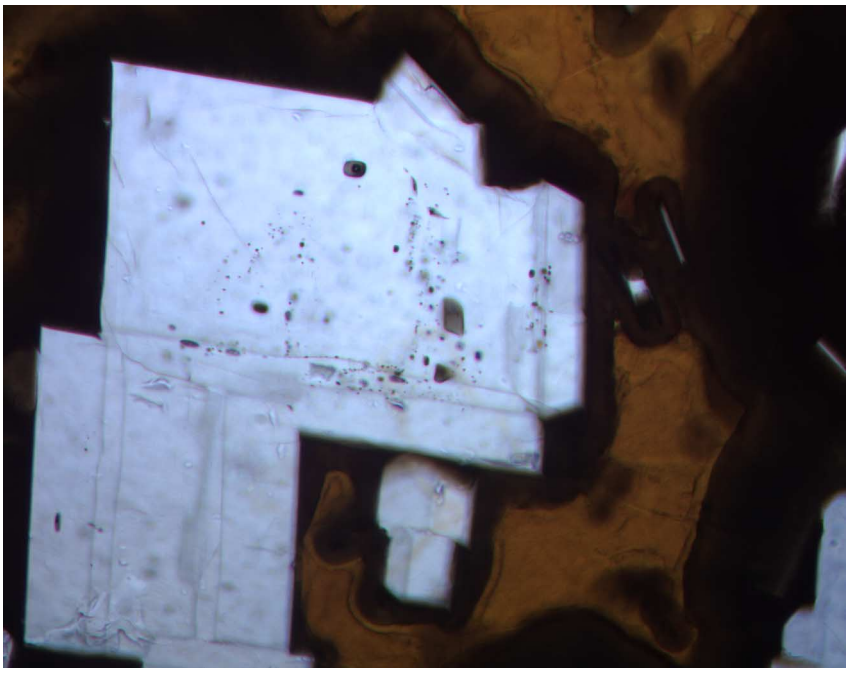

Figure F26. Photomicrograph of resorption of a plagioclase phenocryst that contains melt inclusions (Sample **197-1203A-32R-5 [Piece 1C, 56–58 cm]**) (cross-polarized light; field of view = 2.5 mm; photomicrograph 1203A-58).

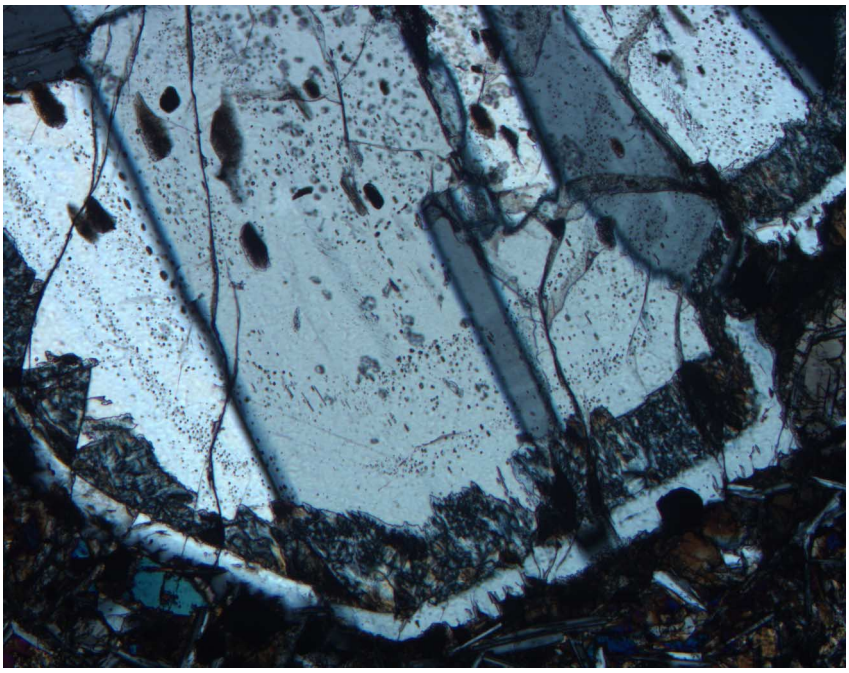

Figure F27. Photomicrograph of a Unit 3 olivine glomerocryst with calcite vein at top (Sample **197-1203A-19R-5 [Piece 2, 13–15 cm]**) (plane-polarized light; field of view = 5.5 mm; photomicrograph 1203A-11).

Figure F28. Photomicrograph of a Unit 3 skeletal olivine pseudomorph (Sample **197-1203A-19R-5 [Piece 2, 13–15 cm]**) (plane-polarized light; field of view = 5.5 mm; photomicrograph 1203A-10).

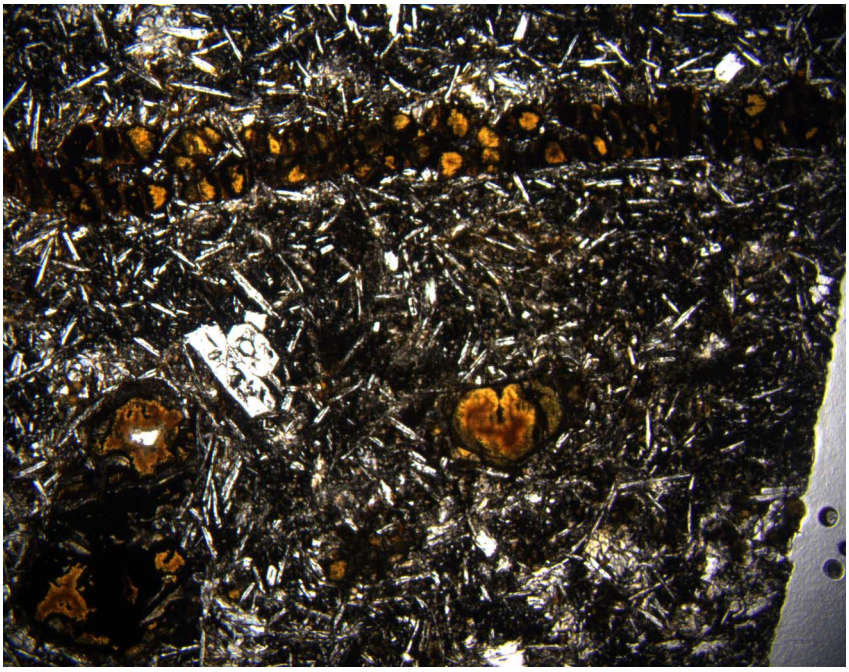

Figure F29. Photomicrograph of the olivine-rich zone in Unit 16 (Sample **197-1203A-37R-3 [Piece 1A, 10–13 cm]**) (cross-polarized light; field of view = 5.5; photomicrograph 1203A-22).

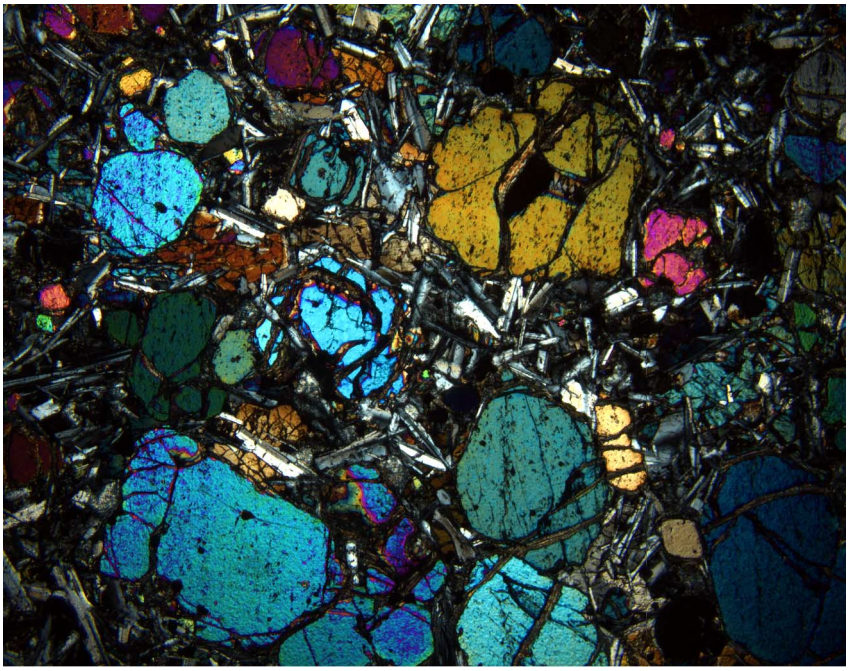

Figure F30. Photomicrograph of Unit 11 Cr spinel inclusions (dark rhombic crystals) in olivine (Sample 197-1203A-32R-3 [Piece 1E, 85–87 cm]) (plane-polarized light; field of view = 2.5 mm; photomicrograph 1203A-40).

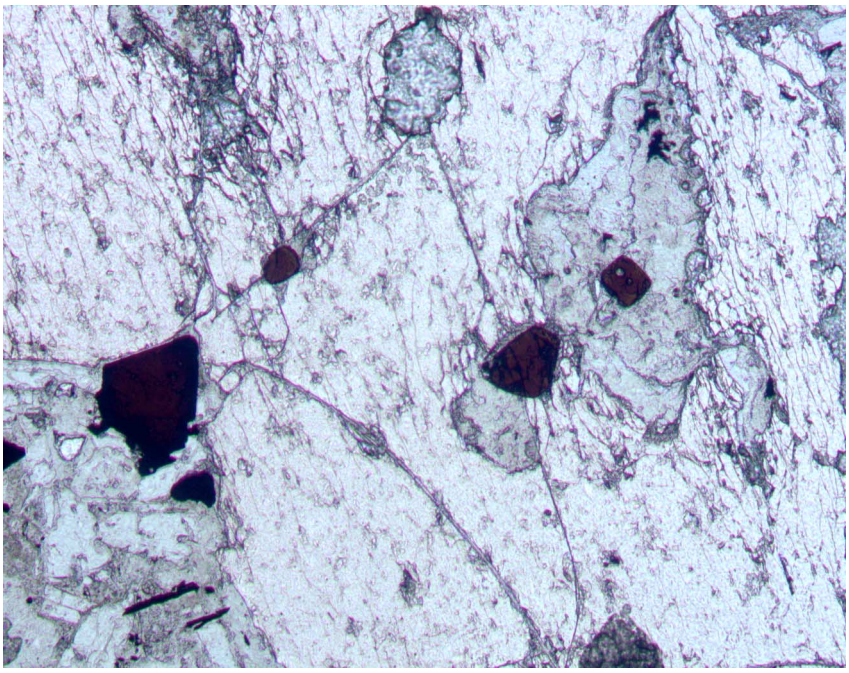

Figure F31. Photomicrograph of subvariolitic texture: Unit 14 skeletal plagioclase and comb texture formed from parallel acicular clinopyroxene crystals (Sample **197-1203A-35R-4 [Piece 1F, 47–49 cm]**) (cross-polarized light; field of view = 0.7 mm; photomicrograph 1203A-21).

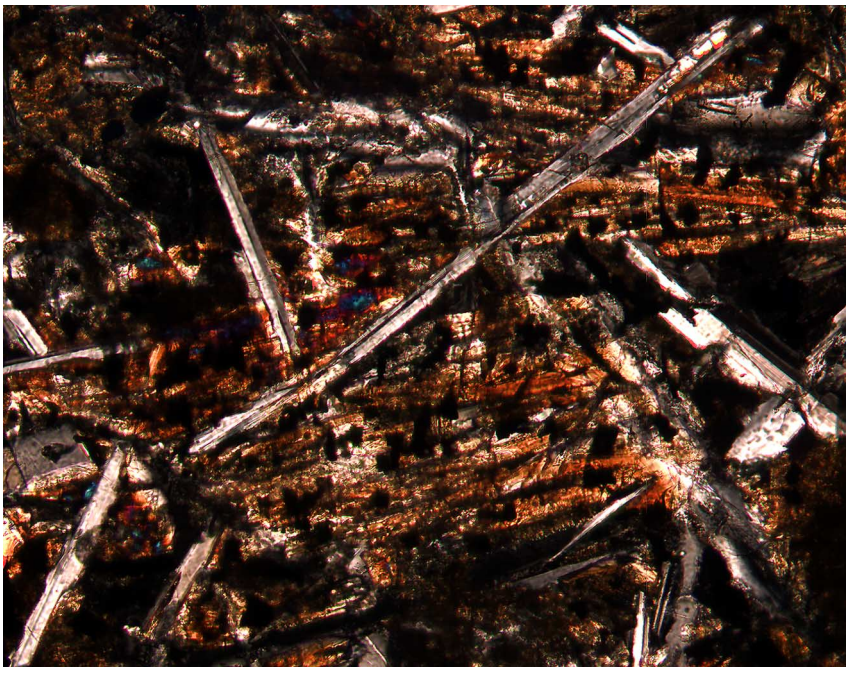

Figure F32. Photomicrograph of an example of subophitic texture (Sample **197-1203A-59R-2 [Piece 2B, 99–102 cm]**) (cross-polarized light; field of view = 2.5 mm; photomicrograph 1203A-49).

Figure F33. Photomicrograph of segregated material in a vesicle cylinder from Unit 23 (Sample **197-1203A-54R-3, 15–18 cm**) (plane-polarized light; field of view = 0.7 mm; photomicrograph 1203A-76).

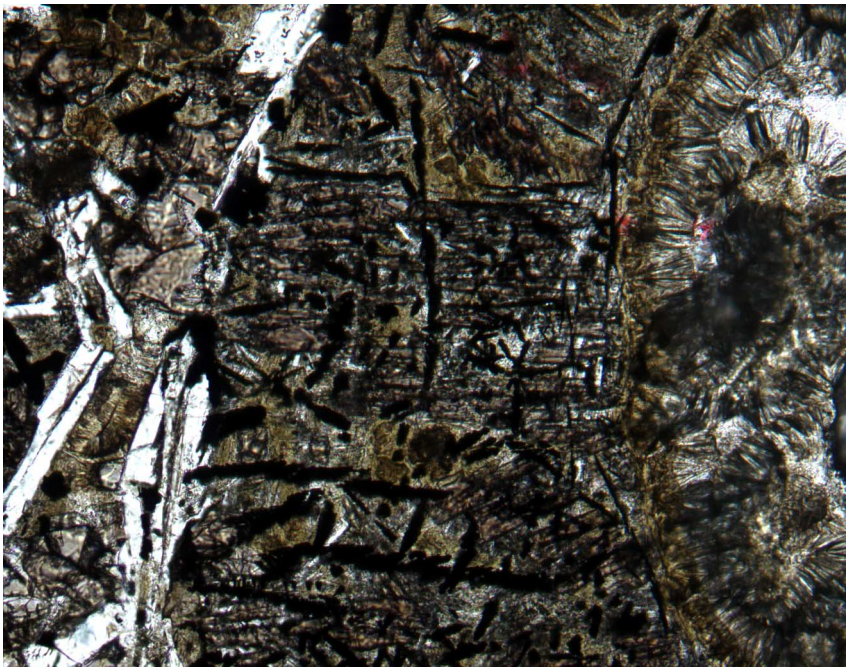

Figure F34. Photomicrograph of segregated material in a vesicle cylinder from Unit 26 (Sample 197-1203A-59R-5 [Piece 5, 30–32 cm]) (plane-polarized light; field of view = 1.4 mm; photomicrograph 1203A-79).

Figure F35. A. Photomicrograph of ilmenite exsolution in titanomagnetite (Sample **197-1203A-32R-3 [Piece 1E, 85–87 cm]**) (reflected light; field of view = 0.5 mm; photomicrograph 1203A-56). **B.** Same picture as A, but rotated 90° (photomicrograph 1203A-57).

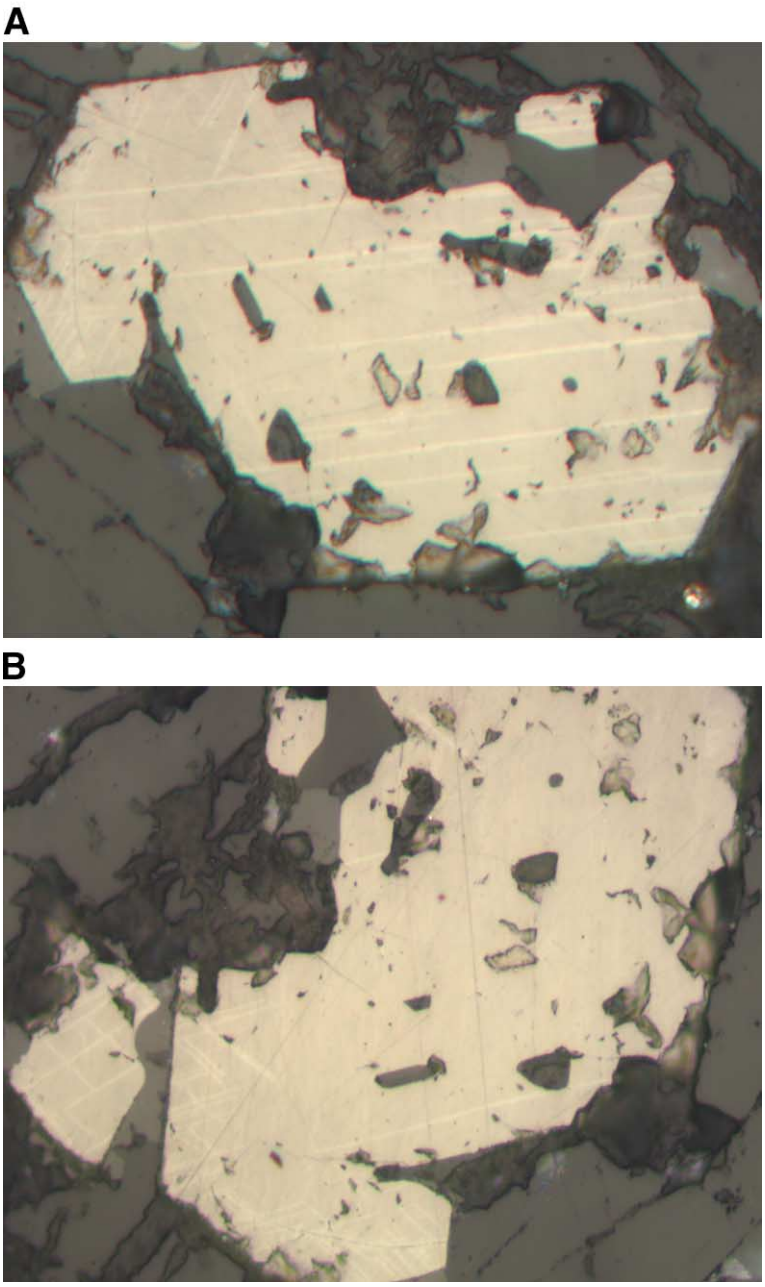

Figure F36. Photomicrograph of Unit 11 titanomagnetite with maghemite alteration along cleavage planes (Sample **197-1203A-32R-3 [Piece 1E, 85–87 cm]**) (reflected light; field of view = 0.5 mm; photomicrograph 1203A-43).

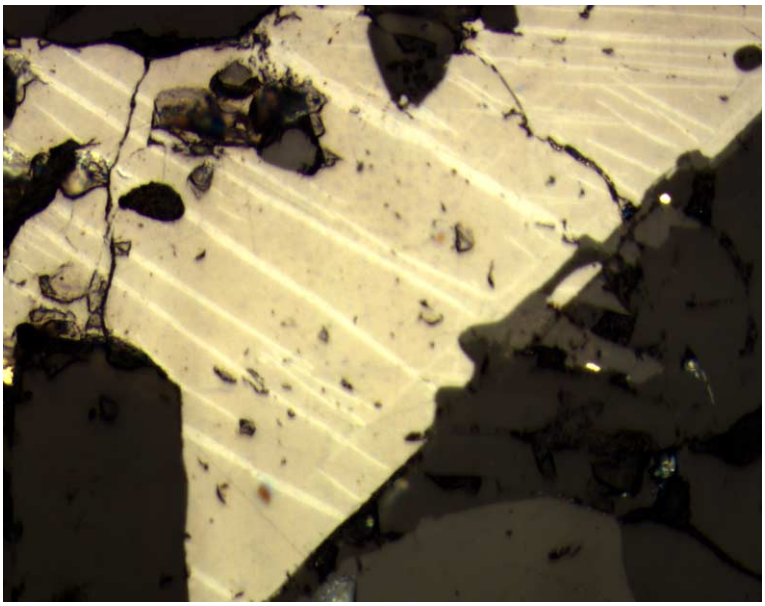

Figure F37. Photomicrograph of Unit 30 titanomagnetite with extensive maghemite alteration (Sample 197-1203A-68R-3 [Piece 4, 16–18 cm]) (reflected light; field of view = 0.5 mm; photomicrograph 1203A-64).

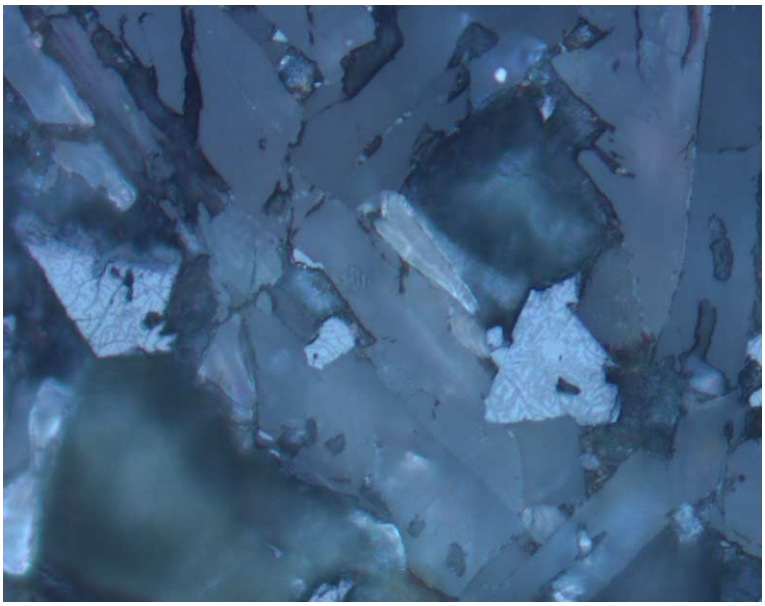

Figure F38. Photomicrograph of Unit 29 titanomagnetite with maghemite rim (Sample **197-1203A-65R-4 [Piece 3, 21–24 cm]**) (reflected light; field of view = 0.5 mm; photomicrograph 1203A-63).

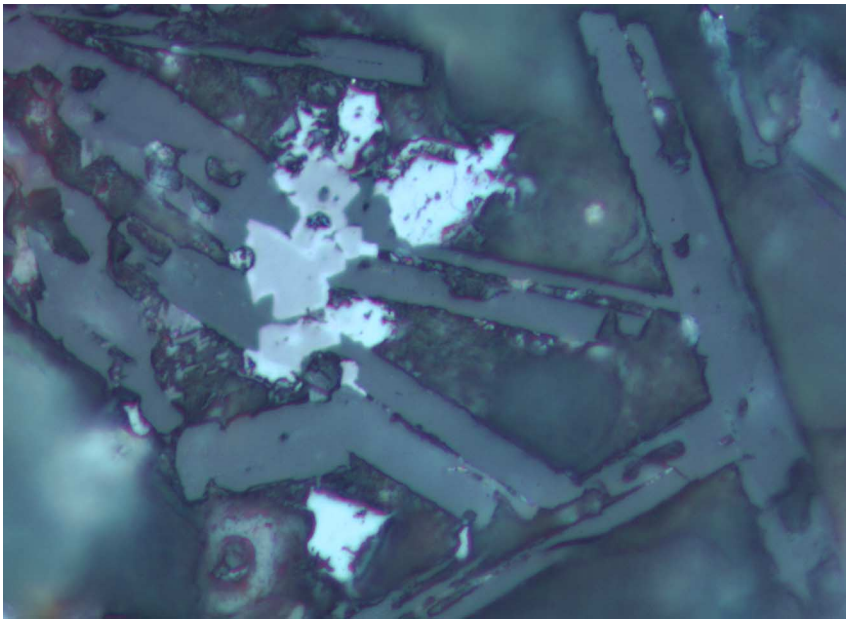

Figure F39. Photomicrograph of unaltered titanomagnetite and pentlandite (Sample **197-1203A-26R-3 [Piece 1B, 39–41 cm]**) (reflected light; field of view = 0.5 mm; photomicrograph 1203A-54).

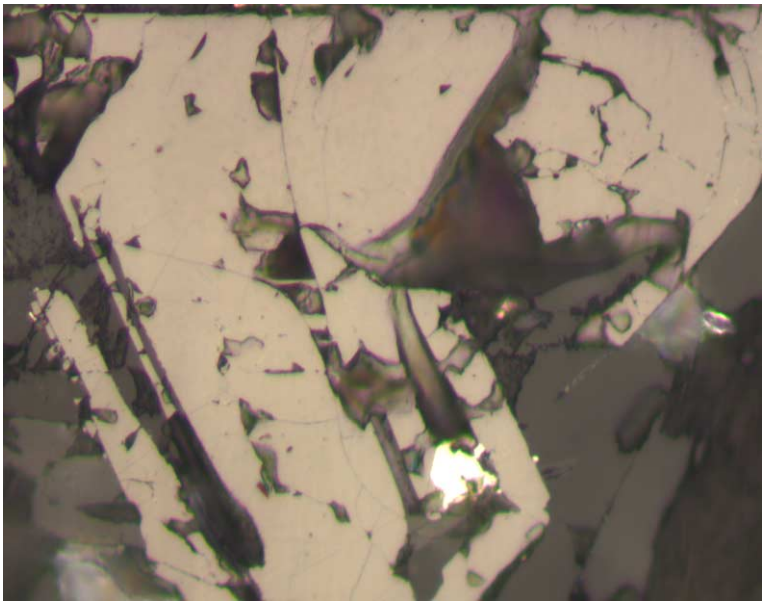

Figure F40. Photomicrograph of a Cr spinel inclusion in olivine (bottom left) and a titanomagnetite crystal (middle right) in Unit 11 (Sample **197-1203A-32R-3 [Piece 1E, 85–87 cm]**) (reflected light; field of view = 0.5 mm; photomicrograph 1203A-120).

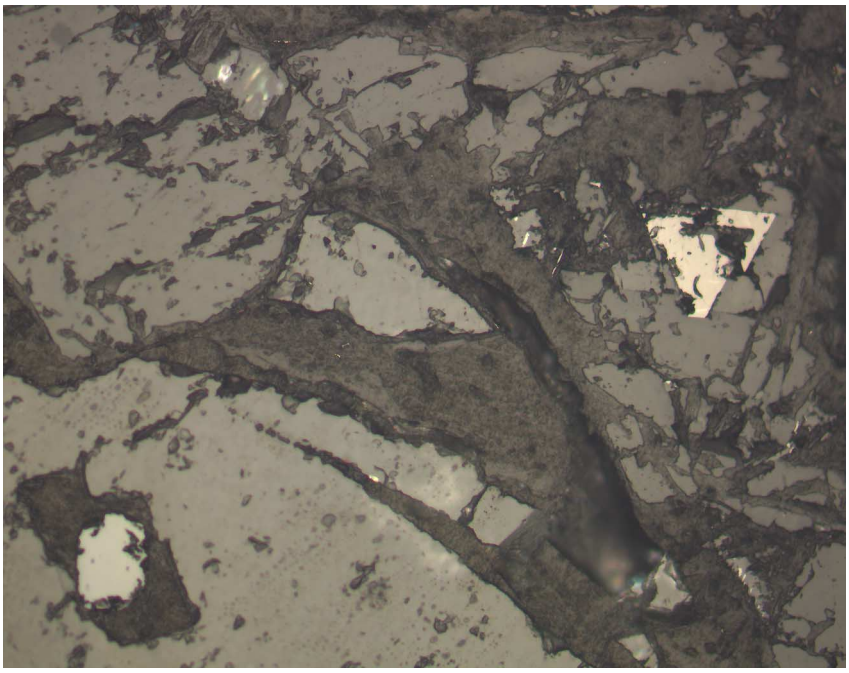

Figure F41. Photomicrograph of Cr spinel with titanomagnetite overgrowth in Unit 16 (Sample 197-1203A-37R-3 [Piece 1A, 10–13 cm]) (reflected light; field of view = 0.5 mm; photomicrograph 1203A-61).

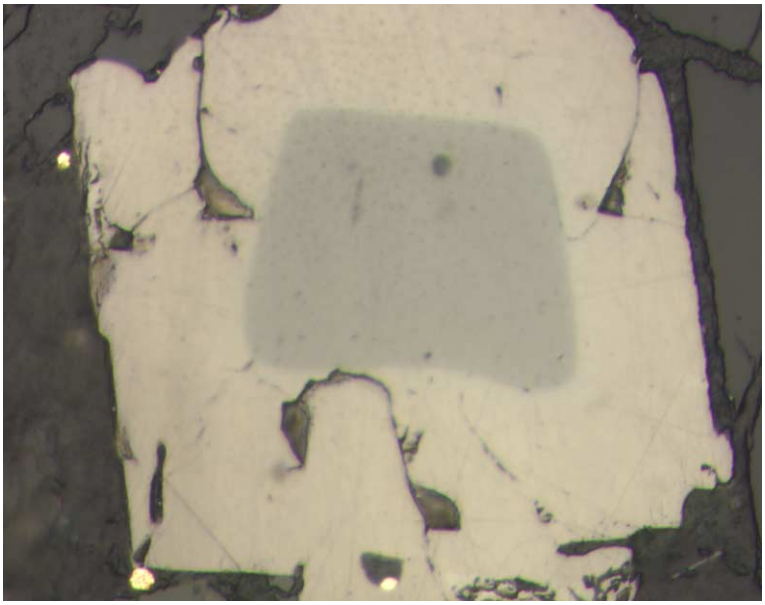

Figure F42. A. Total alkali content ($Na_2O + K_2O$) vs. SiO_2 classification plot for volcanic rocks (LeBas et al., 1986) showing lava compositions from Detroit Seamount. The dashed line is the alkalic-tholeiitic dividing line for Hawaiian basalt (Macdonald and Katsura, 1964). Lavas from Site 884 are tholeiitic basalt, whereas lavas from Site 883 are alkalic basalt, although Keller et al. (1995) inferred that prior to alteration, these lavas were transitional between alkalic and tholeiitic basalt. Data for these two Leg 145 Sites in this and all subsequent figures are from Keller et al. (2000) and M. Regelous et al. (unpubl. data). Lavas from Site 1203 range from tholeiitic, overlapping with Site 884 lavas, to alkalic, overlapping with Site 883 lavas. Most of the alkalic Site 1203 lavas have loss on ignition (LOI) >2 wt%. The volcaniclastite sample has very high total alkalis, which is interpreted as a result of alkali gain during alteration. The two Site 1203 basalts in the tholeiitic field at <45 wt% SiO_2 are picritic as a result of olivine accumulation. **B.** Total alkali content ($Na_2O + K_2O$) vs. SiO_2 comparing Detroit Seamount lava compositions with those from Mauna Kea Volcano (shield- and postshield-stage lavas) on the island of Hawaii (data from Frey et al., 1990, 1991; Rhodes, 1996; J.M. Rhodes and J. Vollinger, unpubl. data). Site 884 and some Site 1203 lavas overlap with the shield-stage tholeiitic basalt, whereas Site 883 and some Site 1203 lavas overlap with Hawaiian alkalic basalt.

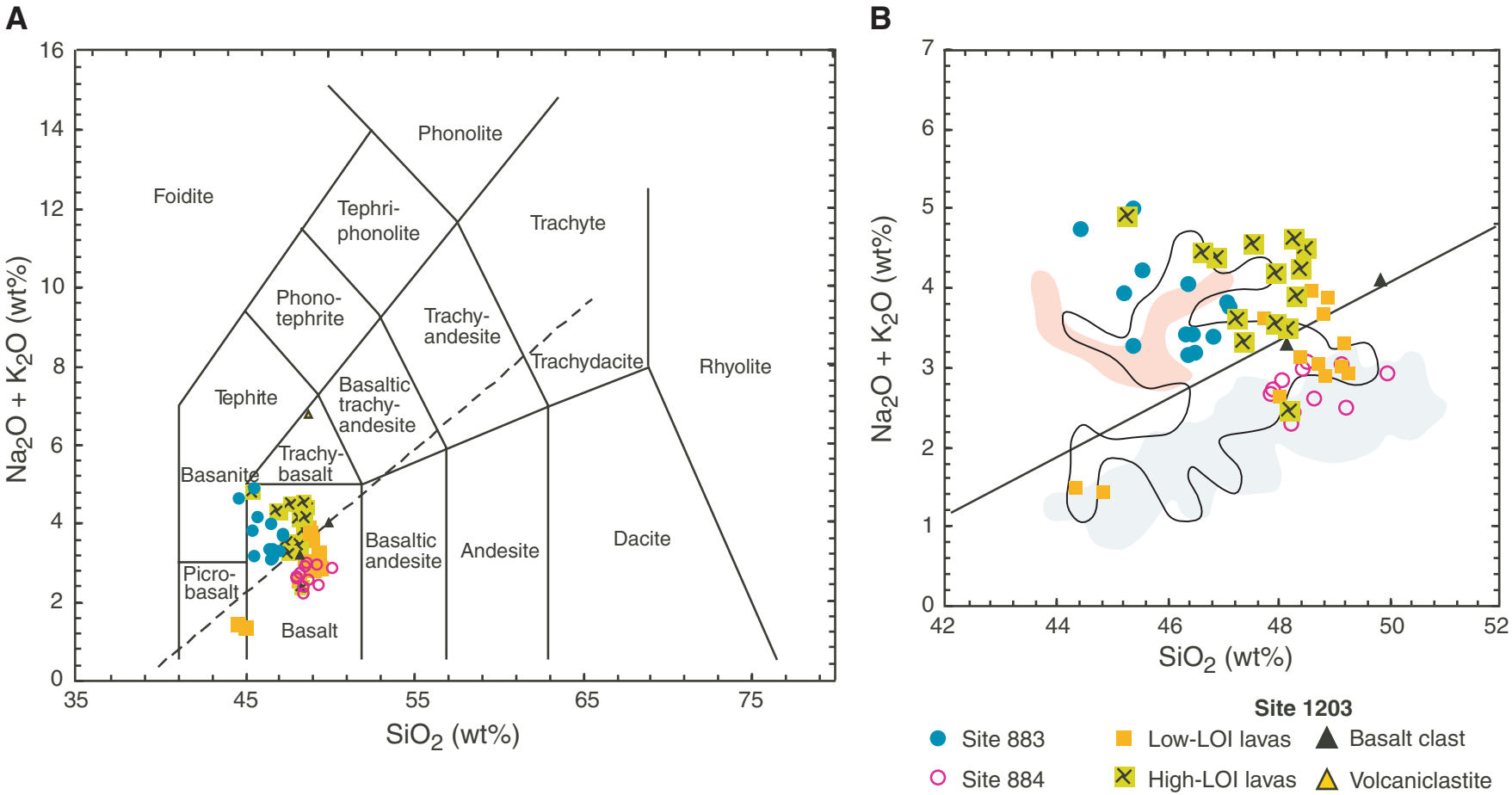

Figure F43. Abundances of the incompatible elements Ti, P, Na, K, Sr, and Ba vs. Zr, a relatively immobile incompatible element. In each panel abundances increase from Site 884 lavas (and the two Site 1203 picrites) to Site 1203 transitional/tholeiitic lavas to Site 883 lavas to Site 1203 alkalic lavas. In detail, the Site 1203 alkalic basalt divides into two groups in the Ti panel; the Site 883 basalt shows a near-vertical trend to high P (also K and Ba), possibly reflecting apatite formation during alteration; Na, Sr, and Ba are much less incompatible than Zr in the Site 1203 alkalic basalt; the abnormally high Ba in one of the three samples from Unit 23 (Sample 197-1203-51R-4, 93–95 cm) in Table T8, p. 158, is probably a result of alteration. In contrast to the other elements, no correlation is shown in the K vs. Zr plot—a result that we infer reflects K mobility during postmagmatic alteration. LOI = loss on ignition.

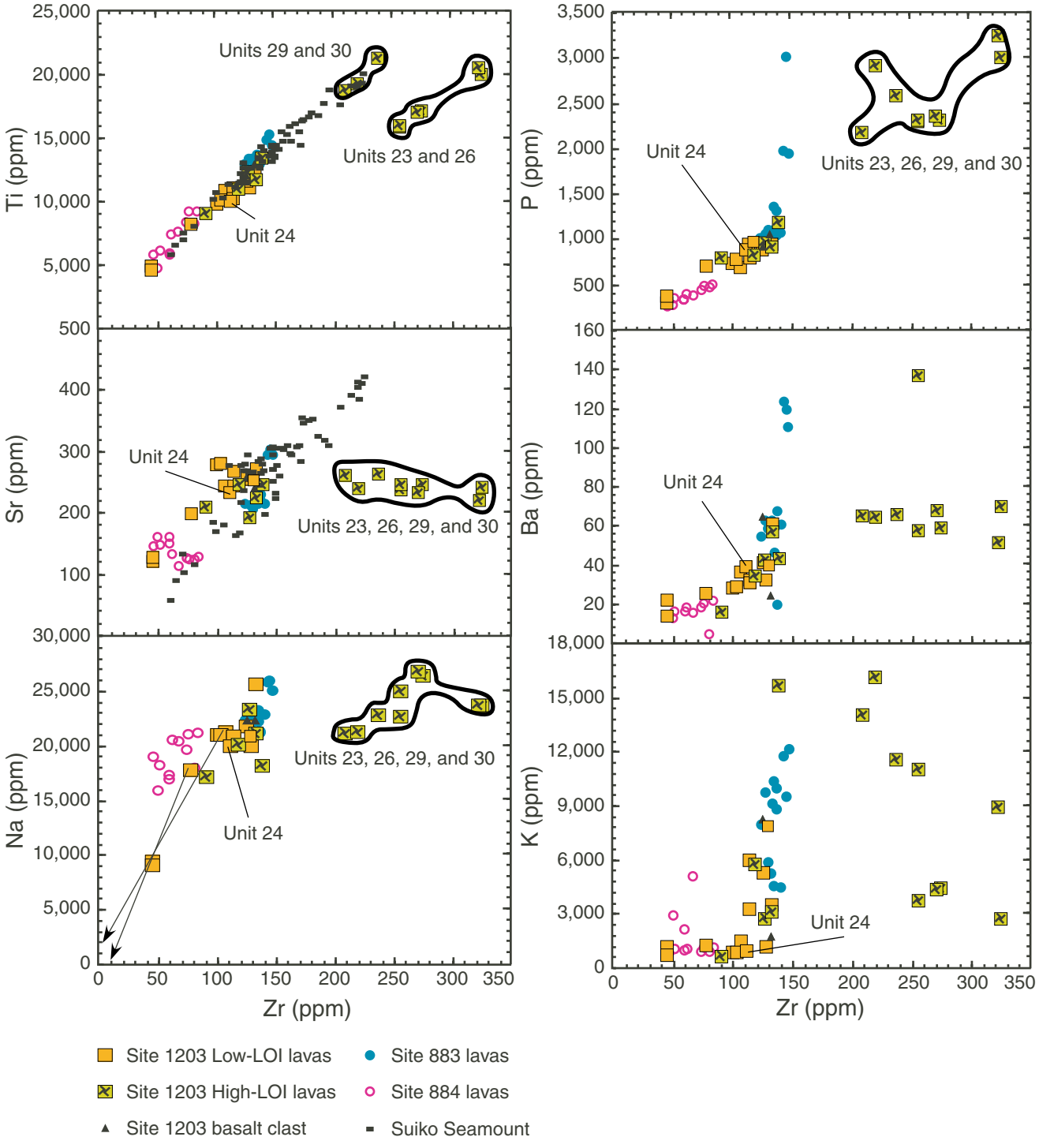

Figure F44. Photomicrograph of segregated material in a vesicle cylinder from Unit 23 (Sample **197-1203A-52R-6, 12–14 cm**) (plane-polarized light; field of view = 1.4 mm; photomicrograph 1203A-77).

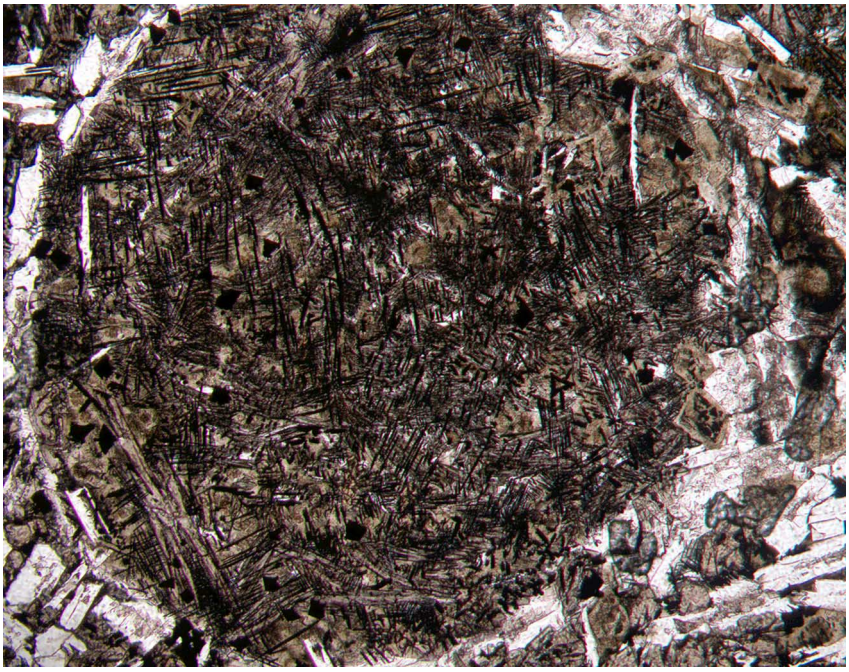

Figure F45. Abundances of Ni, Sc, Sr, and CaO vs. MgO content for Detroit Seamount lavas. Solid lines connect the picritic lavas from Units 11 and 16 with other lavas from the same units. These lines show the effects of olivine accumulation. The unusually low incompatible element content of Site 884 lavas is obvious in the Sr panel. The CaO panel shows that the alkalic basalt from Site 1203 (Unit 23, 26, 29, and 30) extends to the highest MgO content and has relatively low CaO contents.

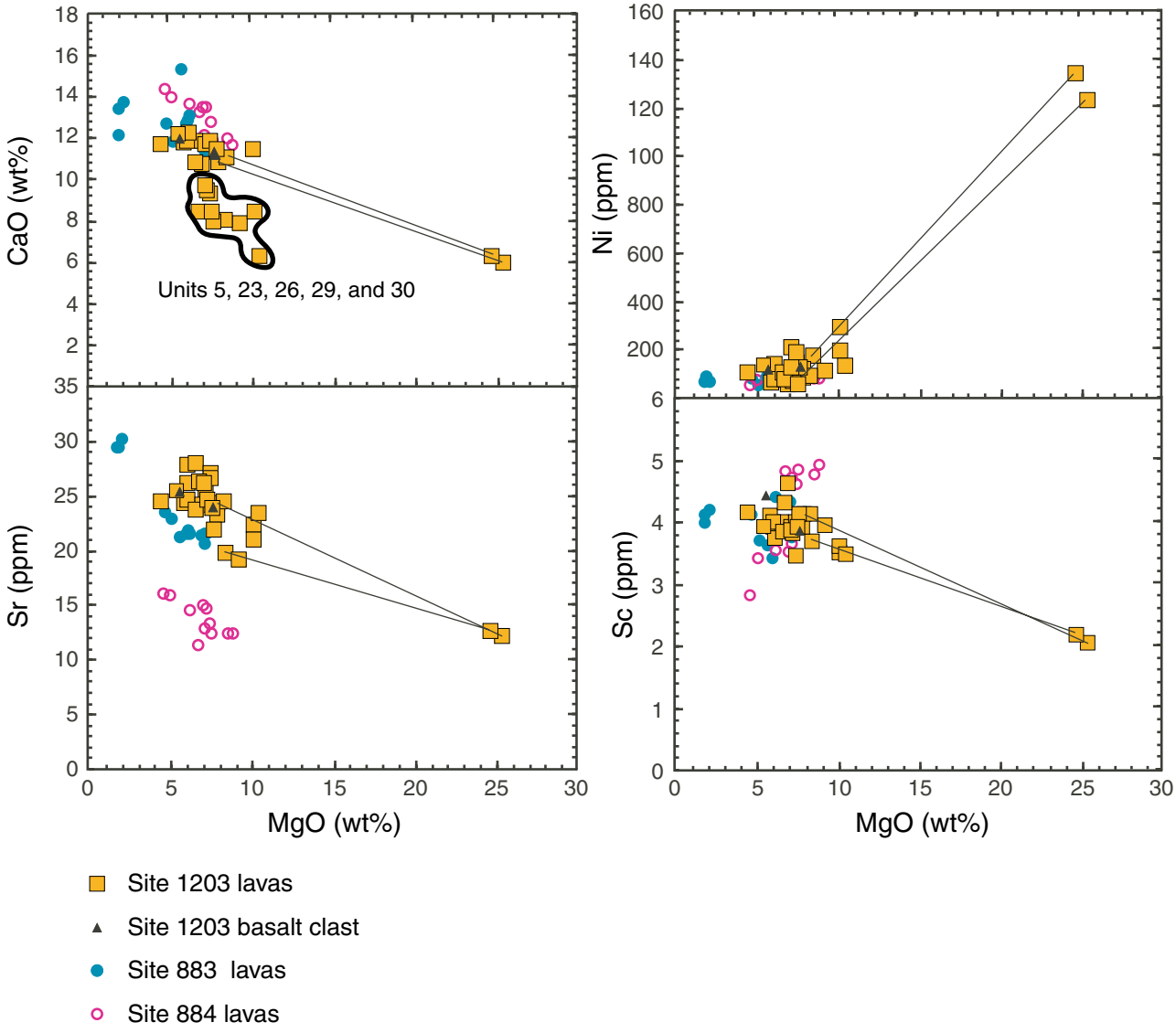

Figure F46. Abundances of TiO_2, P_2O_5, Zr, Sr, and Ba vs. MgO in Detroit Seamount lavas compared to lavas from Mauna Kea and Mauna Loa Volcanoes (only the TiO_2 panel shows the Mauna Loa lavas). Data sources are given in the caption for Figure F42, p. 93. At a given MgO content in the TiO_2, P_2O_5, and Zr panels, Site 884 lavas have much lower abundances of these incompatible elements than lavas from volcanoes on the island of Hawaii. The range of TiO_2 in Hawaiian shield-stage lavas is indicated by the variation from Mauna Loa to Mauna Kea Volcano. Site 883 lavas have slightly lower contents of these elements than the Mauna Loa and Mauna Kea shield-stage lavas. The Site 1203 transitional to tholeiitic lavas, including the two picritic lavas, largely fill the gap between lavas from Sites 883 and 884. In contrast, alkalic basalt from Units 23, 26, 29, and 30 at Site 1203 has high concentrations of these elements and overlaps with the field for postshield-stage lavas from Mauna Kea Volcano. In the Sr and Ba panels, however, this alkalic basalt is not distinguished by higher Ba and Sr contents (except for anomalous Sample 197-1203-51R-4, 93–95 cm). Also see Figure F45, p. 96.

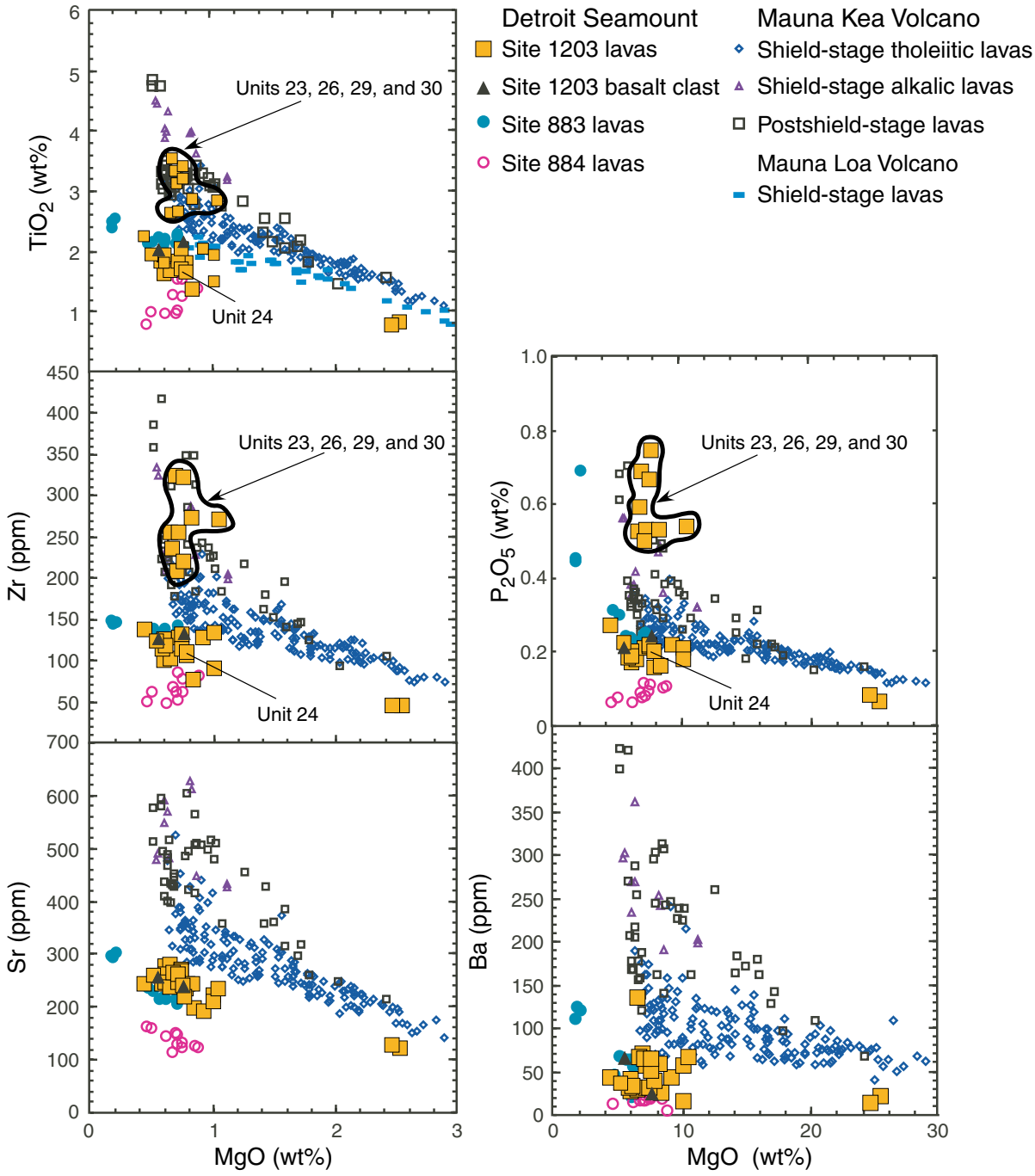

Figure F47. Ti/Zr abundance ratio vs. depth for lavas from Site 1203. The alkalic basalt of Units 23 and 26 near the bottom of the hole has relatively low Ti/Zr ratios. This result contrasts with the classic Hawaiian trend of increasing alkalinity with decreasing eruption age during the transition from shield- to postshield-stage volcanism.

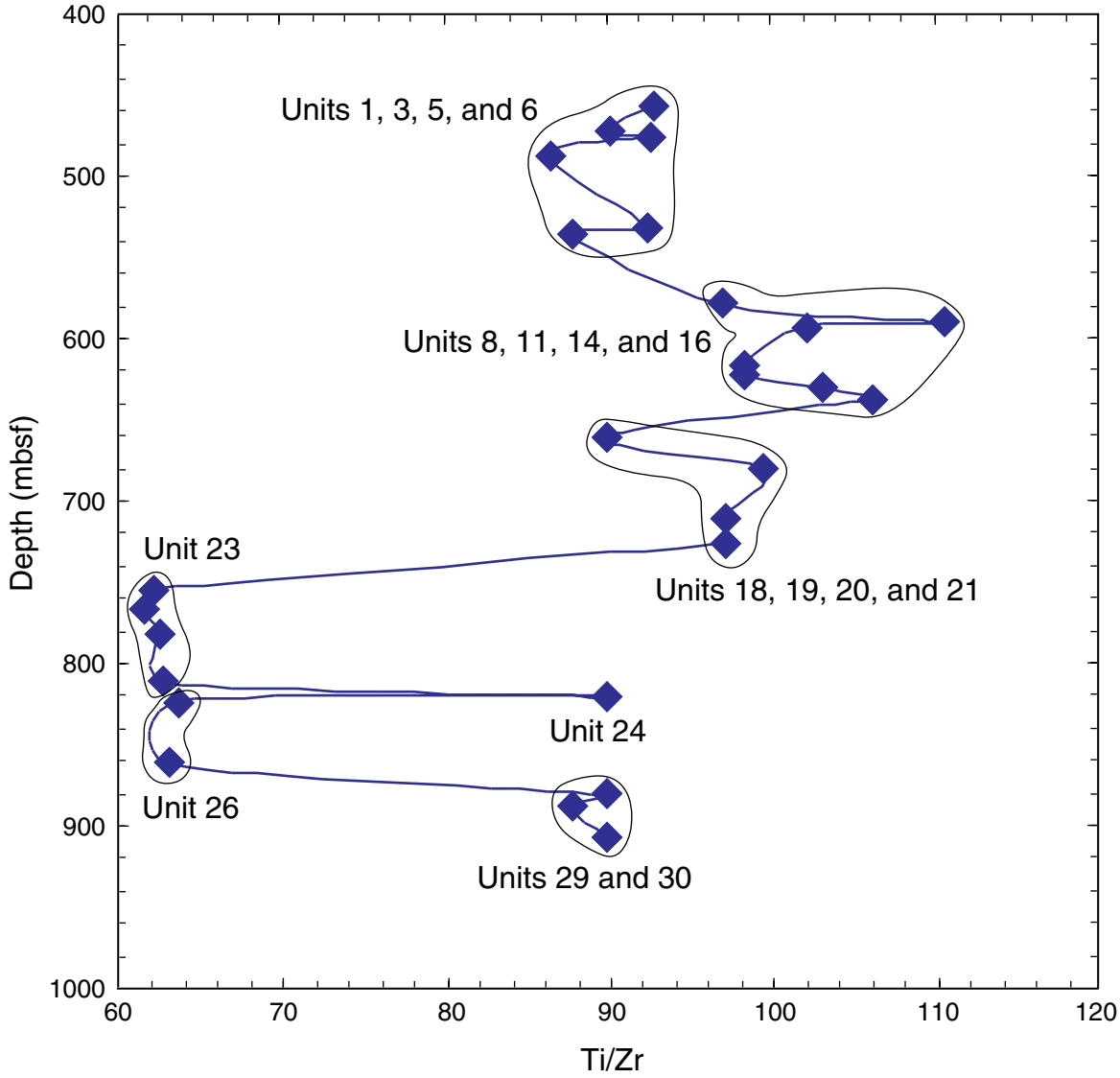

Figure F48. Composite figure showing the occurrence of principal alteration minerals with depth. Blue = basaltic units (labeled), yellow = volcaniclastic units, black curve = degree of alteration from observation in hand specimen. FeOx = Fe oxyhydroxide.

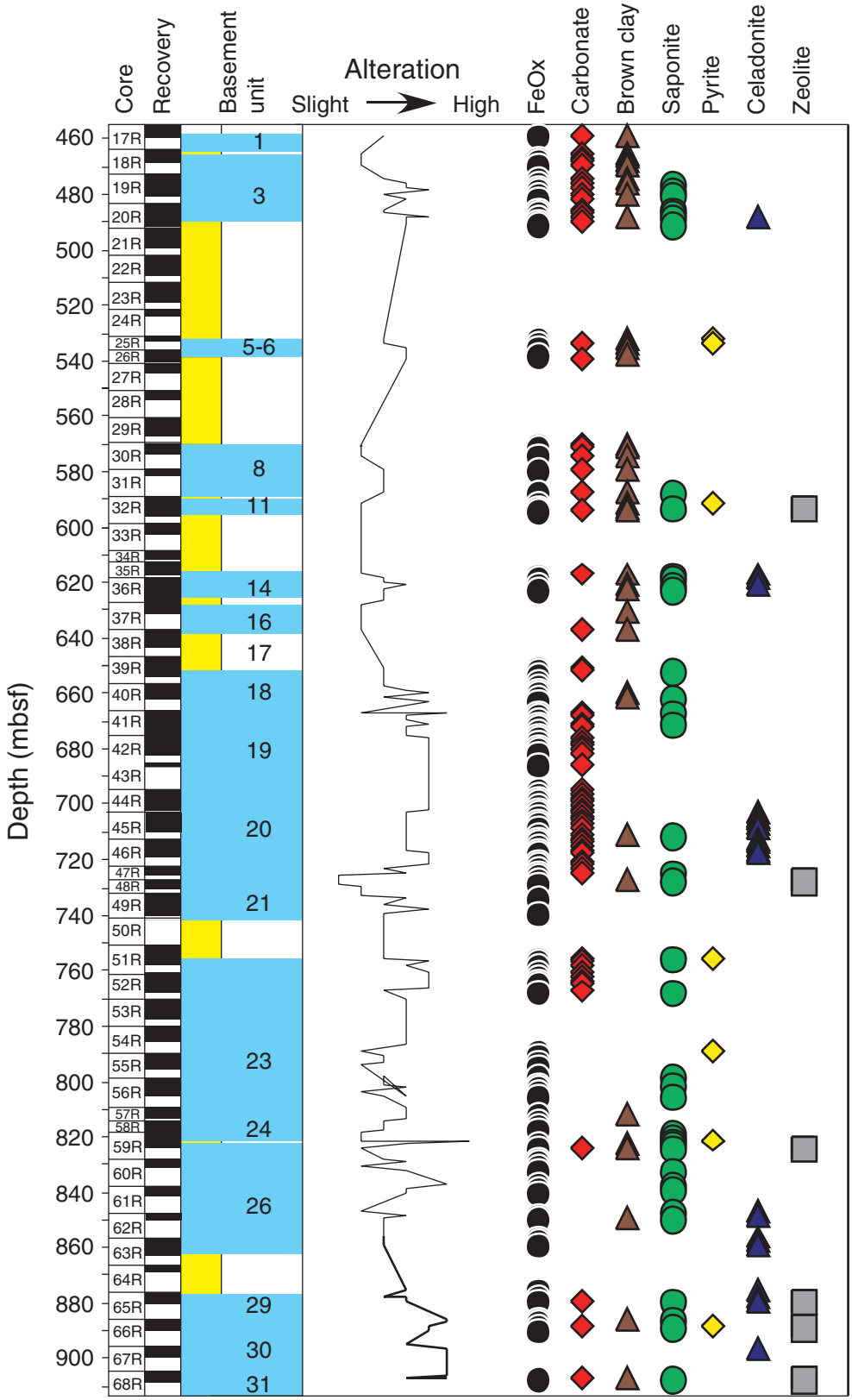

Figure F49. Composite figure showing the vesicle filling with depth. Blue = basaltic units (labeled), yellow = volcaniclastic units, black curve = amount of vesicles from observation in hand specimen.

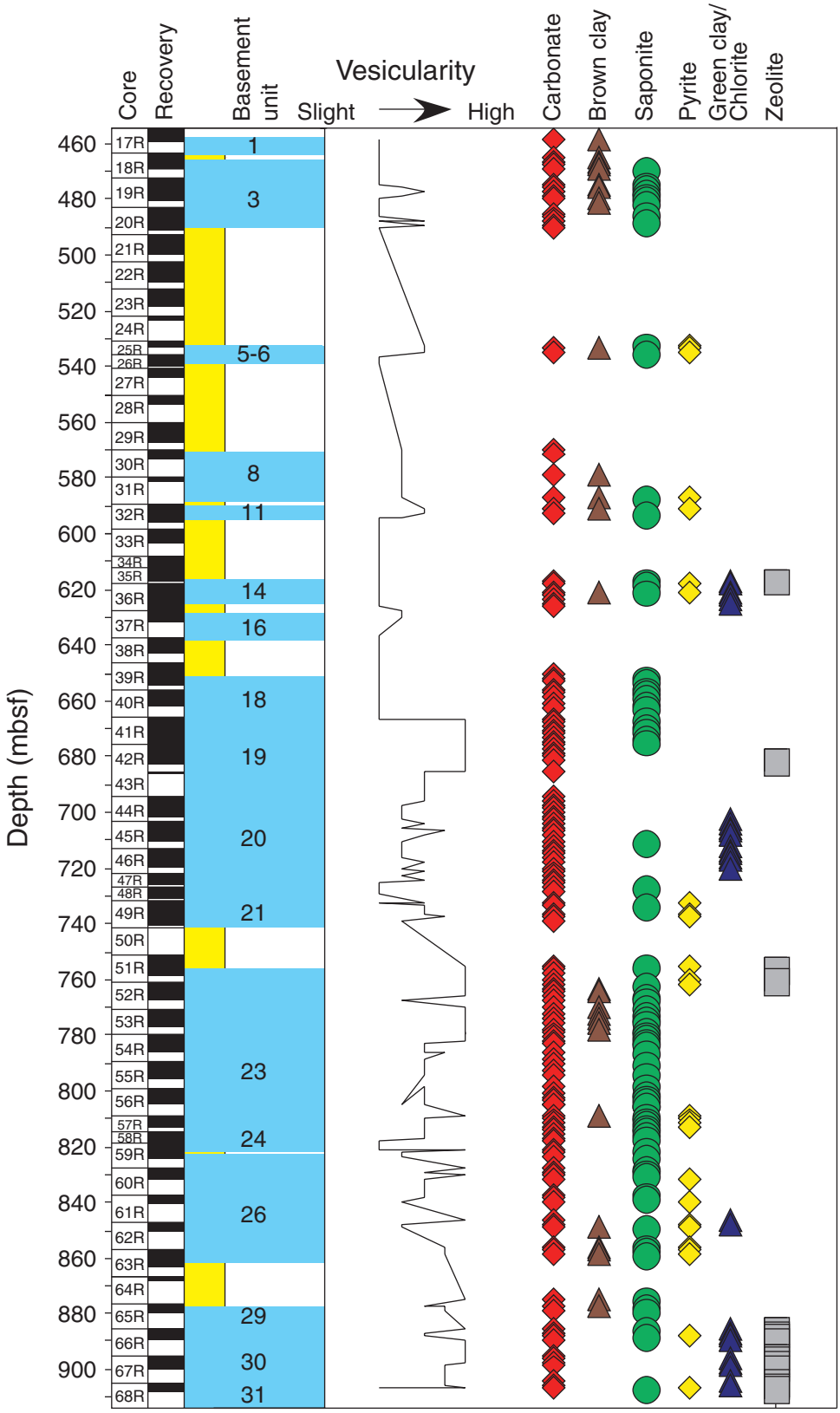

Figure F50. Composite figure showing the vein filling in percent with depth as recorded during observation of split core. Blue = basaltic units (labeled), yellow = volcaniclastic units.

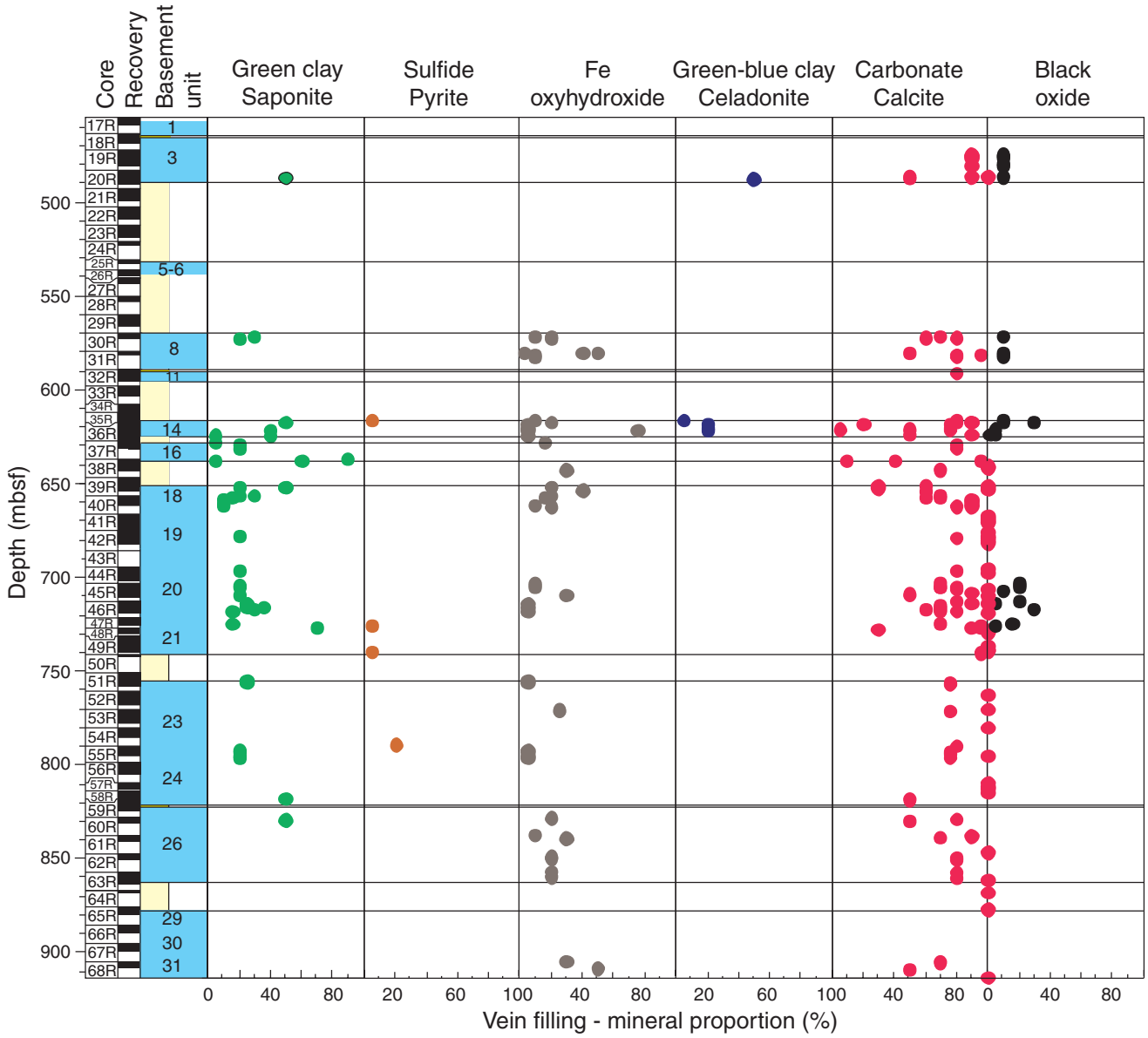

Figure F51. Composite figure showing the vein filling in percent with depth extracted from thin section observation. Blue = basaltic units (labeled), yellow = volcaniclastic units.

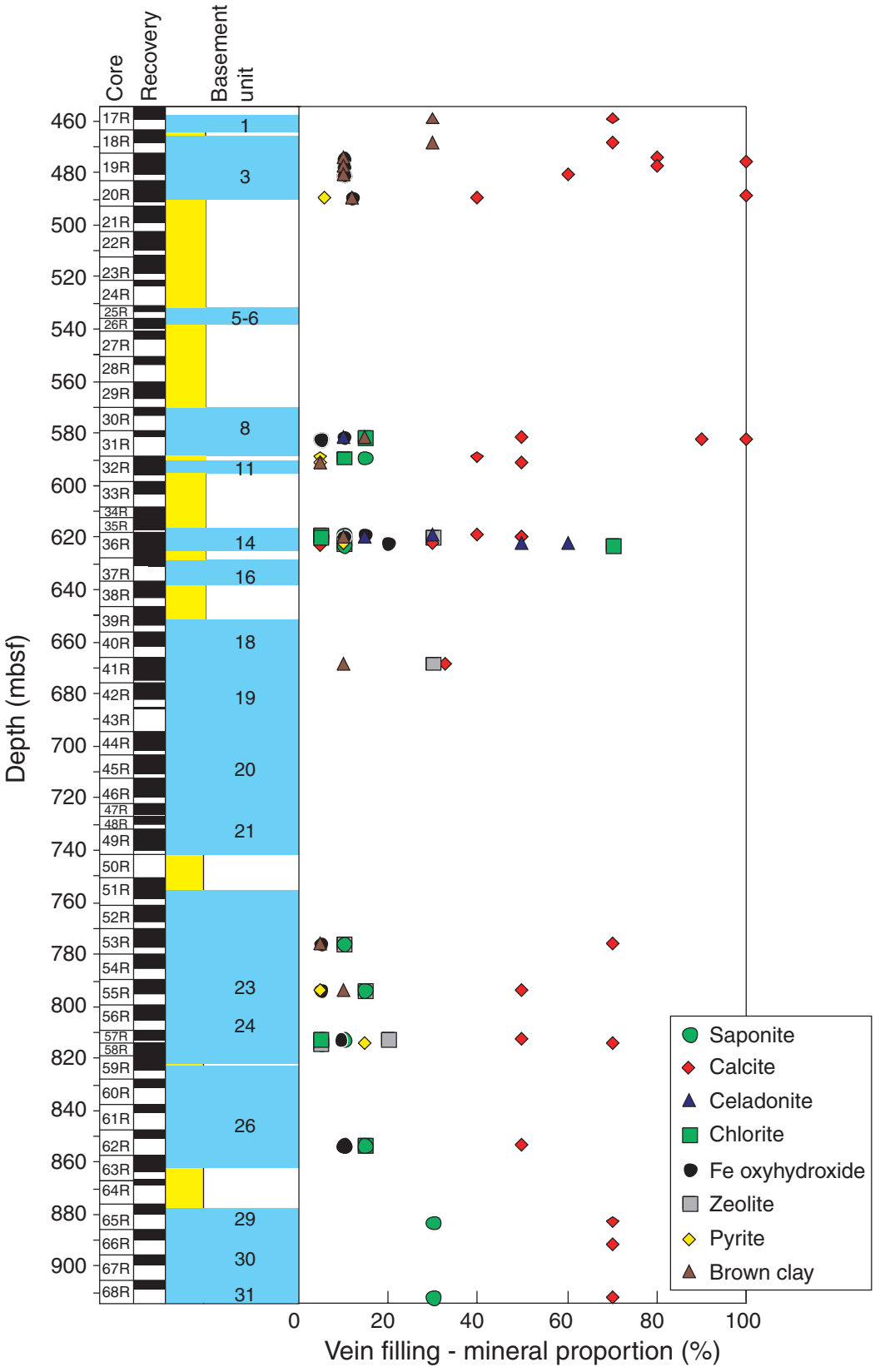

Figure F52. Megavesicle filled with calcite (interval 197-1203A-32R-2, 1–19 cm).

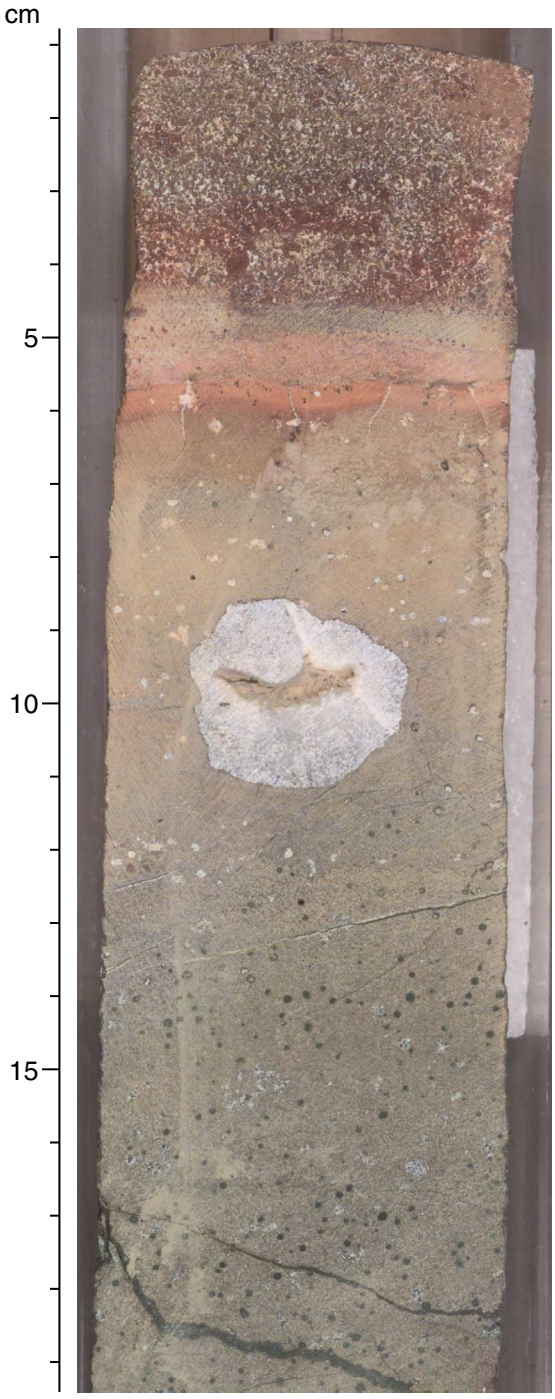

Figure F53. Complex vein filling (interval 197-1203A-36R-2, 121–140 cm).

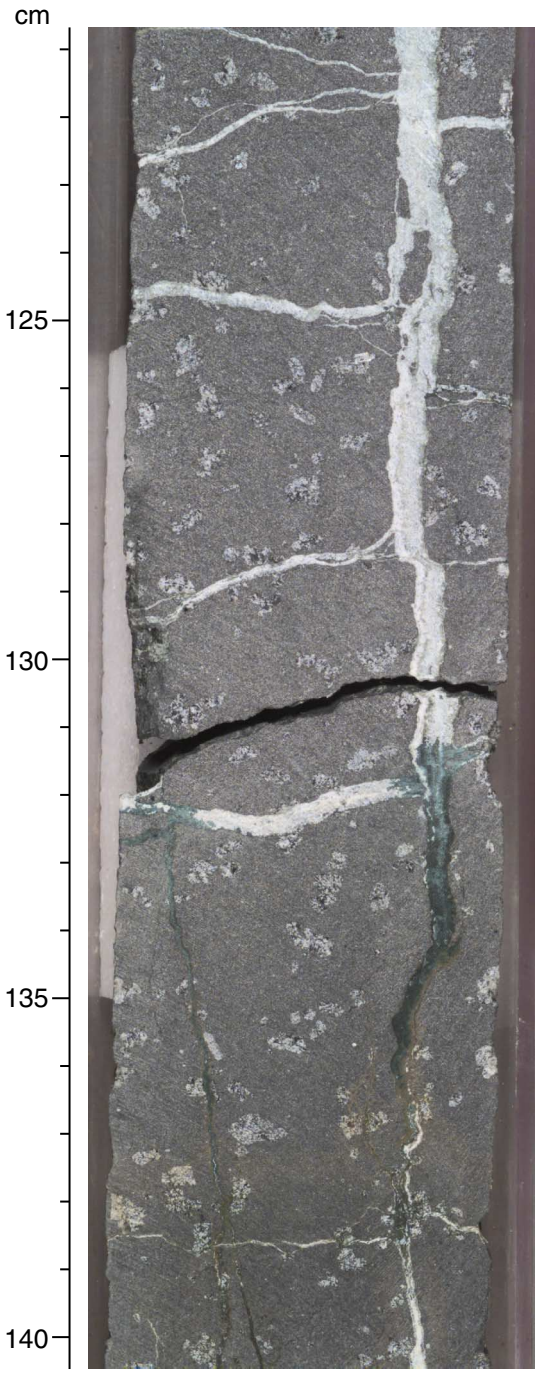

Figure F54. Complex vein filling (interval 197-1203A-36R-3, 33–52 cm).

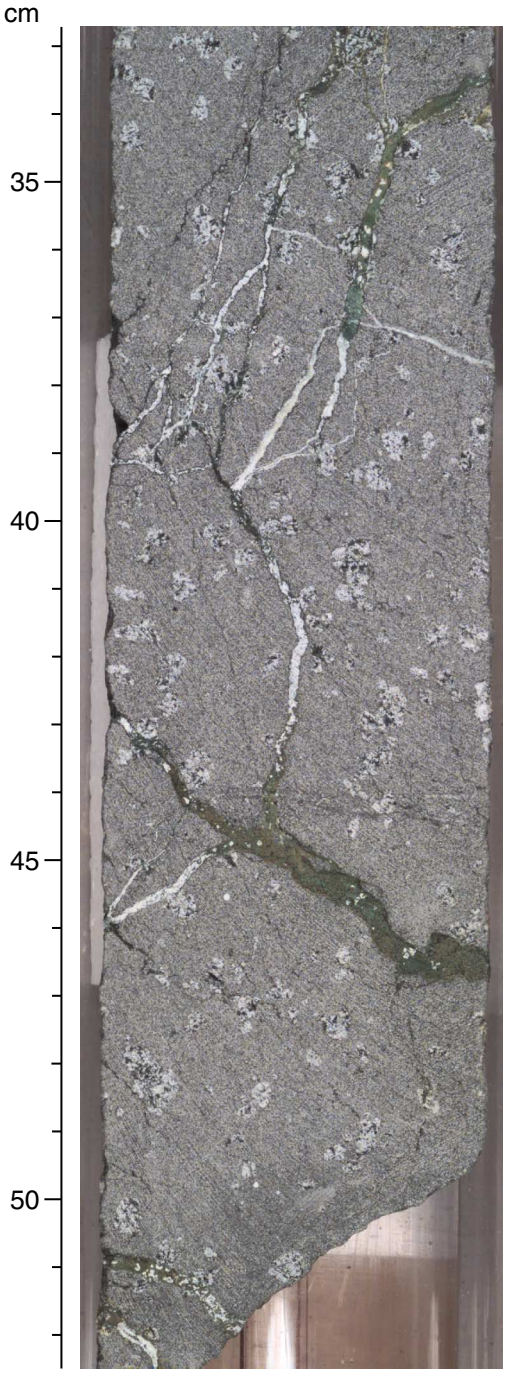

Figure F55. Variations of loss on ignition (LOI), CaO, K_2O, Na_2O, Ba, and Sr with depth. Blue = basaltic units (labeled), yellow = volcaniclastic units.

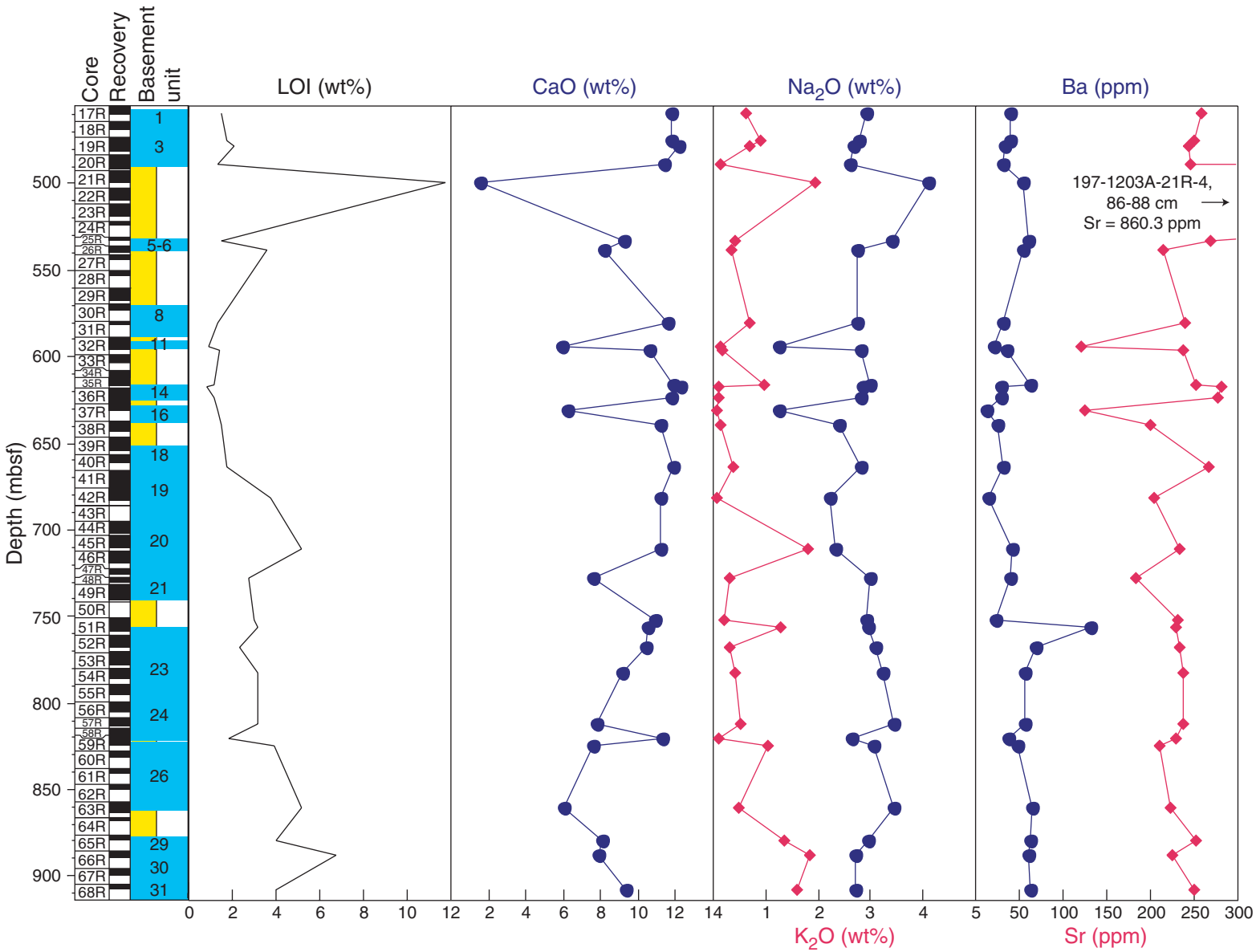

Figure F56. Variations of Zn/Zr, Co/Zr, and Cu/Zr ratios with depth. Blue = basaltic units (labeled), yellow = volcaniclastic units.

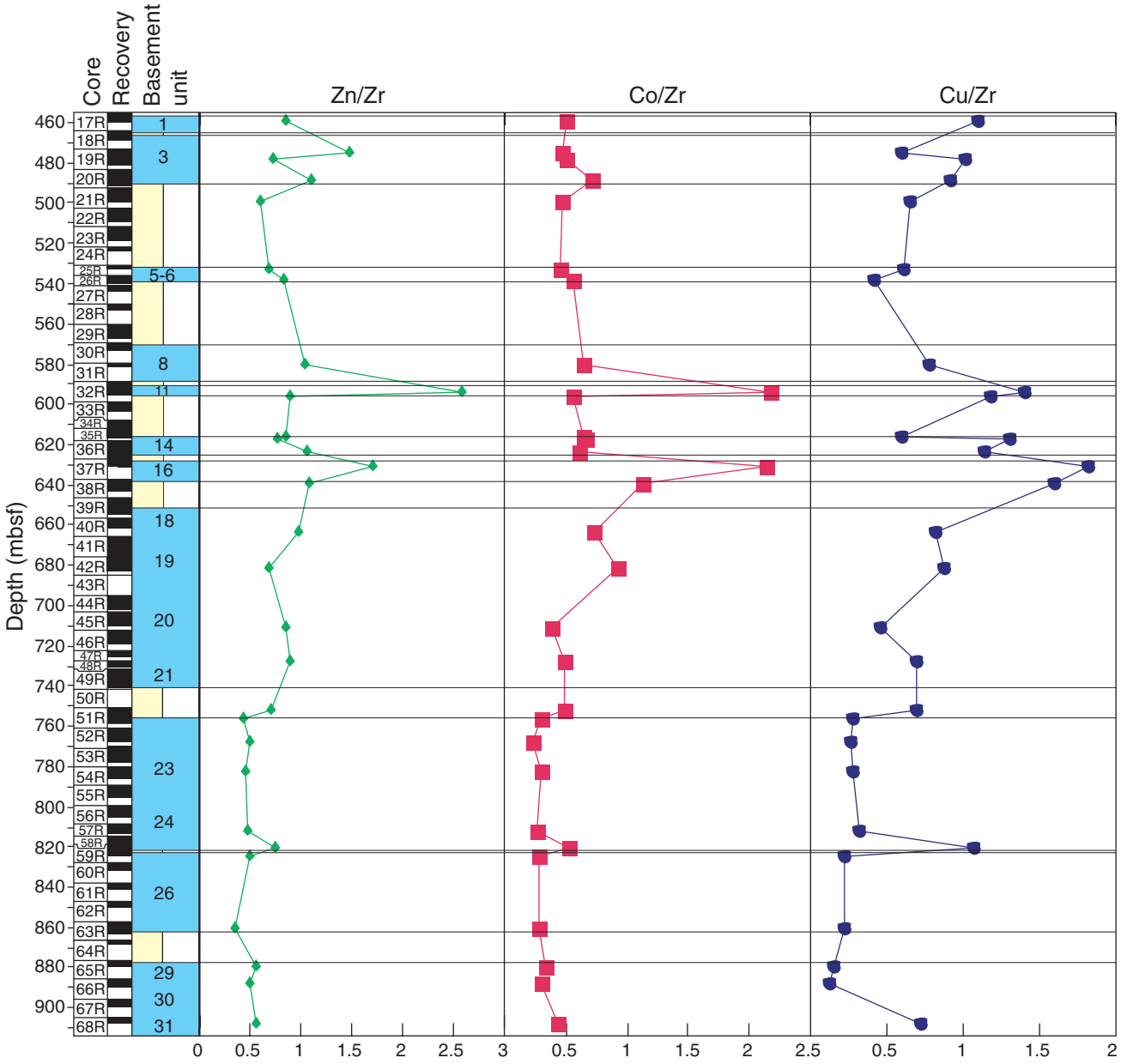

Figure F57. Zr vs. K_2O, Cu, Co, and Zn of Site 1203 samples, Hawaiian lavas (Mauna Kea Volcano and Loihi Seamount), and ODP Sites 883 and 884. Sources of data: Mauna Kea Volcano and Loihi Seamount (Frey et al., 1990, 1991; Macdonald and Katsura, 1964; Rhodes, 1996); ODP Sites 883 and 884 (Rea, Basov, Janecek, Palmer-Julson, et al., 1993; Keller et al., 1995).

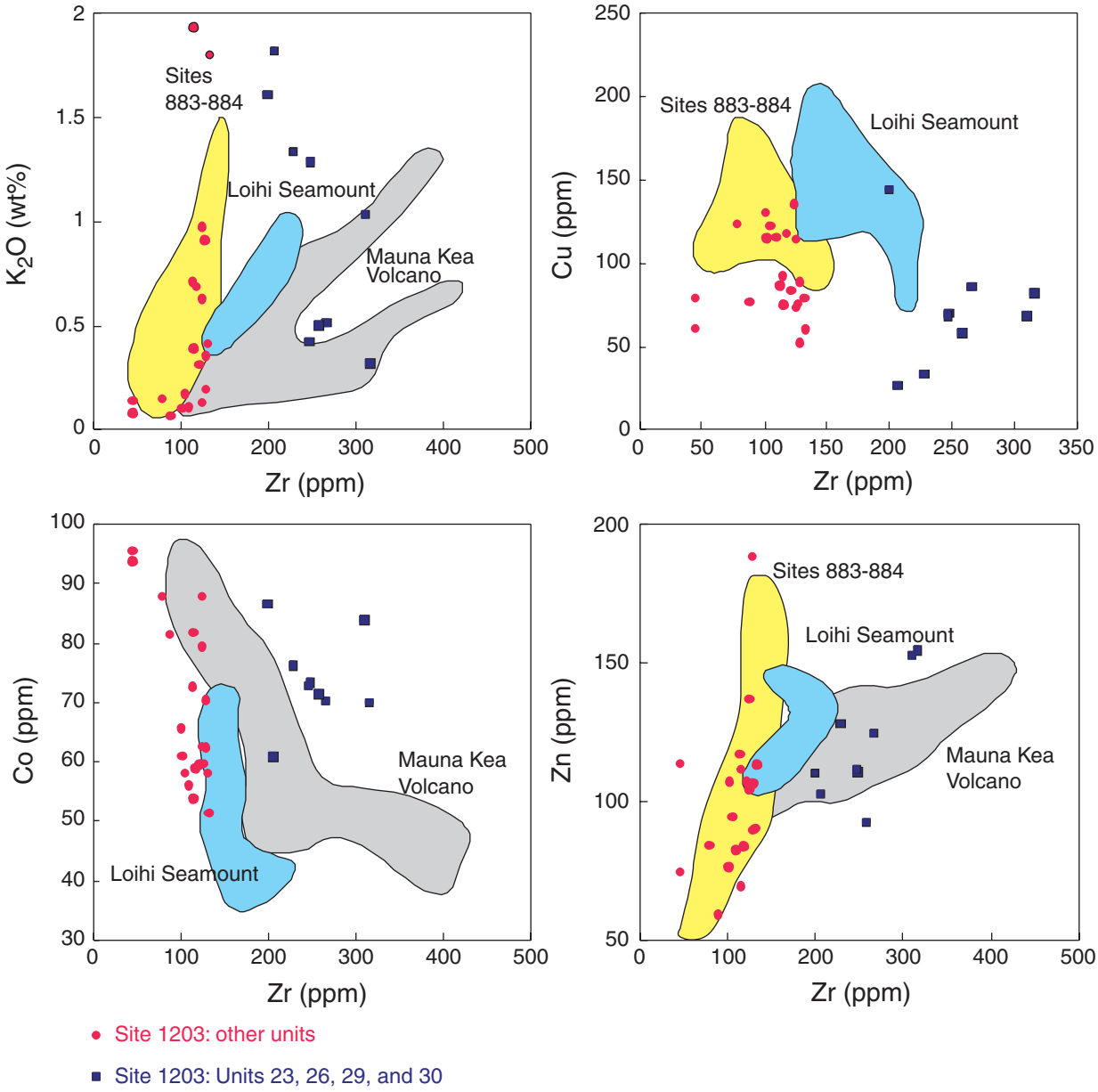

Figure F58. Example orthogonal vector plots for select levels of archive half-round sections of sediment recovered above basement at Site 1203: Samples (**A**) 197-1203A-7R-3, 140 cm, (**B**) 8R-2, 50 cm, (**C**) 11R-2, 45 cm, and (**D**) 12R-3, 85 cm. Open squares = vertical projection of magnetization, solid circles = horizontal projection of magnetization. Labeled data points are alternating-field demagnetization levels. (Continued on next page.)

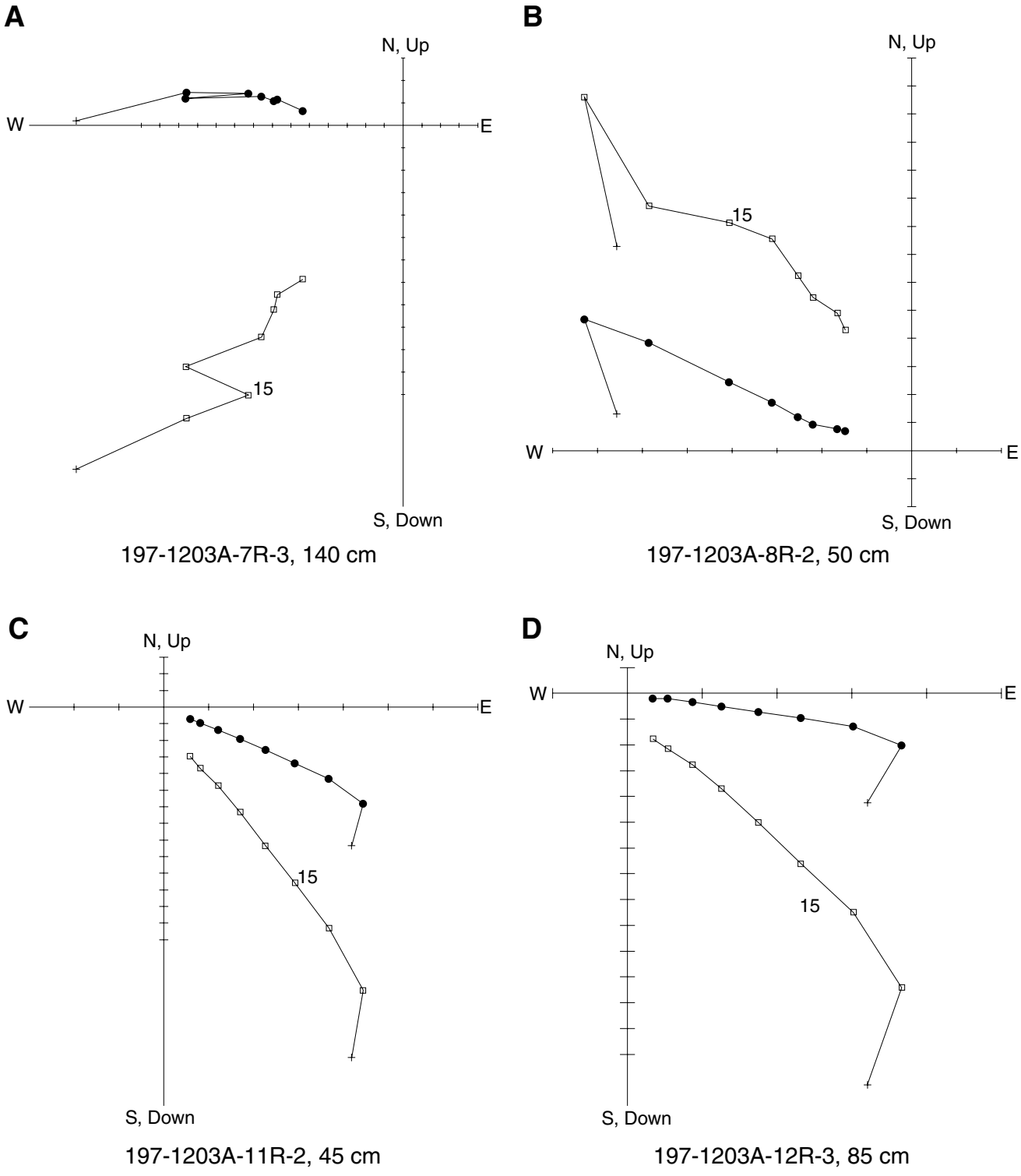

Figure F58 (continued). Samples (**E**) 197-1203A-13R-1, 20 cm, (**F**) 14R-1, 75 cm, (**G**) 15R-3, 115 cm, and (**H**) 17R-1 30 cm.

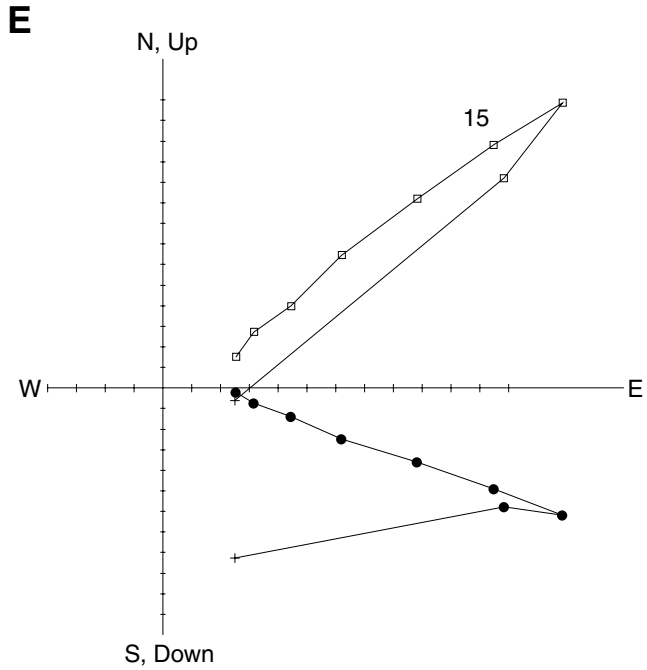

197-1203A-13R-1, 20 cm

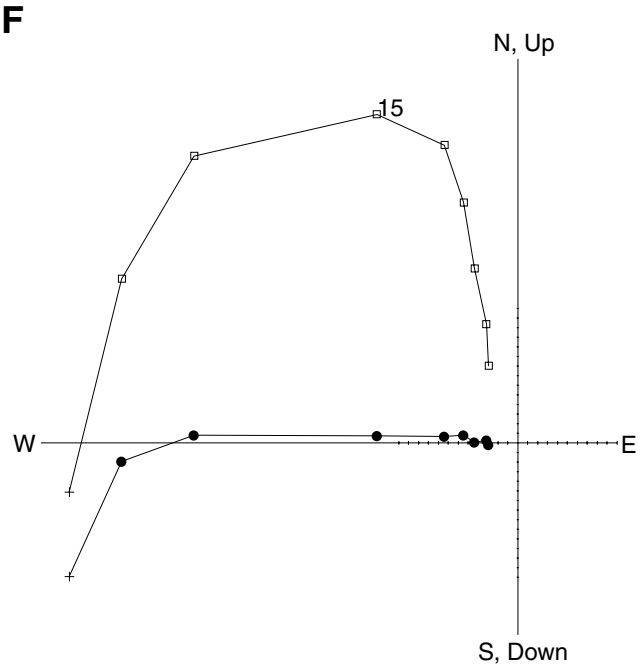

197-1203A-14R-1, 75 cm

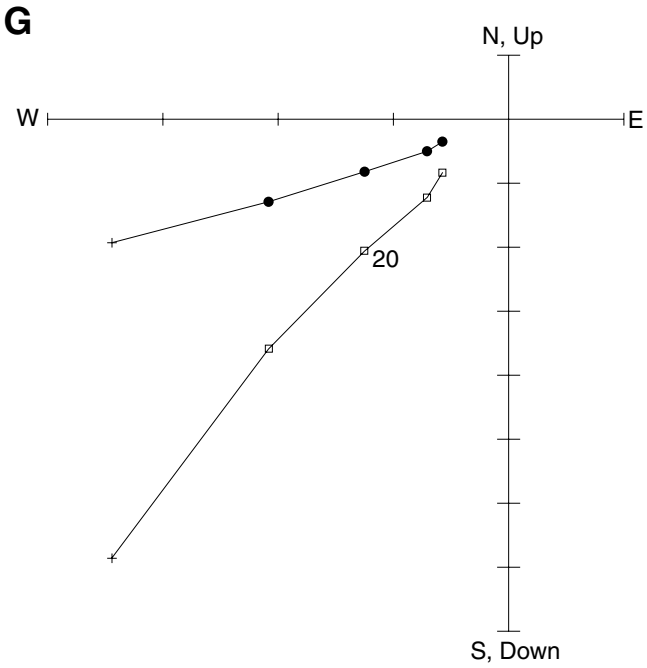

197-1203A-15R-3, 115 cm

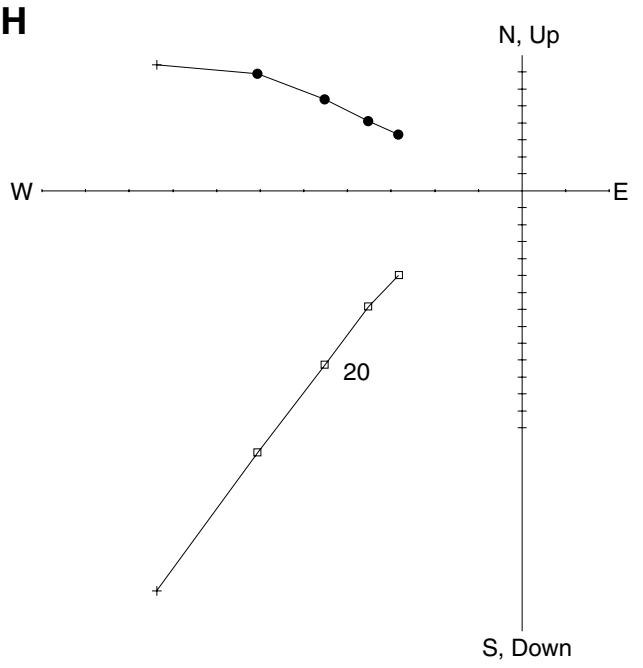

197-1203A-17R-1, 30 cm

Figure F59. Summary polarity column of paleomagnetic inclinations vs. depth. Also shown are tie points linked to geomagnetic polarity for sediment recovered above basement at Site 1203. Geomagnetic polarity timescale is after Cande and Kent (1995). NRM = natural remanent magnetization, AF = alternating field.

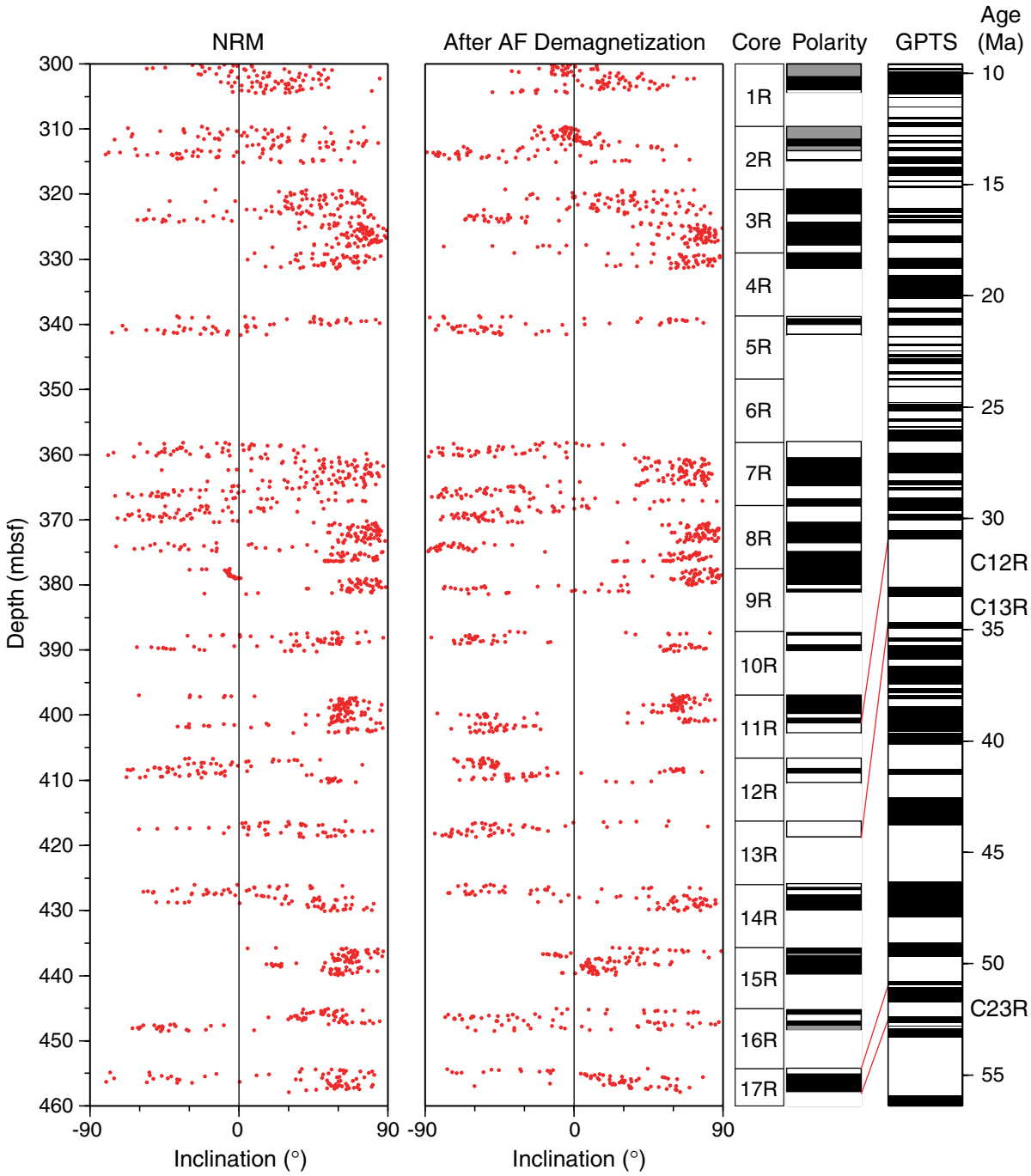

Figure F60. Low-field volume-normalized (bulk) magnetic susceptibility, Koenigsberger ratio, and median destructive field (MDF) vs. depth. Open circles = data from basalt samples, solid circles = data from volcaniclastic sediment samples. Also shown is the generalized basement stratigraphy and basement unit number.

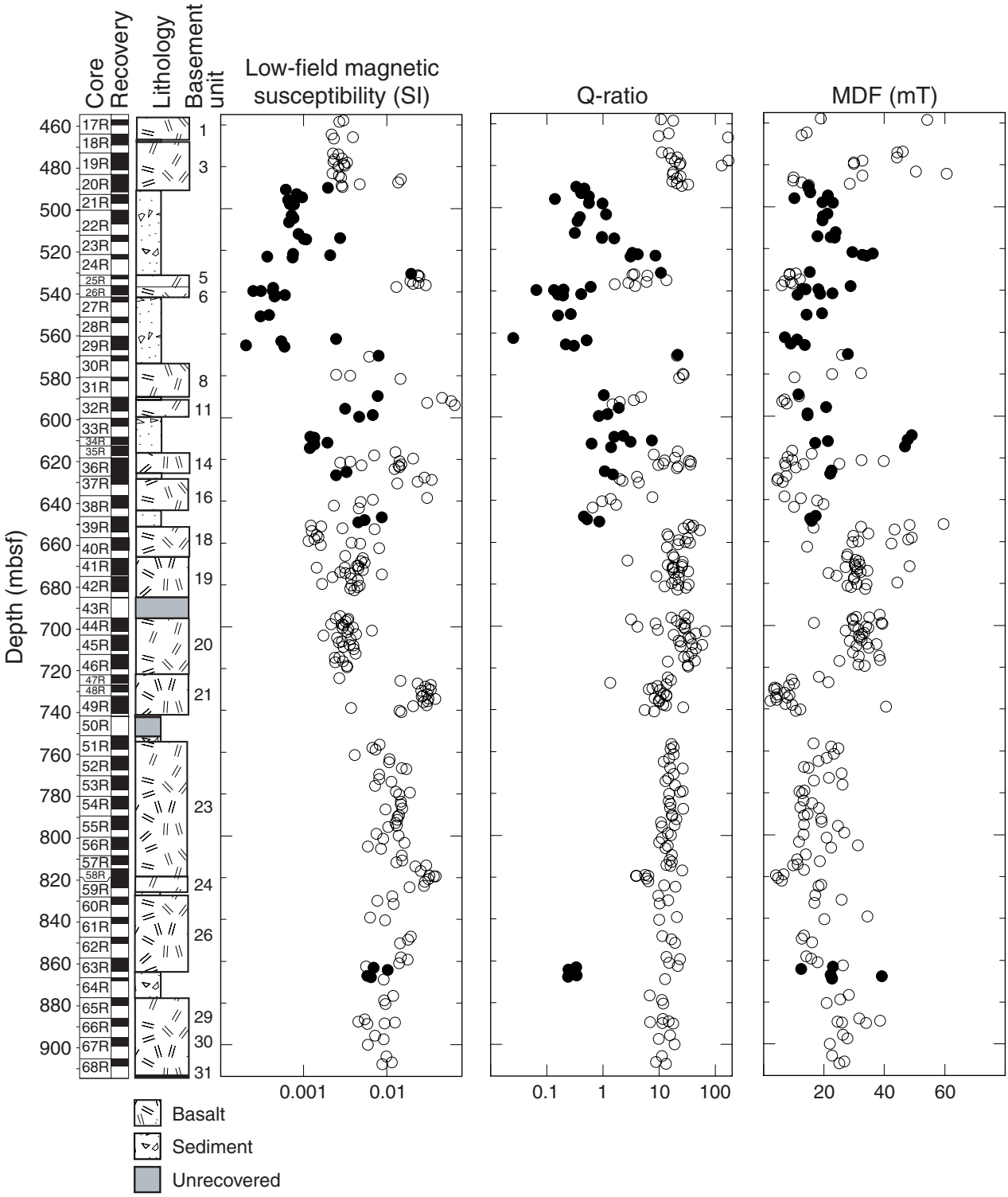

Figure F61. The log of low-field volume-normalized magnetic susceptibility plotted vs. the natural remanent magnetization (NRM) measured prior to demagnetization. Open circles = data from basalt samples, solid circles = data from volcaniclastic sediment samples.

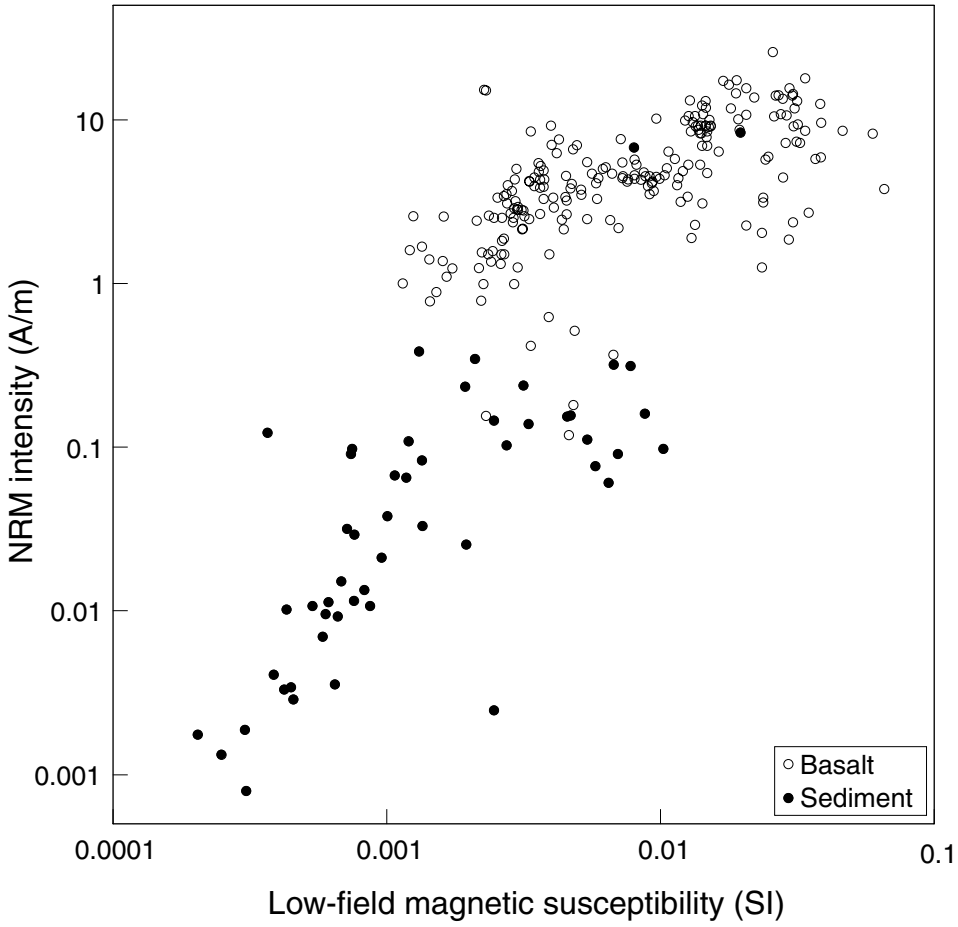

Figure F62. Plot of the log of low-field volume-normalized magnetic susceptibility and median destructive field. Open circles = data from basalt samples, solid circles = data from volcaniclastic sediment samples.

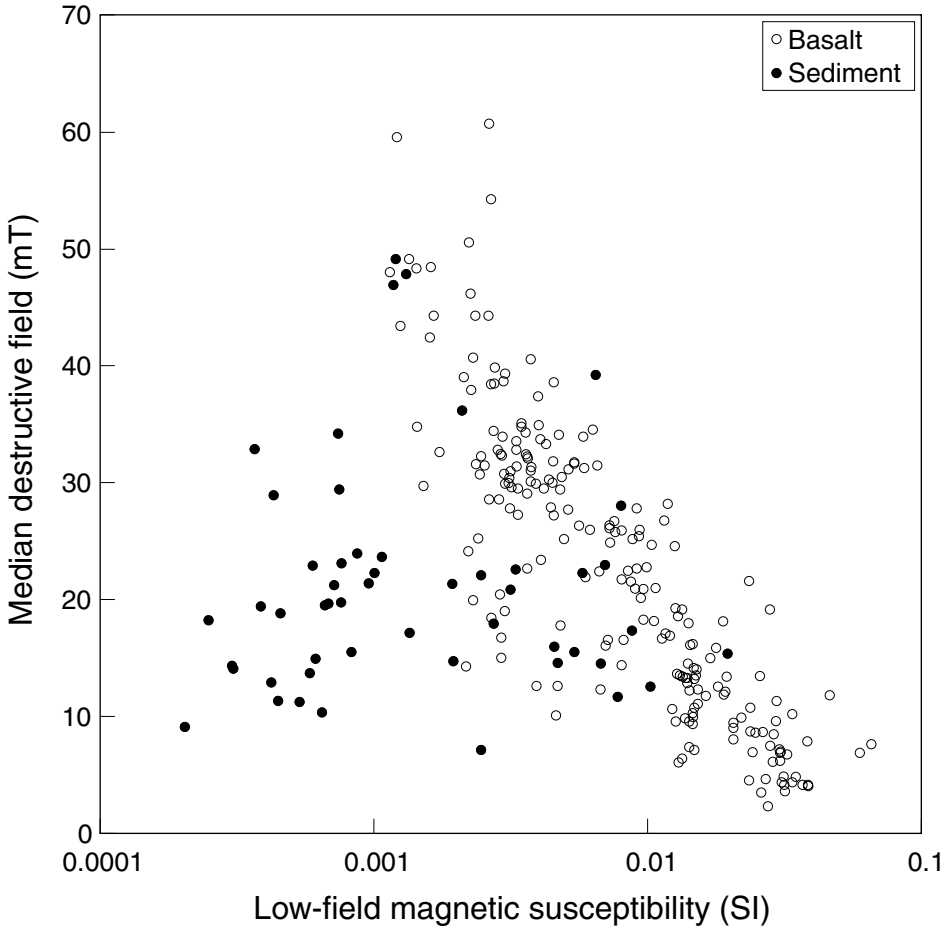

Figure F63. Examples of Lowrie-Fuller (1971) tests conducted on basalt from Site 1203. ARM = anhysteretic remanent magnetization, IRM = isothermal remanent magnetization.

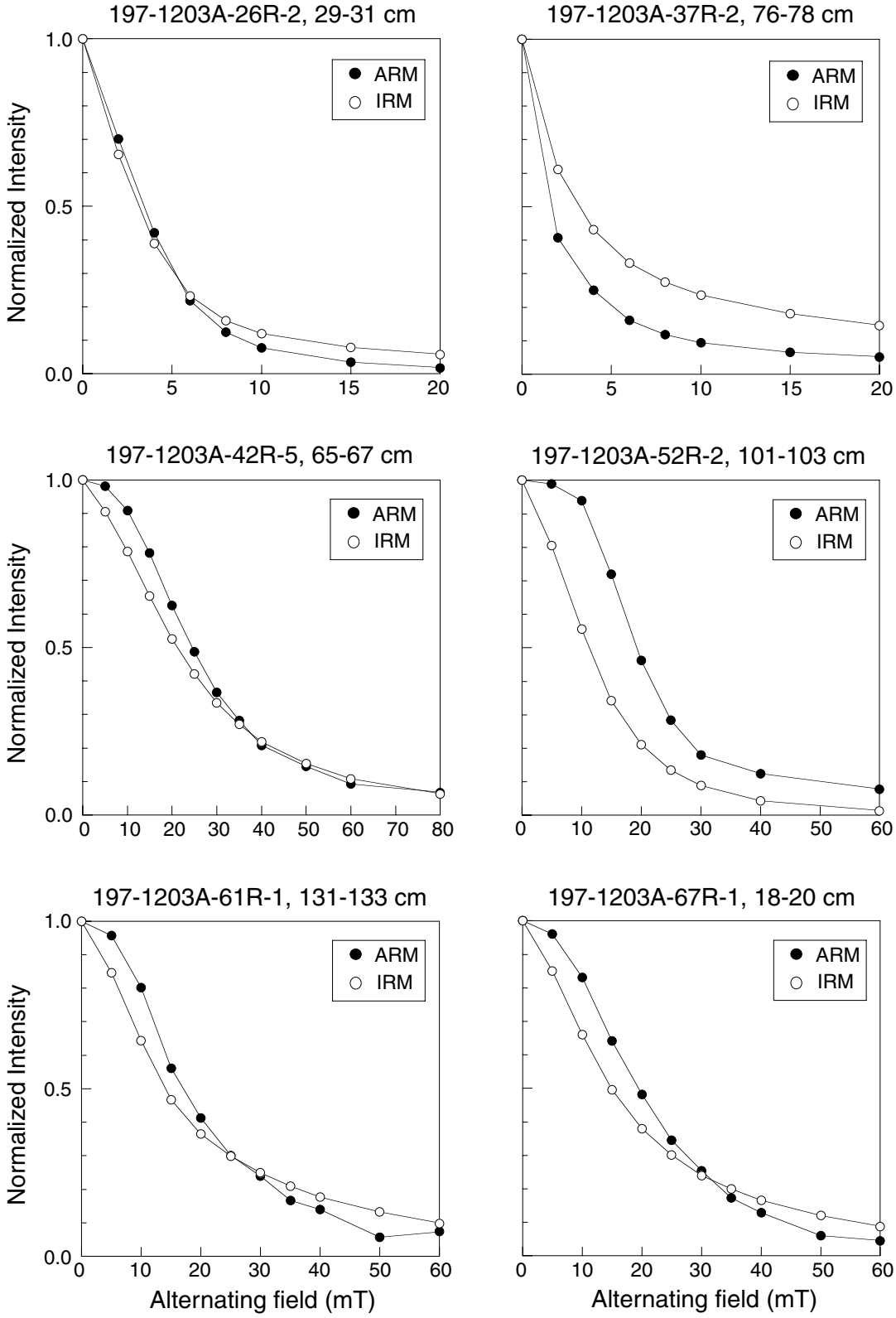

Figure F64. Example orthogonal vector plots showing well-defined, stable magnetic behavior recorded by basalt samples: Samples (**A**) 197-1203A-25R-1, 29–31 cm, (**B**) 26R-1, 75–77 cm, (**C**) 31R-1, 65–67 cm, and (**D**) 36R-3, 60–62 cm. Open squares = vertical projection of magnetization, solid circles = horizontal projection of magnetization. (Continued on next page.)

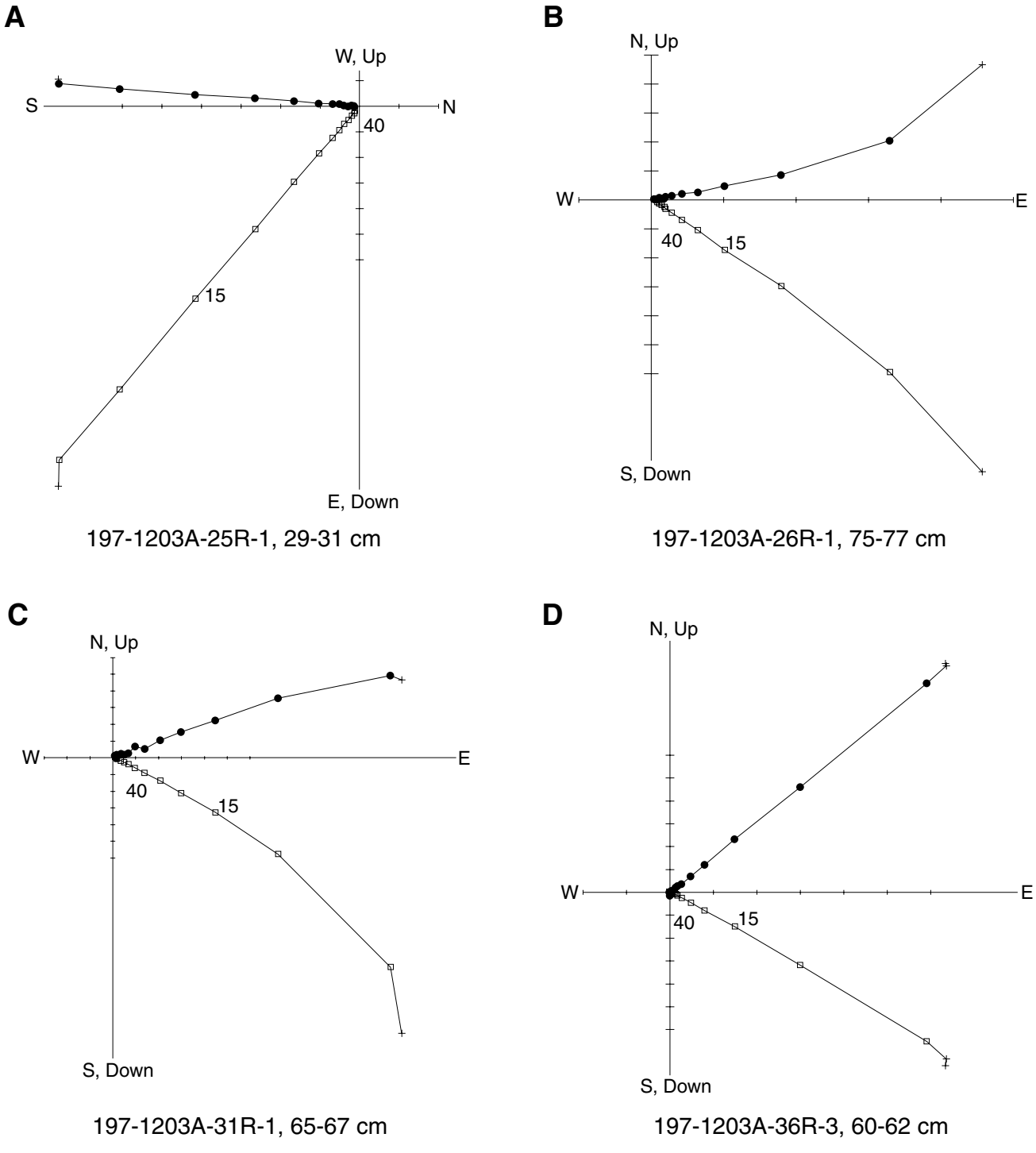

Figure F64 (continued). Samples (**E**) 197-1203A-37R-3, 113–115 cm, (**F**) 47R-4, 18–20 cm, (**G**) 55R-5, 17–19 cm, and (**H**) 59R-4, 124–126 cm.

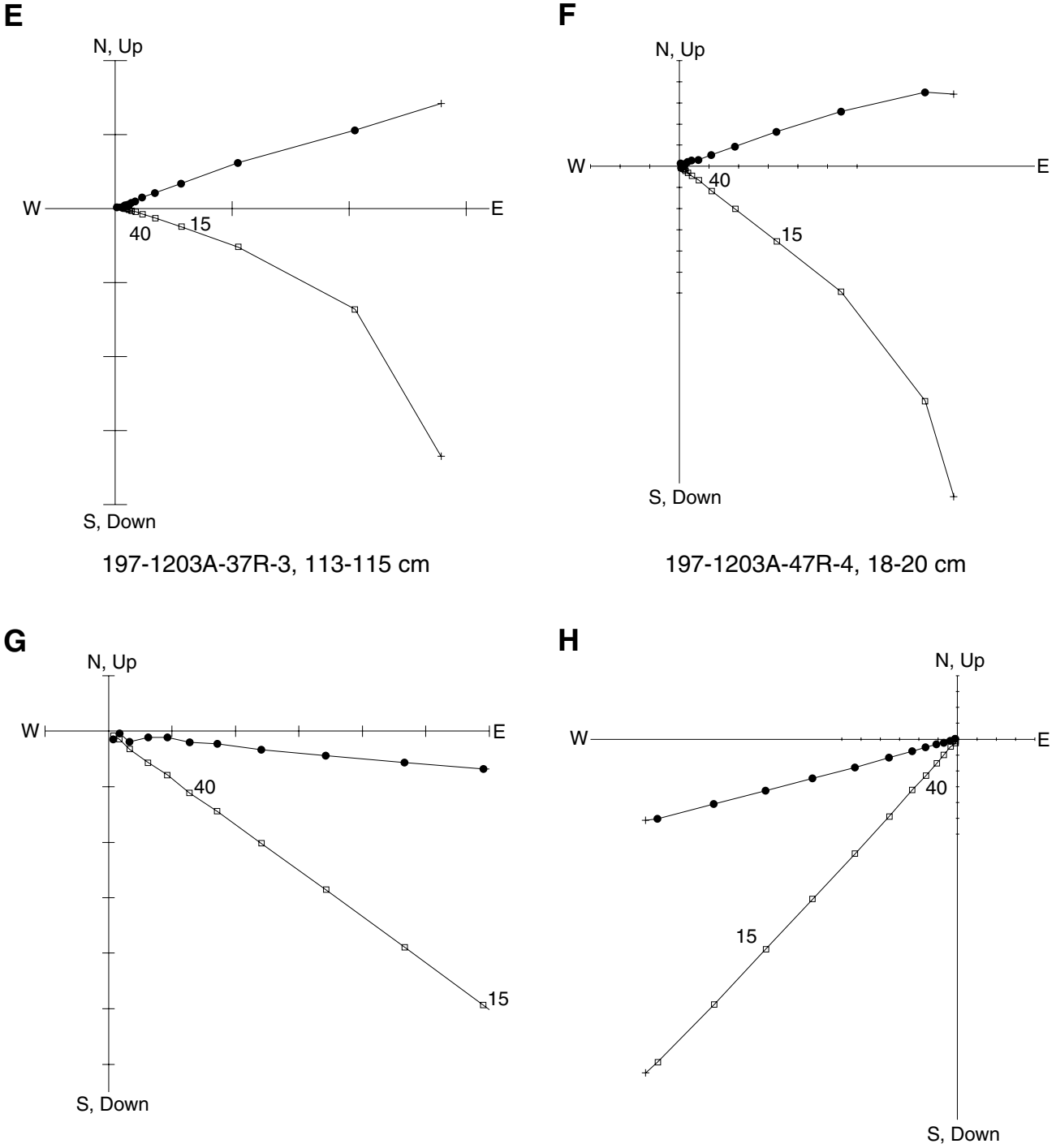

Figure F65. Example orthogonal vector plots showing well-defined, stable magnetic behavior recorded by volcaniclastic sediment samples: Samples (**A**) 197-1203A-24R-1, 30–32 cm, (**B**) 38R-2, 77–79 cm, (**C**) 38R-4, 94–96 cm, and (**D**) 63R-5, 127–129 cm. Open squares = vertical projection of magnetization, solid circles = horizontal projection of magnetization.

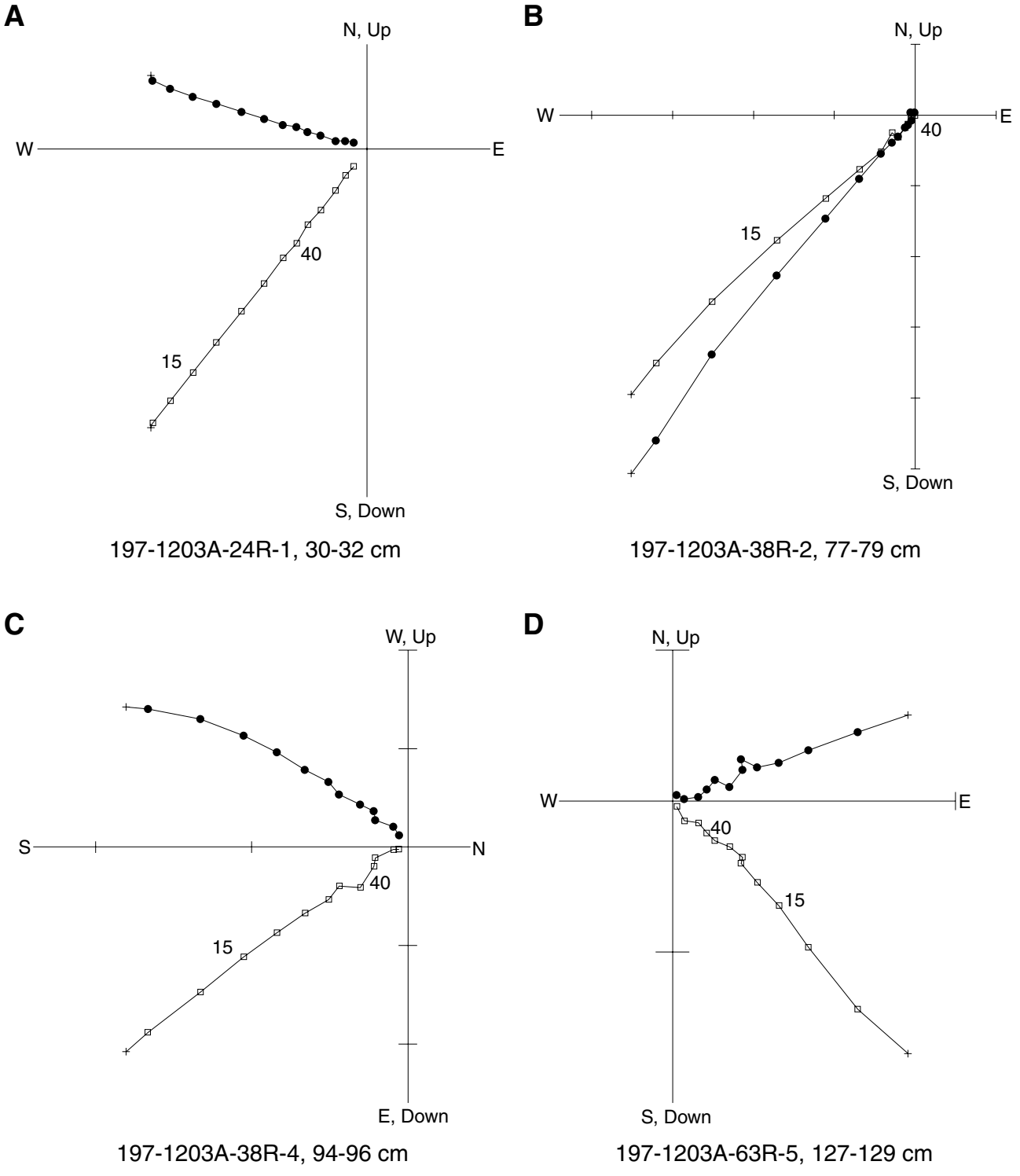

Figure F66. Example orthogonal vector plots showing less well-defined magnetic components recorded by basalt and volcaniclastic sediment samples: Samples (**A**) 197-1203A-60R-1, 86–88 cm, (**B**) 19R-1, 95–97 cm, (**C**) 20R-6, 18–20 cm, and (**D**) 22R-4, 19–21 cm. Open squares = vertical projection of magnetization, solid circles = horizontal projection of magnetization.

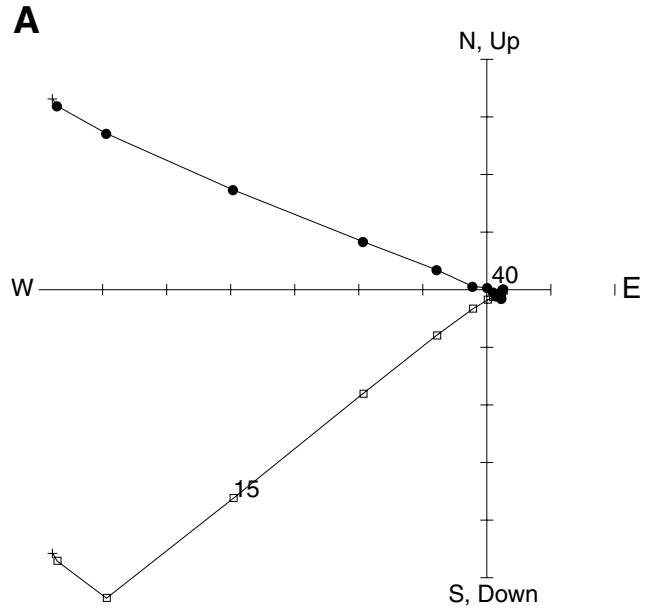

197-1203A-60R-1, 86-88 cm

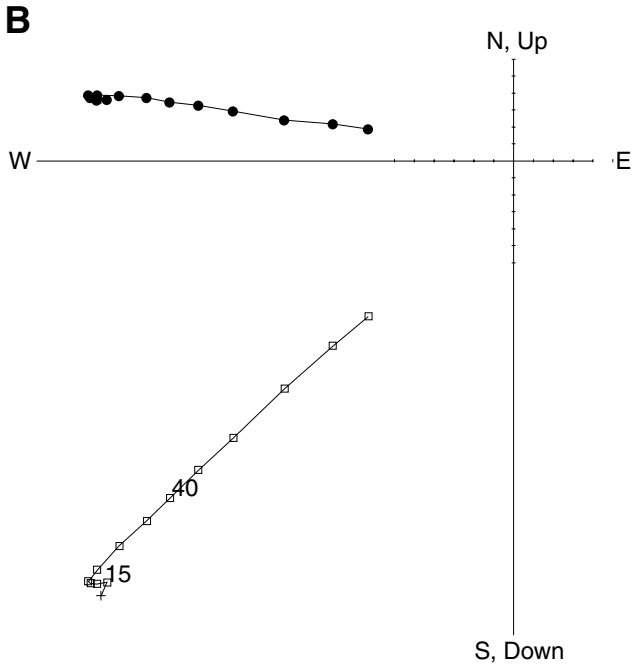

197-1203A-19R-1, 95-97 cm

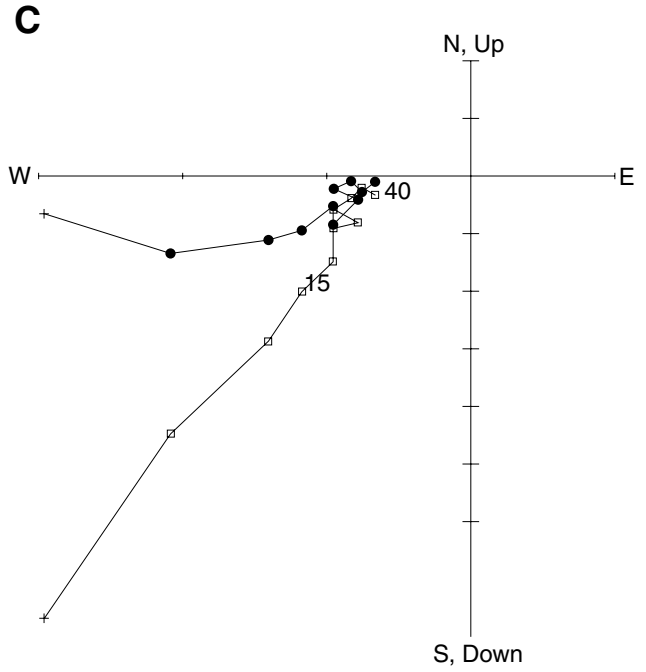

197-1203A-20R-6, 18-20 cm

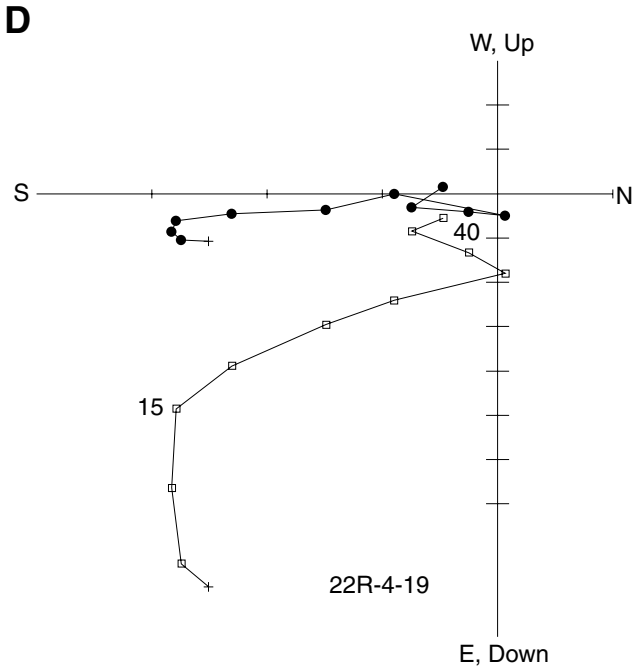

197-1203A-22R-4, 19-21 cm

Figure F67. Example orthogonal vector plots derived from coarse volcaniclastic sediment (breccia) used for a modified conglomerate test: Samples (**A**) 197-1203A-34R-1, 89–91 cm, (**B**) 34R-2 34–36 cm, (**C**) 34R-3, 135–137 cm, and (**D**) 34R-3, 79–81 cm. Open squares = vertical projection of magnetization, solid circles = horizontal projection of magnetization.

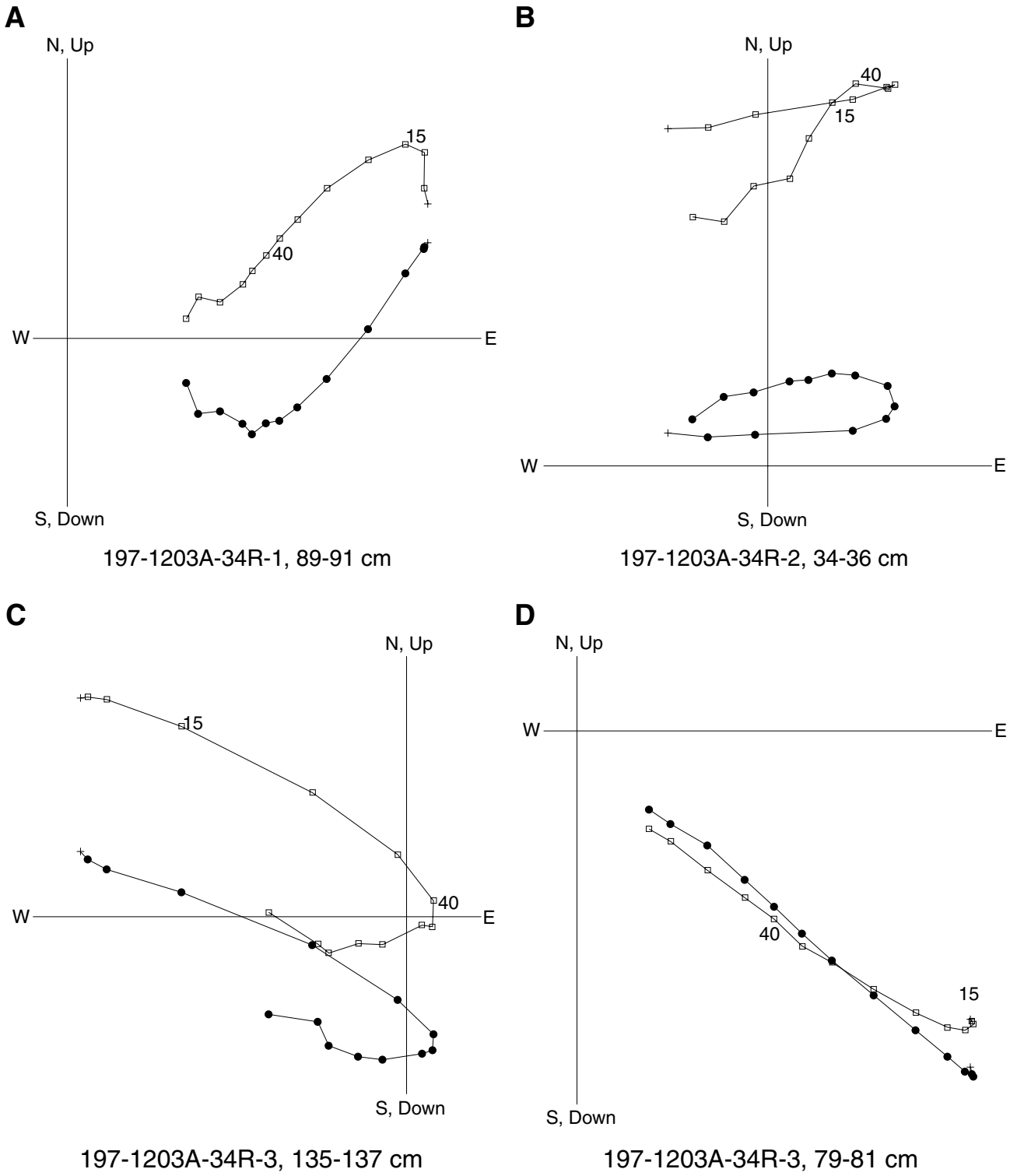

Figure F68. Histogram of inclination values derived from principal component analyses of alternating-field demagnetization data of volcaniclastic sediment samples. ΔI = difference between the inclination of Hawaii and that of Detroit Seamount, Δλ = difference in the latitude of Hawaii and the formative paleolatitude of Detroit Seamount.

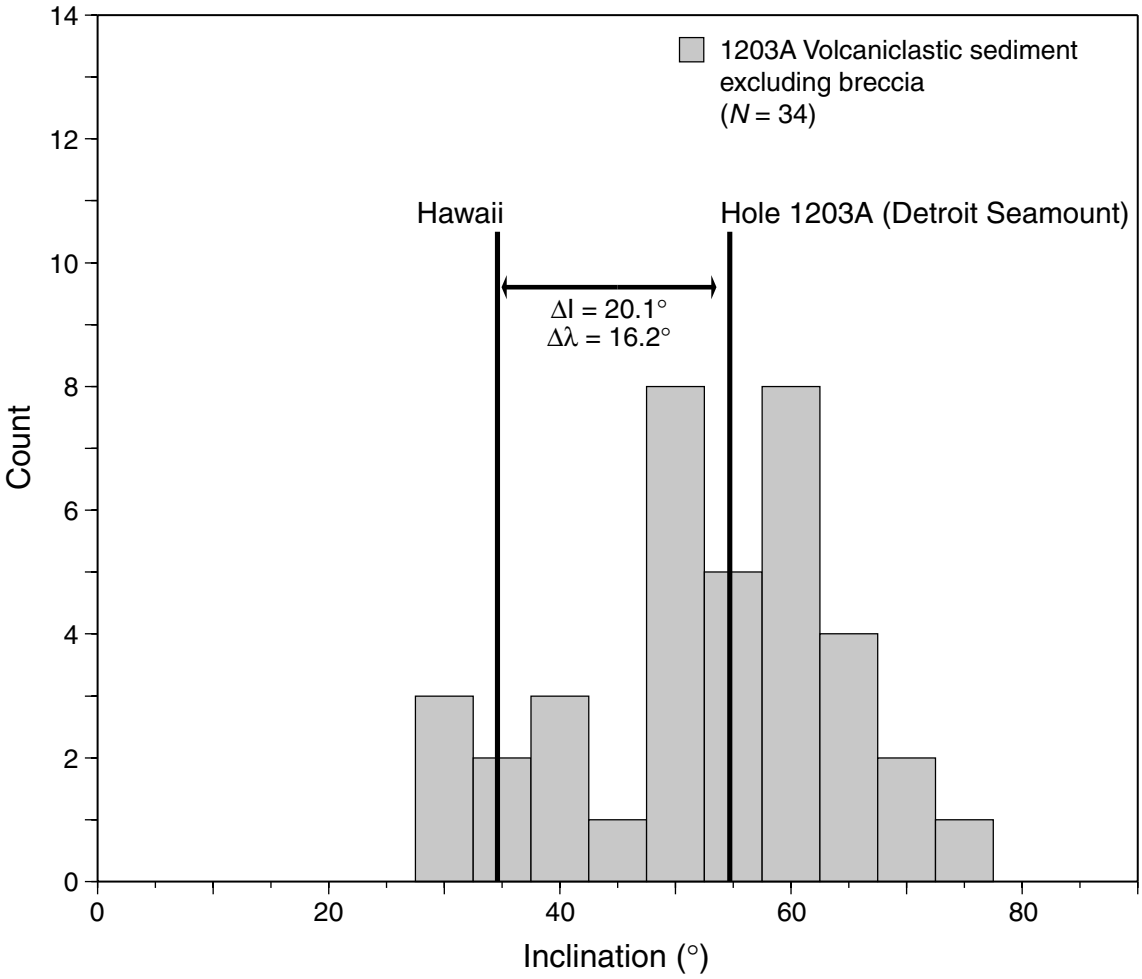

Figure F69. Histogram of inclination values derived from principal component analyses of basalt composing basement. ΔI = difference between the inclination of Hawaii and that of Detroit Seamount, Δλ = difference in the latitude of Hawaii and the formative paleolatitude of Detroit Seamount.

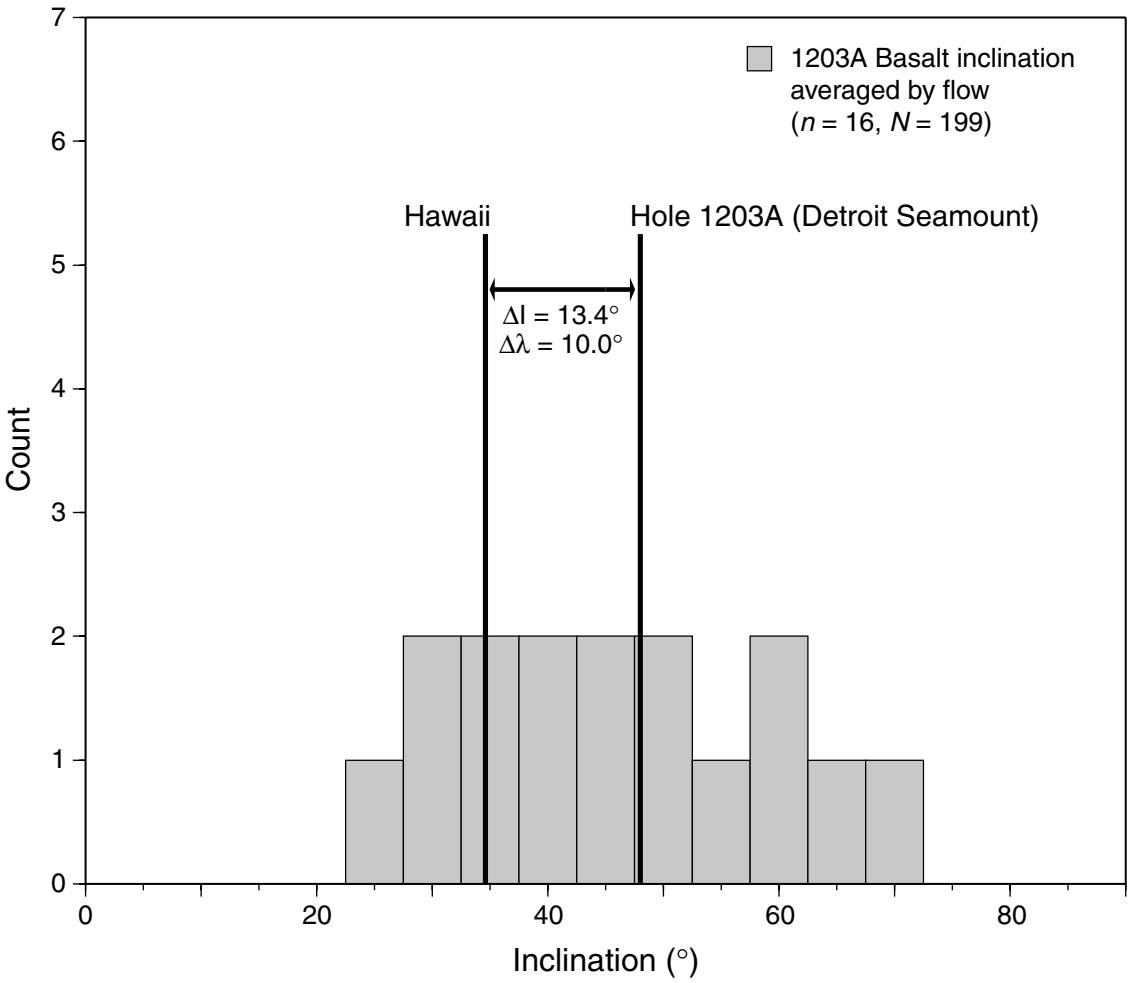

Figure F70. Histogram of inclination values derived from principal component analyses of volcaniclastic sediment samples recovered at Site 1203 compared to a synthetic Fisher distribution (Fisher, 1953).

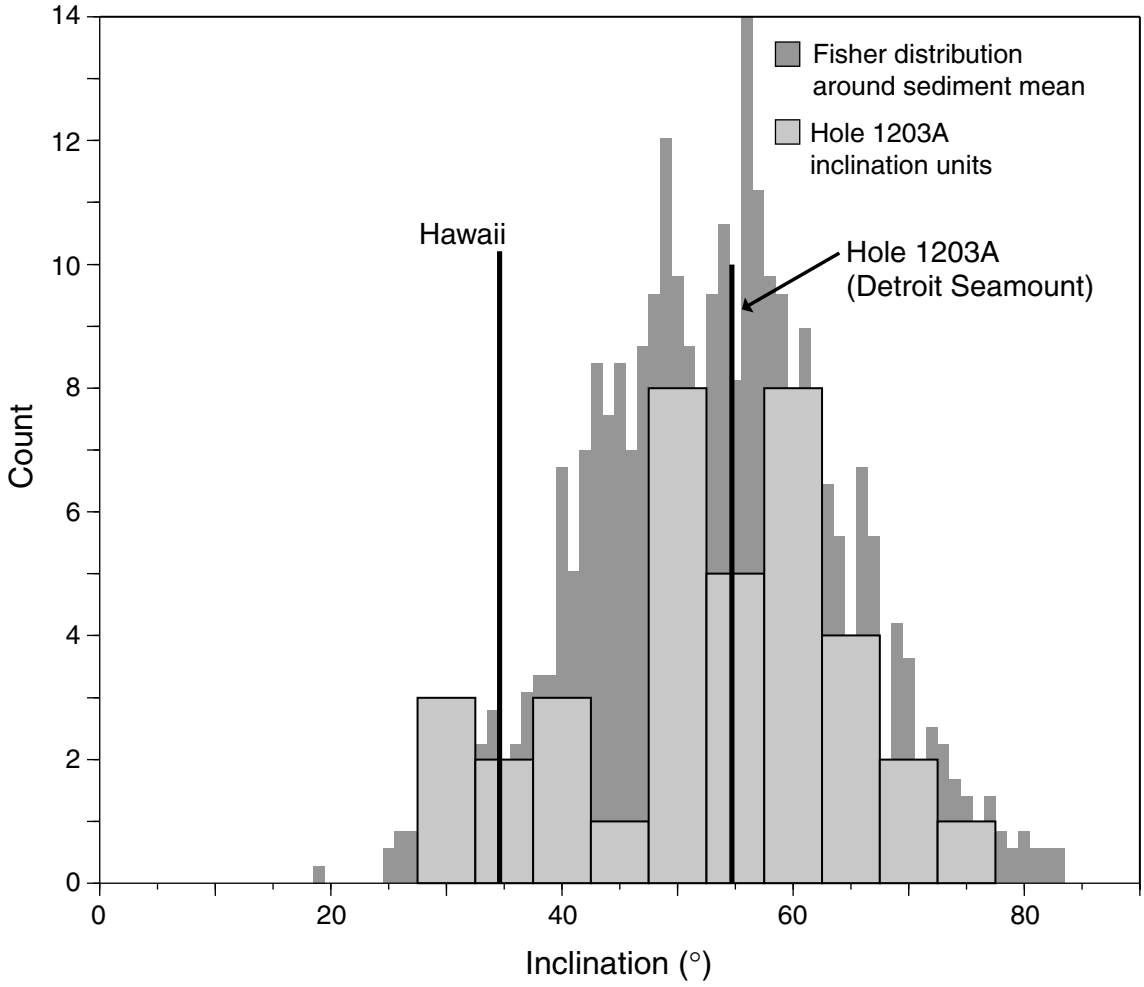

Figure F71. Histogram of inclination values derived from principal component analyses of basalt flows recovered at Site 1203 compared to a synthetic Fisher distribution (Fisher, 1953).

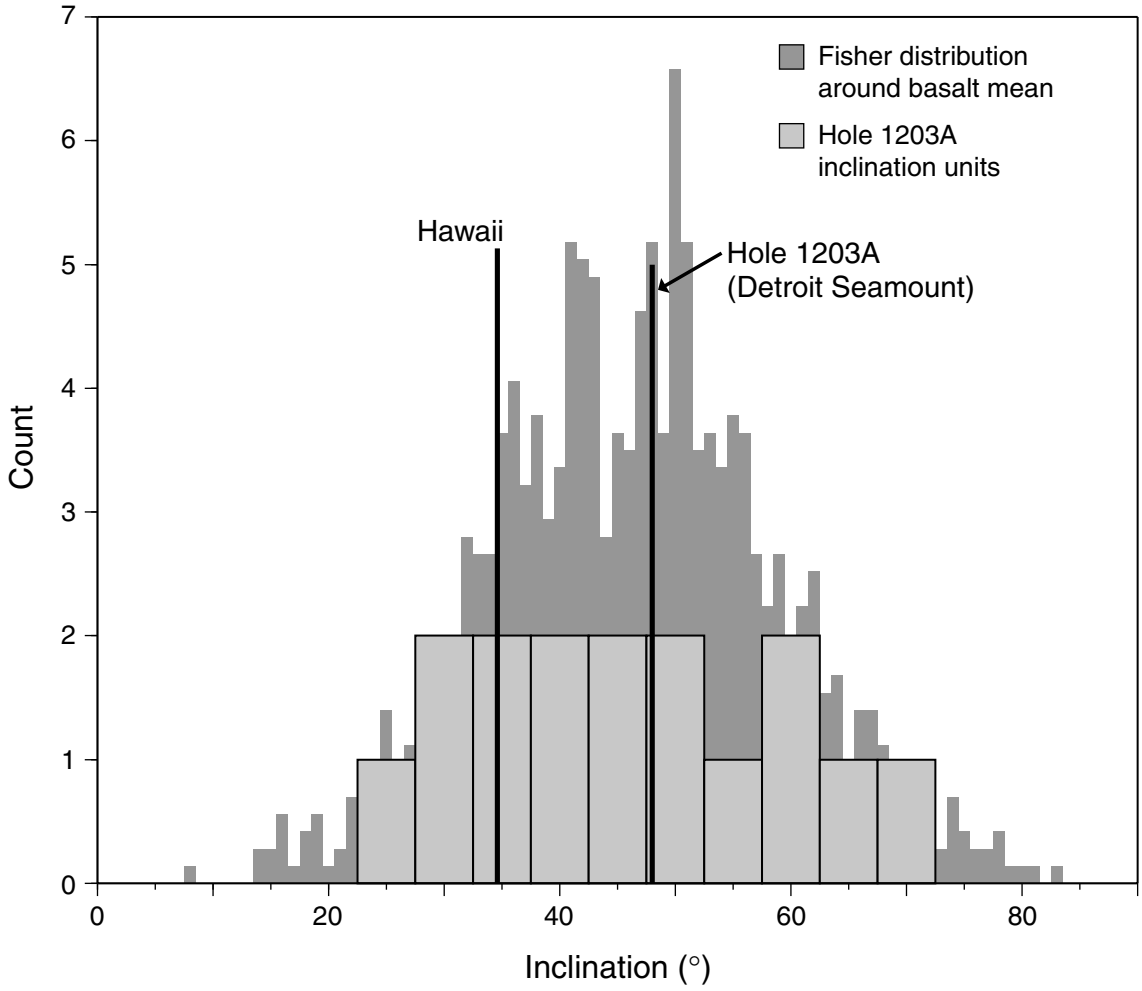

Figure F72. Whole-core measurements in sedimentary units: (**A**) gamma ray attenuation (GRA) bulk density, (**B**) magnetic susceptibility, and (**C**) natural gamma ray vs. depth.

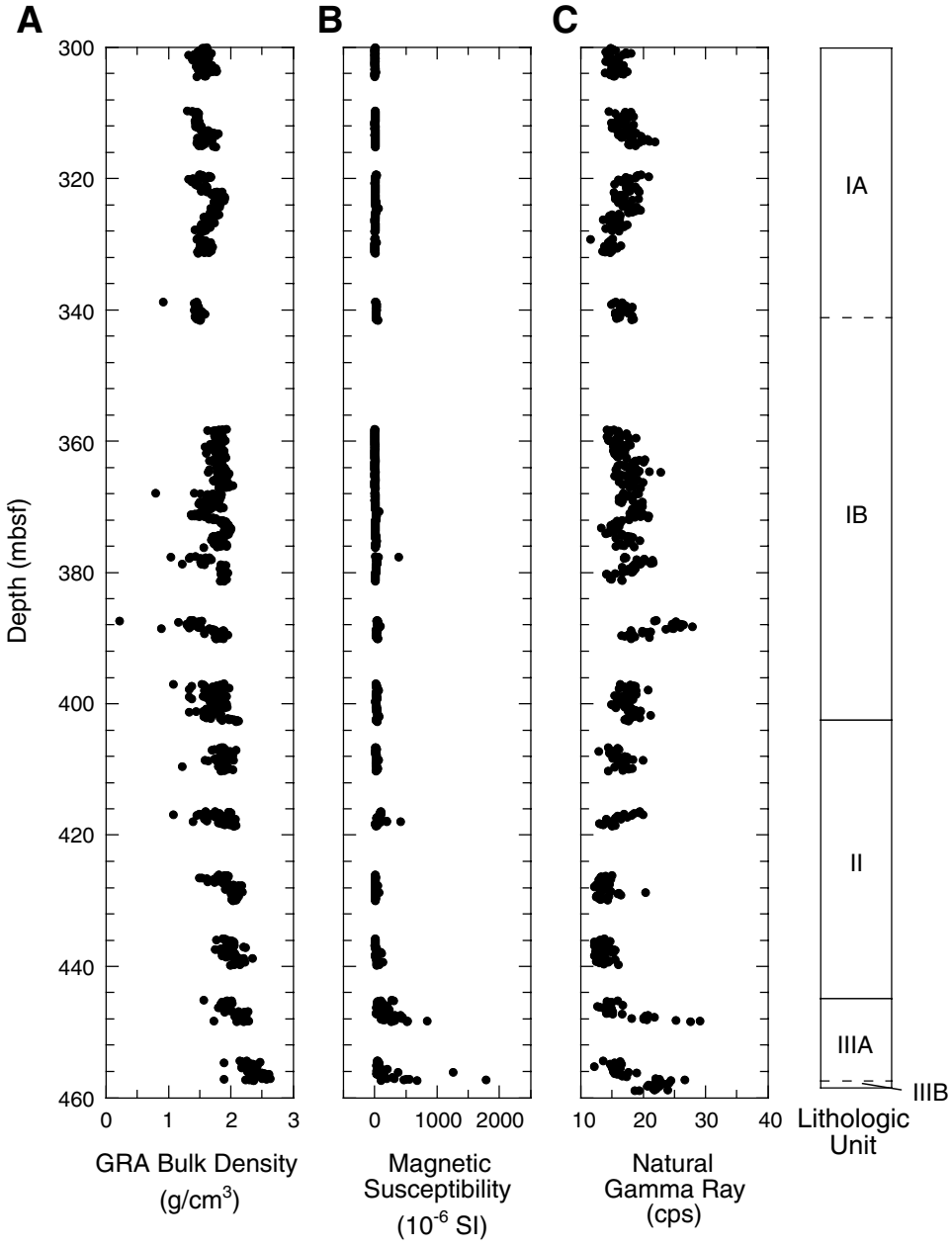

Figure F73. Summary of index properties in sedimentary units: (**A**) GRA bulk density, (**B**) bulk density, (**C**) grain density, and (**D**) porosity.

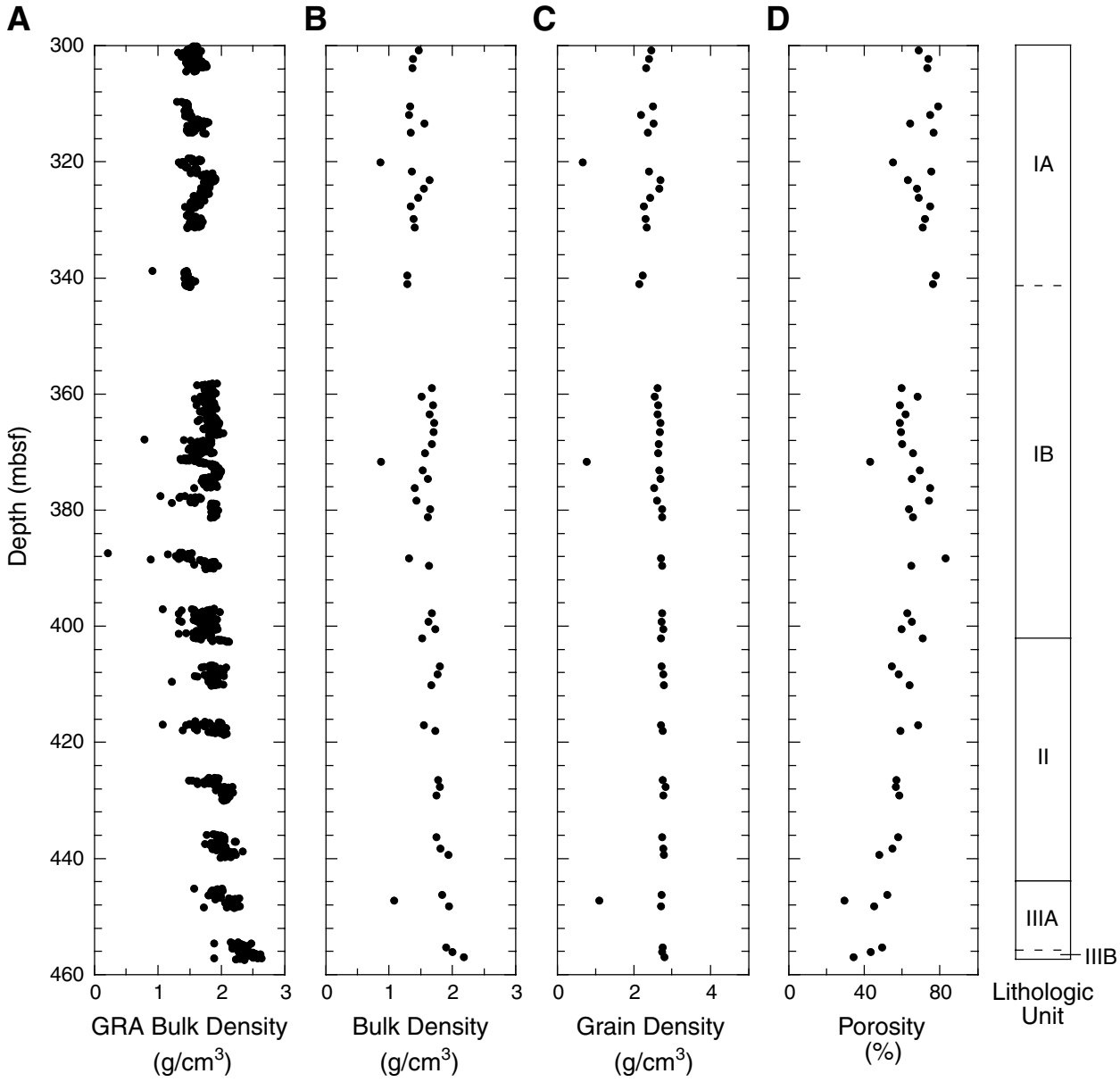

Figure F74. Summary of physical properties measurements in basement units: (**A**) natural gamma ray, (**B**) bulk density, (**C**) grain density, and (**D**) porosity.

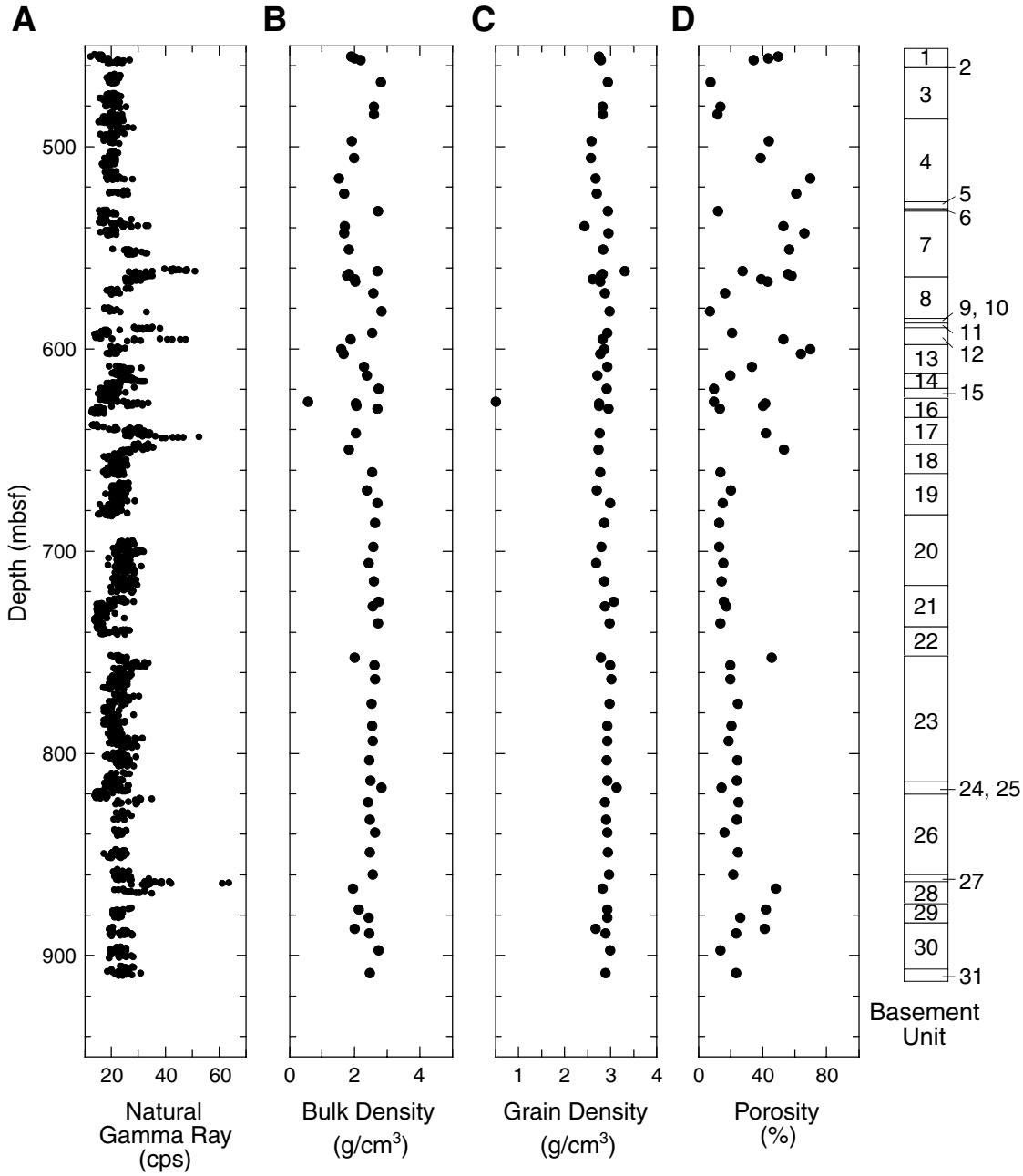

Figure F75. Example core image from the DMT color CoreScan showing a basalt with glassy margin (Section 197-1203-46R-5 [Piece 9]).

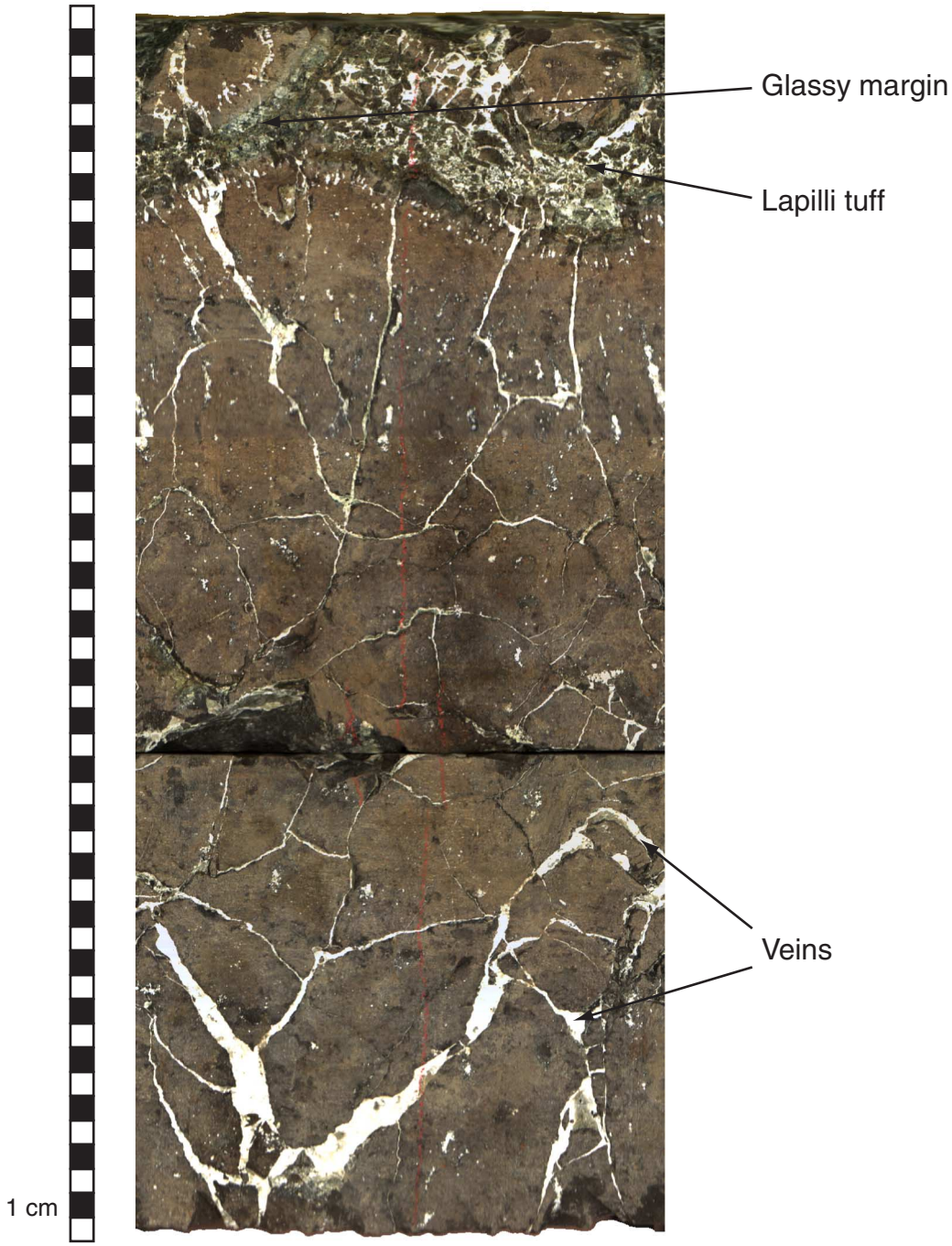

Figure F76. Downhole thermal conductivity measurements in (**A**) sedimentary units and (**B**) basement units.

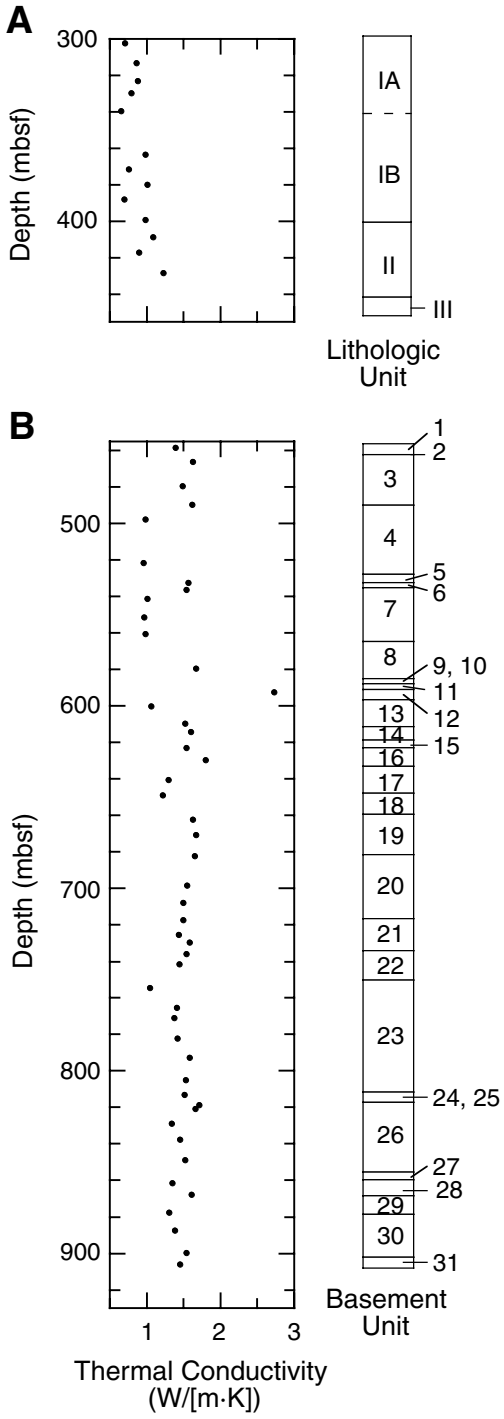

Figure F77. PWS3 velocity in the x-, y-, and z-directions.

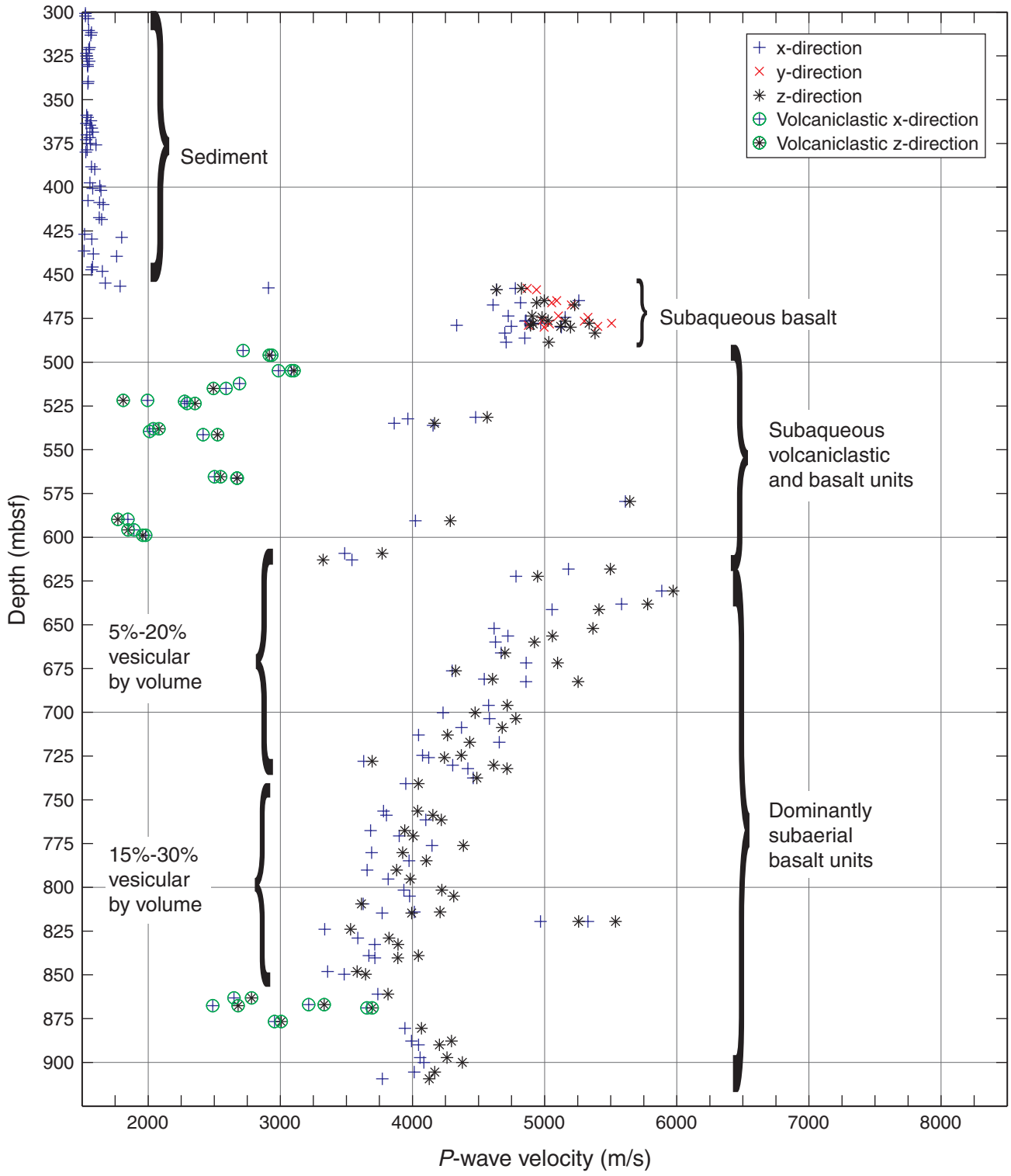

Figure F78. Logging data summary for Hole 1203A. Circles plotted in bulk density, porosity, and *P*-wave logs are discrete measurement values of recovered core samples (see **"Physical Properties,"** p. 37).

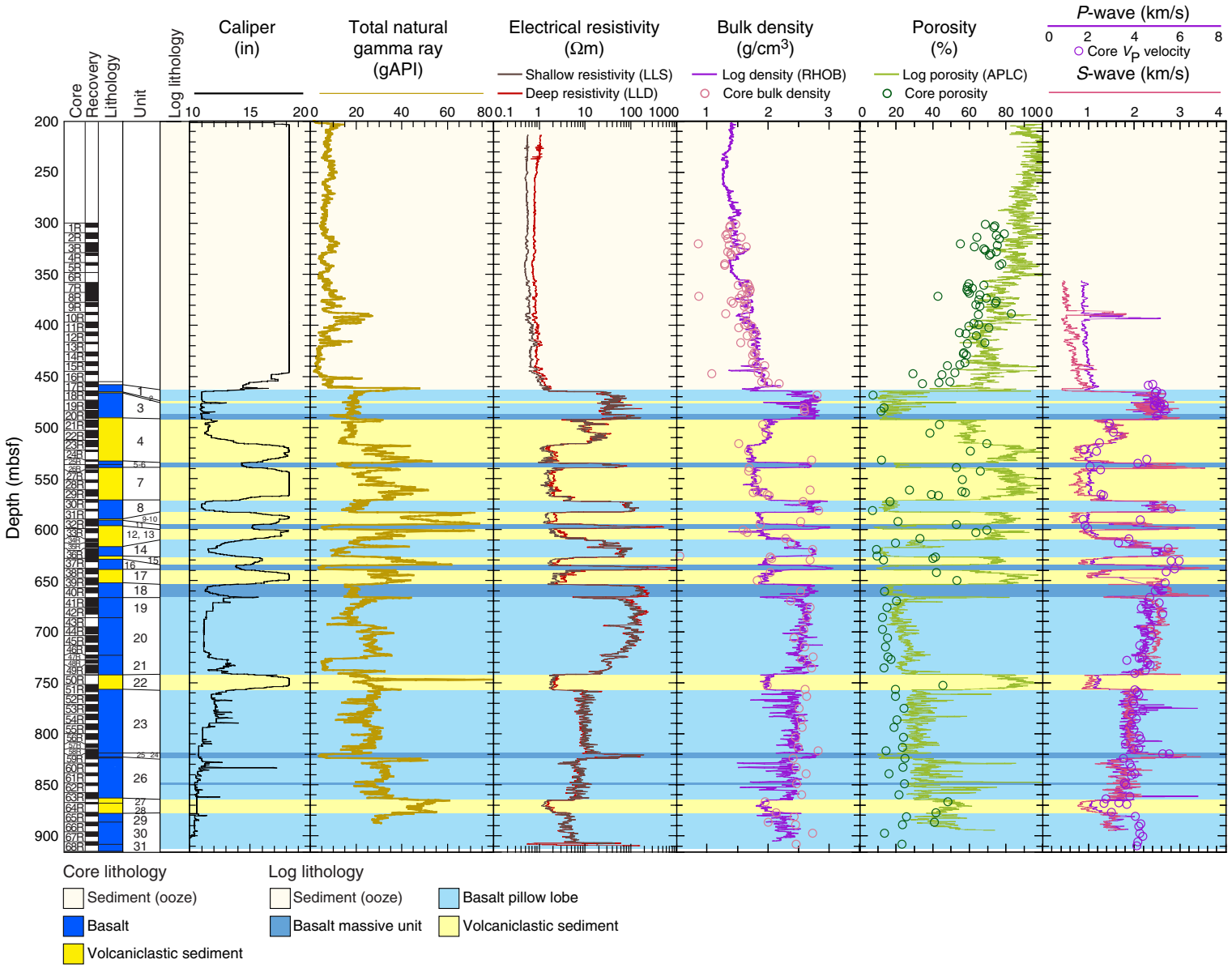

Figure F79. Gamma ray measurements logging data summary for Hole 1203A.

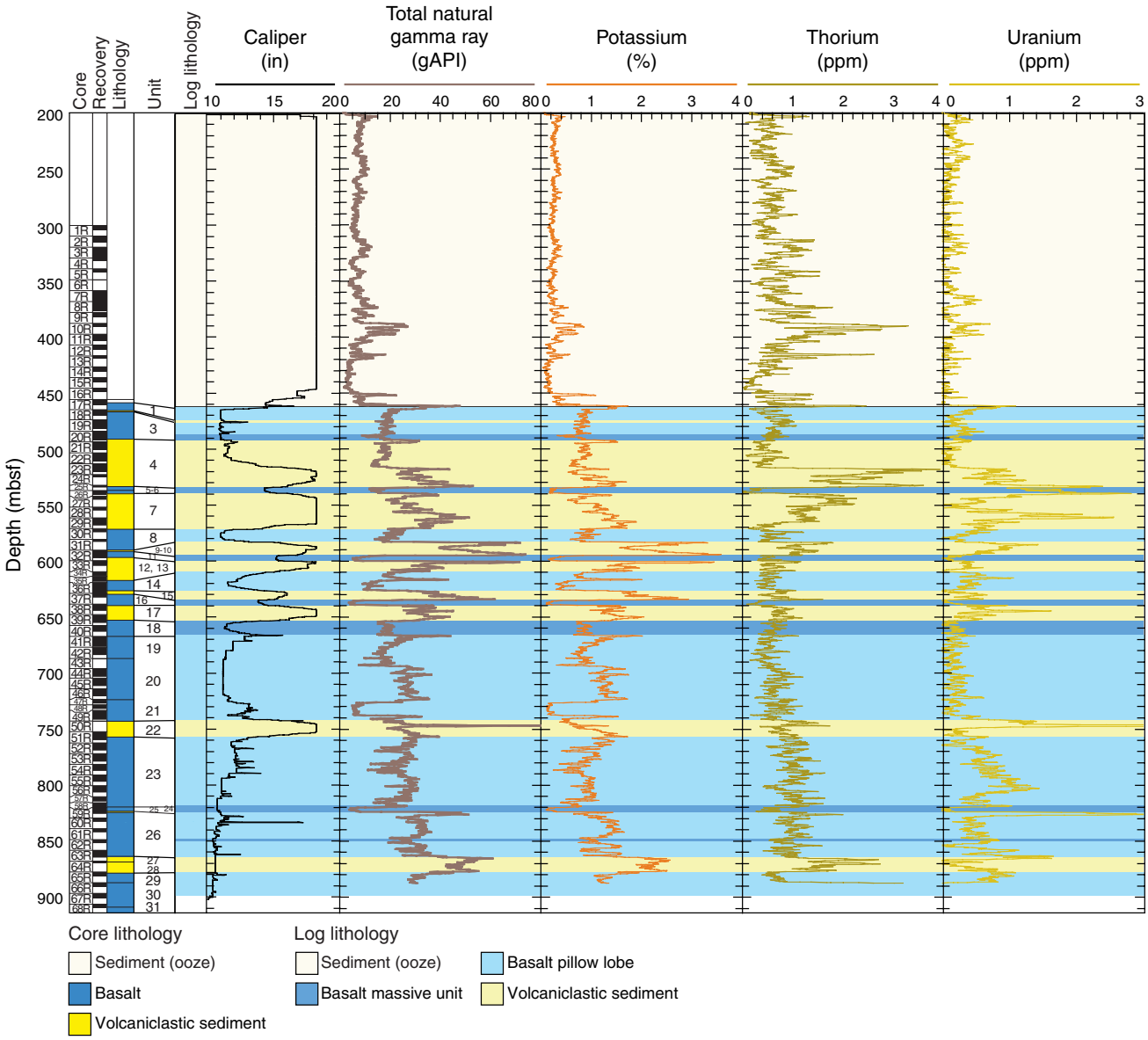

Figure F80. Comparison of Formation MicroScanner (FMS) image and wireline measurements (electrical resistivity, natural gamma ray, porosity, and density) with the core-derived lithology and lithology inferred from logging data in basement.

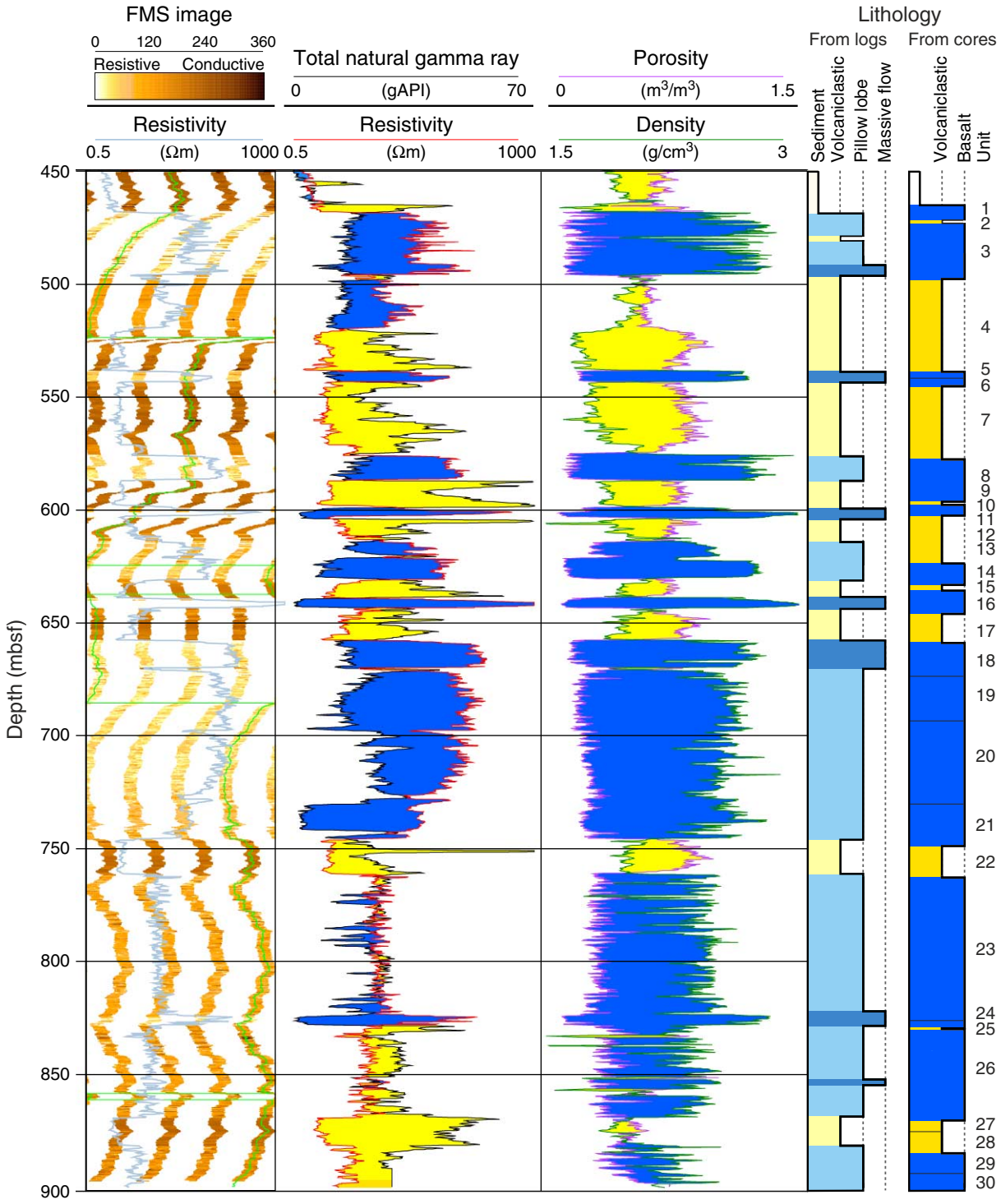

Figure F81. Detailed Formation MicroScanner (FMS) image displaying transition between basement Unit 7 (layered volcaniclastic units) and Unit 8 (pillow lava).

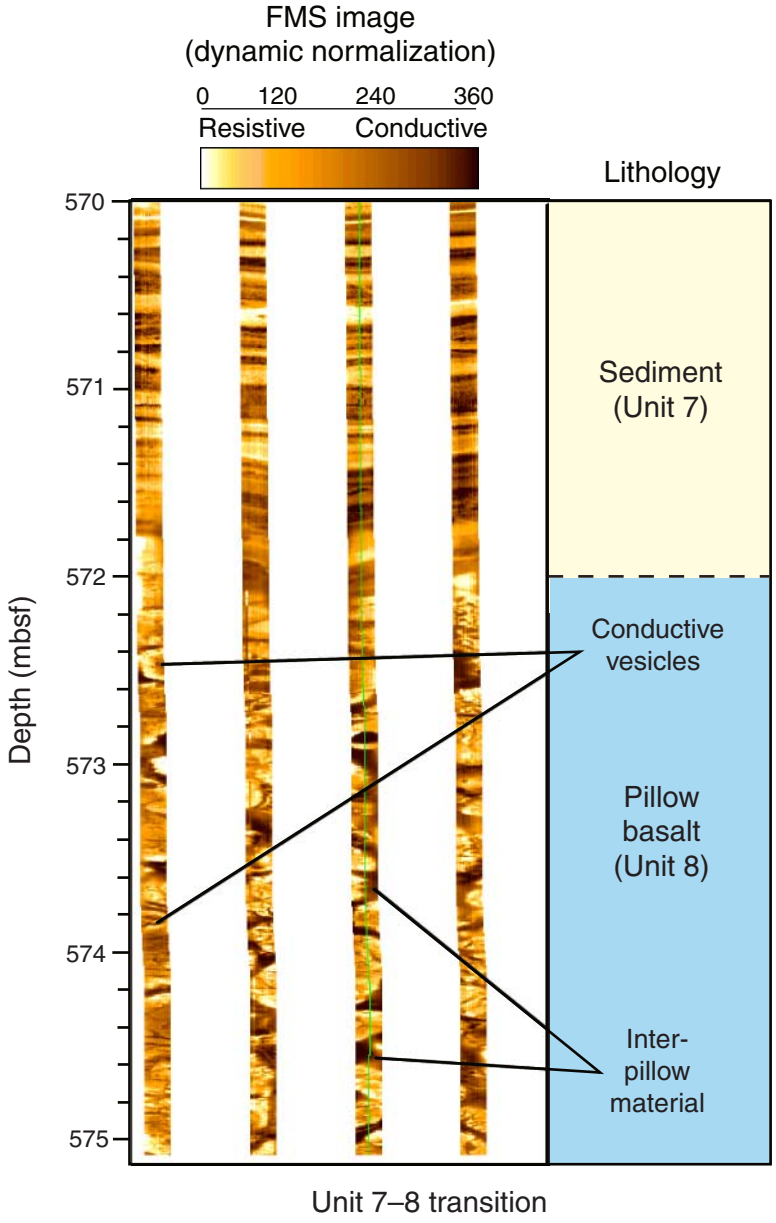

Figure F82. Detailed FMS image displaying typical pillow lobes in basement (part of Unit 23 from 799 to 808 mbsf). On the left is displayed 10 m of this unit section consisting of homogeneous pillow lobes. Both dynamic and static normalization are shown. These different normalizations differ by the computation window size for the color attribution to a selected microresistivity value. For the static normalization, a single computation is carried out in a window covering the entire section, and for the dynamic normalization separate computations are repeated at regularly spaced intervals using a sliding window of relatively short length. The pillow rims are outlined by dark colors corresponding to conductive material. On the right is a detailed display of the pillow. At 799.5 mbsf we note the occurrence of vesicles parallel to the pillow rims.

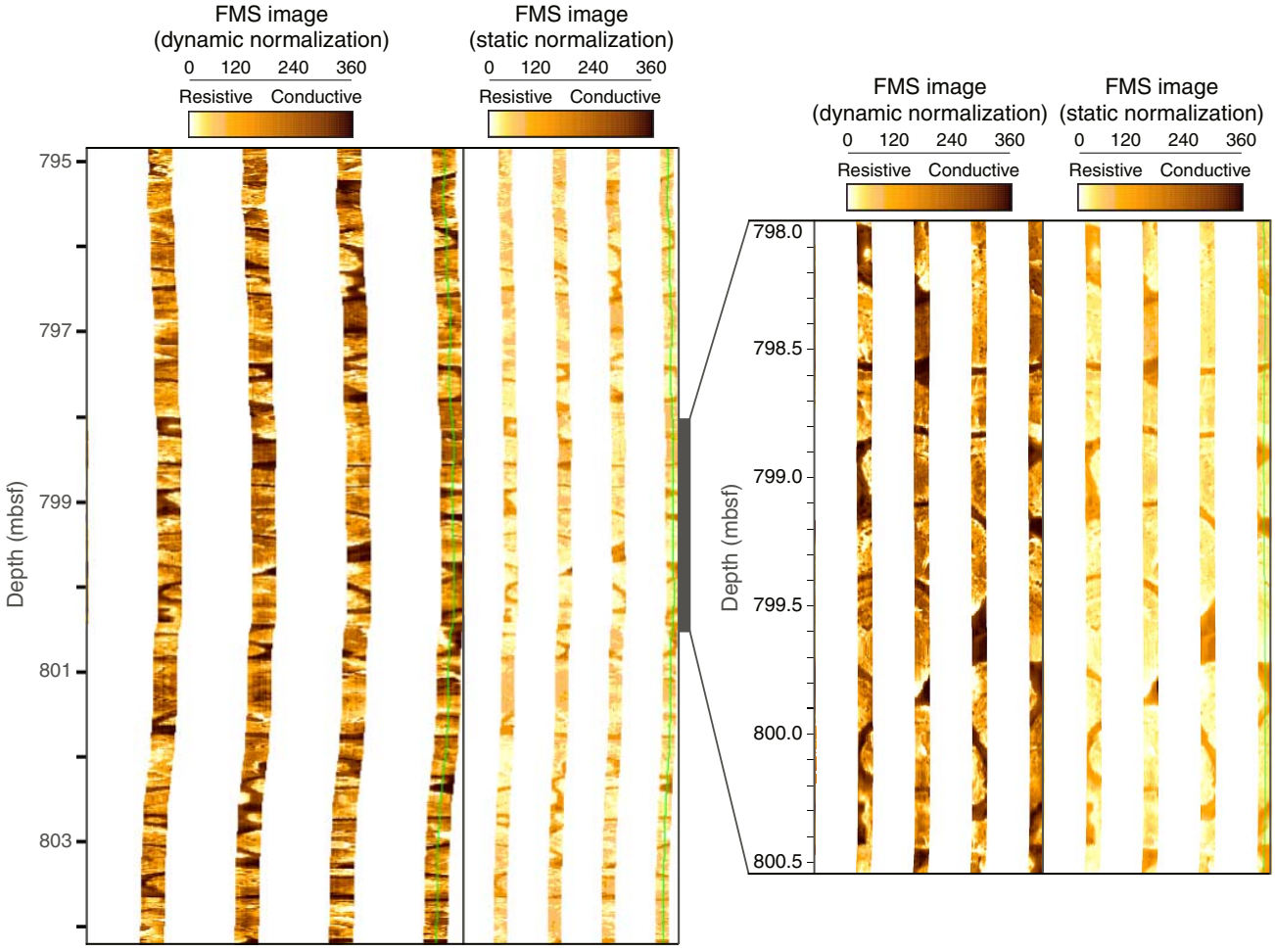

Figure F83. Detailed Formation MicroScanner (FMS) image displaying typical massive intervals within thick pahoehoe flows (Units 11 and 16). Both units present the same internal organization with horizontal vesicles on the top and vertical features in the massive part (jointing structures or pipe vesicles).

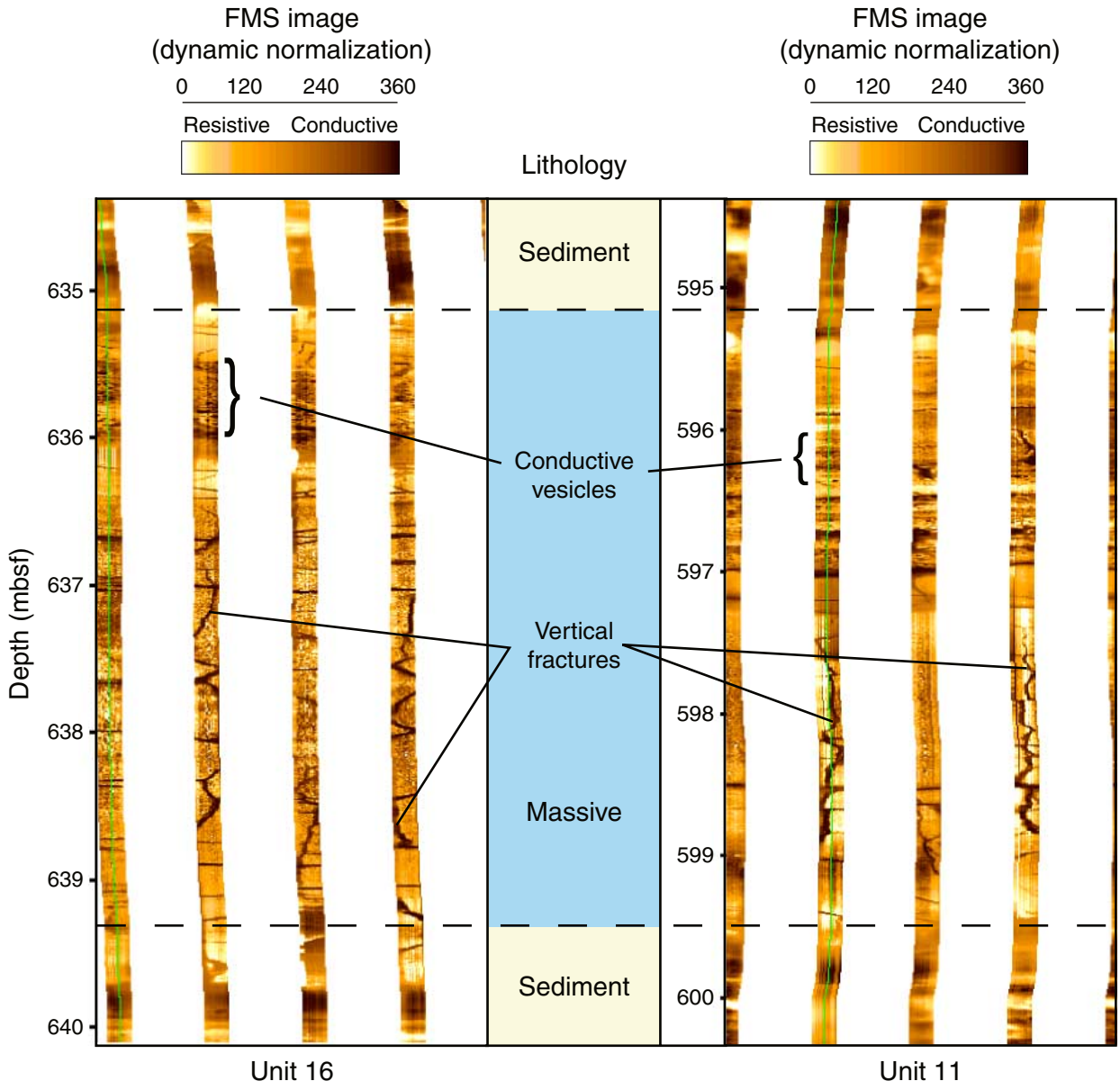

Figure F84. Detailed FMS image displaying breccia (part of Unit 13) from 615.0 to 617.5 mbsf.

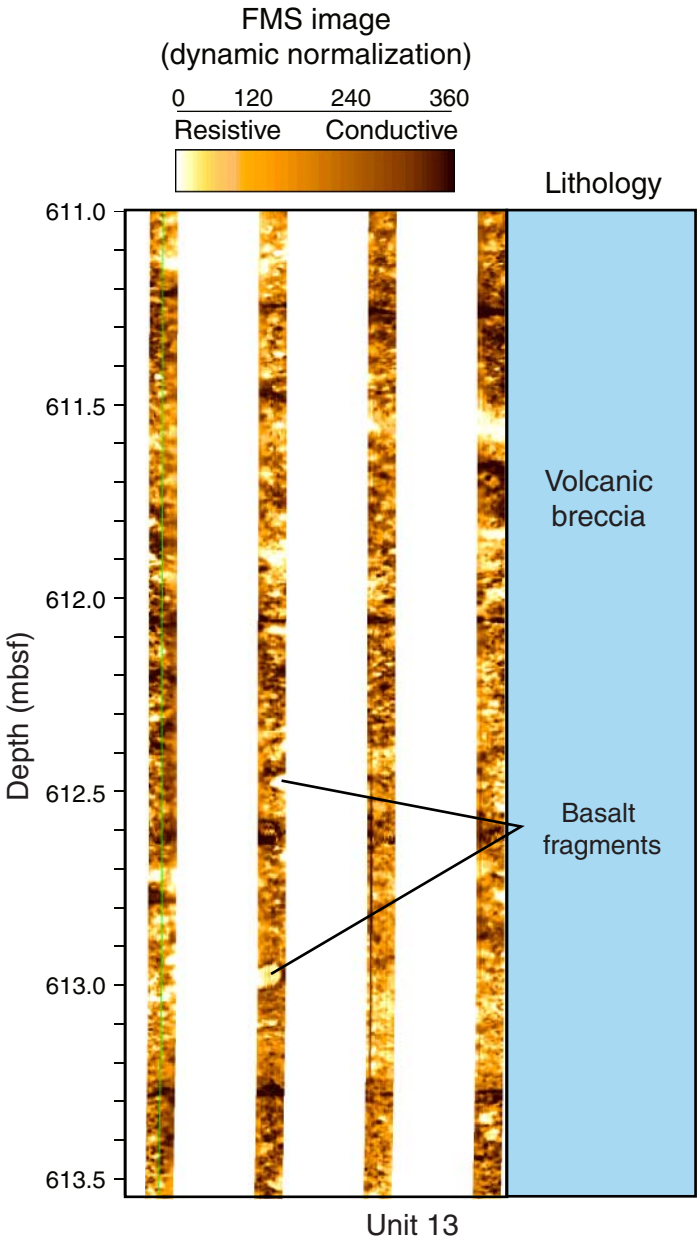

Figure F85. Summarized general purpose inclinometry tool (GPIT) data for Hole 1203A.

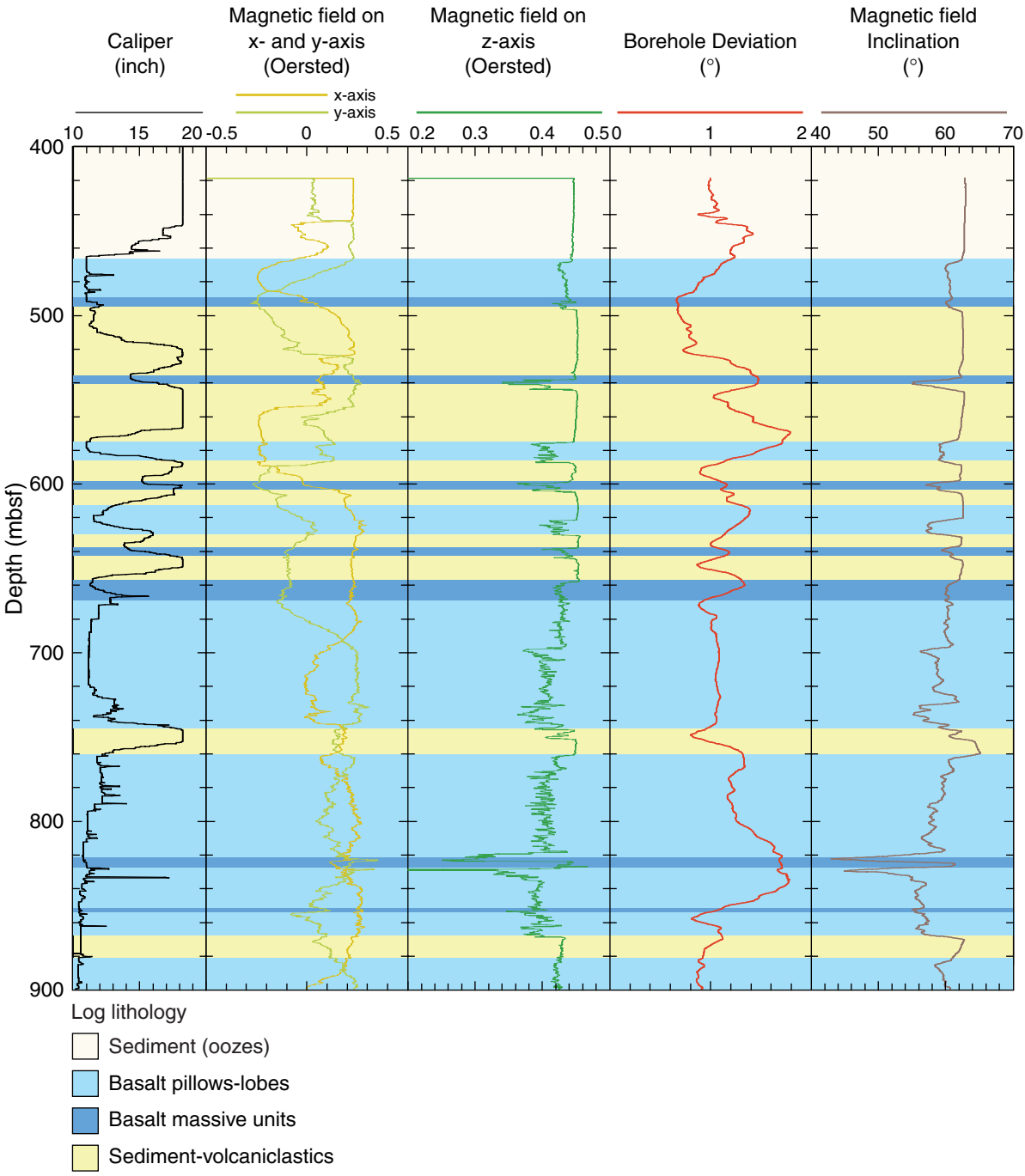

Figure F86. Comparison of the magnetic field components measured with GBM and GPIT.

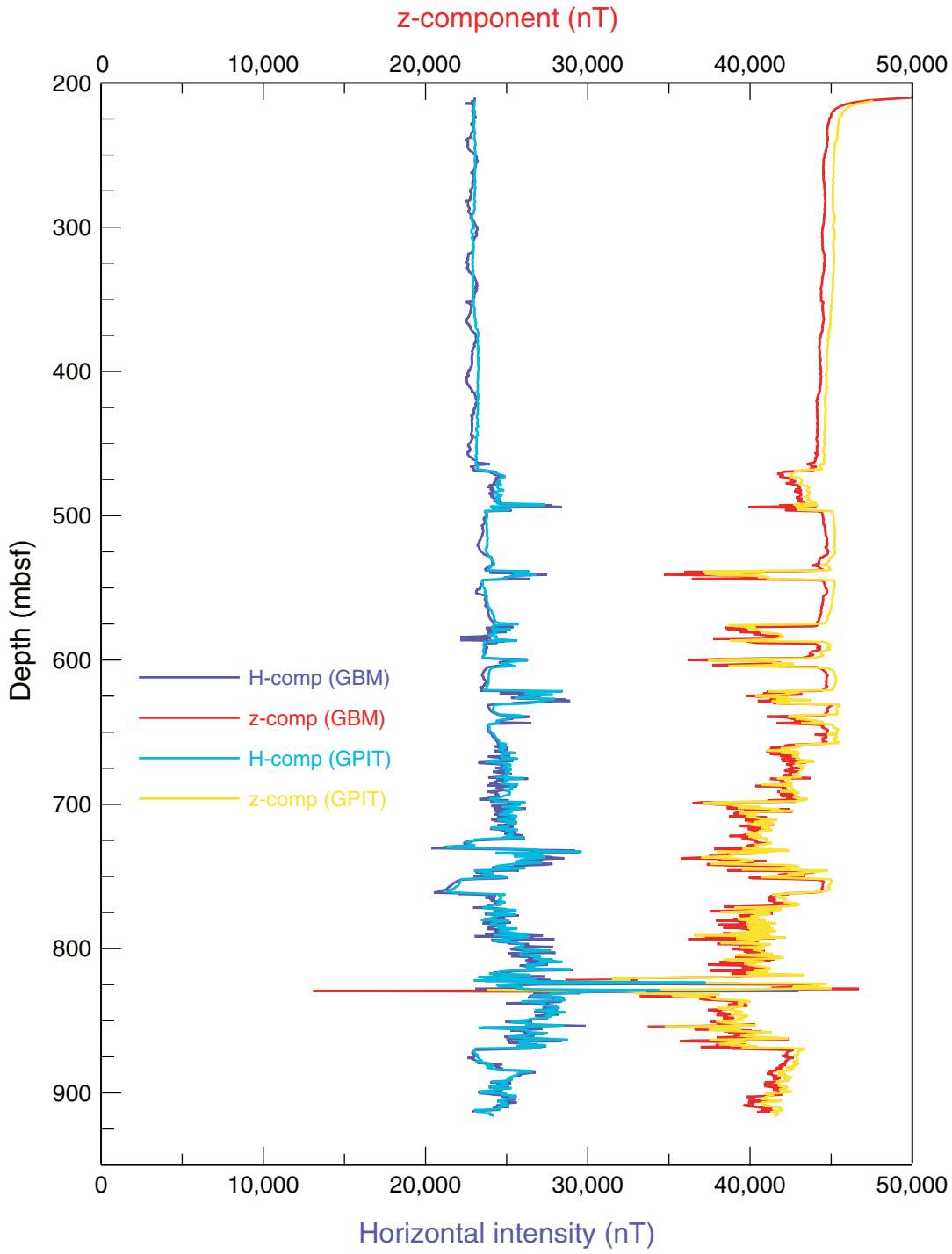

Figure F87. Downhole and uphole run of the GBM in the open hole section.

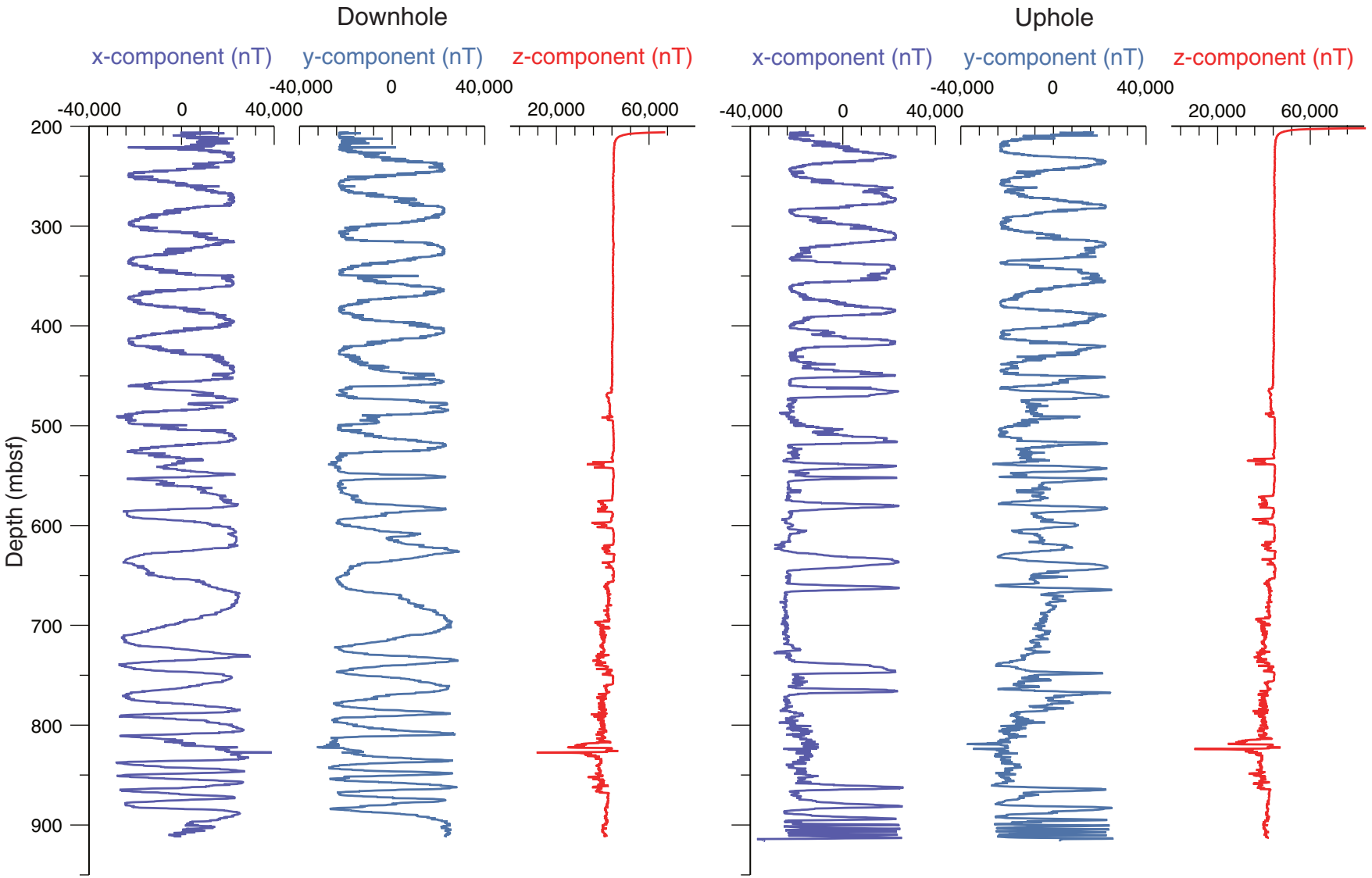

Figure F88. Downhole and uphole run of GBM. Intensities of the horizontal and vertical field compared to the sequences of volcaniclastic sediments and lava flows.

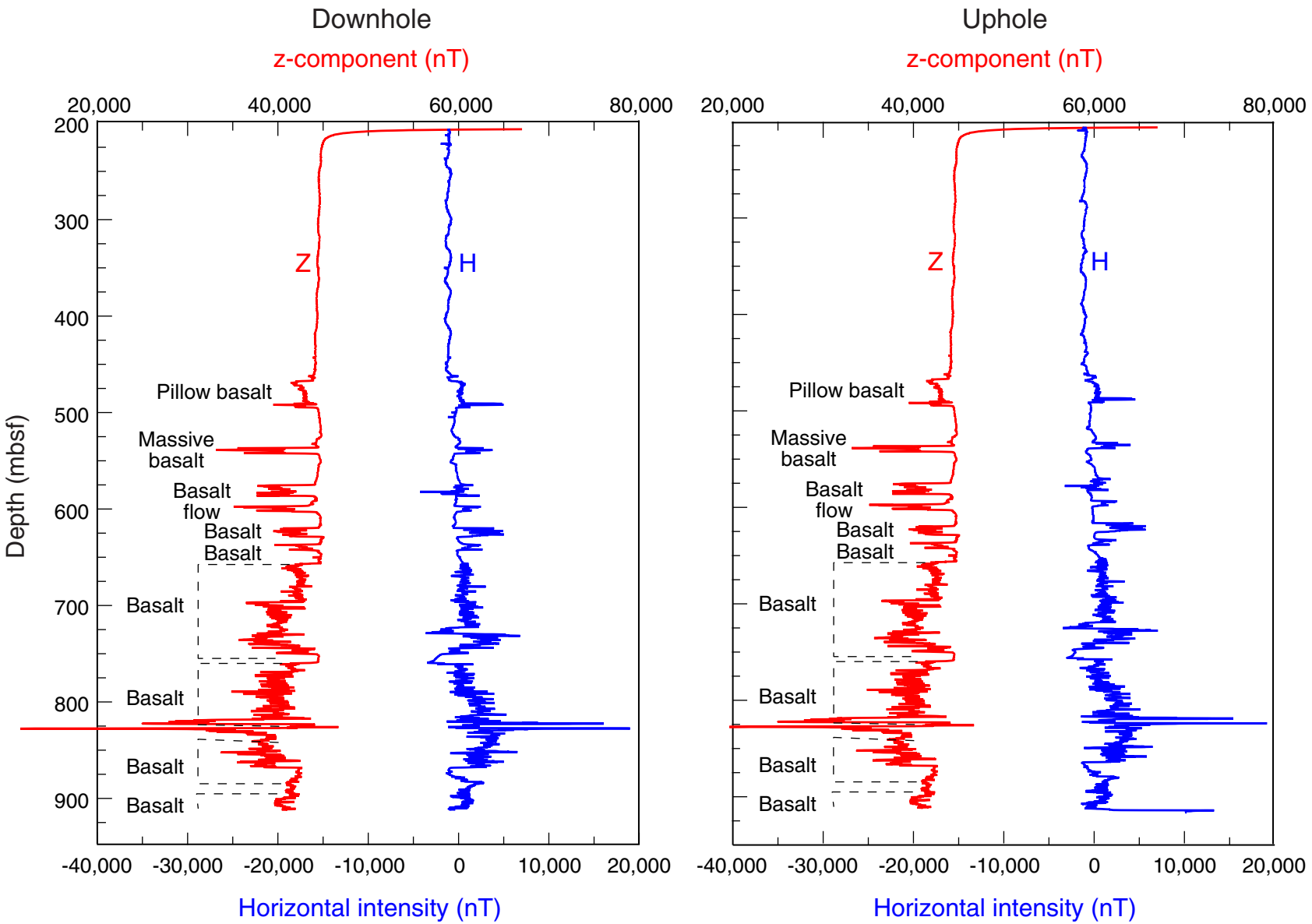

Figure F89. History of rotation about the vertical axis for the magnetometer tool during the downhole and uphole run. BOP = bottom of pipe.

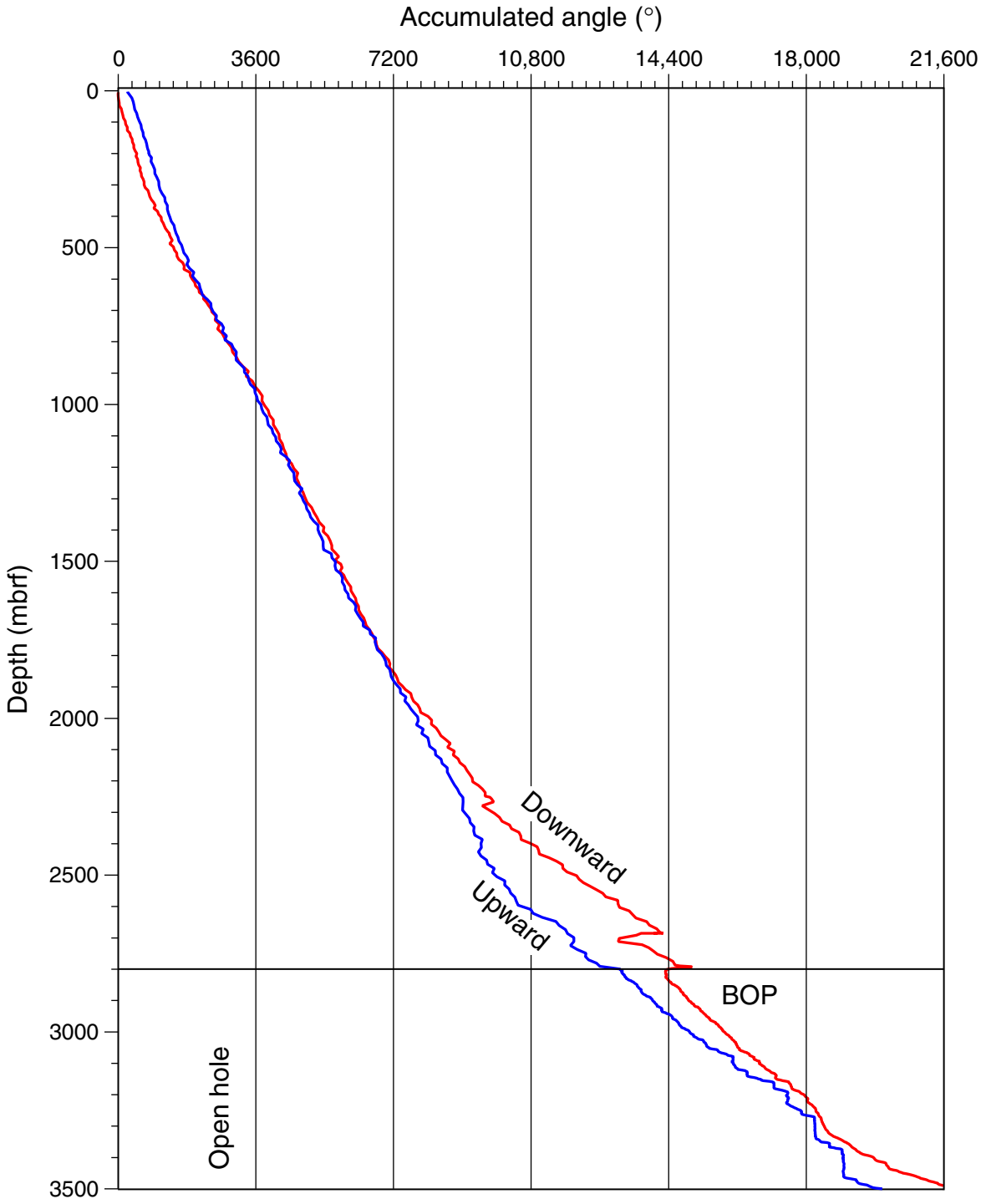

Figure F90. Ship track for seismic Survey 1. Tick marks show half-hour time intervals. Track lines of the *Thomas Washington* survey are shown as well.

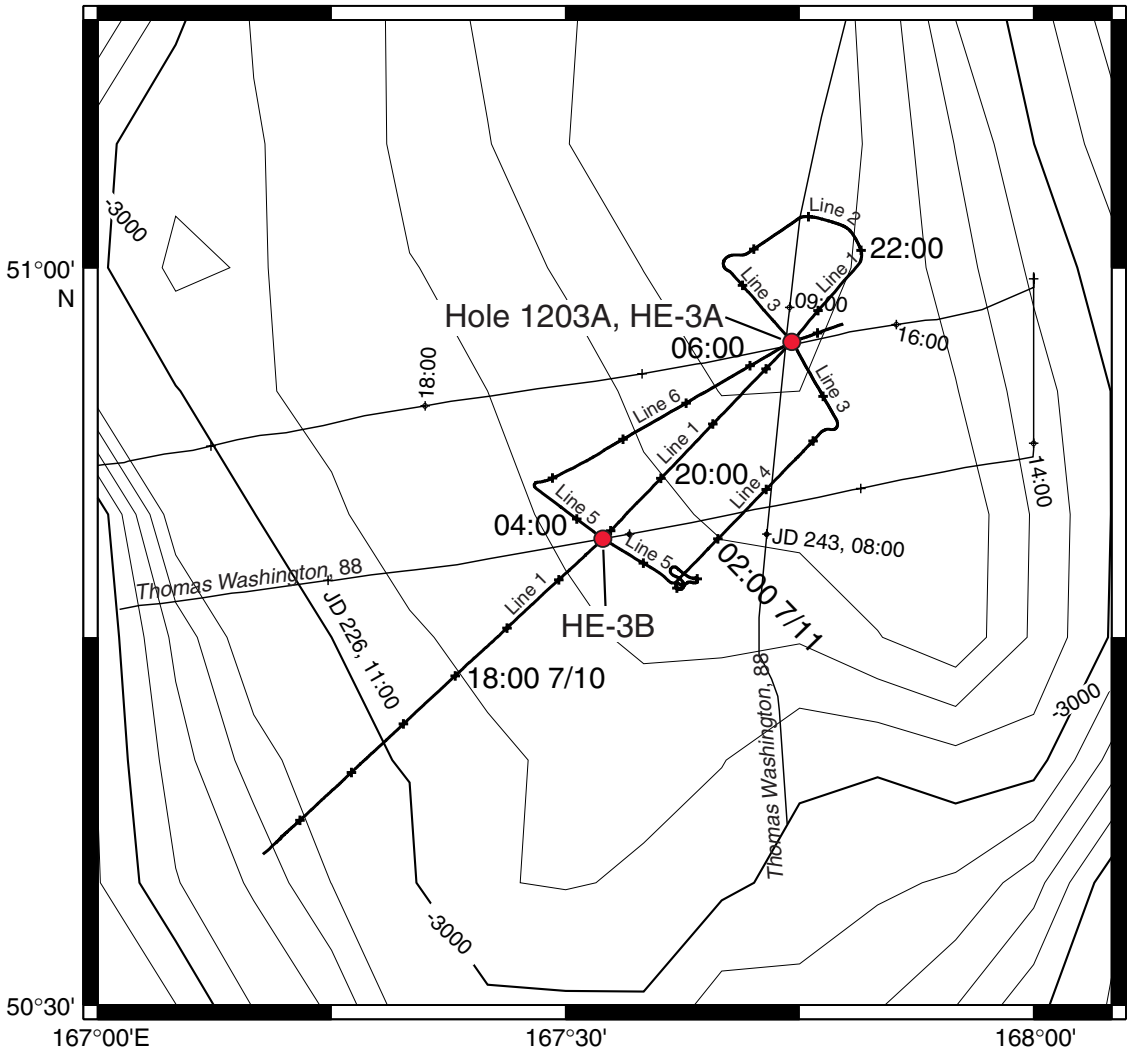

Figure F91. Five-km-long migrated time section of Survey 1, Line 1. Data are bandpass filtered between 40 and 100 Hz. Hole 1203A is at about shotpoint 2386. Trace-to-trace distance = ~19.6 m, vertical exaggeration at the seafloor = ~3:1, bottom of hole = ~4.34 s two-way traveltime.

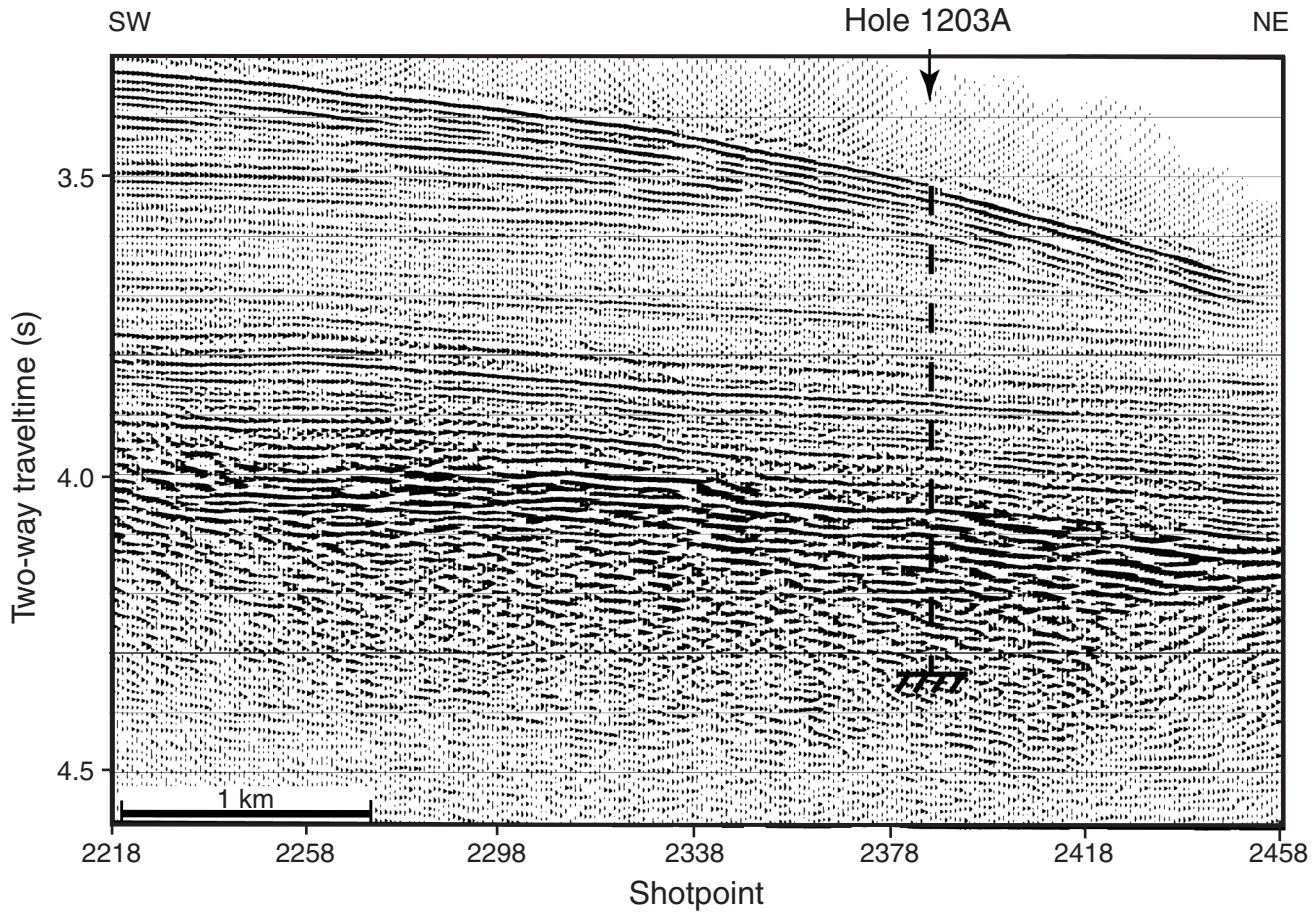

Figure F92. Five-km-long migrated time section of Survey 1, Line 3. Data are bandpass filtered between 40 and 100 Hz. Hole 1203A occurs at about shotpoint 4026. Trace-to-trace distance = ~17.6 m, vertical exaggeration at the seafloor = ~3:1, bottom of hole = ~4.34 s two-way traveltime.

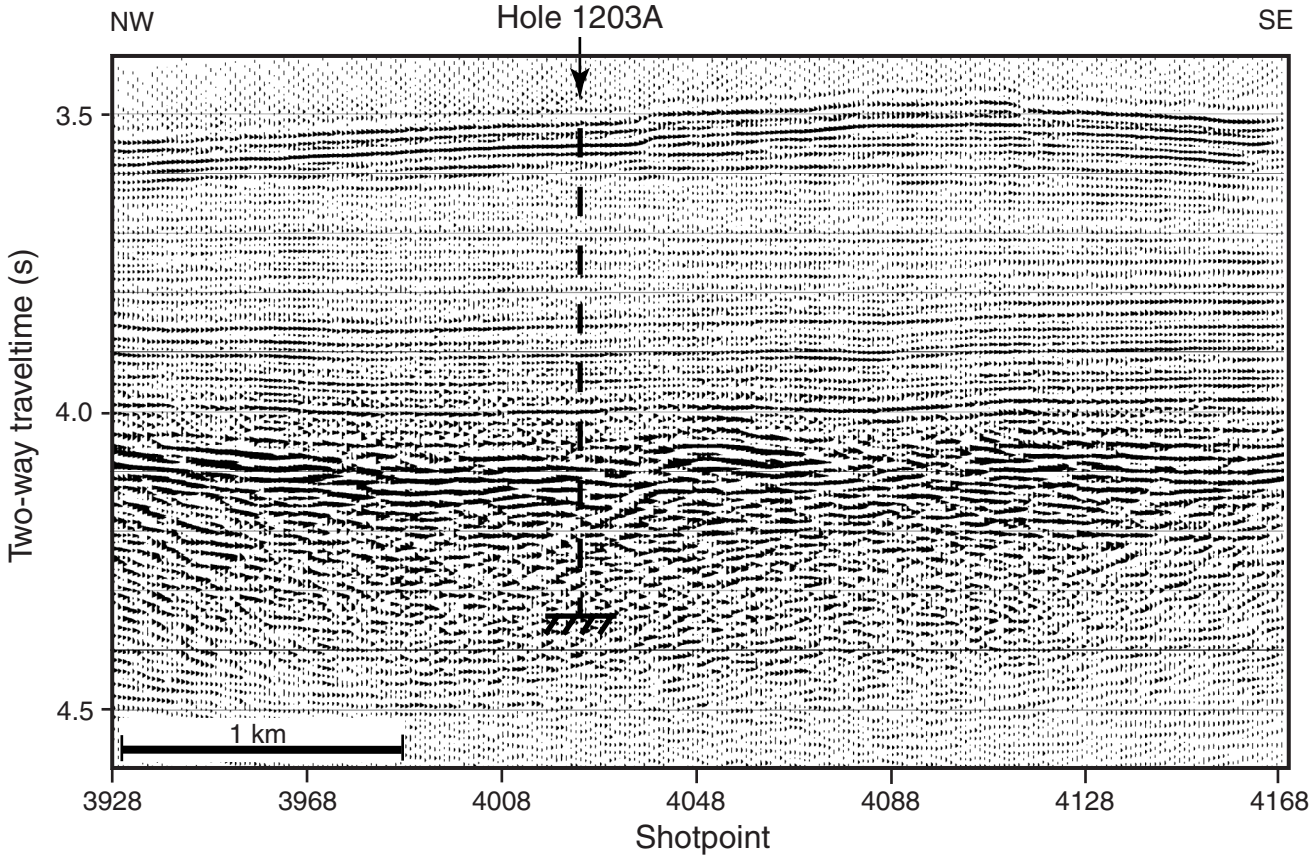

Figure F93. Five-km-long migrated time section of Survey 1, Line 6. Data are bandpass filtered between 40 and 100 Hz. Hole 1203A occurs at about shotpoint 7780. Trace-to-trace distance = ~18.8 m, vertical exaggeration at the seafloor = ~3:1, bottom of hole = ~4.34 s two-way traveltime.

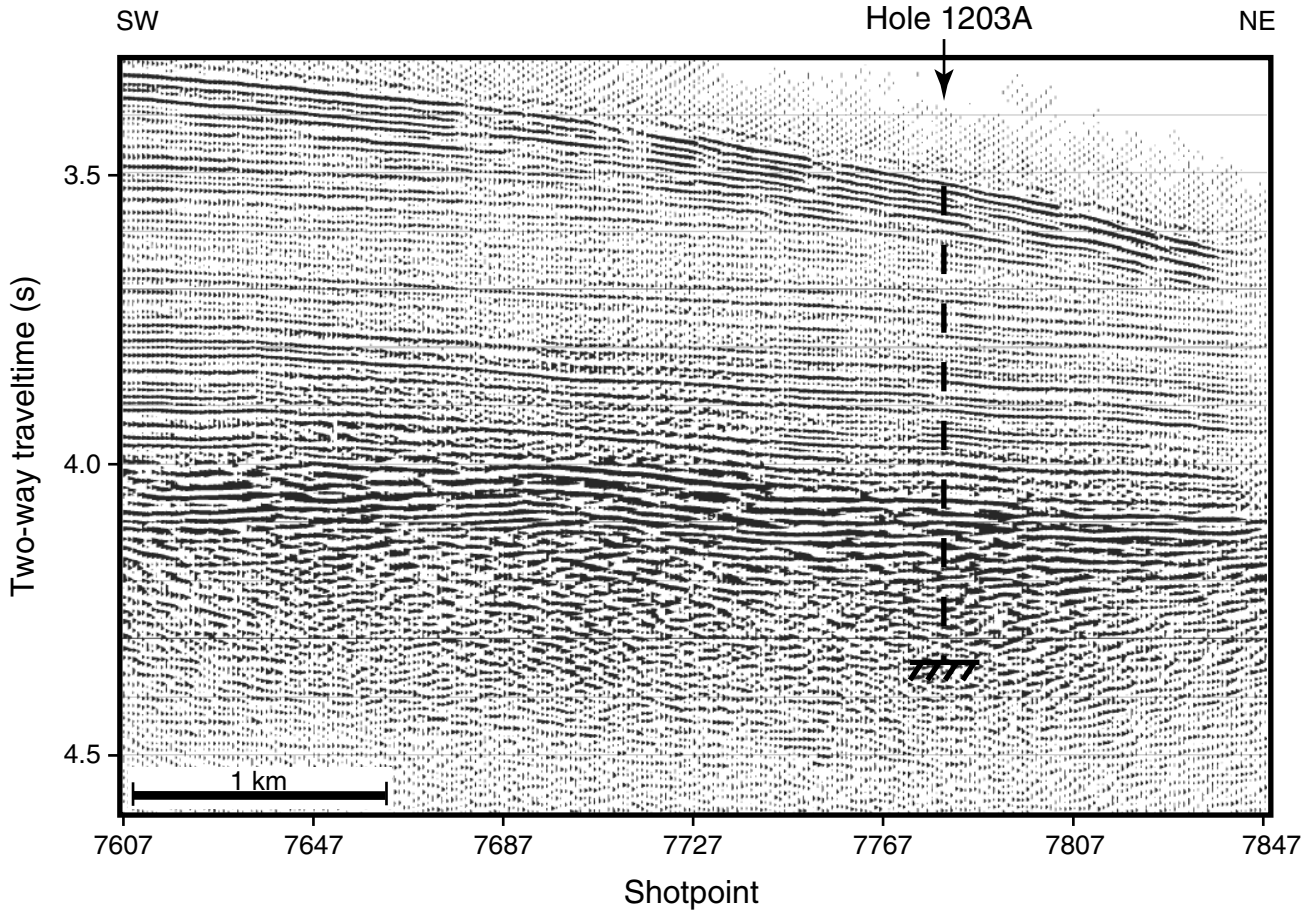

Table T1. Coring summary, Hole 1203A. (See table note. Continued on next page.)

Hole 1203A
Latitude: 50°56.9976′N
Longitude: 167°44.3969′E
Time on site (hr): 326.25 (1715 hr, 11 Jul–1630 hr, 25 Jul 2001)
Seafloor (drill pipe measurement from rig floor, mbrf): 2604.4
Distance between rig floor and sea level (m): 10.9
Water depth (drill pipe measurement from sea level, m): 2593.5
Total depth (drill pipe measurement from rig floor, mbrf): 3519.0
Total penetration (meters below seafloor, mbsf): 914.6
Total length of cored section (m): 614.6
Total length of drilled intervals (m): 300.0
Total core recovered (m): 333.91
Core recovery (%): 54.3
Total number of cores: 68
Total number of drilled intervals: 1

Core	Date (Jul 2001)	Ship time (local)	Depth (mbsf) Top	Depth (mbsf) Bottom	Length (m) Cored	Length (m) Recovered	Recovery (%)	Comments
197-1203A-								
			*****Drilled from 0 to 300.0 mbsf*****					
1R	12	2300	300.0	309.6	9.6	4.65	48.4	
2R	13	0005	309.6	319.3	9.7	5.77	59.5	
3R	13	0050	319.3	329.0	9.7	9.06	93.4	
4R	13	0135	329.0	338.7	9.7	2.55	26.3	
5R	13	0220	338.7	348.4	9.7	3.06	31.6	
6R	13	0305	348.4	358.1	9.7	0.23	2.4	
7R	13	0345	358.1	367.8	9.7	9.33	96.2	
8R	13	0430	367.8	377.5	9.7	8.61	88.8	
9R	13	0505	377.5	387.2	9.7	4.05	41.8	
10R	13	0555	387.2	396.9	9.7	3.20	33.0	
11R	13	0645	396.9	406.6	9.7	5.93	61.1	
12R	13	0730	406.6	416.3	9.7	3.88	40.0	
13R	13	0815	416.3	426.0	9.7	2.60	26.8	
14R	13	0855	426.0	435.7	9.7	4.18	43.1	
15R	13	0945	435.7	445.1	9.4	4.37	46.5	
16R	13	1030	445.1	454.3	9.2	3.53	38.4	
17R	13	1210	454.3	463.8	9.5	4.34	45.7	
18R	13	1705	463.8	473.4	9.6	4.22	44.0	
19R	13	2305	473.4	483.0	9.6	6.32	65.8	
20R	14	0415	483.0	492.6	9.6	7.19	74.9	
21R	14	0710	492.6	502.2	9.6	4.71	49.1	
22R	14	0935	502.2	511.9	9.7	6.58	67.8	
23R	14	1120	511.9	521.5	9.6	3.53	36.8	
24R	14	1225	521.5	531.1	9.6	2.26	23.5	
25R	14	1450	531.1	534.8	3.7	1.95	52.7	
26R	14	1810	534.8	540.8	6.0	4.53	75.5	
27R	14	1945	540.8	550.5	9.7	3.11	32.1	
28R	14	2145	550.5	560.2	9.7	3.01	31.0	
29R	14	2355	560.2	569.8	9.6	6.88	71.7	
30R	15	0545	569.8	579.4	9.6	2.67	27.8	
31R	15	0900	579.4	589.0	9.6	1.99	20.7	
32R	15	1240	589.0	598.6	9.6	6.52	67.9	
33R	15	1450	598.6	608.3	9.7	4.03	41.6	
34R	15	1810	608.3	612.3	4.0	3.71	92.8	
35R	15	2230	612.3	617.9	5.6	5.06	90.4	
36R	16	0330	617.9	627.5	9.6	9.63	100.3	
37R	16	0610	627.5	637.1	9.6	3.89	40.5	
38R	16	0855	637.1	646.6	9.5	6.24	65.7	
39R	16	1155	646.6	656.2	9.6	7.42	77.3	
40R	16	1630	656.2	665.9	9.7	5.90	60.8	
41R	16	2120	665.9	675.5	9.6	9.20	95.8	AHC
42R	17	0155	675.5	685.1	9.6	7.22	75.2	AHC
43R	17	0715	685.1	694.7	9.6	0.65	6.8	AHC
44R	18	0850	694.7	703.1	8.4	7.47	88.9	AHC
45R	18	1420	703.1	712.7	9.6	7.52	78.3	AHC
46R	18	1910	712.7	722.3	9.6	7.02	73.1	AHC
47R	18	2245	722.3	727.1	4.8	4.18	87.1	AHC
48R	19	0435	727.1	732.0	4.9	3.62	73.9	AHC

Table T1 (continued).

Core	Date (Jul 2001)	Ship time (local)	Depth (mbsf) Top	Depth (mbsf) Bottom	Length (m) Cored	Length (m) Recovered	Recovery (%)	Comments
49R	19	1105	732.0	741.6	9.6	8.66	90.2	AHC
50R	19	1455	741.6	751.2	9.6	0.11	1.2	AHC
51R	19	1940	751.2	760.8	9.6	6.70	69.8	AHC
52R	20	0040	760.8	770.4	9.6	6.72	70.0	AHC
53R	20	0540	770.4	780.0	9.6	6.59	68.7	AHC
54R	20	1200	780.0	789.7	9.7	6.32	65.2	AHC
55R	20	1730	789.7	799.3	9.6	6.20	64.6	AHC
56R	20	2320	799.3	808.9	9.6	5.80	60.4	AHC
57R	21	0400	808.9	814.5	5.6	4.38	78.2	AHC
58R	21	0800	814.5	818.5	4.0	4.10	102.5	AHC
59R	21	1210	818.5	828.1	9.6	5.85	60.9	AHC
60R	21	1550	828.1	837.7	9.6	3.69	38.4	AHC
61R	21	1955	837.7	847.4	9.7	3.41	35.2	AHC
62R	22	0100	847.4	857.0	9.6	3.39	35.3	AHC
63R	22	0450	857.0	866.6	9.6	6.36	66.3	AHC
64R	22	0650	866.6	876.2	9.6	1.90	19.8	AHC
65R	22	1000	876.2	885.8	9.6	3.89	40.5	AHC
66R	22	1355	885.8	895.4	9.6	3.92	40.8	AHC
67R	22	1805	895.4	905.0	9.6	4.56	47.5	AHC
68R	22	2240	905.0	914.6	9.6	3.79	39.5	AHC
				Cored totals:	614.6	333.91	54.3	
				Drilled totals:	300.0			
				Total:	914.6			

Note: AHC = active heave compensation.

Table T2. Carbonate abundance data for Units I, II, and III, Site 1203.

Core, section, interval (cm)	Depth (mbsf)	$CaCO_3$ (wt%)
197-1203A-		
1R-1, 102–103	301.02	44.09
1R-1, 124–125	301.24	16.99
2R-2, 103–104	312.13	0.58
2R-2, 119–120	312.29	26.03
3R-2, 9–11	320.89	3.29
3R-2, 80–82	321.60	19.70
3R-2, 128–130	322.08	69.74
3R-4, 49–51	324.29	62.50
4R-1, 71–72	329.71	51.57
4R-2, 6–7	330.56	20.77
4R-2, 6–7	330.56	21.27
5R-2, 35–36	340.55	24.67
5R-2, 135–136	341.55	3.12
Subunit IA minimum:		0.58
Subunit IA maximum:		69.74
Subunit IA average:		28.02
197-1203A-		
7R-3, 95–96	362.05	86.17
7R-5, 57–58	364.67	34.50
7R-6, 57–58	366.17	81.57
8R-1, 97–98	368.77	65.73
8R-3, 36–37	371.16	1.36
8R-3, 129–130	372.09	79.55
9R-1, 119–120	378.69	47.12
9R-1, 147–148	378.97	80.42
9R-2, 58–59	379.58	70.57
10R-1, 25–26	387.45	0.22
10R-2, 11–12	388.81	79.16
10R-2, 23–24	388.93	49.57
Subunit IB minimum:		0.22
Subunit IB maximum:		86.17
Subunit IB average:		56.33
197-1203A-		
11R-1, 74–75	397.64	77.31
11R-1, 80–81	397.70	77.02
11R-4, 65–66	402.05	60.22
12R-1, 24–25	406.84	80.14
12R-2, 36–38	408.25	81.54
12R-2, 74–75	408.63	80.18
12R-3, 73–74	410.12	87.38
13R-1, 26–27	416.56	63.11
13R-1, 74–76	417.04	56.44
13R-2, 18–20	417.98	85.11
14R-1, 35–37	426.35	93.32
14R-2, 120–121	428.70	61.11
14R-3, 3–5	429.03	93.10
14R-3, 25–26	429.25	93.63
15R-2, 75–76	437.95	79.93
15R-2, 83–84	438.03	94.95
16R-2, 68–69	447.28	88.31
16R-3, 7–8	447.67	5.15
Unit II minimum:		5.15
Unit II maximum:		94.95
Unit II average:		75.44
197-1203A-		
16R-3, 65–66	448.25	63.07
17R-2, 29–30	456.09	3.98
17R-2, 49–50	456.29	83.30
17R-2, 91–92	456.71	43.73
17R-2, 103–104	456.83	64.27
17R-3, 15–16	457.09	1.60
17R-3, 22–23	457.16	90.56
Unit III minimum:		1.60
Unit III maximum:		90.56
Unit III average:		50.07

Table T3. Summary of distribution and abundance of nannofossils and biozonal assignments, Site 1203. (See table notes. Continued on next three pages.)

Core, section, interval (cm)	Depth (mbsf)	Sample code	Zone		Age	Preparation*	Preservation	Group abundance	Nannofossils																													
			From	To	From				*Ceratolithoides aculeus*	*Cretarhabdus crenulatus*	*Cretarhabdus loriei*	*Marthasterites inconspicuus*	*Micula decussata*	*Quadrum sissinghii*	*Quadrum trifidum*	*Watznaueria barnesae*	*Chiasmolithus grandis*	*Coccolithus pelagicus*	*Discoaster barbadiensis*	*Discoaster binodosus*	*Discoaster lodoensis*	*Ericsonia formosa*	*Sphenolithus moriformis*	*Sphenolithus radians*	*Thoracosphaera saxea*	*Toweius crassus*	*Tribrachiatus orthostylus*	*Zygrhablithus bijugatus*	*Chiasmolithus oamaruensis*	*Cyclicargolithus floridanus*	*Dictyococcites bisectus*	*Discoaster saipanensis*	*Reticulofenestra dictyoda*	*Reticulofenestra hillae*	*Reticulofenestra umbilica*	*Discoaster adamanteus*	*Ericsonia subdisticha*	*Isthmolithus recurvus*
197-1203A-																																						
1R-1, 68–69	300.68	BIO		NN10	late Miocene		P	C										R																				
1R-3, 67–68	303.67	BIO	NN8	NN10	late Miocene		P	C										F																				
1R-CC, 8–14	304.59	PAL	NN8	NN10	late Miocene	Smear slide	P	C										F																				
2R-1, 105–106	310.65	BIO	NN8	NN10	late Miocene		P	C																														
2R-3, 100–101	313.60	BIO	NN8	NN10	late Miocene		P	C																														
2R-CC, 13–18	315.32	PAL	NN8	NN10	late Miocene		P	C										F																				
3R-1, 50–52	319.80	BIO	NN8	NN10	late Miocene		P	C																														
3R-3, 50–52	322.80	BIO	NN8	NN10	late Miocene																																	
3R-5, 50–52	325.80	BIO																																				
3R-CC, 15–20	328.31	PAL			Miocene		P	C										C																				
4R-1, 50–51	329.50	BIO																																				
4R-CC, 9–14	331.50	PAL			Miocene	Smear slide	P	C										F																				
5R-1, 50–51	339.20	BIO																																				
5R-CC, 10–15	341.71	PAL			Miocene		P	F										F																				
6R-CC, 18–23	348.58	PAL			Miocene		P	C										F																				
7R-1, 50–51	358.60	BIO			Miocene		P	C										F																				
7R-3, 50–51	361.60	BIO																																				
7R-5, 49–50	364.59	BIO			Miocene																																	
7R-CC, 9–14	367.38	PAL			Miocene		P	C										F																				
8R-1, 50–51	368.30	BIO																																				
8R-3, 50–51	371.30	BIO																																				
8R-5, 50–51	374.30	BIO	NN2	NN5	early Miocene		P	C										F					R							F								
8R-CC, 14–19	376.36	PAL																																				
9R-1, 50–51	378.00	BIO	NN2		early Miocene		P	F										R												R								
9R-3, 50–51	381.00	BIO																																				
9R-CC, 14–19	381.50	PAL			early Miocene		P	F										R					R							R								
10R-1, 50–51	387.70	BIO																																				
10R-CC, 15–20	390.35	PAL	NP24	NP25	late Oligocene		P	C																							C							
11R-1, 50–51	397.40	BIO			early Oligocene		M	C										R					R							F	A							
11R-3, 50–51	400.40	BIO																																				
11R-CC, 8–13	402.78	PAL	NP21	NP22	early Oligocene		P	C										F					F						R	R	C				F			
12R-1, 49–50	407.09	BIO	NP21	NP22	early Oligocene		P	C										R												F	C				R			
12R-3, 50–51	409.89	BIO	NP21	NP22	early Oligocene		P	F																									F		F			

Table T3 (continued).

Core, section, interval (cm)	Depth	Sample code	Zone		Age	Preparation*	Preservation	Group abundance	Nannofossils																	
			From	To	From				*Cyclicargolithus abisectus*	*Reticulofenestra daviesii*	*Discoaster deflandrei*	*Discoaster druggii*	*Sphenolithus calyculus*	*Sphenolithus delphix*	*Reticulofenestra minutula*	*Reticulofenestra pseudoumbilicus*	*Scyphospaera* spp.	*Calcidiscus leptoporus*	*Discoaster brouweri*	*Discoaster variabilis*	*Discoaster calcaris*	*Reticulofenestra gelida*	*Discoaster hamatus*	*Discoaster bollii*
197-1203A-																										
1R-1, 68–69	300.68	BIO		NN10	late Miocene		P	C							C				R							
1R-3, 67–68	303.67	BIO	NN 8	NN10	late Miocene		P	C												R						
1R-CC, 8–14	304.59	PAL	NN 8	NN10	late Miocene	Smear slide	P	C							C											R
2R-1, 105–106	310.65	BIO	NN 8	NN10	late Miocene		P	C												R				R		
2R-3, 100–101	313.60	BIO	NN 8	NN10	late Miocene		P	C												R						
2R-CC, 13–18	315.32	PAL	NN 8	NN10	late Miocene		P	C							C	C					R	C				
3R-1, 50–52	319.80	BIO	NN 8	NN10	late Miocene		P	C								C			R	R						
3R-3, 50–52	322.80	BIO	NN 8	NN10	late Miocene																					
3R-5, 50–52	325.80	BIO																								
3R-CC, 15–20	328.31	PAL			Miocene		P	C							C											
4R-1, 50–51	329.50	BIO																								
4R-CC, 9–14	331.50	PAL			Miocene	Smear slide	P	C							R			R								
5R-1, 50–51	339.20	BIO																								
5R-CC, 10–15	341.71	PAL			Miocene		P	F																		
6R-CC, 18–23	348.58	PAL			Miocene		P	C							F											
7R-1, 50–51	358.60	BIO			Miocene		P	C																		
7R-3, 50–51	361.60	BIO																								
7R-5, 49–50	364.59	BIO			Miocene												R									
7R-CC, 9–14	367.38	PAL			Miocene		P	C							C	F										
8R-1, 50–51	368.30	BIO																								
8R-3, 50–51	371.30	BIO																								
8R-5, 50–51	374.30	BIO	NN 2	NN 5	early Miocene		P	C				R	R		C											
8R-CC, 14–19	376.36	PAL																								
9R-1, 50–51	378.00	BIO	NN 2		early Miocene		P	F				R	R	F												
9R-3, 50–51	381.00	BIO																								
9R-CC, 14–19	381.50	PAL			early Miocene		P	F			R		F													
10R-1, 50–51	387.70	BIO																								
10R-CC, 15–20	390.35	PAL	NP24	NP25	late Oligocene		P	C	C																	
11R-1, 50–51	397.40	BIO			early Oligocene		M	C	C	R																
11R-3, 50–51	400.40	BIO																								
11R-CC, 8–13	402.78	PAL	NP21	NP22	early Oligocene		P	C																		
12R-1, 49–50	407.09	BIO	NP21	NP22	early Oligocene		P	C	C																	
12R-3, 50–51	409.89	BIO	NP21	NP22	early Oligocene		P	F																		

Table T3 (continued).

Core, section, interval (cm)	Depth	Sample code	Zone		Age	Preparation*	Preservation	Group abundance	Nannofossils																													
			From	To	From				*Ceratolithoides aculeus*	*Cretarhabdus crenulatus*	*Cretarhabdus loriei*	*Marthasterites inconspicuus*	*Micula decussata*	*Quadrum sissinghii*	*Quadrum trifidum*	*Watznaueria barnesae*	*Chiasmolithus grandis*	*Coccolithus pelagicus*	*Discoaster barbadiensis*	*Discoaster binodosus*	*Discoaster lodoensis*	*Ericsonia formosa*	*Sphenolithus moriformis*	*Sphenolithus radians*	*Thoracosphaera saxea*	*Toweius crassus*	*Tribrachiatus orthostylus*	*Zygrhablithus bijugatus*	*Chiasmolithus oamaruensis*	*Cyclicargolithus floridanus*	*Dictyococcites bisectus*	*Discoaster saipanensis*	*Reticulofenestra dictyoda*	*Reticulofenestra hillae*	*Reticulofenestra umbilica*	*Discoaster adamanteus*	*Ericsonia subditicha*	*Isthmolithus recurvus*
12R-CC, 12–16	410.44	PAL	NP21	NP22	early Oligocene		P	C																					R	C	C				C			
13R-1, 50–51	416.80	BIO	NP21	NP22	early Oligocene		P	C																							F							R
13R-CC, 12–17	418.85	PAL	NP21	NP22	early Oligocene		P	C										F					F								F				F			
14R-1, 49–50	426.49	BIO																																				
14R-3, 50–51	429.50	BIO																																				
14R-CC, 8–11	430.15	PAL	NP21				M	C																							C				C		F	R
15R-1, 50–51	436.20	BIO			late Eocene		P	C																				R							A			
15R-3, 50–51	439.20	BIO			late Eocene		P	C																				R								R		
15R-CC, 15–18	440.04	PAL			late Eocene		P	C											R			R	R						R	C	R	R	R	R	R			
16R-1, 50–51	445.60	BIO																																				
16R-3, 50–51	448.10	BIO																																				
16R-CC, 10–13	448.60	PAL	NP12		early Eocene		M	C									R	C	F	R	C	R	R	C	R	F	C	C										
17R-1, 50–51	454.80	BIO																																				
17R-3, 46–47	457.40	BIO																																				
28R-CC, 15–18	553.48	PAL																																				
33R-CC, 3–8	602.56	PAL	CC22	CC23	Campanian		M	F	R	R	R	R	R	R	R	F																						

Notes: * = all smear slides were prepared at variable concentrations. Preservation: M = moderate, P = poor. Abundance: C = common, F = few, R = rare. PAL = paleontology, BIO = biostratigraphy.

Table T3 (continued).

Core, section, interval (cm)	Depth	Sample code	Zone		Age	Preparation	Preservation	Group abundance	Nannofossils												
			From	To	From				*Cyclicargolithus abisectus*	*Reticulofenestra daviesii*	*Discoaster deflandrei*	*Discoaster druggii*	*Sphenolithus calyculus*	*Sphenolithus delphix*	*Reticulofenestra minutula*	*Reticulofenestra pseudoumbilicus*	*Scyphospaera* spp.	*Calcidiscus leptoporus*	*Discoaster brouweri*	*Discoaster variabilis*	*Discoaster calcaris*	*Reticulofenestra gelida*	*Discoaster hamatus*	*Discoaster bollii*
12R-CC, 12–16	410.44	PAL	NP21	NP22	early Oligocene		P	C																
13R-1, 50–51	416.80	BIO	NP21	NP22	early Oligocene		P	C																
13R-CC, 12–17	418.85	PAL	NP21	NP22	early Oligocene		P	C																
14R-1, 49–50	426.49	BIO																						
14R-3, 50–51	429.50	BIO																						
14R-CC, 8–11	430.15	PAL	NP21				M	C																
15R-1, 50–51	436.20	BIO			late Eocene		P	C																
15R-3, 50–51	439.20	BIO			late Eocene		P	C																
15R-CC, 15–18	440.04	PAL			late Eocene		P	C																
16R-1, 50–51	445.60	BIO																						
16R-3, 50–51	448.10	BIO																						
16R-CC, 10–13	448.60	PAL	NP12		early Eocene		M	C																
17R-1, 50–51	454.80	BIO																						
17R-3, 46–47	457.40	BIO																						
28R-CC, 15–18	553.48	PAL																						
33R-CC, 3–8	602.56	PAL	CC22	CC23	Campanian		M	F																

Table T4. Division of the basement sequence into units and subunits with names and curated thickness, Site 1203.

Unit/ Subunit	Core, section	Depth (mbsf)	Unit name	Curated thickness (m)
	197-1203A-			
1	17R-4	457.56	Highly plagioclase-olivine-phyric basalt	7.95
2	18R-2	465.51	Calcareous interbed	0.10
3	18R-2	465.61	Highly plagioclase-olivine-phyric basalt	24.60
4a	20R-6	490.21	Nannofossil-silty-chalk	0.31
4b	20R-6	490.52	Resedimented basalt-tuff	0.42
4c	20R-6	490.94	Basalt-tuff?	1.66
4d	21R-1	492.60	Resedimented basalt-tuff	0.19
4e	21R-1	492.79	Resedimented synvolcanic basalt-tuff	0.70
4f	21R-1	493.49	Basalt-tuff	3.18
4g	21R-3	496.67	Laminated basalt-tuff	0.43
4h	21R-4	497.10	Basalt-tuff	11.24
4i	22R-5	508.34	Resedimented synvolcanic basalt-tuff	5.64
4j	23R-2	513.98	Laminated-bedded vitric siltstone-sandstone	2.19
4k	23R-3	516.17	Resedimented basalt-tuff	6.52
4l	24R-2	522.69	Basalt lapilli-tuff	0.25
4m	24R-2	522.94	Resedimented basalt-tuff	8.19
5	25R-1	531.13	Moderately plagioclase-olivine-phyric basalt	1.94
6	25R-2	533.07	Sparsely plagioclase-phyric basalt	4.78
7a	26R-4	537.85	Bedded vitric siltstone-sandstone	23.72
7b	29R-1	561.57	Laminated volcaniclastic siltstone-sandstone	3.21
7c	29R-4	564.78	Basalt hyaloclastite-tuff	5.37
7d	30R-1	570.15	Hyaloclastite-tuff	0.15
8	30R-1	570.30	Highly plagioclase-olivine-phyric basalt	18.70
9	32R-1	589.00	Basalt-lapilli-tuff	0.77
10	32R-1	589.77	Bedded volcaniclastic siltstone-sandstone	0.56
11	32R-2	590.33	Olivine-plagioclase-phyric basalt	4.58
12	32R-5	594.91	Bedded volcaniclastic siltstone-sandstone	7.76
13	33R-CC	602.67	Plagioclase-basalt hyaloclastite breccia	13.58
14	35R-4	616.25	Moderately plagioclase-phyric basalt	9.49
15a	36R-7	625.74	Bedded vitric siltstone-sandstone	1.76
15b	37R-1	627.50	Calcareous vitric siltstone-sandstone	0.79
16	37R-1	628.29	Aphyric to highly-olivine-phyric basalt	10.37
17	38R-2	638.66	Bedded olivine-plagioclase-basalt hyaloclastite tuff	12.71
18	39R-4	651.37	Moderately plagioclase-olivine-phyric basalt	14.57
19	41R-1	665.94	Vesicular moderately olivine-phyric basalt	19.63
20	43R-1	685.57	Moderately olivine-phyric basalt	36.73
21	47R-1	722.30	Moderately olivine-phyric basalt	19.05
22a	49R-7	741.01	Volcaniclastic vitric-lithic sandstone	0.25
22b	50R-1	741.60	Basalt-lapillistone	13.78
23	51R-3	755.38	Vesicular sparsely olivine-plagioclase-phyric to aphyric basalt	63.39
24	58R-3	818.77	Vesicular aphyric basalt	3.38
25	59R-3	822.15	Basalt hyaloclastite-tuff	0.41
26	59R-3	822.56	Vesicular aphyric basalt	40.55
27	63R-5	863.11	Volcaniclastic sandstone	3.53
28	64R-1	866.64	Volcaniclastic breccia	10.78
29	65R-1	877.42	Vesicular aphyric basalt	8.38
30	66R-1	885.80	Vesicular, sparsely plagioclase-phyric basalt	23.76
31a	68R-4	909.56	Basalt hyaloclastite-tuff	0.10
31b	68R-4	909.66	Highly plagioclase-phyric basalt	0.20
Bottom of hole:		914.60	Total:	452.30

Table T5. Summary of the key characteristics of the volcaniclastic units.

Unit/ Subunit	Sediment type	Stratification	Bedforms	Soft sediment deformation	Grain size	Size grading	Sorting	Components	Basalt glass/clast vesicularity	Cement	Comments
2, 4a	Calcareous interbeds	Laminated	Massive to cross-bedded	Bioturbated at top	Silt to fine sand			Ca = 75%, Cl = 10%, Do = 5%, BGS = 10%			Unit 4a contains nannofossils.
4j, 7a, 15, 7b, 10, 12, 22a, and 27	Vitric and volcaniclastic siltstone-sandstone	Laminated to thin bedded	Plane bedded (massive and cross-stratified beds; internal erosion surfaces)	Loading structures on bedding planes; slump disturbed bedding and microfaults in Unit 4j	Silt to medium sand	Reverse and normal graded beds	Good to moderate	Mixture of basalt glass fragments, carbonate, and siliciclastic material		Carbonate and zeolite?	Units 7b, 10, and 27 contain nannofossils.
4b, 4d, 4e, 4i, 4k, and 4m	Resedimented basalt tuff	Laminated to thin bedded	Plane bedded, with intercalated massive, graded or cross-stratified beds		Very fine to medium ash	Normal, symmetric, or reverse	Moderate (good to poor)	VBG/BGS = 85%–95%, Cy = 5%–10%, L = 0%–10%	Typically highly vesicular	Carbonate or zeolite	Units 4d and 4e may have been emplaced as density currents.
4c, 4f, 4g, 4h, and 25	Basalt tuff (scoria fall deposit)	Medium to thick bedded	Massive to graded beds		Fine to coarse ash	Normal	Good to moderate	VBG = >90%, Cy = <10%	40% to >70%	Zeolite	Deposit contains highly vesicular and delicate reticulite-like clasts. Bedded tephra fall deposited in water.
7c, 7d, 17, and 31a	Basalt hyaloclastite tuff	Thin to medium bedded	Massive or graded beds with rare cross-stratified beds		Very fine to very coarse ash	Normal	Poor	BGS = 60%–90%, Cy = 5%–20%, L = 5%–20%	Non- to poorly vesicular	Carbonate	These deposits comprise non- to poorly vesicular, angular, splinterlike clasts identical to those in hyaloclastite tuffs formed by quenched fragmentation. Unit 17 contains nannofossils.
4l, 9, and 22b	Basalt-lapillistone/ lapilli tuff	None or thick bedded	Massive to graded beds		Fine to medium lapilli	Normal	Moderate	VBG = 95%, L = 5%	40% to >70%	Zeolite or carbonate	Subaerial scoria fall deposits. Unit 22b contains ballistic lava blocks and armored lapilli.
13	Breccia: plagioclase-basalt hyaloclastite breccia	None	Massive		Breccia	None	Very poor	BG = 50%, L = 50%		Carbonate	10- to 125-mm plagioclase-basalt lithic blocks in a lapilli matrix consisting of plagioclase-basalt glass and lithic fragments. Lithology is identical to the underlying lava.
28	Breccia: volcaniclastic breccia	None	Massive		Breccia	None	Very poor	L = 50%, Ca = 50%		Carbonate	Matrix supported; 50- to 100-mm basalt lava lobes and lithic blocks in calcareous mud matrix (peperite-like association). Lithology is identical to the underlying lava.

Note: Ca = carbonate, Cl = clay, Do = dolomite, BGS = basalt glass shards, VBG = vesicular basalt glass fragments (tephra or scoria clasts), Cy = crystal fragments, L = lithic fragments, BG = splinter-shaped basalt glass fragments.

Table T6. Key structural and morphological features of the basement lava flow units, Site 1203.

Unit/ Subunit	Core, section	Depth (mbsf)	Unit name	Thickness (m) Recovered	Thickness (m) Cored	Recovery (%)	Simple	Lobed	Average lobe thickness (m)	Smooth glassy lobe margins	Vesicularity	VUcr	Mai	VBcr	PV	VC	HVS	Jointing pattern	Phenocryst concentration in lobe interior	Lava flow type
	197-1203A-																			
1	17R-4	457.56	Highly plagioclase-olivine-phyric basalt	3.20	7.95	40		x	0.53 (0.25)	x	nv-spv							Cube jointing		Pillow lava
3	18R-2	465.61	Highly plagioclase-olivine-phyric basalt	18.00	24.60	73		x	0.58 (0.40)	x	nv-spv							Cube jointing		Pillow lava
5	25R-1	531.13	Moderately plagioclase-olivine-phyric basalt	1.81	1.94	93	x		—	x	spv		x	x	x			Irregular	x	Pahoehoe sheet lobe
6	25R-2	533.07	Sparsely plagioclase-phyric basalt	3.23	4.78	68	x		—	NR	nv-hiv(?)	NR	x				x	Nob		Pahoehoe sheet lobe
8	30R-1	570.30	Highly plagioclase-olivine-phyric basalt	5.38	18.70	29		x	0.34 (0.15)	x	nv-spv							Cube jointing		Pillow lava
11	32R-2	590.33	Olivine-plagioclase-phyric basalt	4.67	4.58	102	x		—	x	nv-hiv	x	x	x		x		Irregular	x	Pahoehoe sheet lobe
14	35R-4	616.25	Moderately plagioclase-phyric basalt	8.29	9.49	87		x	0.83 (0.34)	x	nv-spv							Cube jointing	x	Pillow lava
16	37R-1	628.29	Highly olivine-phyric basalt	5.05	10.37	49	x		—	x	nv-hiv	x	x	x				Irregular	x	Pahoehoe sheet lobe
18	39R-4	651.37	Moderately plagioclase-olivine-phyric basalt	10.56	14.57	72		x	0.56 (0.33)	x	nv-spv							Cube jointing		Pillow lava
19	41R-1	665.94	Vesicular, moderately olivine-phyric basalt	16.77	19.63	85		x	0.51 (0.35)	x	hiv	x	x	x	x	x	x	Irregular	x	Compound pahoehoe
20	43R-1	685.57	Moderately olivine basalt	23.47	36.73	64		x	0.57 (0.39)	x	spv-mov		x	x	x	x	x	Cube jointing		Hybrid pillow-pahoehoe lava
21	47R-1	722.30	Moderately olivine basalt(?)	16.51	19.05	87		x	0.37 (0.6)	x	spv-mov				x		x	Irregular/ cube jointing		Hybrid pillow-pahoehoe lava*
23	51R-3	755.38	Vesicular, sparsely olivine-plagioclase-phyric to aphyric basalt	53.70	63.39	85		x	0.59 (0.44)	x	hiv	x	x	x	x	x	x	Irregular		Compound pahoehoe
24	58R-3	818.77	Vesicular aphyric basalt	4.39	4.65	94	x	x	—	NR	nv-hiv	NR		NR				Irregular		Pahoehoe sheet lobe†
26	59R-3	822.56	Vesicular aphyric basalt	21.98	40.55	54		x	0.85 (0.79)	x	mov-hiv	x	x	x		x		Irregular		Compound pahoehoe
29	65R-1	877.42	Vesicular aphyric basalt	3.96	8.38	47		x	0.40 (0.27)	x	mov-hiv	x	x	x	x			Irregular		Compound pahoehoe
30	66R-1	885.80	Vesicular, sparsely plagioclase-phyric basalt	14.80	23.76	62		x	0.38 (0.17)	x	hiv	x	x	x	x	x		Irregular		Compound pahoehoe
31b	68R-4	909.66	Highly plagioclase-phyric basalt	0.20	0.20	100		x	—	x	nv							Cube jointing		Pillow lava
Bottom of hole:		914.60	Total:	215.97	313.32	69														
			Average recovery:			57														

Notes: VUcr = vesicular upper crust, Mai = massive lobe interior, VBcr = vesicular basal crust, PV = pipe vesicles, VC = vesicle cylinders, HVS = horizontal vesicle sheet. Vesicularity: nv = nonvesicular, spv = sparsely vesicular, hiv = highly vesicular, mov = moderately vesicular. NR = not recovered. Average lobe thickness includes standard deviation in parentheses. * = largest lobe is ~14.2 m and is not included in the average. † = thick lobe, irregular jointing; small lobes, cube jointing.

Table T7. Summary of the opaque mineralogy of basement rocks, Site 1203.

Basalt unit	Core, section, interval (cm)	Titanomagnetite description	Other opaque minerals
	197-1203A-		
1	17R-4, 27–30	Completely altered to maghemite	None
3	18R-3, 46–48	Completely altered to maghemite	None
5	25R-1, 65–67	Ilmenite oxidation exsolution lamellae	Pentlandite
6	26R-3, 39–41	Unaltered	Pentlandite
8	31R-1, 29–32	Very fine grained, indistinct	None
11	32R-1, 85–87	Unaltered/slight ilmenite oxidation lamellae	Cr spinel, pentlandite
14	35R-4, 47–49	Unaltered	Cr spinel, pentlandite
16	37R-3, 10–13	Unaltered/slight ilmenite oxidation lamellae	Cr spinel, pentlandite
18	40R-5, 119–121	Unaltered	Secondary pyrite
19	42R-5, 20–23	Unaltered, very fine grained	Secondary pyrite
20	45R-6, 45–47	Unaltered, very fine grained	None
21	48R-1, 57–61	Slight maghemite alteration	Secondary pyrite
23	51R-4, 93–96	Unaltered	Secondary pyrite
24	59R-2, 99–101	Unaltered	Pentlandite, secondary pyrite
26	59R-5, 30–32	Very sparse and small titanomagnetite	None
29	65R-4, 21–24	Partially to completely altered to maghemite	None
30	68R-3, 16–18	Very fine grained, partially altered to maghemite	None
31	68R-4, 29–30	Very fine grained, indistinct	Pentlandite

Table T8. Whole-rock major and trace elements for basement rocks determined by ICP-AES, Hole 1203A. (Continued on next two pages.)

Core, section:	17R-4	19R-1	19R-2	20R-4	21R-4	25R-1	26R-3	31R-1	32R-3	32R-5	35R-3	35R-4	36R-4
Interval (cm):	34–36	19–21	136–138	44–47	86–88	65–67	39–41	27–28	85–87	87–88	49–52	47–49	92–95
Piece:	1C	2A	15	1B	8	4C	1B	4	1E	1C	5	1F	2D
Unit:	1	3	3	3	4	5	6	8	11	11	13	14	14
Rock type:	Plagioclase-olivine-phyric basalt	Plagioclase-olivine-phyric basalt	Plagioclase-olivine-phyric basalt	Plagioclase-olivine-phyric basalt	Basalt tuff	Plagioclase-olivine-phyric basalt	Plagioclase phyric basalt	Plagioclase-olivine phyric basalt	Olivine-rich basalt (center)	Olivine-rich basalt (margin)	Basalt clast	Plagioclase-phyric basalt	Plagioclase-phyric basalt
Depth (mbsf):	457.90	473.59	476.26	487.70	497.96	531.75	536.82	579.67	592.63	594.74	615.41	616.65	622.37
Major element oxide (wt%):													
SiO_2	48.4	48.2	47.7	48.0	43.4	48.2	45.7	47.2	44.2	47.6	49.6	49.8	48.3
TiO_2	1.91	1.90	1.80	1.79	1.63	2.02	1.87	1.81	0.81	1.78	1.99	1.65	1.66
Al_2O_3	16.2	15.8	15.3	15.1	15.1	16.4	15.4	15.0	8.5	15.6	15.5	18.2	17.9
Fe_2O_3	10.8	11.2	12.2	10.9	10.2	11.6	11.9	13.5	13.0	11.6	10.3	9.78	9.59
MnO	0.15	0.15	0.17	0.16	0.15	0.13	0.17	0.18	0.19	0.13	0.19	0.14	0.13
MgO	5.92	5.30	5.96	6.89	10.8	7.30	9.67	5.70	25.1	7.69	5.51	6.06	6.40
CaO	11.7	11.8	12.1	11.3	1.59	9.25	8.14	11.6	5.94	10.6	11.8	12.2	11.8
Na_2O	2.90	2.78	2.68	2.61	4.09	3.41	2.74	2.76	1.26	2.81	2.99	2.85	2.80
K_2O	0.63	0.91	0.69	0.13	1.93	0.41	0.36	0.71	0.14	0.18	0.98	0.10	0.10
P_2O_5	0.20	0.22	0.19	0.21	0.17	0.21	0.20	0.18	0.07	0.16	0.21	0.17	0.18
Totals:	98.75	98.23	98.84	97.17	89.03	98.93	96.11	98.62	99.19	98.13	99.15	100.94	98.84
LOI	1.48	1.74	2.10	1.33	11.73	1.54	3.59	1.31	0.90	1.45	1.13	0.86	1.14
Mg#	0.55	0.51	0.52	0.58	0.70	0.58	0.64	0.48	0.81	0.59	0.54	0.58	0.59
Trace element (ppm):													
Sr	258	250	244	247	860	269	214	239	121	238	253	281	277
Ba	40.6	38.9	33.6	31.1	55.1	59.9	54.8	31.5	21.8	35.5	63.5	28.4	28.7
Sc	39.4	38.6	37.0	38.1	33.4	34.3	33.8	40.5	20.3	40.6	43.8	39.5	39.4
V	270	301	301	299	251	298	278	315	146	313	358	294	302
Cr	262	263	259	329	244	251	261	243	814	260	268	298	276
Co	42.6	42.0	45.7	68.4	42.8	40.6	53.5	55.4	73.8	44.7	58.6	50.8	45.6
Ni	75.8	131	138	201	112	145	188	61.8	1224	82.1	114	82.8	86.3
Cu	150	91	122	128	58.7	80.4	47.6	91.9	61.5	145	77.8	130	119
Zn	105	189	84.0	138	69.7	90.9	107	118	114	94.6	107	76.9	107
Y	29.1	31.8	29.5	26.8	25.2	27.4	27.6	27.9	12.9	26.0	31.4	25.4	24.7
Zr	123	127	117	124	115	131	128	112	44.2	104	124	100	102

Notes: LOI = loss on ignition at 1025°C for 4 hr. Mg# = MgO/(MgO+FeO), in molar percent, with FeO calculated (as 90% of total Fe). In all figures all major element data are renormalized to 100% to correct for variable LOI. This table is also available in **ASCII.**

Table T8 (continued).

Core, section:	37R-3	38R-1	40R-5	42R-5	45R-6	48R-1	51R-1	51R-4	52R-6	54R-3	57R-2
Interval (cm):	10–13	125–128	121–123	20–23	45–47	57–58	14–17	93–95	12–14	15–18	127–129
Piece:	1A	1I	9B	1A	2B	2	4	2A	1B	1G	29
Unit:	16	16	18	19	20	21	22	23	23	23	23
Rock type:	Olivine-rich basalt (center)	Olivine-rich basalt (margin)	Plagioclase-olivine-phyric basalt	Olivine-phyric basalt	Olivine-phyric basalt	Olivine-phyric basalt	Basalt clast	Olivine-plagioclase-phyric to aphyric basalt	Olivine-plagioclase-phyric to aphyric basalt	Olivine-plagioclase-phyric to aphyric basalt	Olivine-plagioclase-phyric to aphyric basalt
Depth (mbsf):	630.60	638.35	662.43	681.39	710.78	727.67	751.34	756.45	767.98	783.03	811.67
Major element oxide (wt%):											
SiO_2	44.5	48.4	49.3	46.9	44.8	45.9	46.7	47.0	46.0	46.7	46.6
TiO_2	0.76	1.38	1.70	1.46	2.14	1.96	2.08	2.56	3.23	2.56	2.77
Al_2O_3	9.24	15.8	16.7	15.2	15.4	14.9	15.6	14.8	13.0	14.7	14.8
Fe_2O_3	12.2	12.5	9.41	9.89	13.3	12.7	10.6	10.5	13.4	11.9	12.3
MnO	0.16	0.16	0.19	0.18	0.22	0.14	0.19	0.31	0.28	0.17	0.19
MgO	24.3	8.39	7.37	9.73	4.17	8.72	7.40	6.29	6.67	6.90	7.99
CaO	6.22	11.1	11.9	11.2	11.2	7.55	10.9	10.5	10.4	9.15	7.78
Na_2O	1.24	2.41	2.82	2.24	2.34	3.00	2.90	2.96	3.09	3.24	3.45
K_2O	0.08	0.15	0.39	0.07	1.81	0.31	0.20	1.28	0.32	0.43	0.52
P_2O_5	0.08	0.16	0.22	0.18	0.26	0.21	0.23	0.51	0.67	0.51	0.51
Totals:	98.83	100.42	99.88	97.08	95.61	95.38	96.76	96.65	97.07	96.21	96.86
LOI	1.31	1.51	1.79	3.71	5.20	2.76	3.03	3.16	2.31	3.17	3.19
Mg #	0.81	0.60	0.63	0.68	0.41	0.60	0.61	0.57	0.52	0.56	0.59
Trace element (ppm):											
Sr	125	199	267	204	234	183	231	229	234	237	237
Ba	13.5	25.4	30.4	15.4	41.3	40.5	22.9	131.8	67.9	55.5	56.9
Sc	21.6	37.0	39.9	35.1	39.6	37.5	37.3	37.1	44.9	36.7	40.0
V	156	270	291	262	371	332	331	336	395	329	353
Cr	1715	351	285	543	282	248	247	212	190	211	188
Co	69.1	65.3	56.9	59.9	40.6	45.0	47.9	55.7	53.2	55.9	53.1
Ni	1330	174	189	283	97.8	104	122	103	55.8	65.2	85.7
Cu	72.1	155	106	79.5	51.3	86.5	89.3	68.4	82.9	70.7	83.4
Zn	75.1	84.7	112	59.7	114	107	89.8	111	155	112	125
Y	16.3	23.5	27.6	23.0	35.3	31.1	32.3	46.3	57.6	44.2	45.5
Zr	44.0	77.7	113	88.0	132	121	128	247	315	246	265

Table T8 (continued).

Core, section:	59R-2	59R-5	63R-3	65R-4	66R-3	68R-3
Interval (cm):	99–101	30–32	134–137	24–25	11–14	16–18
Piece:	2B	5	24A	3	1C	4
Unit:	24	26	26	29	30	30
Rock type:	Aphyric basalt	Aphyric basalt	Aphyric basalt	Aphyric basalt	Plagioclase-phyric basalt	Plagioclase-phyric basalt
Depth (mbsf):	820.85	824.40	861.30	880.18	888.87	908.16
Major element oxide (wt%):						
SiO_2	48.2	45.2	46.3	45.8	42.7	46.2
TiO_2	1.63	3.28	2.71	3.40	3.02	2.98
Al_2O_3	15.5	14.4	14.4	14.5	13.1	13.7
Fe_2O_3	11.0	13.3	11.3	12.8	15.0	11.5
MnO	0.15	0.19	0.20	0.18	0.14	0.23
MgO	7.66	7.30	9.89	6.40	7.04	6.73
CaO	11.3	7.64	6.01	8.10	7.91	9.29
Na_2O	2.65	3.07	3.44	2.94	2.69	2.71
K_2O	0.11	1.04	0.50	1.34	1.83	1.61
P_2O_5	0.20	0.72	0.51	0.57	0.63	0.48
Totals:	98.41	96.14	95.26	95.98	94.03	95.48
LOI	1.82	3.91	5.21	3.97	6.73	3.99
Mg #	0.61	0.55	0.66	0.52	0.51	0.56
Trace element (ppm):						
Sr	229	211	223	253	225	249
Ba	38.3	49.0	64.4	63.3	60.7	61.8
Sc	38.7	39.8	33.1	41.4	37.0	36.9
V	289	389	324	379	411	404
Cr	291	154	171	177	156	161
Co	44.5	63.1	54.4	60.1	45.4	66.5
Ni	117	119	128	75.8	51.9	118
Cu	122	59.7	55.7	28.2	14.3	142
Zn	82.7	153	93.0	129	103	111
Y	27.9	63.8	42.4	46.0	47.2	44.7
Zr	109	310	257	227	206	199

Table T9. Shipboard characteristic remanent magnetization inclination averages and summary statistics based on principal component analyses of alternating-field demagnetization data, Site 1203.

Basalt unit	*N*	Point inc (°)	Inc_{95} (°)	*k*
1	5	36.0	10.5	74
3	17	29.8	4.3	63
5	4	62.8	5.4	489
6	5	60.3	5.2	295
8	5	62.2	25.6	13
11	4	70.6	11.2	116
14	11	26.9	4.9	87
16	5	31.0	15.2	35
18	13	35.2	5.2	62
19	22	43.3	2.6	126
20	26	49.9	3.8	53
21	19	51.3	3.5	88
23	31	46.4	1.8	191
24	5	53.8	6.8	176
26	12	42.3	4.5	91
29, 30	13	40.9	2.9	199
Average:	16	48.0	8.4	19

Notes: Estimate of dispersion (*S*), based on the transformation of Cox (1970) = 17.7°. *N* = number of determinations within each unit. Point inc = estimation of the inclination mean based on the averaging method of McFadden and Reid (1982). Inc_{95} = estimation of 95% confidence interval of inclination. *k* = estimate of precision parameter. *N* for "Average" values is the estimated number of independent time units (see text).

Table T10. Shipboard characteristic remanent magnetization inclination averages and summary statistics based on principal component analyses of alternating-field demagnetization data, excluding results from basement Units 1 and 3, Site 1203.

Basalt unit	*N*	Point inc (°)	Inc_{95} (°)	*k*
5	4	62.8	5.4	489
6	5	60.3	5.2	295
8	5	62.2	25.6	13
11	4	70.6	11.2	116
14	11	26.9	4.9	87
16	5	31.0	15.2	35
18	13	35.2	5.2	62
19	22	43.3	2.6	126
20	26	49.9	3.8	53
21	19	51.3	3.5	88
23	31	46.4	1.8	191
24	5	53.8	6.8	176
26	12	42.3	4.5	91
29, 30	13	40.9	2.9	199
Average:	14	50.0	9.0	20

Notes: Because of the presence of maghemite, alternating-field demagnetization may be insufficient to clearly separate multiple directional components that could compose the natural remanent magnetization of basement Units 1 and 3 (see **"Discussion,"** p. 36, in "Paleomagnetism and Rock Magnetism."). Estimate of dispersion (*S*), based on the transformation of Cox (1970) = 17.3°. *N* = number of determinations within each unit. Point inc = estimation of the inclination mean based on the averaging method of McFadden and Reid (1982). Inc_{95} = estimation of 95% confidence interval of inclination. *k* = estimate of precision parameter. *N* for "Average" values is the estimated number of independent time units (see text).

Table T11. Magnetic susceptibility measurements, Site 1203.

Core, section, interval (cm)	Depth (mbsf)	Magnetic susceptibility (10^{-6} SI)	Corrected susceptibility (10^{-6} SI)
197-1203A-			
1R-1, 5	300.05	3.0	3.03
1R-1, 10	300.10	2.8	2.85
1R-1, 15	300.15	1.8	1.87
1R-1, 20	300.20	1.6	1.70
1R-1, 25	300.25	–0.2	–0.08
1R-1, 30	300.30	5.8	5.95
1R-1, 35	300.35	1.6	1.77
1R-1, 40	300.40	1.8	1.99
1R-1, 45	300.45	1.0	1.22
1R-1, 50	300.50	0.4	0.64
1R-1, 55	300.55	0.6	0.86
1R-1, 60	300.60	–0.6	–0.29
1R-1, 65	300.65	–0.4	–0.05
1R-1, 70	300.70	–0.2	0.19
1R-1, 75	300.75	–0.2	0.24
1R-1, 80	300.80	–0.2	0.28
1R-1, 85	300.85	2.4	2.92
1R-1, 90	300.90	3.6	4.17
1R-1, 95	300.95	1.2	1.81
1R-1, 100	301.00	3.2	3.86
1R-1, 105	301.05	–0.4	0.30
1R-1, 110	301.10	1.0	1.74
1R-1, 115	301.15	–1.4	–0.61
1R-1, 120	301.20	–1.2	–0.37
1R-1, 125	301.25	–1.4	–0.49
1R-1, 130	301.30	–1.6	–0.64
1R-1, 135	301.35	–1.4	–0.36
1R-1, 140	301.40	–1.8	–0.71
1R-2, 5	301.55	1.4	1.41
1R-2, 10	301.60	2.4	2.42
1R-2, 15	301.65	1.6	1.64
1R-2, 20	301.70	5.0	5.05
1R-2, 25	301.75	3.4	3.46
1R-2, 30	301.80	3.6	3.67
1R-2, 35	301.85	1.4	1.48
1R-2, 40	301.90	0.6	0.69
1R-2, 45	301.95	1.4	1.50
1R-2, 50	302.00	3.6	3.71
1R-2, 55	302.05	1.8	1.93
1R-2, 60	302.10	6.4	6.55
1R-2, 65	302.15	0.6	0.77
1R-2, 70	302.20	1.4	1.59
1R-2, 75	302.25	1.4	1.61
1R-2, 80	302.30	0.8	1.03
1R-2, 85	302.35	1.2	1.45
1R-2, 90	302.40	1.6	1.87
1R-2, 95	302.45	1.6	1.89
1R-2, 100	302.50	0.8	1.11
1R-2, 105	302.55	1.4	1.73
1R-2, 110	302.60	0.8	1.15
1R-2, 115	302.65	0.4	0.77
1R-2, 120	302.70	0.4	0.79
1R-2, 125	302.75	1.0	1.43
1R-2, 130	302.80	3.4	3.86
1R-2, 135	302.85	5.2	5.70
1R-2, 140	302.90	0.6	1.12
1R-2, 145	302.95	0.0	0.56
1R-3, 5	303.05	2.4	2.41
1R-3, 10	303.10	5.2	5.22
1R-3, 15	303.15	5.8	5.83
1R-3, 20	303.20	3.6	3.64
1R-3, 25	303.25	3.0	3.05
1R-3, 30	303.30	1.0	1.06
1R-3, 35	303.35	1.0	1.07
1R-3, 40	303.40	1.0	1.08
1R-3, 45	303.45	1.8	1.89
1R-3, 50	303.50	2.0	2.10
1R-3, 55	303.55	3.4	3.51
1R-3, 60	303.60	2.6	2.73
1R-3, 65	303.65	3.0	3.14
1R-3, 70	303.70	3.2	3.36
1R-3, 75	303.75	3.2	3.38
1R-3, 80	303.80	18.0	18.20
1R-3, 85	303.85	4.2	4.42
1R-3, 90	303.90	0.6	0.83
1R-3, 95	303.95	0.4	0.65
1R-3, 100	304.00	1.6	1.87
1R-3, 105	304.05	0.0	0.29
1R-3, 110	304.10	0.0	0.30
1R-3, 115	304.15	0.0	0.32
1R-3, 120	304.20	–0.4	–0.06
1R-3, 125	304.25	–0.6	–0.23
1R-3, 130	304.30	–0.4	–0.01
1R-3, 135	304.35	–0.2	0.23
1R-3, 140	304.40	0.0	0.45
1R-3, 145	304.45	0.0	0.48
2R-1, 5	309.65	4.0	3.98
2R-1, 10	309.70	2.6	2.57
2R-1, 15	309.75	4.0	3.95
2R-1, 20	309.80	2.8	2.74
2R-1, 25	309.85	2.6	2.52
2R-1, 30	309.90	3.2	3.10
2R-1, 35	309.95	3.4	3.29
2R-1, 40	310.00	2.8	2.67
2R-1, 45	310.05	4.6	4.46
2R-1, 50	310.10	2.8	2.64
2R-1, 55	310.15	3.0	2.83
2R-1, 60	310.20	3.0	2.80
2R-1, 65	310.25	3.2	2.97
2R-1, 70	310.30	2.6	2.34
2R-1, 75	310.35	3.0	2.71
2R-1, 80	310.40	3.2	2.88
2R-1, 85	310.45	2.8	2.45
2R-1, 90	310.50	3.4	3.03
2R-1, 95	310.55	3.2	2.80
2R-1, 100	310.60	3.6	3.17
2R-1, 105	310.65	3.4	2.94
2R-1, 110	310.70	3.6	3.11
2R-1, 115	310.75	4.4	3.88
2R-1, 120	310.80	4.8	4.25
2R-1, 125	310.85	3.6	3.00
2R-1, 130	310.90	3.4	2.77
2R-1, 135	310.95	3.2	2.51
2R-1, 140	311.00	3.2	2.48
2R-1, 145	311.05	3.0	2.23
2R-2, 5	311.15	2.0	2.01
2R-2, 10	311.20	2.0	2.01
2R-2, 15	311.25	1.8	1.82
2R-2, 20	311.30	2.0	2.02
2R-2, 25	311.35	1.0	1.03
2R-2, 30	311.40	1.6	1.64
2R-2, 35	311.45	1.4	1.44
2R-2, 40	311.50	1.2	1.25
2R-2, 45	311.55	0.8	0.85
2R-2, 50	311.60	1.0	1.06
2R-2, 55	311.65	0.6	0.67
2R-2, 60	311.70	0.4	0.48
2R-2, 65	311.75	1.2	1.29
2R-2, 70	311.80	1.0	1.10
2R-2, 75	311.85	1.2	1.31
2R-2, 80	311.90	2.0	2.12
2R-2, 85	311.95	2.0	2.13

Note: Only a portion of this table appears here. The complete table is available in **ASCII.**

Table T12. GRA bulk density measurements, Site 1203.

Core, section, interval (cm)	Depth (mbsf)	Bulk density (g/cm^3)
197-1203A-		
1R-1, 5	300.05	1.613
1R-1, 10	300.10	1.573
1R-1, 15	300.15	1.547
1R-1, 20	300.20	1.577
1R-1, 25	300.25	1.584
1R-1, 30	300.30	1.545
1R-1, 35	300.35	1.521
1R-1, 40	300.40	1.533
1R-1, 45	300.45	1.522
1R-1, 50	300.50	1.494
1R-1, 55	300.55	1.500
1R-1, 60	300.60	1.539
1R-1, 65	300.65	1.462
1R-1, 70	300.70	1.521
1R-1, 75	300.75	1.632
1R-1, 80	300.80	1.648
1R-1, 85	300.85	1.681
1R-1, 90	300.90	1.675
1R-1, 95	300.95	1.666
1R-1, 100	301.00	1.631
1R-1, 105	301.05	1.578
1R-1, 110	301.10	1.468
1R-1, 115	301.15	1.406
1R-1, 120	301.20	1.316
1R-1, 125	301.25	1.387
1R-1, 130	301.30	1.399
1R-1, 135	301.35	1.389
1R-1, 140	301.40	1.406
1R-2, 5	301.55	1.551
1R-2, 10	301.60	1.628
1R-2, 15	301.65	1.640
1R-2, 20	301.70	1.633
1R-2, 25	301.75	1.576
1R-2, 30	301.80	1.484
1R-2, 35	301.85	1.376
1R-2, 40	301.90	1.385
1R-2, 45	301.95	1.396
1R-2, 50	302.00	1.461
1R-2, 55	302.05	1.463
1R-2, 60	302.10	1.480
1R-2, 65	302.15	1.478
1R-2, 70	302.20	1.503
1R-2, 75	302.25	1.538
1R-2, 80	302.30	1.537
1R-2, 85	302.35	1.558
1R-2, 90	302.40	1.536
1R-2, 95	302.45	1.480
1R-2, 100	302.50	1.488
1R-2, 105	302.55	1.501
1R-2, 110	302.60	1.564
1R-2, 115	302.65	1.619
1R-2, 120	302.70	1.685
1R-2, 125	302.75	1.696
1R-2, 130	302.80	1.678
1R-2, 135	302.85	1.503
1R-2, 140	302.90	1.442
1R-2, 145	302.95	1.445
1R-3, 5	303.05	1.558
1R-3, 10	303.10	1.590
1R-3, 15	303.15	1.683
1R-3, 20	303.20	1.752
1R-3, 25	303.25	1.741
1R-3, 30	303.30	1.512
1R-3, 35	303.35	1.487
1R-3, 40	303.40	1.469
1R-3, 45	303.45	1.496
1R-3, 50	303.50	1.553
1R-3, 55	303.55	1.771
1R-3, 60	303.60	1.770
1R-3, 65	303.65	1.761
1R-3, 70	303.70	1.708
1R-3, 75	303.75	1.652
1R-3, 80	303.80	1.577
1R-3, 85	303.85	1.520
1R-3, 90	303.90	1.554
1R-3, 95	303.95	1.529
1R-3, 100	304.00	1.566
1R-3, 105	304.05	1.586
1R-3, 110	304.10	1.579
1R-3, 115	304.15	1.559
1R-3, 120	304.20	1.579
1R-3, 125	304.25	1.594
1R-3, 130	304.30	1.597
1R-3, 135	304.35	1.593
1R-3, 140	304.40	1.570
1R-3, 145	304.45	1.449
2R-1, 5	309.65	1.300
2R-1, 10	309.70	1.370
2R-1, 15	309.75	1.390
2R-1, 20	309.80	1.414
2R-1, 25	309.85	1.445
2R-1, 30	309.90	1.460
2R-1, 35	309.95	1.460
2R-1, 40	310.00	1.460
2R-1, 45	310.05	1.426
2R-1, 50	310.10	1.477
2R-1, 55	310.15	1.453
2R-1, 60	310.20	1.462
2R-1, 65	310.25	1.457
2R-1, 70	310.30	1.452
2R-1, 75	310.35	1.439
2R-1, 80	310.40	1.441
2R-1, 85	310.45	1.442
2R-1, 90	310.50	1.467
2R-1, 95	310.55	1.456
2R-1, 100	310.60	1.446
2R-1, 105	310.65	1.473
2R-1, 110	310.70	1.467
2R-1, 115	310.75	1.447
2R-1, 120	310.80	1.451
2R-1, 125	310.85	1.450
2R-1, 130	310.90	1.459
2R-1, 135	310.95	1.458
2R-1, 140	311.00	1.458
2R-1, 145	311.05	1.439
2R-2, 5	311.15	1.432
2R-2, 10	311.20	1.418
2R-2, 15	311.25	1.419
2R-2, 20	311.30	1.450
2R-2, 25	311.35	1.491
2R-2, 30	311.40	1.436
2R-2, 35	311.45	1.445
2R-2, 40	311.50	1.462
2R-2, 45	311.55	1.462
2R-2, 50	311.60	1.454
2R-2, 55	311.65	1.461
2R-2, 60	311.70	1.435
2R-2, 65	311.75	1.450
2R-2, 70	311.80	1.458
2R-2, 75	311.85	1.447
2R-2, 80	311.90	1.469
2R-2, 85	311.95	1.450
2R-2, 90	312.00	1.519
2R-2, 95	312.05	1.496
2R-2, 100	312.10	1.427
2R-2, 105	312.15	1.457
2R-2, 110	312.20	1.467
2R-2, 115	312.25	1.499
2R-2, 120	312.30	1.536
2R-2, 125	312.35	1.528
2R-2, 130	312.40	1.523
2R-2, 135	312.45	1.499
2R-2, 140	312.50	1.516
2R-2, 145	312.55	1.514
2R-3, 5	312.65	1.634
2R-3, 10	312.70	1.633
2R-3, 15	312.75	1.618
2R-3, 20	312.80	1.642
2R-3, 25	312.85	1.657
2R-3, 30	312.90	1.623
2R-3, 35	312.95	1.599
2R-3, 40	313.00	1.539
2R-3, 45	313.05	1.722
2R-3, 50	313.10	1.767
2R-3, 55	313.15	1.796
2R-3, 60	313.20	1.732
2R-3, 65	313.25	1.615
2R-3, 70	313.30	1.669
2R-3, 75	313.35	1.711
2R-3, 80	313.40	1.757
2R-3, 85	313.45	1.718
2R-3, 90	313.50	1.686
2R-3, 95	313.55	1.699
2R-3, 100	313.60	1.694
2R-3, 105	313.65	1.690
2R-3, 110	313.70	1.640
2R-3, 115	313.75	1.629
2R-3, 120	313.80	1.464
2R-3, 125	313.85	1.525
2R-3, 130	313.90	1.558
2R-3, 135	313.95	1.556
2R-3, 140	314.00	1.577
2R-3, 145	314.05	1.672
2R-4, 5	314.15	1.693
2R-4, 10	314.20	1.627
2R-4, 15	314.25	1.508
2R-4, 20	314.30	1.465
2R-4, 25	314.35	1.473
2R-4, 30	314.40	1.516
2R-4, 35	314.45	1.536
2R-4, 40	314.50	1.487
2R-4, 45	314.55	1.452
2R-4, 50	314.60	1.559
2R-4, 55	314.65	1.579
2R-4, 60	314.70	1.468
2R-4, 65	314.75	1.529
2R-4, 70	314.80	1.551
2R-4, 75	314.85	1.544
2R-4, 80	314.90	1.542
2R-4, 85	314.95	1.483
2R-4, 90	315.00	1.528
2R-4, 95	315.05	1.712
2R-4, 100	315.10	1.755
3R-1, 5	319.35	1.486
3R-1, 10	319.40	1.514
3R-1, 15	319.45	1.518
3R-1, 20	319.50	1.542
3R-1, 25	319.55	1.554
3R-1, 30	319.60	1.646

Note: Only a portion of this table appears here. The complete table is available in **ASCII.**

Table T13. Natural gamma ray measurements, Site 1203.

Core, section	Depth (mbsf)	Total counts (cps)
197-1203A-		
1R-1	300.10	14.75
1R-1	300.20	14.60
1R-1	300.30	15.20
1R-1	300.40	15.00
1R-1	300.50	15.55
1R-1	300.60	14.40
1R-1	300.70	13.90
1R-1	300.80	17.20
1R-1	300.90	17.95
1R-1	301.00	17.40
1R-1	301.10	16.75
1R-1	301.20	14.60
1R-1	301.30	14.25
1R-2	301.60	16.00
1R-2	301.70	16.05
1R-2	301.80	15.75
1R-2	301.90	15.30
1R-2	302.00	15.70
1R-2	302.10	13.95
1R-2	302.20	15.95
1R-2	302.30	15.20
1R-2	302.40	14.70
1R-2	302.50	14.75
1R-2	302.60	16.30
1R-2	302.70	16.80
1R-2	302.80	16.00
1R-2	302.90	16.50
1R-3	303.10	16.05
1R-3	303.20	16.35
1R-3	303.30	14.85
1R-3	303.40	15.15
1R-3	303.50	15.50
1R-3	303.60	16.60
1R-3	303.70	17.45
1R-3	303.80	14.55
1R-3	303.90	13.85
1R-3	304.00	16.35
1R-3	304.10	16.80
1R-3	304.20	14.65
1R-3	304.30	15.15
1R-3	304.40	15.35
2R-1	309.70	14.40
2R-1	309.80	18.00
2R-1	309.90	17.10
2R-1	310.00	17.25
2R-1	310.10	15.45
2R-1	310.20	17.60
2R-1	310.30	16.80
2R-1	310.40	17.65
2R-1	310.50	18.40
2R-1	310.60	17.05
2R-1	310.70	15.95
2R-1	310.80	17.20
2R-1	310.90	17.40
2R-1	311.00	15.90
2R-2	311.20	17.15
2R-2	311.30	16.90
2R-2	311.40	17.05
2R-2	311.50	14.90
2R-2	311.60	15.10
2R-2	311.70	16.15
2R-2	311.80	18.45
2R-2	311.90	17.15
2R-2	312.00	18.20
2R-2	312.10	17.35
2R-2	312.20	17.40
2R-2	312.30	15.00
2R-2	312.40	18.05
2R-2	312.50	15.55
2R-3	312.70	17.35
2R-3	312.80	16.25
2R-3	312.90	16.90
2R-3	313.00	18.85
2R-3	313.10	16.55
2R-3	313.20	17.85
2R-3	313.30	16.00
2R-3	313.40	17.85
2R-3	313.50	19.60
2R-3	313.60	17.05
2R-3	313.70	16.45
2R-3	313.80	18.25
2R-3	313.90	17.95
2R-3	314.00	20.65
2R-4	314.20	20.00
2R-4	314.30	21.00
2R-4	314.40	21.90
2R-4	314.50	19.35
2R-4	314.60	17.65
2R-4	314.70	18.70
2R-4	314.80	17.55
2R-4	314.90	17.80
2R-4	315.00	18.70
3R-1	319.40	19.60
3R-1	319.50	19.15
3R-1	319.60	18.95
3R-1	319.70	20.90
3R-1	319.80	17.25
3R-1	319.90	18.75
3R-1	320.00	17.80
3R-1	320.10	18.00
3R-1	320.20	16.00
3R-1	320.30	16.45
3R-1	320.40	16.70
3R-1	320.50	16.50
3R-1	320.60	17.35
3R-1	320.70	17.70
3R-2	320.90	15.35
3R-2	321.00	17.25
3R-2	321.10	17.50
3R-2	321.20	18.75
3R-2	321.30	17.35
3R-2	321.40	17.35
3R-2	321.50	17.85
3R-2	321.60	17.35
3R-2	321.70	19.15
3R-2	321.80	19.15
3R-2	321.90	17.80
3R-2	322.00	19.35
3R-2	322.10	15.25
3R-3	322.40	16.95
3R-3	322.50	16.25
3R-3	322.60	15.45
3R-3	322.70	17.00
3R-3	322.80	16.25
3R-3	322.90	16.05
3R-3	323.00	19.20
3R-3	323.10	15.50
3R-3	323.20	15.75
3R-3	323.30	18.15
3R-3	323.40	16.75
3R-3	323.50	16.90
3R-3	323.60	15.95
3R-3	323.70	17.75
3R-4	323.90	16.90
3R-4	324.00	17.25
3R-4	324.10	17.75
3R-4	324.20	16.70
3R-4	324.30	18.95
3R-4	324.40	17.70
3R-4	324.50	18.40
3R-4	324.60	18.90
3R-4	324.70	19.30
3R-4	324.80	19.55
3R-4	324.90	18.70
3R-4	325.00	17.55
3R-4	325.10	18.15
3R-4	325.20	17.60
3R-5	325.40	16.10
3R-5	325.50	14.95
3R-5	325.60	16.30
3R-5	325.70	14.50
3R-5	325.80	16.15
3R-5	325.90	15.25
3R-5	326.00	16.20
3R-5	326.10	15.90
3R-5	326.20	13.55
3R-5	326.30	15.10
3R-5	326.40	14.75
3R-5	326.50	14.45
3R-5	326.60	15.40
3R-6	326.90	16.35
3R-6	327.00	17.40
3R-6	327.10	16.90
3R-6	327.20	16.50
3R-6	327.30	16.90
3R-6	327.40	15.40
3R-6	327.50	15.00
3R-6	327.60	13.95
3R-6	327.70	15.10
3R-6	327.80	15.10
3R-6	327.90	15.00
3R-6	328.00	16.10
4R-1	329.10	15.05
4R-1	329.20	11.55
4R-1	329.30	14.95
4R-1	329.40	14.75
4R-1	329.50	14.70
4R-1	329.60	14.60
4R-1	329.70	14.35
4R-1	329.80	14.60
4R-1	329.90	14.65
4R-1	330.00	14.95
4R-1	330.10	15.20
4R-1	330.20	16.35
4R-1	330.30	13.75
4R-1	330.40	15.35
4R-2	330.60	15.75
4R-2	330.70	14.45
4R-2	330.80	14.15
4R-2	330.90	14.35
4R-2	331.00	14.95
4R-2	331.10	13.45
4R-2	331.20	13.80
4R-2	331.30	14.65
5R-1	338.80	15.60
5R-1	338.90	16.60
5R-1	339.00	15.20
5R-1	339.10	16.70
5R-1	339.20	14.85

Note: Only a portion of this table appears here. The complete table is available in **ASCII.**

Table T14. Thermal conductivity, Site 1203.

Core, section, interval (cm)	Depth (mbsf)	Thermal conductivity (W/[m·K])
197-1203A-		
1R-2, 75	302.25	0.703
2R-3, 75	313.35	0.866
3R-3, 75	323.05	0.881
4R-1, 75	329.75	0.795
5R-1, 75	339.45	0.651
7R-4, 75	363.35	0.990
8R-3, 75	371.55	0.755
9R-2, 75	379.75	1.009
10R-1, 75	387.95	0.696
11R-2, 75	399.15	0.983
12R-2, 82	408.71	1.094
13R-1, 77	417.07	0.900
14R-2, 75	428.25	1.227
17R-4, 92–105	458.48	1.397
18R-2, 115–138	466.45	1.632
19R-5, 41–56	479.59	1.488
20R-5, 115–124	489.74	1.620
21R-4, 85–120	497.95	0.990
24R-1, 38–47	521.88	0.962
25R-2, 23–38	532.69	1.567
26R-3, 0–11	536.43	1.545
27R-1, 54–67	541.34	1.009
28R-1, 92–101	551.42	0.970
29R-1, 43–68	560.63	0.985
31R-1, 38–50	579.78	1.676
32R-3, 88–102	592.66	2.731
33R-2, 79–89	600.32	1.066
34R-2, 44–54	609.81	1.527
35R-2, 58–76	614.13	1.603
36R-5, 19–27	622.86	1.539
37R-2, 65–79	629.65	1.802
38R-3, 67–80	640.55	1.298
39R-2, 104–119	649.05	1.222
40R-5, 110–123	662.32	1.630
41R-4, 48–66	670.83	1.676
42R-5, 115–124	682.34	1.657
44R-3, 93–104	698.56	1.548
45R-4, 63–89	707.96	1.503
46R-4, 49–61	717.47	1.498
47R-3, 49–63	725.47	1.435
48R-3, 0–17	729.87	1.587
49R-4, 0–17	736.05	1.543
50R-1, 0–13	741.60	1.449
51R-3, 29–40	754.45	1.046
52R-4, 44–61	765.63	1.410
53R-1, 81–90	771.21	1.375
54R-2, 99–122	782.49	1.419
55R-3, 15–27	792.80	1.585
56R-5, 7–17	805.15	1.529
57R-3, 118–136	813.08	1.515
58R-4, 0–16	818.87	1.719
59R-2, 113–124	820.99	1.662
60R-1, 79–92	828.89	1.342
61R-1, 22–33	837.92	1.457
62R-2, 4–17	848.94	1.523
63R-4, 10–33	861.56	1.351
64R-1, 134–142	867.94	1.608
65R-2, 0–14	877.70	1.307
66R-2, 39–51	887.69	1.383
67R-4, 9–28	899.89	1.543
68R-1, 101–111	906.01	1.452

Note: This table is also available in **ASCII.**

Table T15. Index properties, Site 1203. (See table note. Continued on next page.)

Core, section, interval (cm)	Depth (mbsf)	Water content (%)		Density (g/cm^3)			Porosity (%)	Void ratio
		Bulk	Dry	Bulk	Dry	Grain		
197-1203A-								
1R-1, 83–85	300.83	48.0	92.2	1.47	0.76	2.45	68.8	2.21
1R-2, 83–85	302.33	54.7	121.0	1.38	0.62	2.39	73.9	2.83
1R-3, 83–85	303.83	55.0	122.0	1.37	0.62	2.32	73.4	2.76
2R-1, 83–85	310.43	60.6	153.9	1.33	0.52	2.50	79.0	3.75
2R-2, 83–85	311.93	58.3	140.0	1.31	0.55	2.18	74.9	2.98
2R-3, 83–85	313.43	42.0	72.5	1.56	0.90	2.52	64.1	1.78
2R-4, 83–85	314.93	58.6	141.6	1.34	0.55	2.36	76.5	3.26
3R-1, 83–85	320.13	65.6	190.9	1.25	3.43	2.20	80.4	4.09
3R-2, 83–85	321.63	56.7	131.0	1.36	0.59	2.39	75.4	3.06
3R-3, 83–85	323.13	39.3	64.7	1.64	1.00	2.69	62.9	1.70
3R-4, 83–85	324.63	44.7	80.8	1.55	0.86	2.66	67.8	2.10
3R-5, 83–85	326.13	48.1	92.6	1.46	0.76	2.42	68.6	2.19
3R-6, 83–85	327.63	57.2	133.8	1.34	0.57	2.26	74.7	2.95
4R-1, 83–85	329.83	53.1	113.3	1.39	0.65	2.31	71.9	2.56
4R-2, 83–85	331.33	51.7	106.9	1.40	0.68	2.33	70.8	2.43
5R-1, 83–85	339.53	61.6	160.2	1.29	0.50	2.23	77.7	3.49
5R-2, 83–85	341.03	60.5	152.9	1.29	0.51	2.15	76.3	3.21
7R-1, 83–85	358.93	36.6	57.8	1.67	1.06	2.62	59.6	1.48
7R-2, 83–85	360.43	46.1	85.5	1.51	0.81	2.55	68.1	2.13
7R-3, 83–85	361.93	35.7	55.5	1.69	1.09	2.63	58.8	1.43
7R-4, 86–88	363.46	38.6	62.9	1.64	1.00	2.62	61.7	1.61
7R-5, 83–85	364.93	35.0	53.8	1.71	1.11	2.69	58.6	1.41
7R-6, 89–91	366.49	35.7	55.6	1.70	1.09	2.67	59.2	1.45
8R-1, 83–85	368.63	36.7	58.0	1.67	1.06	2.64	60.0	1.50
8R-2, 83–85	370.13	42.8	74.8	1.57	0.90	2.63	65.7	1.92
8R-3, 83–85	371.63	50.4	101.7	1.45	0.72	2.53	71.5	2.51
8R-4, 83–85	373.13	46.4	86.6	1.53	0.82	2.66	69.3	2.25
8R-5, 83–85	374.63	41.5	70.8	1.61	0.94	2.69	65.1	1.86
8R-6, 83–85	376.13	54.4	119.5	1.40	0.64	2.53	74.7	2.95
9R-1, 83–85	378.33	53.0	113.0	1.43	0.67	2.60	74.2	2.87
9R-2, 83–85	379.83	39.5	65.3	1.65	1.00	2.73	63.5	1.74
9R-3, 69–71	381.19	41.9	72.1	1.61	0.94	2.73	65.8	1.92
10R-1, 106–108	388.26	64.7	183.4	1.31	0.46	2.71	82.9	4.85
10R-2, 90–92	389.60	40.7	68.8	1.63	0.96	2.74	64.8	1.84
11R-1, 80–82	397.70	38.4	62.3	1.67	1.03	2.74	62.5	1.66
11R-2, 80–82	399.20	41.2	70.1	1.62	0.95	2.72	65.1	1.86
11R-3, 60–62	400.50	35.4	54.7	1.73	1.12	2.77	59.7	1.48
11R-4, 62–64	402.02	47.7	91.1	1.52	0.80	2.71	70.7	2.41
12R-1, 30–32	406.90	31.0	44.9	1.80	1.24	2.72	54.5	1.20
12R-2, 40–42	408.29	33.9	51.2	1.76	1.16	2.77	58.1	1.38
12R-3, 74–76	410.13	39.4	65.0	1.66	1.01	2.78	63.9	1.77
13R-1, 69–71	416.99	45.1	82.3	1.55	0.85	2.71	68.5	2.18
13R-2, 19–21	417.99	34.8	53.4	1.73	1.13	2.75	58.9	1.44
14R-1, 38–40	426.38	32.9	49.1	1.77	1.19	2.75	56.9	1.32
14R-2, 6–8	427.56	32.3	47.7	1.80	1.22	2.82	56.8	1.32
14R-3, 6–8	429.06	34.3	52.3	1.75	1.15	2.76	58.5	1.41
15R-1, 63–65	436.33	33.8	51.0	1.75	1.16	2.74	57.7	1.36
15R-2, 103–105	438.23	31.0	44.8	1.81	1.25	2.77	54.8	1.21
15R-3, 69–71	439.39	25.4	34.1	1.94	1.44	2.78	48.0	0.93
16R-1, 112–114	446.22	29.0	40.9	1.84	1.30	2.72	52.1	1.09
16R-2, 62–64	447.22	27.9	38.7	1.08	0.78	1.10	29.3	0.41
16R-3, 62–64	448.22	23.6	30.9	1.95	1.49	2.71	45.0	0.82
17R-1, 96–98	455.26	26.7	36.5	1.90	1.39	2.75	49.5	0.98
17R-2, 25–27	456.05	22.2	28.5	2.00	1.55	2.74	43.3	0.76
17R-3, 4–6	456.98	16.1	19.2	2.18	1.83	2.79	34.3	0.52
18R-3, 140–150	468.20	2.7	2.8	2.80	2.72	2.94	7.4	0.08
19R-5, 110–114	480.28	5.3	5.6	2.59	2.45	2.83	13.4	0.16
20R-1, 107–109	484.07	4.6	4.9	2.60	2.48	2.82	11.8	0.13
21R-4, 0–11	497.10	23.4	30.5	1.91	1.46	2.59	43.6	0.77
22R-3, 39–48	505.59	20.0	25.1	1.97	1.58	2.57	38.6	0.63
23R-3, 89–91	515.69	46.9	88.3	1.52	0.81	2.67	69.7	2.30
24R-2, 61–63	523.11	36.9	58.6	1.68	1.06	2.70	60.7	1.55
25R-1, 67–69	531.77	4.5	4.7	2.71	2.59	2.94	11.9	0.14
26R-4, 138–140	539.19	32.0	47.0	1.69	1.15	2.43	52.8	1.12
27R-2, 36–38	542.66	40.3	67.5	1.68	1.00	2.95	66.0	1.95
28R-1, 25–27	550.75	31.7	46.4	1.82	1.24	2.84	56.3	1.29

Table T15 (continued).

Core, section, interval (cm)	Depth (mbsf)	Water content (%)		Density (g/cm³)			Porosity (%)	Void ratio
		Bulk	Dry	Bulk	Dry	Grain		
29R-1, 116–118	561.36	10.4	11.6	2.69	2.41	3.31	27.3	0.38
29R-2, 117–119	562.87	31.4	45.8	1.82	1.25	2.82	55.8	1.26
29R-3, 65–67	563.85	33.6	50.6	1.76	1.17	2.79	57.9	1.38
29R-4, 82–84	565.52	20.2	25.3	1.99	1.59	2.61	39.2	0.64
29R-5, 56–58	566.76	21.9	28.0	2.02	1.57	2.77	43.1	0.76
30R-2, 128–141	572.58	6.6	7.1	2.57	2.40	2.87	16.6	0.20
31R-2, 29–33	581.19	2.6	2.6	2.83	2.76	2.97	7.1	0.08
32R-3, 27–31	592.05	8.5	9.2	2.53	2.32	2.93	20.9	0.26
32R-5, 86–91	595.03	28.8	40.5	1.87	1.33	2.83	52.8	1.12
33R-2, 69–71	600.22	44.8	81.2	1.59	0.88	2.86	69.4	2.26
33R-CC, 0–2	602.53	39.3	64.8	1.66	1.01	2.77	63.7	1.75
34R-1, 34–36	608.64	14.7	17.3	2.29	1.96	2.92	33.0	0.49
35R-1, 73–75	613.03	8.4	9.2	2.38	2.18	2.71	19.6	0.24
36R-2, 69–71	619.56	3.5	3.7	2.73	2.63	2.91	9.4	0.10
36R-7, 71–73	626.08	17.7	21.5	2.09	1.72	2.69	36.1	0.57
36R-8, 36–38	627.03	20.9	26.5	2.03	1.61	2.74	41.5	0.71
37R-1, 49–58	627.99	20.0	25.0	2.06	1.65	2.75	40.2	0.67
37R-2, 47–66	629.47	5.0	5.3	2.69	2.56	2.95	13.2	0.15
38R-4, 48–53	641.76	21.2	26.8	2.03	1.60	2.76	41.9	0.72
39R-3, 31–41	649.77	29.9	42.6	1.82	1.28	2.73	53.2	1.14
40R-4, 105–107	660.77	5.5	5.8	2.53	2.39	2.77	13.5	0.16
41R-3, 107–109	669.92	8.7	9.5	2.37	2.16	2.70	20.1	0.25
42R-1, 77–80	676.27	5.7	6.1	2.69	2.54	2.99	15.1	0.18
43R-1, 77–83	685.87	4.9	5.2	2.63	2.50	2.86	12.6	0.14
44R-3, 31–33	697.94	5.0	5.3	2.58	2.45	2.80	12.6	0.14
45R-2, 135–137	705.95	6.4	6.9	2.43	2.28	2.68	15.3	0.18
46R-2, 92–94	714.90	5.6	5.9	2.60	2.45	2.86	14.2	0.17
47R-2, 101–103	724.78	5.8	6.2	2.74	2.58	3.06	15.5	0.18
48R-1, 10–12	727.20	6.9	7.4	2.55	2.37	2.87	17.2	0.21
49R-3, 105–107	735.60	5.1	5.4	2.71	2.57	2.97	13.4	0.16
51R-1, 130–132	752.50	23.5	30.7	1.99	1.52	2.79	45.5	0.84
51R-4, 89–91	756.41	7.7	8.3	2.61	2.41	2.99	19.6	0.24
52R-2, 102–104	763.32	7.7	8.3	2.63	2.42	3.02	19.8	0.25
53R-4, 31–35	775.21	10.0	11.1	2.51	2.26	2.98	24.4	0.32
54R-5, 65–69	786.48	8.2	8.9	2.54	2.34	2.93	20.3	0.25
55R-3, 125–127	793.90	7.5	8.1	2.56	2.37	2.92	18.8	0.23
56R-3, 121–123	803.40	10.0	11.2	2.45	2.21	2.91	24.0	0.32
57R-4, 0–7	813.41	9.7	10.7	2.49	2.24	2.93	23.5	0.31
58R-2, 73–75	816.74	5.2	5.5	2.82	2.68	3.13	14.4	0.17
59R-5, 11–17	824.21	10.6	11.8	2.41	2.16	2.87	24.9	0.33
60R-4, 50–52	832.64	9.9	10.9	2.46	2.21	2.90	23.7	0.31
61R-1, 131–133	839.01	6.2	6.7	2.62	2.46	2.92	16.0	0.19
62R-2, 0–5	848.90	10.1	11.3	2.47	2.22	2.94	24.5	0.32
63R-2, 128–133	859.74	8.6	9.5	2.55	2.33	2.96	21.5	0.27
64R-1, 24–30	866.84	25.3	33.9	1.95	1.46	2.82	48.2	0.93
65R-1, 95–104	877.15	20.0	25.0	2.13	1.71	2.93	41.8	0.72
65R-4, 117–125	881.11	10.8	12.2	2.43	2.17	2.92	25.8	0.35
66R-1, 72–74	886.52	21.0	26.6	2.00	1.58	2.67	41.0	0.69
66R-3, 18–20	888.94	9.7	10.8	2.45	2.22	2.89	23.3	0.30
67R-2, 34–36	897.20	5.1	5.3	2.73	2.59	2.99	13.5	0.16
68R-3, 42–44	908.42	9.7	10.7	2.46	2.22	2.89	23.2	0.30

Note: This table is also available in **ASCII.**

Table T16. *P*-wave velocity, Site 1203.

Core, section, interval (cm)	Depth (mbsf)	Direction	Velocity (m/s)
197-1203A-			
1R-1, 78	300.78	x	1525.0
1R-2, 72	302.22	x	1525.9
1R-3, 73	303.73	x	1546.3
2R-1, 92	310.52	x	1550.3
2R-2, 59	311.69	x	1571.2
2R-3, 57	313.17	x	1565.3
2R-4, 70	314.80	x	1542.2
3R-1, 100	320.30	x	1556.7
3R-2, 57	321.37	x	1550.4
3R-3, 118	323.48	x	1532.1
3R-4, 130	325.10	x	1532.9
3R-5, 126	326.56	x	1538.8
3R-6, 126	328.06	x	1554.0
4R-1, 100	330.00	x	1541.2
4R-2, 49	330.99	x	1542.4
5R-1, 93	339.63	x	1546.0
5R-2, 52	340.71	x	1543.7
7R-1, 120	359.30	x	1534.6
7R-2, 55	360.15	x	1542.7
7R-3, 89	361.99	x	1567.0
7R-4, 98	363.58	x	1532.5
7R-5, 48	364.58	x	1558.8
7R-6, 70	366.30	x	1573.1
8R-1, 76	368.56	x	1581.4
8R-2, 79	370.09	x	1536.2
8R-3, 93	371.73	x	1558.1
8R-4, 58	372.88	x	1532.1
8R-5, 111	374.91	x	1563.5
8R-6, 56	375.86	x	1604.7
9R-1, 115	378.65	x	1539.0
9R-2, 96	379.96	x	1528.4
9R-3, 46	380.96	x	1591.1
10R-1, 113	388.33	x	1571.5
10R-2, 101	389.70	x	1596.3
11R-1, 60	397.49	x	1559.1
11R-2, 97	399.37	x	1633.9
11R-3, 75	400.65	x	1580.0
11R-4, 45	401.85	x	1642.8
12R-1, 108	407.67	x	1544.8
12R-2, 86	408.75	x	1632.2
12R-3, 51	409.90	x	1659.4
13R-1, 110	417.40	x	1629.6
13R-2, 63	418.43	x	1647.7
14R-1, 88	426.88	x	1519.2
14R-2, 112	428.62	x	1799.6
14R-3, 64	429.64	x	1574.1
15R-1, 72	436.42	x	1514.7
15R-2, 94	438.14	x	1585.4
15R-3, 80	439.50	x	1762.1
16R-1, 54	445.64	x	1578.7
16R-2, 54	447.14	x	1570.9
16R-3, 43	448.03	x	1653.9
17R-1, 43	454.73	x	1675.9
17R-2, 70	456.50	x	1788.2
17R-3, 55	457.49	x	2910.4
17R-4, 31	457.87	x	4777.9
17R-4, 31	457.87	y	4867.8
17R-4, 31	457.87	z	4824.9
17R-4, 110	458.66	x	4635.6
17R-4, 110	458.66	y	4938.9
17R-4, 110	458.66	z	4636.2
18R-1, 97	464.77	x	6693.7
18R-1, 98	464.78	x	5258.4
18R-1, 98	464.78	y	5091.6
18R-1, 98	464.78	z	4997.6
18R-2, 66	465.96	x	4817.0
18R-2, 66	465.96	y	5053.2
18R-2, 66	465.96	z	4939.9
18R-3, 46	467.26	x	4609.8
18R-3, 46	467.26	y	5202.0
18R-3, 46	467.26	z	5226.6
19R-1, 23	473.63	x	4724.1
19R-1, 23	473.63	y	5104.9
19R-1, 23	473.63	z	4904.5
19R-1, 96	474.36	x	5155.6
19R-1, 96	474.36	y	5327.0
19R-1, 96	474.36	z	4980.2
19R-2, 134	476.24	x	4858.6
19R-2, 134	476.24	y	4980.9
19R-2, 134	476.24	z	5026.3
19R-3, 29	476.58	x	6016.6
19R-3, 30	476.59	x	4854.0
19R-3, 30	476.59	z	5155.8
19R-3, 30	476.59	y	5300.4
19R-3, 141	477.70	x	4970.4
19R-3, 141	477.70	z	5337.0
19R-3, 141	477.70	y	5506.5
19R-4, 41	478.17	x	4889.9
19R-4, 41	478.17	y	5035.9
19R-4, 41	478.17	z	4914.2
19R-4, 111	478.87	x	4334.0
19R-4, 111	478.87	y	4877.6
19R-4, 111	478.87	z	4893.6
19R-5, 35	479.53	x	4748.0
19R-5, 35	479.53	y	5401.9
19R-5, 35	479.53	z	5121.7
19R-5, 86	480.04	x	5126.7
19R-5, 86	480.04	y	4995.8
19R-5, 86	480.04	z	5195.9
20R-1, 32	483.32	x	4698.0
20R-1, 32	483.32	z	5381.7
20R-3, 17	486.17	x	4849.9
20R-4, 127	488.53	x	4708.5
20R-4, 127	488.53	z	5031.1
21R-1, 71	493.31	x	2718.0
21R-3, 41	496.01	x	2772.5
21R-3, 41	496.01	x	2935.1
21R-3, 41	496.01	z	2916.8
22R-2, 111	504.81	x	2985.5
22R-2, 112	504.82	x	3084.5
22R-2, 112	504.82	z	3103.8
23R-1, 28	512.18	x	2690.6
23R-3, 14	514.94	x	2589.5
23R-3, 14	514.94	z	2494.5
24R-1, 31	521.81	x	1995.0
24R-1, 31	521.81	z	1811.7
24R-1, 86	522.36	x	2275.5
24R-2, 104	523.54	x	2294.4
24R-2, 104	523.54	z	2354.4
25R-1, 30	531.40	x	4478.0
25R-1, 30	531.40	z	4565.9
25R-1, 124	532.34	x	3964.6
26R-1, 11	534.91	x	3861.6
26R-1, 11	534.91	z	4167.0
26R-2, 30	536.09	x	4155.0
26R-4, 23	538.04	x	2038.4
26R-4, 23	538.04	z	2081.0
26R-5, 34	539.57	x	2010.4
27R-1, 63	541.43	x	2331.3
27R-1, 63	541.43	x	2416.2
27R-1, 63	541.43	z	2525.3
29R-4, 71	565.41	x	2501.6
29R-4, 71	565.41	z	2548.4
29R-5, 7	566.27	x	2592.5
29R-5, 7	566.27	x	2670.8
29R-5, 7	566.27	z	2674.5
31R-1, 17	579.57	x	5610.9
31R-1, 17	579.57	z	5645.4
32R-1, 83	589.83	x	1846.1
32R-1, 83	589.83	z	1770.6
32R-2, 29	590.57	x	4022.9
32R-2, 29	590.57	z	4285.4
32R-6, 8	595.75	x	1891.8
32R-6, 8	595.75	z	1848.0
33R-1, 26	598.86	x	1980.8
33R-1, 26	598.86	z	1959.3
34R-1, 90	609.20	x	3487.5
34R-1, 90	609.20	z	3770.1
35R-1, 65	612.95	x	3542.0
35R-1, 65	612.95	z	3324.4
36R-1, 27	618.17	x	5179.6
36R-1, 27	618.17	z	5496.7
36R-4, 90	622.35	x	4783.6
36R-4, 90	622.35	z	4946.7
37R-3, 22	630.72	x	5617.5
37R-3, 22	630.72	x	5886.5
37R-3, 22	630.72	z	5641.4
37R-3, 22	630.72	z	5971.9
38R-1, 111	638.21	x	5581.9
38R-1, 111	638.21	z	5779.8
38R-4, 6	641.34	x	5056.2
38R-4, 6	641.34	z	5410.6
39R-4, 124	652.09	x	4617.1
39R-4, 124	652.09	z	5365.4
40R-1, 16	656.36	x	4721.4
40R-1, 16	656.36	z	5059.1
40R-4, 15	659.87	x	4627.4
40R-4, 15	659.87	z	4923.6
41R-1, 17	666.07	x	4671.4
41R-1, 17	666.07	z	4700.4
41R-4, 145	671.80	x	4860.9
41R-4, 145	671.80	z	5098.1
42R-1, 78	676.28	x	4300.1
42R-1, 78	676.28	z	4326.2
42R-4, 131	681.09	x	4543.7
42R-4, 131	681.09	z	4606.0
42R-5, 134	682.53	x	4859.0
42R-5, 134	682.53	z	5253.6
44R-1, 133	696.03	x	4575.7
44R-1, 133	696.03	z	4716.3
44R-4, 127	700.24	x	4231.7
44R-4, 127	700.24	z	4473.9
45R-1, 55	703.65	x	4582.0
45R-1, 55	703.65	z	4781.7
45R-4, 142	708.75	x	4371.2
45R-4, 142	708.75	z	4678.6
46R-1, 31	713.01	x	4045.6
46R-1, 31	713.01	z	4264.5
46R-4, 12	717.10	x	4656.1
46R-4, 12	717.10	z	4434.1
47R-2, 87	724.64	x	4075.6
47R-2, 87	724.64	z	4369.2
47R-4, 18	725.87	x	4122.4
47R-4, 18	725.87	z	4241.2
48R-1, 86	727.96	x	3631.1
48R-1, 86	727.96	z	3694.4
48R-3, 38	730.25	x	4304.2
48R-3, 38	730.25	z	4615.6
49R-1, 18	732.18	x	4418.9
49R-1, 18	732.18	z	4715.1
49R-4, 142	737.47	x	4459.5
49R-4, 142	737.47	z	4487.2

Note: Only a portion of this table appears here. The complete table is available in **ASCII.**

Table T17. Comparison of rock content inferred from log response and core lithology over the borehole depth interval 220–930 mbsf.

Rock type:	Basalt (%)			Volcaniclastics (%)	Sediments (%)
	Massive	Pillow	Total		
Log response	5.80	38.60	44.40	20.60	35.00
Core lithology			45.80	19.70	34.50

Table T18. SIOSEIS process parameters for predictive deconvolution, bandpass filtering, and finite-difference migration.

```
Line 1:
  decon
    fno 2218 lno 2218 prewhi 1 sedts 3.30 4.00 4.10 5.0 seats 3.30 4.00 4.10 4.6 fillen .045 .400 pdist .005 end
    fno 2338 lno 2338 prewhi 1 sedts 3.37 4.05 4.15 5.0 seats 3.37 4.05 4.15 4.6 fillen .045 .400 pdist .005 end
    fno 2360 lno 2360 prewhi 1 sedts 3.41 4.09 4.19 5.0 seats 3.41 4.09 4.19 4.6 fillen .045 .400 pdist .005 end
    fno 2408 lno 2408 prewhi 1 sedts 3.50 4.13 4.23 5.0 seats 3.50 4.12 4.23 4.6 fillen .045 .400 pdist .005 end
    fno 2458 lno 2458 prewhi 1 sedts 3.62 4.18 4.28 5.0 seats 3.53 4.18 4.28 4.6 fillen .045 .400 pdist .005 end
    end
  filter
    fno 2218 lno 2458 pass 40 150 fillen 111 end
    end
  fdmigr
    fno 2218 lno 2218 vtp 1500 3.32 1580 3.95 4000 4.10 4500 4.20 4750 5
    dx 19.6 nx 441 bpad 100 epad 100 tsteps 3.3 .1 3.90 .05 4.6 .02 end
    fno 2338 lno 2338 vtp 1500 3.42 1580 4.00 4000 4.15 4500 4.25 4750 5
    dx 19.6 nx 441 bpad 100 epad 100 tsteps 3.3 .1 3.90 .05 4.6 .02 end
    fno 2360 lno 2360 vtp 1500 3.46 1580 4.04 4000 4.19 4500 4.29 4750 5
    dx 19.6 nx 441 bpad 100 epad 100 tsteps 3.3 .1 3.90 .05 4.6 .02 end
    fno 2408 lno 2408 vtp 1500 3.55 1580 4.08 4000 4.23 4500 4.33 4750 5
    dx 19.6 nx 441 bpad 100 epad 100 tsteps 3.3 .1 3.90 .05 4.6 .02 end
    fno 2458 lno 2458 vtp 1500 3.67 1580 4.13 4000 4.28 4500 4.38 4750 5
    dx 19.6 nx 441 bpad 100 epad 100 tsteps 3.3 .1 3.90 .05 4.6 .02 end
    end
Line 3:
  decon
    prewhi 1 sedts 3.4 4.1 4.2 5.1 seats 3.4 4.1 4.2 4.6 fillen .045 .400 pdist .005 end
    end
  filter
    fno 3928 lno 4168 pass 40 100 fillen 111 end
    end
  fdmigr
    fno 3928 lno 3928  vtp 1500 3.540 1580 4.05 4000 4.20 4500 4.30 4750 5
    dx 17.6 nx 441 bpad 100 epad 100 tsteps 3.4 .1 4.0 .05 4.5 .02 end
    fno 4010 lno 4010  vtp 1500 3.510 1580 4.06 4000 4.21 4500 4.30 4750 5
    dx 17.6 nx 441 bpad 100 epad 100 tsteps 3.4 .1 4.0 .05 4.5 .02 end
    fno 4070 lno 4070  vtp 1500 3.480 1580 4.05 4000 4.20 4500 4.30 4750 5
    dx 17.6 nx 441 bpad 100 epad 100 tsteps 3.4 .1 4.0 .05 4.5 .02 end
    fno 4146 lno 4146  vtp 1500 3.500 1580 4.04 4000 4.20 4500 4.30 4750 5
    dx 17.6 nx 441 bpad 100 epad 100 tsteps 3.4 .1 4.0 .05 4.5 .02 end
    fno 4168 lno 4168  vtp 1500 3.510 1580 4.04 4000 4.20 4500 4.30 4750 5
    dx 17.6 nx 441 bpad 100 epad 100 tsteps 3.4 .1 4.0 .05 4.5 .02 end
    end
Line 6:
  decon
    fno 7607 lno 7607 prewhi 1 sedts 3.30 4.05 4.15 5.0 seats 3.30 4.05 4.15 4.6 fillen .045 .400 pdist .005 end
    fno 7697 lno 7697 prewhi 1 sedts 3.38 4.05 4.15 5.0 seats 3.38 4.05 4.15 4.6 fillen .045 .400 pdist .005 end
    fno 7817 lno 7817 prewhi 1 sedts 3.55 4.13 4.23 5.0 seats 3.50 4.13 4.23 4.6 fillen .045 .400 pdist .005 end
    fno 7847 lno 7847 prewhi 1 sedts 3.60 4.15 4.25 5.0 seats 3.50 4.15 4.25 4.6 fillen .045 .400 pdist .005 end
    end
  filter
    fno 7607 lno 7847 pass 40 100 fillen 111 end
    end
  fdmigr
    fno 7607 lno 7607 vtp 1500 3.33 1580 4.00 4000 4.15 4500 4.25 4750 5
    dx 18.8 nx 441 bpad 100 epad 100 tsteps 3.3 .1 3.95 .05 4.6 .02 end
    fno 7698 lno 7698 vtp 1500 3.40 1580 4.00 4000 4.15 4500 4.25 4750 5
    dx 18.8 nx 441 bpad 100 epad 100 tsteps 3.3 .1 3.95 .05 4.6 .02 end
    fno 7752 lno 7752 vtp 1500 3.47 1580 4.06 4000 4.21 4500 4.31 4750 5
    dx 18.8 nx 441 bpad 100 epad 100 tsteps 3.3 .1 3.95 .05 4.6 .02 end
    fno 7816 lno 7816 vtp 1500 3.57 1580 4.08 4000 4.23 4500 4.33 4750 5
    dx 18.8 nx 441 bpad 100 epad 100 tsteps 3.3 .1 3.95 .05 4.6 .02 end
    fno 7847 lno 7847 vtp 1500 3.64 1580 4.09 4000 4.24 4500 4.34 4750 5
    dx 18.8 nx 441 bpad 100 epad 100 tsteps 3.3 .1 3.95 .05 4.6 .02 end
    end
```

Notes: Processing was performed in the order shown. See **http://sioseis.ucsd.edu.**